Super-resolved imaging of proteins at colloidal interfaces

Abbas Jabermoradi

Propositions

1. Super-resolution microscopy is the best tool for mapping distributions of emulsifiers at colloidal interfaces.
   (this thesis)

2. Resolution below the diffraction limit, combined with molecular specificity, highlights protein coverage at interfaces as a key factor in oxidation susceptibility.
   (this thesis)

3. Emphasizing biophysics in the interplay between food and health is key to elucidating lifestyle-related diseases.

4. Personal development goals, mirroring Schrödinger's cat, exist in states both achievable and elusive, unveiling their true state only through dedicated effort.

5. The burden of knowledge is its dissemination. (Imam Ali ibn Abi Talib)

6. Double ethical standards threaten global justice, particularly the protection of human rights in international conflicts.

Propositions belonging to the thesis, entitled

Super-resolved imaging of proteins at colloidal interfaces

Abbas Jabermoradi
Wageningen, 15 March 2024

Super-resolved imaging of proteins at colloidal interfaces

Abbas Jabermoradi

Thesis committee

Promotors
Prof. Dr John P.M. van Duynhoven
Special professor, Magnetic Resonance in Relation to Food
Wageningen University & Research

Dr Johannes Hohlbein
Associate professor, Laboratory of Biophysics
Wageningen University & Research

Other members
Prof. Dr Jasper van der Gucht, Wageningen University & Research
Prof. Dr Dominik Wöll, RWTH Aachen University, Germany
Dr Claire Berton-Carabin, INRAE, Paris, France
Dr Carlas S. Smith, Delft University of Technology

This research was conducted under the auspices of VLAG Graduate School (Biobased, Biomolecular, Chemical, Food, and Nutrition sciences)

Super-resolved imaging of proteins at colloidal interfaces

Abbas Jabermoradi

Thesis

submitted in fulfilment of the requirements for the degree of doctor
at Wageningen University
by the authority of the Rector Magnificus,
Prof. Dr C Kroeze,
in the presence of the
Thesis Committee appointed by the Academic Board
to be defended in public
on Friday 15 March 2024
at 11:00 a.m. in the Omnia Auditorium.

Abbas Jabermoradi

Super-resolved imaging of proteins at colloidal interfaces,
172 pages.
PhD thesis, Wageningen University, Wageningen, the Netherlands (2024)
With references, with summary in English

DOI: https://doi.org/10.18174/647010

Contents

Abbreviations

AAB	amplitude of arrangement of proteins broadening
AB	arrangement of proteins broadening
AFM	atomic force microscopy
ALP	amplitude of localization precision
AO	adaptive optics
ARB	amplitude of RPD broadening
AU	airy unit
BFP	back focal plane
BME	beta-mercaptoethanol
BSA	bovine serum albumin
CL	collimating lens
CLSM	confocal laser scanning microscopy
DM	deformable mirror
DMSO	dimethyl sulfoxide
dSTORM	direct stochastic optical reconstruction microscopy
ELISA	enzyme-linked immunosorbent assay
FITC	fluorescein isothiocyanate
FOV	fields of view
FRC	Fourier ring correlation
FTM	fast temporal median
FW90M	full width at 90% of the maximum
FWHM	full width at half maximum
HDL	high-density lipoprotein
HILO	highly inclined and laminated optical sheet
HPH	high-pressure homogenizer
LDL	low-density lipoprotein
LMW	low molecular weight
LP	localization precision
MES	2-N-porpholino ethane sulfonic acid
MINFLUX	minimal photon flux
MLE	maximum likelihood estimation
MMF	multi-mode fiber
MNND	mean nearest neighbor distance
NA	numerical aperture
NND	nearest neighbor distance

PAINT	point accumulation for imaging in nanoscale topography
PALM	photoactivated localization microscopy
PBS	phosphate-buffered saline
PC	phosphatidylcholine
PEG	polyethylene glycol
PERPL	pattern extraction from relative positions of localizations
PSF	point spread function
QE	quantum efficiency
RB	RPD broadening
RCM	re-scan confocal microscopy
REALM	robust and effective adaptive optics in localization microscopy
RESOLFT	reversible, saturable optical linear fluorescence transitions
ROI	region of interest
RPD	relative position distribution
RR	radius of averaged droplets
SDS	sodium dodecyl sulfate
SLM	spatial light modulators
SMLM	single molecule localization microscopy
STED	stimulated emission depletion
TIRF	total internal reflection fluorescence
TL	TIRF lens
TS	top hat beam shaper
ZOLA	Zernike optimized localization approach

1

Introduction

1.1 A closer look at food emulsions

When two immiscible liquids, such as water and oil, come into contact with each other, the differences in their intermolecular forces prevent them from mixing. Water molecules are polar and form strong hydrogen bonds with each other, while oil molecules are nonpolar and interact through weaker van der Waals forces. As a result, these two types of molecules do not mix homogeneously, leading to the formation of a distinct interface. This interface does not only represent a geometric boundary but also serves as a transitional region for the molecular properties of the two phases. Upon mixing these phases, one liquid disperses within the other. Molecules at the interface have higher energy due to exposure to a different environment. In response, thermodynamic forces compel the dispersed droplets to become spherical, minimizing the contact area between the phases[1]. This process leads to the formation of emulsions: the droplets of one liquid are dispersed within the other liquid. The size of these droplets plays a crucial role in determining the properties of the emulsion. To illustrate, when a single droplet with a 1 μm radius is split into eight droplets with 0.5 μm radii to have the same volume, the total surface area doubles from around 13 μm^2 to 25 μm^2, leading to an unfavourable rise in Gibbs free energy. To minimize this energy, emulsions naturally tend to evolve into fewer, larger droplets.

While all emulsions are thermodynamically unstable, they can exhibit kinetic stability over certain periods of time. Achieving kinetic stability in food-related emulsions requires the addition of thickening agents or emulsifiers. Thickeners such as carrageenan, agar, guar gum, xanthan gum, and pectin[2–4] prevent phase separation by increasing the viscosity of the aqueous phase, which slows down the movement of the dispersed droplets. This viscosity enhancement also modifies the texture and mouthfeel of the final product. Emulsifiers, on the other hand, adsorb onto the interface and create a protective layer around the droplets, hindering their ability to coalesce. Emulsifiers are essential ingredients in creating and stabilizing emulsion-based food products[5]. In the food industry, a broad array of emulsifiers can be employed, including both natural and synthetic varieties. Natural emulsifiers include proteins, polysaccharides, phospholipids, and other biopolymers sourced from plants and animals. With the emulsifiers playing a pivotal role in stabilizing emulsions, they indirectly contribute to functional enhancements, such as improved texture and modified mouthfeel. Conversely, synthetic food emulsifiers such as Tween20 are specifically designed to exhibit outstanding emulsifying capabilities[6].

The process of producing emulsions can be accomplished through a variety of methods, each suitable for specific needs based on factors such as desired droplet sizes, ingredients used, and the required scale of production. High-shear dispersion uses mechanical force to break down the particles in a fluid, reducing their size and improving their distribution[7,8]. Colloid mills function by applying extreme mechanical shear to the mixture, facilitating the dispersion of one phase into another, with typical shear rates ranging from 10^4 to 10^6 s^{-1}[9]. High-pressure homogenizers work by forcing the emulsion through a narrow gap under pressures up to 2,000 bar. This process results in the breakup of droplets and disperses them evenly throughout the liquid[10]. Micro fluidization also utilizes high pressure but introduces the concept of 'fixed-geometry' interaction chambers where the mixture is passed multiple times to achieve a consistent and uniform size reduction[11]. Ultrasonic homogenizers use ultrasonic waves to create cavitation bubbles in the fluid, which, upon collapse, generate strong hydrodynamic forces that break up and disperse particles or droplets[12,13]. Typically, a two-step process is employed to produce emulsions with sub-micron droplets. This process starts with a pre-homogenization step that generates an emulsion with coarse droplets. Subsequently, one of the aforementioned high-shear techniques is applied to further reduce the droplet size[14].

1.1.1 Physical instability of emulsions

Once an emulsion has formed, it will destabilize over time due to several physical and chemical mechanisms[15]. Physical instabilities stem from changes in the spatial distribution or structural organization of molecules at the interface, which can lead to phenomena such as creaming, flocculation, coalescence, and Ostwald ripening (**Figure 1.1**). **Creaming** is a common form of physical instability observed in oil-in-water emulsions, where the lower-density oil droplets, influenced by buoyancy, migrate upward to form a creamy layer at the top of the emulsion[16,17]. **Flocculation**, another such mechanism, occurs when two or more droplets aggregate while maintaining their individuality, forming larger entities more susceptible to gravitational forces with no alteration in droplet radii[18]. **Coalescence** happens when two or more oil droplets collide due to Brownian motion, leading to rupture of the interfacial film and subsequent fusion into larger droplets[19]. This mechanism predominantly occurs when droplets are closely spaced, and it relies heavily on the nature of the emulsifier used for stabilization. Unlike creaming and flocculation, coalescence reduces the interfacial area between phases, thereby moving the system toward a more thermodynamically stable state. In the realm of food emulsions, coalescence can result in the formation of an oil layer on top of the emulsion[20]. **Ostwald ripening** is another mechanism predominantly observed in systems where the dispersed phase has some degree of solubility in the continuous phase. In this phenomenon, larger droplets grow at the expense of smaller ones in a polydisperse emulsion, facilitated by the higher internal Laplace pressure within smaller droplets, promoting mass transfer through the adjacent aqueous phase[21]. However, in food emulsions that utilize vegetable oils containing slowly diffusing long-chain triacylglycerols, Ostwald ripening tends to be negligible[22].

The rate at which these instability mechanisms develop depends on the emulsion properties. For instance, physical instability mechanisms rely on the strength of interactions between oil droplets[23]. During flocculation, adsorbed molecules can generate electrostatic or steric repulsion between droplets, the strength of which depends on factors like molecular structure and environmental conditions such as ionic strength and pH. Coalescence, on the other hand, involves the draining of the continuous phase and the subsequent creation of a rupture in the interfacial layers between droplets, a process akin to dilatational deformation[24]. The rate of coalescence can be influenced by the mobility of adsorbed molecules and the viscoelasticity of the interfacial layer[25].

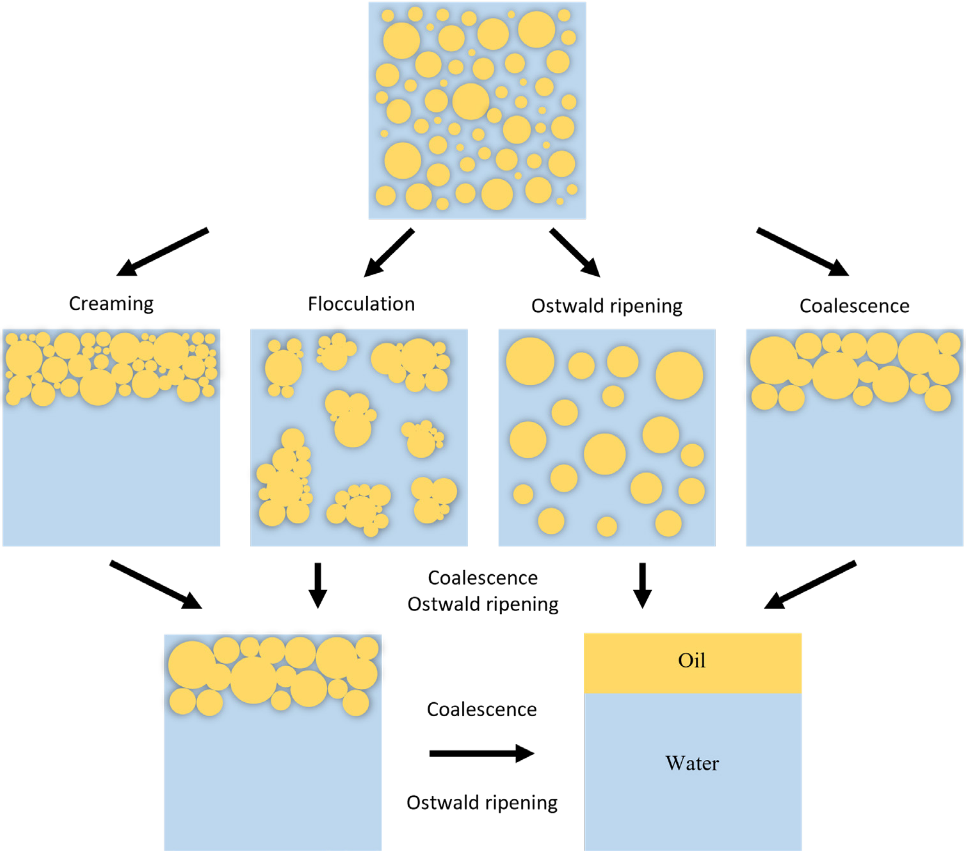

Figure 1.1. Schematic illustration of mechanisms that can destabilize an emulsion: creaming, flocculation, coalescence, and Ostwald ripening. During the creaming, oil droplets of lower density move upward due to buoyancy, forming a distinct creamy layer. Flocculation is illustrated by the aggregation of droplets. Coalescence is displayed by the merging of two droplets into a larger droplet, thereby reducing the interfacial area. Lastly, Ostwald ripening is depicted by the gradual enlargement of larger droplets due to mass transfer from smaller ones via the intervening aqueous phase. These processes often influence each other over time, contributing to changes in the overall stability of the emulsion.

1.1.2 Chemical instability of emulsions: oxidation

Chemical instability of emulsions arises from the presence of catalytic activity at droplet interfaces, which is the main cause of lipid and protein oxidation in food emulsions. Here, the affinity of droplet interfaces for transition metal ions brings them close to the oil phase. These ions catalyze radical formation of hydroperoxides, which in turn form lipid radicals that consume oxygen in their reaction to peroxides. These reactions are propagated by redox cycling of transition metal ions at the droplet interface[26].

The oxidative stability of an oil-in-water emulsion is influenced by the strength of the affinity of the interfacial layer for transition metal ions. This property can be shaped by emulsifiers and co-emulsifiers that can either inhibit or promote oxidation[27]. For instance, proteins acting as emulsifiers can play both pro- and anti-oxidation roles in lipid oxidation. On one hand, the proteins can strongly bind transition metals at pH levels above their isoelectric point, thereby delaying oxidation[28]. On the other hand, proteins adsorbed at the interfaces can undergo oxidative reactions themselves, generating protein radicals[29–31]. These radicals can further interact with unsaturated lipids, propelling the chain reaction of lipid oxidation. Additionally, the oxidative breakdown of proteins may release secondary compounds that can promote oxidation[32].

1.2 Exploring complexity in food emulsions: The case of mayonnaise

Mayonnaise is a widely consumed oil-in-water food emulsion. Vegetable oil, water, egg yolk, vinegar, and salt form the core ingredients of mayonnaise. Egg yolk can be separated into egg yolk granules and yellow plasma through mild centrifugation. Egg yolk granules contain emulsifying lipoproteins and proteins, with the protein phosvitin constituting about 16% w/w[33,34]. Structurally, phosvitin is a protein with around 200 amino acids, a molar mass of 35-40 kDa, and a high degree of phosphorylation[35]. The structure of phosvitin resembles a triblock copolymer, with a long central hydrophilic chain of about 100 phosphorylated serine residues flanked by two hydrophobic amino acid blocks[34]. When the pH is higher than the isoelectric point of phosvitin, which is around pH 2[36], the middle block of phosvitin becomes negatively charged due to its many phosphoric acid groups[37]. Owing to its abundant charged phosphoserine groups, phosvitin can chelate multivalent ions, including magnesium, calcium, and iron. The chelation capacity varies with pH and ionic strength[38].

In mayonnaise, phosvitin stabilizes the emulsion despite not being a potent surfactant[39]. At neutral pH values, chelation of ferric ions by phosvitin has been suggested to play an anti-oxidant role[40,41]. However, under the acidic conditions of mayonnaise, the affinity for ferric ions is lower, and the redox couple of ferric/ferrous ions can then act as pro-oxidant[42,43].

In addition to phosvitin, egg yolk is also a rich source of lipoproteins, which are nano-assemblies of proteins and lipids. The dry matter of egg yolk contains 68% of low-density lipoprotein (LDL) and 16% of high-density lipoprotein (HDL)[44]. HDL has a higher protein content and fewer lipids than LDL and is primarily confined within the egg yolks' non-dissolved granules, exhibiting limited solubility and emulsifying properties under neutral scenarios[33,45]. LDL particles, spherical in shape and measuring between 17-60 nm in diameter[46], possess a lipid center filled with triglycerides and cholesterol esters in a fluid state. This core is encased by a layer of phospholipids and proteins. LDL particles have a density of 0.982 g/mL, are soluble in water-based media and are unaffected by variations in pH or ionic conditions[33,47]. The stability of the LDL structure is largely attributed to the presence of phospholipids, as the association forces are predominantly hydrophobic[48]. Additionally, cholesterol is integrated into the phospholipid layer, increasing its structural rigidity. The surface of LDL exhibits a mosaic pattern[49], wherein lipids and proteins reside in separate zones without forming close connections. Compositionally, LDL encompasses 11-17% proteins and 83-89% lipids, with the lipid portion being made of 69% triglycerides, 26% phospholipids, and 5% cholesterol[50]. LDL particles interact with interfaces, whereby neutral lipids, phospholipids, and proteins are released from the lipoprotein and dispersed over the interface.

Among the proteins present in LDL, apolipoprotein B (apoB) is the most abundant one[44,47]. ApoB displays stronger interfacial adsorption than phosvitin, attributable to its flexible structure and higher surface hydrophobicity[51]. Moreover, as the emulsifiers present in egg yolk ingredients are added in excess to what is needed to stabilize the droplet interfaces, a major fraction ends up in the aqueous phase of mayonnaise, adding to the overall complexity of its composition and structure (**Figure 1.2**). Apoproteins, in their intact LDL particle state or when distributed at these boundaries, can undergo oxidation reactions. The oxidation of proteins within LDL was examined using UV/VIS and fluorescence spectroscopy, which indicated a rise in fluorescence intensity in the 430 nm emission range following auto-oxidation[52,53]. Recent studies have delved into the formation of oxidative protein radicals in LDL particles, both in their original state and when dispersed at droplet interfaces or within the aqueous phase[54].

To shed light on the structural complexity of mayonnaise outlined in **Figure 1.2**, it is imperative to commence studies at the droplet interface. By employing advanced microscopy techniques, this thesis aims to discern the spatial distribution of protein emulsifiers at the interface with molecular specificity and determine whether the emulsifiers are distributed heterogeneously or homogeneously. Of particular interest is the competition between low-molecular weight surfactants and proteins at the droplet interface. Additionally, the measurements will allow to ascertain which protein is more vulnerable to oxidation: is it phosvitin, due to its iron-binding capability, or apoproteins that deteriorate more swiftly?

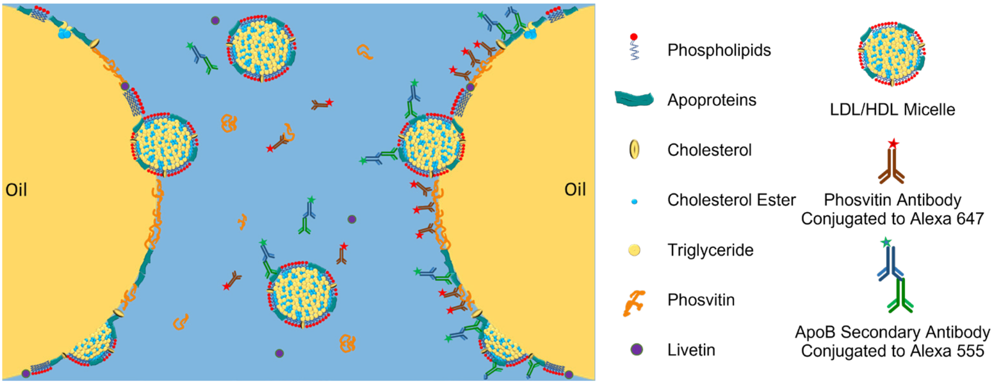

Figure 1.2. Schematic representation of the microstructure of mayonnaise. The diagram presents two oil droplets suspended in the aqueous phase, highlighting the adsorption process of key egg yolk constituents at the interface. The left droplet shows intact LDL/HDL particles adsorbing to the interface, as well as released and adsorbed apoB, phosvitin, and phospholipids. Excess phosvitin and apoB also pervade the aqueous phase, contributing to the intricate structure of the emulsion. The right droplet illustrates how phosvitin and apoB antibodies, conjugated to fluorophores, are used for specific labelling.

1.3 Direct visualization of interfacial structure: Insights and obstacles

During homogenization, competition for adsorption at the interface may occur between various proteins or phospholipids, or they might even displace each other over time. As a result, the overall composition of the emulsifiers in the system does not necessarily correspond to the interfacial composition[55–57]. A common method for assessing interfacial composition involves measuring surface load via the supernatant or cream phases post-centrifugation. However, this method, while straightforward, is invasive and destructive and is not applicable to all types of food emulsions. To gain direct insight into the interfacial structure and behavior of fluid interfaces, researchers employ methods involving model films and optical techniques[58,59]. Interfacial rheology, which allows monitoring of the interfacial stress response induced by shear or dilatational deformation, serves as another critical instrument in the study of emulsifier interactions[60,61]. Non-destructive methods, such as spectroscopic methods, have been employed to monitor the displacement of globular proteins such as bovine serum albumin (BSA) from the surface of oil droplets by a non-ionic surfactant. However, while these methods can detect such displacements, they often lack spatial information[62]. Fluorescence microscopy offers another non-destructive option for assessing droplet interfacial composition in food emulsions but currently lacks molecular specificity.

The main obstacle to employing optical microscopy to localize emulsifiers at interfaces is turbidity. Turbidity is inherently present in emulsions and arises from both the absorption and scattering of light by oil droplets. Emulsion turbidity peaks when the droplet diameter is approximately 1 μm (at a wavelength of 650 nm)[63], a phenomenon primarily driven by Mie scattering[64]. A second obstacle is the limited spatial resolution of conventional optical microscopy. These limitations underscore the necessity for advances in microscopy techniques.

In this thesis, the limitations of conventional microscopy are addressed by adopting super-resolution microscopy techniques capable of achieving resolutions down to a few tens of nanometres. Additionally, considering the prevalent turbidity in food emulsions, adaptive optics is used to counteract blurring. For the implementation of these solutions, this thesis work relied on the miCube framework[65], capitalizing on its flexibility and open-access nature. The following sections will delve into these methodological advancements in greater detail.

1.4 Evolution of optical microscopy

1.4.1 Diffraction limit of light

When a camera detects photons coming from a sample, the detected pattern is influenced by the optical components involved. Factors such as imperfections of involved lenses or misalignment of the optical path affect this response. As a result, the image of the emitter can appear larger than its actual size and will display a diffraction pattern. In the 19th century, Abbe defined a constraint for optical microscopy: any point source smaller than the microscope's resolution or optical diffraction limit is observed as a distinct spatial distribution known as the microscope's point spread function (PSF). This PSF is often characterized by the Airy diffraction pattern, a spatial distribution that manifests as a central disk surrounded by fainter concentric rings. These rings arise from the Fraunhofer diffraction of light by a circular aperture as given when using microscope objectives for detection[66]. The smallest distance at which two PSFs can be differentiated is referred to as the Rayleigh limit. This limit is defined by the alignment of the brightest spot of one point image with the first minimum, or the dimmest spot, of the other. If the two points are closer than the Rayleigh limit, they blur into a single image; if they are farther apart, they remain distinct[67] (**Figure 1.3**). This critical separating distance, known as the Rayleigh criterion, can be approximated by

$$d = \frac{0.61\,\lambda}{NA}, \tag{1.1}$$

where λ is the wavelength of the emitted light, and *NA* is the lens's numerical aperture[68]. In a standard fluorescence microscope with a high numerical aperture objective (e.g., *NA*=1.4), the resolution limit set by the Rayleigh criterion is around 170 to 240 nm laterally and around 470 to 670 nm axially.

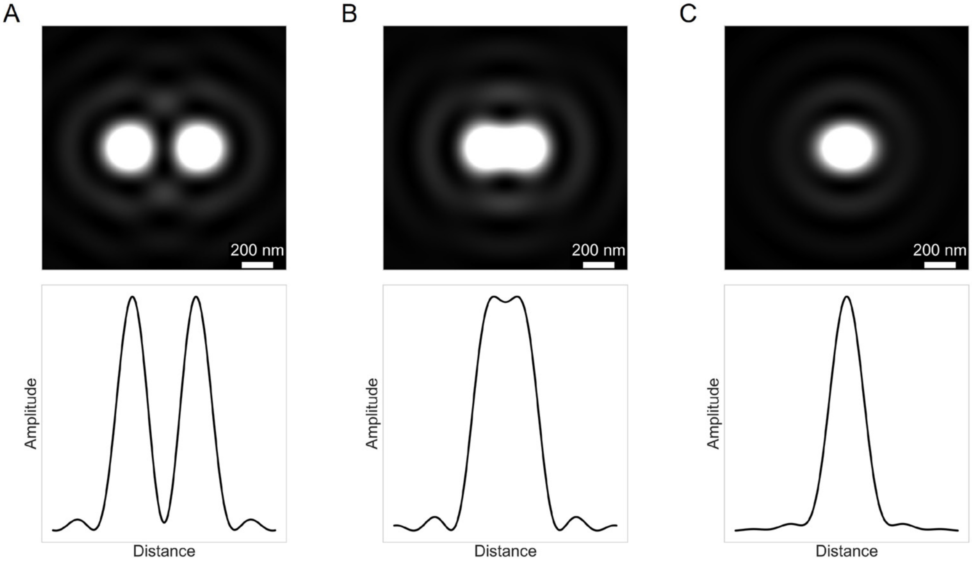

Figure 1.3. Visual depiction of the PSF and the Rayleigh criterion in optical microscopy. The figure conveys how a single emitter with a size below the microscope's resolution limit manifests as an expanded image, forming a disk encircled by faint rings. It further underscores the Rayleigh limit concept - the minimal distance at which two PSFs can be individually discerned. In our simulation, we set the numerical aperture (NA) to 1.45 and used a wavelength of 530 nm. Three conditions are presented: (A) when two light points are sufficiently separated, they appear as distinct entities, (B) at the Rayleigh limit, the points are at the brink of distinguishability, and (C) for distances shorter than the Rayleigh limit, the points merge into a single spot.

1.4.2 Unveiling details: Scanning based confocal microscopy

Conventional transmission brightfield microscopes capture the image of a specimen by illuminating it with a light source. The transmitted light is collected by an objective lens and then focused through an additional lens onto a camera or magnified for viewing through an eyepiece. Expanding on these basic methods, fluorescence-based optical microscopy adds a new dimension by tagging structures or entities like molecules or proteins with specific fluorophores. This method not only offers notably precise targeting but also enhances the signal-to-noise ratio. Lasers, favored for their monochromatic light emission, stimulate these fluorophores. The narrow excitation spectrum of lasers facilitates the implementation of dichroic mirrors and filters to optimize the accessible spectral range for capturing fluorescence from the emitters. The imaging begins with collimating the laser light and is directed towards the microscope objective's back focal plane to excite the sample. The same objective captures the fluorescence emitted from the sample, allowing imaging of non-transparent samples. The red-shifted fluorescence passes the dichroic mirror, reflecting the laser's excitation wavelengths, and is then focused through a lens to the camera.

When imaging non-transparent samples with fluorescence microscopes, the laser is focused on a specific plane. However, as the laser light travels to the targeted focal plane, it also excites adjacent layers, leading to the emission of photons. The co-collection of in-focus and out-of-focus light diminishes the signal-to-noise ratio and contrast, resulting in blurry images. To address these limitations, confocal microscopy uses a pinhole in the detection path, placed in a virtual image plane of the objective lens of a microscope. This pinhole effectively blocks unwanted light originating from non-focal planes, thereby reducing background fluorescence. It is worth noting that confocal microscopy can, under ideal conditions with an infinitesimally small pinhole, enhance image resolution by a factor of $\sqrt{2}$. Confocal microscopy improves image clarity and allows revealing details that are often obscured in conventional microscopy[68]. However, the degree of resolution improvement in a confocal microscope relies upon the size of the pinhole in the detection path. Though a smaller pinhole radius theoretically yields the highest resolution, it comes at the cost of a reduced signal-to-noise ratio. The pinhole size is commonly defined in terms of Airy unit. An Airy unit is equivalent to the zeroth-order portion of the Airy disk, which is the central part of the diffraction pattern created when light passes through a circular aperture. When the pinhole is sized at one Airy unit, the system operates under diffraction-limited conditions. As a result, most commercial confocal microscopes are engineered with a pinhole radius of one Airy unit to achieve an optimal compromise between resolution and signal quality.

Re-scan confocal microscopy (RCM)[69] is an optical technique that enhances the resolution in a confocal microscope using optics without requiring any software-based image reconstruction. RCM builds upon the standard confocal microscope by adding a re-scanning module, which allows for decoupling the scanning magnification of the object from the magnification of the scanning spot. This decoupling of magnifications forms the fundamental concept of RCM, enabling the system's resolution to be independent of the pinhole size. This is often referred to as "confocal microscopy with an open pinhole," a feature that allows for lateral super-resolution while preserving optical sectioning, as depicted in **Figure 1.4**. The crucial aspect of this method is that the second mirror must sweep with double the angular amplitude of the first mirror. This results in the image being stretched by a factor of $\sqrt{2}$, enhancing the resolution from 240 nm at 520 nm wavelength (Abbe diffraction limit) to 170 nm[70] (**Figure 1.4**).

1.5 Going beyond limits: Super-resolution microscopy

Super-resolution techniques have revolutionized the field of imaging by overcoming the resolution limitations imposed by the diffraction limit of light. These techniques can be broadly categorized into two groups: point-scanning-based and camera-based approaches[71,72]. Point-scanning-based approaches, including stimulated emission depletion (STED)[73], MINSTED[74],

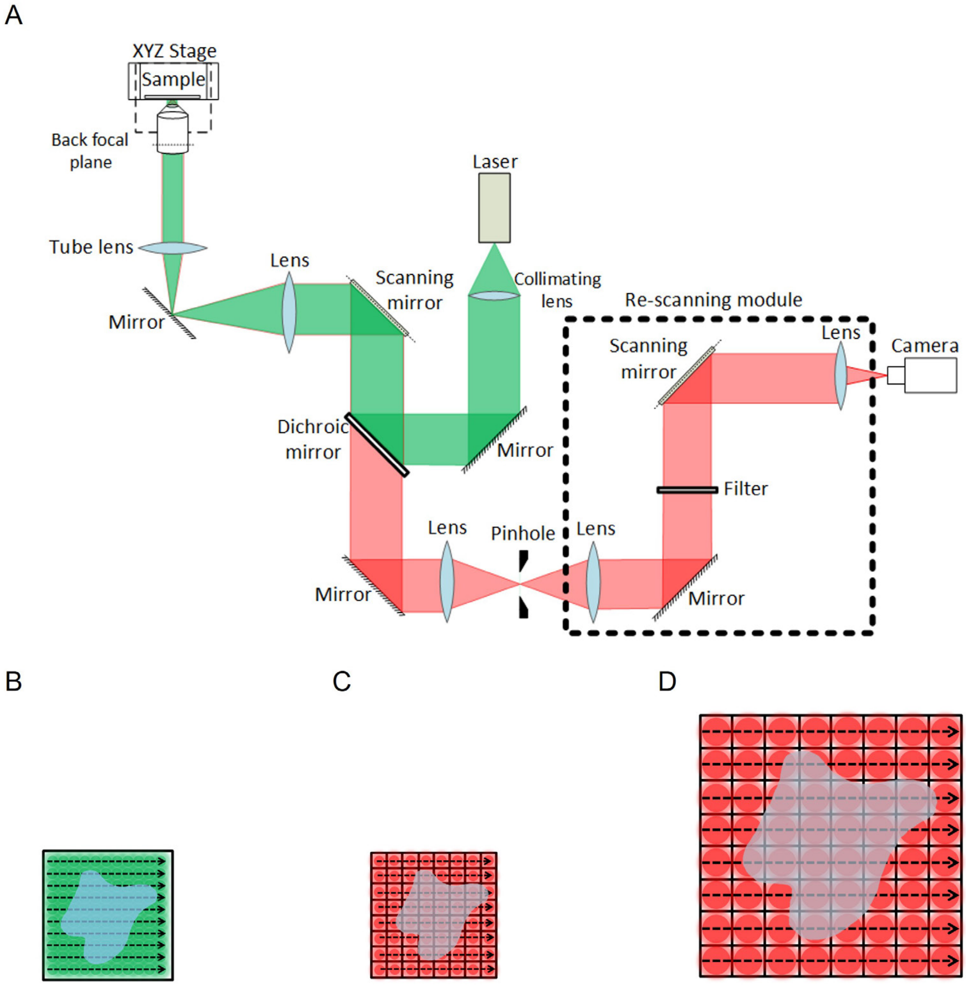

Figure 1.4. (A) Schematic representation of RCM operation building upon standard confocal microscopy through the addition of a re-scanning module. The subfigures depict three distinct operational steps: (B) the initial scanning of the excitation laser beam by the first scanning mirror, (C) the de-scanning of the image onto the camera in a conventional confocal microscope, and (D) the unique RCM feature wherein the re-scanning mirror sweeps with double the angular amplitude of the first mirror. This mechanism enables the decoupling of scanning magnifications, allowing for lateral super-resolution and preserving optical sectioning.

and reversible, saturable optical linear fluorescence transitions (RESOLFT)[75], rely on reducing the effective excitation volume with a depletion laser. Another novel and notable super-resolution microscopy technique is minimal photon flux (MINFLUX)[76]. Unlike other point-scanning-based methods, MINFLUX employs a nanoscale doughnut-shaped excitation beam to localize single molecules by pinpointing where the photon flux is minimal. MINFLUX enables unparalleled precision, potentially achieving resolutions down to a few nanometers. On the other hand, camera-based approaches in the domain of single molecule localization microscopy (SMLM), such as stochastic optical reconstruction microscopy (STORM)[77], photoactivated localization microscopy (PALM)[78], stochastically activate a subset of photo switchable probes at a given time and then determine the centroid position of each point spread function. Another SMLM technique, points accumulation for imaging in nanoscale topography (PAINT)[79], operates based on capturing images through the transient binding of diffusing fluorescent molecules to target structures. The STORM technique was originally developed using a Cy3-Cy5 organic dye pairing. In this setup, Cy3 aids in converting Cy5 from its dark state to the fluorescent state. Subsequently, the technique was further refined to use conventional organic dyes such as Alexa Fluor 647. This improved version, which does not rely on the proximity of paired dyes, is referred to as 'direct' STORM[80] and also facilitated the use of standard antibodies conjugated to these dyes. In contrast to STORM, where target binding sites are permanently attached to fluorophores and gradually bleach over time, in PAINT, fluorophores freely diffuse in solution and bind temporarily to target sites. This transient binding and subsequent immobilization leads to localizable emission. These events are then detected and captured by the camera. To enhance target specificity, the DNA-PAINT[81] method was developed. It involves designing DNA 'docking strands' to attach to the target of interest while complementary DNA 'imager strands' conjugated to fluorophores diffuse in the solution. Therefore, when the imager strands bind to the docking strands, they become temporarily immobilized and emit photons from a specific location. Subsequently, the imager strands dissociate, freeing the docking site for subsequent binding by other strands. This cyclical binding and release mechanism does not only amplify the signal but also increases localization precision, given that photobleaching is not a concern.

To construct an image using SMLM, an image stack, typically comprising of 10,000 or more frames, is first recorded with a frame rate between 20 Hz and 100 Hz to capture the on-off events. These events are acquired in the form of a PSF due to the diffraction-limited detection of fluorophores. Subsequently, the position of each PSF in all frames is determined using various approaches, such as fitting the intensity profile of the individual PSFs with a 2D Gaussian function[82], center of mass (CoM) calculations[83], radial symmetry[84], cubic splines[85], or phasor based methods[86]. After all localizations from all frames are obtained, the image is reconstructed with super-resolved resolution, thereby providing an exceptionally detailed view (**Figure 1.5**).

The accurate localization of each PSF is critical in achieving high-quality super-resolved images. This process is significantly influenced by two key parameters: localization precision and localization accuracy[87]. If we denote r_t as the true position of a fluorophore, the localization precision can be described as the variability of the position estimates when this fluorophore's

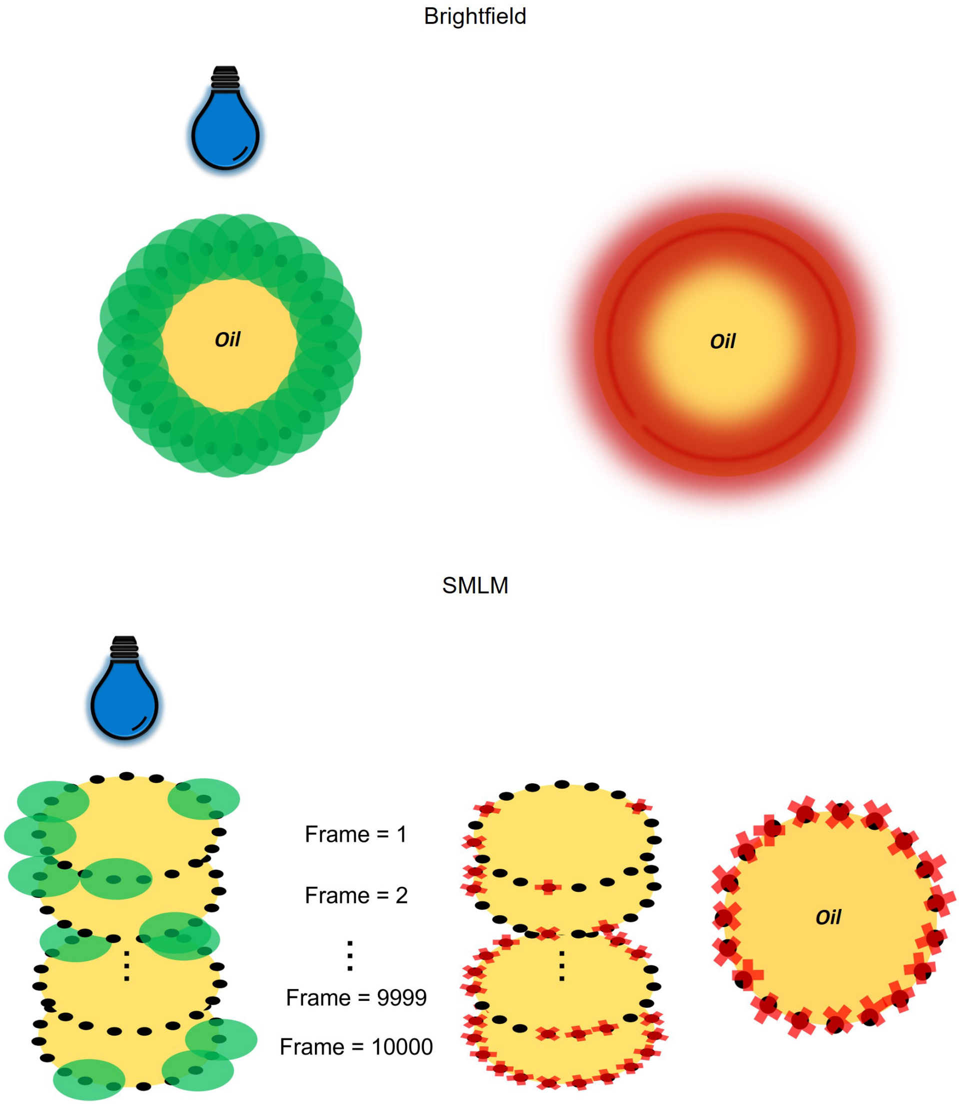

Figure 1.5. Comparative representation of brightfield imaging and SMLM at an interface of oil droplets where fluorophores are anticipated. The brightfield image illustrates the traditional approach where simultaneous excitation of all fluorophores (black circles, hidden) leads to overlapping PSFs (green circles). This results in diffraction-limited resolution indistinct visualizations (red ring) due to the limitations set by the Rayleigh criterion. Conversely, the SMLM image is a composite of thousands of frames, each capturing distinct blinking events (green circles) of individual fluorophores (black circles). This method enables the precise localization of each fluorophore (red crosses), exceeding the resolution of conventional brightfield and confocal microscopy.

position is measured multiple times. Conversely, localization accuracy reflects the deviation of the mean measured position $\bar{r}$ from the true position r_t (**Figure 1.6**).

While super-resolution techniques have significantly improved the resolution capabilities of optical microscopy, they still face challenges when imaging through samples with varying refractive indices. Optical aberrations introduced by these inhomogeneous samples can distort the wavefront of the light, leading to blurred images and loss of resolution. One technology that holds promise in addressing these challenges is adaptive optics, a technique originally developed in the field of astronomy.

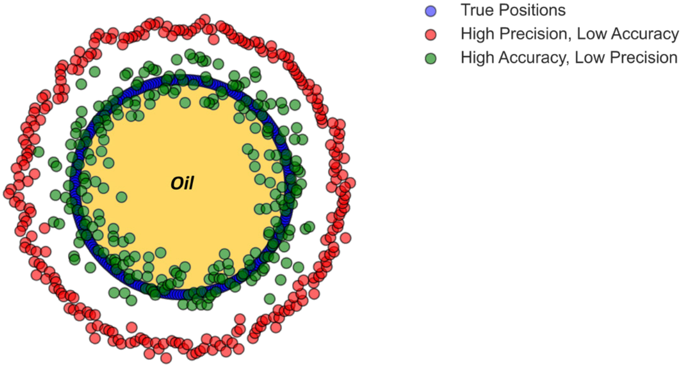

Figure 1.6. Illustrating the concepts of localization precision and accuracy in super-resolution imaging, focusing on the ring-like pattern observed at the interface of oil droplets. The diagram presents localization precision as the variance in position estimates when a fluorophore's position is measured multiple times, visually depicted as the thickness of a ring. Conversely, localization accuracy is illustrated as the divergence of the average measured position from the actual position of the fluorophore, represented by the radius size. The figure further highlights green localizations as highly accurate due to their similar radii to the true positions (blue localizations), while the red localizations indicate low accuracy due to their larger radii and high precision, as evidenced by their narrow ring.

1.6 Correcting aberrations: Adaptive optics in microscopy

Light can be described as a superposition of propagating electromagnetic waves. The spatial propagation of the waves is described by a wavefront. For instance, when light emanates from a point source, the wavefronts are spherical, much like the ripples in a pond when a stone is dropped. However, when light propagates through environments with varying refractive indices—such as when passing through the atmosphere—the wavefront becomes distorted. While telescopes and microscopes have traditionally catered to distinct observational scales, they share foundational principles of optics. These common principles have facilitated a notable exchange of technologies, particularly evident in addressing the shared challenge of correcting optical aberrations[88]. In astronomy, the development of adaptive optics (AO) was primarily aimed at compensating for atmospheric turbulence, causing variations in refractive indexes across different layers leading to wavefront distortions and image blurring[89]. AO technology in astronomy involves real-time wavefront measurements and the use of deformable mirrors (DMs) to correct these aberrations dynamically[90].

Microscopy encounters similar challenges when imaging through samples such as food or biological specimens, which introduce optical aberrations due to varying refractive indexes. As the imaging depth increases, the image travels through obstructing volumes or layers with inhomogeneous or mismatched refractive indexes. Consequently, the reflection, absorption, and scattering of photons result in a loss of resolution and increased blurriness in the final image[90,91]. To address this challenge, techniques inspired by adaptive optics in astronomy have been adopted. These techniques employ similar principles, including wavefront sensing and the use of DMs, to compensate for aberrations[92]. When focusing light toward a plane close to the coverslip of a food emulsion sample, the amount of aberration is minimal. Consequently, the photons emitted from the sample and collected by the camera do not show significant wavefront distortion (**Figure 1.7A**). However, focusing light into planes deeper within the sample, particularly in a turbid food sample, causes the emitted light to become aberrated. When imaging such a sample, the resulting image appears blurry due to these distortions. The implementation of a DM in the detection path can counteract this by producing a conjugate aberration of the aberrated light. As this aberrated wavefront hits the surface of the DM, it is corrected, yielding a sharp and distortion-free image. This is a fundamental principle of the custom-built microscope setup that will be developed in this thesis (**Figure 1.7B**).

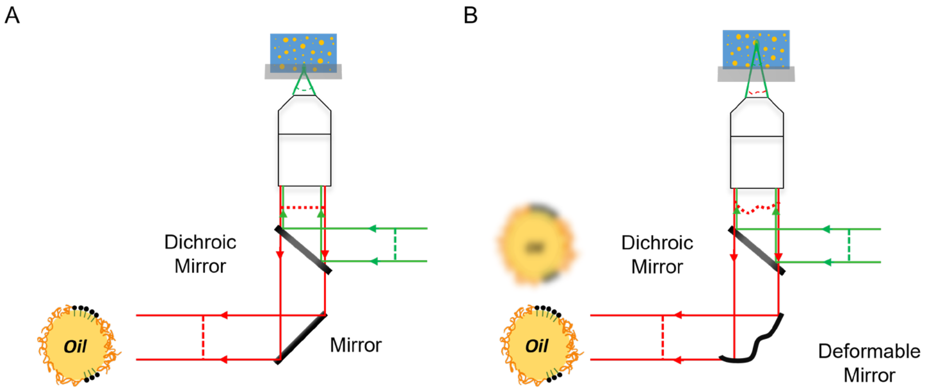

Figure 1.7. Schematic of the impact of optical aberrations and the mitigating role of adaptive optics in microscopy. (A) Focusing light near the surface of a food emulsion sample leads to minimal aberrations, resulting in a clear, undistorted image. (B) In contrast, focusing light deeper within the turbid sample introduces wavefront distortions due to refractive index mismatch, leading to a blurry image. In this case, an adaptive optics system featuring a deformable mirror (DM) is placed instead of a plane mirror in the detection path. The DM produces a conjugate aberration to correct the distorted wavefronts emitted from deeper within the sample. As the aberrated wavefront encounters the DM, it is corrected, resulting in a sharp and distortion-free image.

A DM is a commonly used component in wavefront correction systems in reflecting mode and is often referred to as a multichannel corrector. It consists of a grid of individual actuators that can introduce conjugate aberrations to counteract the aberrations arising within the optical system. There are different types of DMs, each with its own design and actuation mechanism. The surface of DMs can be continued, such as in a membrane mirror[93], a bimorph mirror[94], or segmented DMs with stacked piezoelectric actuators[95,96]. However, the range and amount of wavefront distortions that a particular DM can correct are limited by several factors, such as the actuation technology, number of actuators, coating types, and dimensions of the optical elements[97].

1.7 Aberration correction without a sensor

DMs can be implemented using either direct or indirect wavefront sensing techniques[98]. In the direct sensing mode, an additional wavefront sensor, such as a Shack-Hartmann wavefront sensor[99,100], a shearing interferometer sensor[101,102], a rotational wavefront shearing sensor[103], or a Pyramid wavefront sensor[104] is utilized to provide instantaneous feedback to the optical element responsible for modulating the wavefront. In indirect wavefront sensing methods, the wavefront is not directly sensed but calculated from specific metrics or characteristics of the resulting image[105]. One common approach is the use of image-based metrics. Instead of directly measuring the wavefront, certain characteristics or metrics of the resulting images are evaluated. These metrics, such as sharpness, contrast, or resolution, provide an indication of the wavefront quality. The correction is then determined based on optimizing these image metrics using optimization algorithms[106,107].

Operating adaptive optics systems in direct sensing mode has a downside in SMLM[108]. In direct mode, a portion of the photons that would be available for image formation is instead used for wavefront sensing, which leads to a reduction in the overall photon count and potentially affects the performance of SMLM techniques. The localization precision is strongly influenced by the number of detected photons from each molecule, as higher photon counts result in more precise position determination. Therefore, any reduction in the number of photons available for detection can have a detrimental effect on the achievable resolution and accuracy in SMLM. On the other hand, one advantage of working with food and biological samples in comparison to astronomy is that the aberrations in these samples are relatively stable and do not change over time. Unlike atmospheric turbulence, which can introduce rapid and unpredictable variations in the wavefront, the aberrations in these samples show minimal variations over time. To effectively compensate for aberrations using sensorless methods, it is necessary to employ an image-based metric that can estimate the aberrations independently of the specimen. In the case of SMLM, the raw images often contain blinking events originating from the sample itself, which is small and subject to diffraction limitations. These blinking events are observed as the PSF of the microscope and are influenced by aberrations. Considering the impact of aberrations on the PSF, it is common practice to utilize an image sharpness metric that remains insensitive to the intensity and number of blinking events. This sharpness metric *M* is defined based on the second moment of the Fourier transform of the image[109]

$$M = \sum_{n,m} \mu_{n,m} \hat{I}_{n,m} (\acute{n}^2 + \acute{m}^2) / \sum_{n,m} \hat{I}_{n,m}, \tag{1.2}$$

where $\hat{I}_{n,m}$ is the discrete Fourier transform of the image, $\acute{n} = n - \frac{N-1}{2}$, $\acute{n} = n - \frac{N-1}{2}$, and *n* and *m* are coordinates representing the pixel positions within the image, ranging from 0 to N and M, respectively, corresponding to the number of pixels in each image dimension. Additionally, $\mu_{n,m}$is a circular mask given by

$$\mu_{n,m} = \begin{cases} 1, & \sqrt{\acute{n}^2 + \acute{m}^2} \leq {}^{NA}/_{\lambda} \\ 0, & \sqrt{\acute{n}^2 + \acute{m}^2} > {}^{NA}/_{\lambda} \end{cases}, \tag{1.3}$$

where it shows that this mask filters high spatial frequency noise and ensures accurate assessment of the metric. Consequently, the sharpness metric provides a reliable measure for quantifying and compensating for the effects of aberrations in SMLM imaging.

Describing aberrations mathematically requires a specific mathematical framework. Given the prevalence of circular apertures in optical systems, Zernike introduced a set of polynomials that are orthonormal over a disk[110]. These Zernike polynomials play a crucial role in adaptive optics. Each term of the polynomial corresponds to a specific type of aberration, that is described below (**Figure 1.8**):

- **Piston/Tilt-Tip**: The initial three terms, representing a constant shift and linear tilt in the wavefront, do not contribute to image distortions.
- **Defocus**: This is the primary optical aberration term. It describes the deviation of an optical system's focal point from the ideal.
- **Astigmatism (Oblique and Vertical)**: This aberration causes the focal point to diverge in two perpendicular directions.
- **Coma (Vertical and Horizontal)**: This aberration causes point sources, like distant stars, to appear elongated or comet-like.
- **Trefoil (Oblique and Vertical)**: This aberration manifests as a distortion, producing a three-pointed star-shaped appearance in images.
- **Spherical Aberration**: Results in the outer rays of a beam focusing differently than the central rays, causing a blur.

- **Secondary Astigmatism (Oblique and Vertical)**: Represents a more intricate form of the astigmatism aberration.
- **Quatrefoil (Oblique and Vertical)**: Results in a four-pointed star-shaped distortion in images.

Thus, by analyzing the coefficients of these polynomials, the type and severity of the aberrations in an optical system can be discerned. Furthermore, the Zernike polynomials possess the advantage of easily transforming under rotations around the Cartesian axes. Additionally, the coefficients of these polynomials can be employed for aberration correction[66]. Within this thesis, we used a DM that supports the first 15 terms of Zernike polynomials.

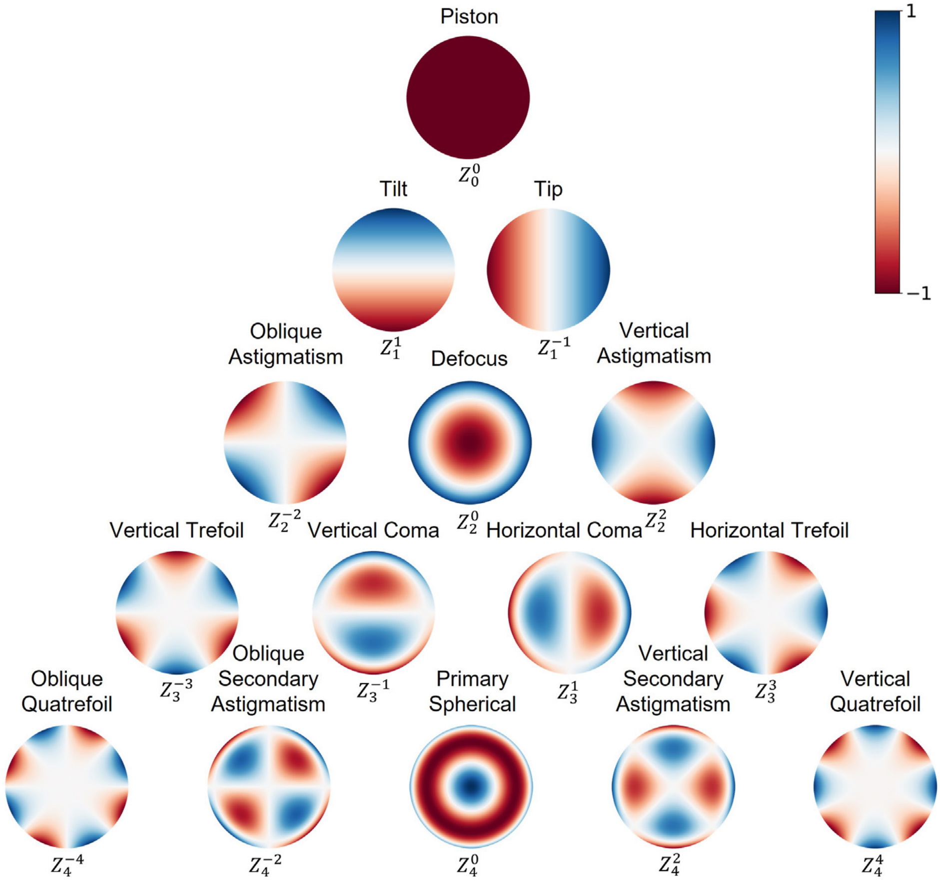

Figure 1.8. Visualization of the first 15 terms of Zernike polynomials, organized vertically by radial degree and horizontally by azimuthal degree. These terms, supported by the DM used in our research, serve as a fundamental tool for modeling and correcting optical aberrations in adaptive optics systems. Each term corresponds to a specific aberration type, providing a comprehensive framework for aberration analysis.

Robust and effective adaptive optics in localization microscopy (REALM) is a sensorless approach that uses model-based optimization to iteratively correct all available Zernike modes[111]. In REALM, each Zernike mode undergoes independent correction by applying varying biases or amplitudes of the Zernike modes within the DM. For every single bias applied to the DM, an image is captured, and from these images, the sharpness metric is calculated for all the biases associated with a specific Zernike mode. This calculated metric is subsequently fitted using a Gaussian function to identify the optimum. This procedure is replicated across all Zernike modes that successively changed in the DM and is executed over multiple rounds until an optimal solution is achieved. As per the simulation provided by the authors of REALM, an optimal strategy might consist of three correction rounds with 13 biases for each Zernike mode to effectively compensate for aberration, which means 297 acquisitions (3 rounds * 9 biases * 11 Zernike modes – excluding piston, tip, tilt, and defocus). Implementing the REALM technique in conjunction with SMLM can effectively compensate for aberrations present in turbid samples. Furthermore, it is important to note that aberrations can also be introduced by the microscope setup itself due to the inherent characteristics of the optical elements and potential fabrication errors in the DM. In such cases, the REALM method is first employed to correct the aberrations from the microscope before addressing those introduced by the turbid sample.

After applying the REALM technique for aberration correction in SMLM, this thesis will leverage the versatility of the DM. Its capabilities in PSF engineering are harnessed to advance our imaging techniques into the three-dimensional. The following section delves into how incorporating PSF engineering enables 3D imaging in SMLM.

1.8 PSF engineering in 3D SMLM

In a well-aligned microscope, we can observe how spherical aberration impacts the shape of the PSF both at the top and bottom of the focal plane. Notably, this effect is manifested symmetrically on either side. It is important to highlight our understanding of how the PSF shape varies with depth. By intentionally breaking this symmetry between the top and bottom of the focal plane, we can encode the depth z within the PSF shape at different planes. This technique, known as PSF engineering, is a powerful method used in 3D SMLM and multiplexing applications. One commonly used technique in PSF engineering involves adding a cylindrical lens in the detection path. The cylindrical lens induces astigmatism, resulting in the creation of two distinct focal planes for the x and y axes. As a result, the symmetry of the PSF is broken, causing changes in ellipticity and orientation as we move through different depths. By implementing this method, a z-range of 1 µm can be achieved[83,105]. A different strategy involves modulating the shape of PSF by the placement of a transmission mask within the detection path, using a 4f configuration to generate unique PSF shapes such as a saddle point, tetrapod, and double helix[112,113]. However, these phase masks are expensive to fabricate and are primarily used for creating a specific PSF shape. As an alternative, spatial light modulators (SLMs)[114,115] can replace phase masks, facilitating the creation of various phase masks within the detection path for PSF engineering. Nevertheless, it is worth mentioning that the use of liquid crystal SLMs may lead to photon loss and reduced resolution[116]. An alternative approach involves the use of a DM, which can generate a wide range of PSF shapes with different lateral and axial extensions, thereby providing greater versatility in PSF engineering. By adjusting the settings of the DM, we can generate a range of PSF shapes. For instance, for Saddle Point PSF modulation, Z_2^2 to 0.5 and Z_4^2 to -0.65. The DM allows recording of 3D SMLM data with axial ranges between 1 µm and 6 µm, dependent on the chosen PSF shape[117]. However, larger axial distances are challenging to achieve due to the overlap of PSFs from neighboring emitters. Furthermore, localizing modulated PSFs presents more challenges compared to using Gaussian-based methods or other approaches for symmetrical PSFs. Fitting algorithms rely on experimentally retrieved PSFs[118], phase retrieving methods[117,119], spline interpolation[120], or a fast retrieval localizing method using a standard CPU based on phasor method[121]. Having explained the principles of super-resolution microscopy using adaptive optics, the following section will detail the microscope setup to be further developed in this thesis.

1.9 Revamping the miCube: Implementing beam shaping and deformable mirrors

The miCube is an open framework for single-molecule microscopy, constructed using 3D printed components and a custom aluminum stand aimed at minimizing thermal drift. It has been detailed in previous publications[14,65,121]. In this thesis, the miCube was chosen for its customization potential, which not only permitted to tailor its components to our food samples' specific requirements but also to add or remove specialized components as necessary. Such adaptability was crucial for adjustments in both the excitation and detection paths. Most SMLM microscopes utilize laser fibers that generate a Gaussian intensity profile of the laser beam. This presents a challenge because uneven illumination can adversely affect quantitative analysis. Various solutions have been proposed, including using a pair of micro lens arrays with identical spherical lenslets[122], employing a multimode fiber laser with speckle or rotating reducers[123,124], and incorporating two galvanometer scanning mirrors placed in a plane conjugated to the back focal plane of the microscope objective[125]. In this thesis, we have incorporated a top-hat beam shaper to modify the Gaussian intensity distribution into a homogeneous flat-field profile[126,127]. This refractive beam shaping method redistributes the laser beam into a flat-top profile, ensuring uniform illumination of the sample during SMLM measurements. Furthermore, measuring turbid samples can result in heavily aberrated images. To address the aberrations in the detection path, a DM can be implemented in the Fourier plane of the objective. The DM does not only compensate for aberrations but also facilitates PSF engineering for 3D SMLM imaging. This improved SMLM microscope setup is specially designed to address challenges presented by turbid samples such as food emulsions (**Figure 1.9**).

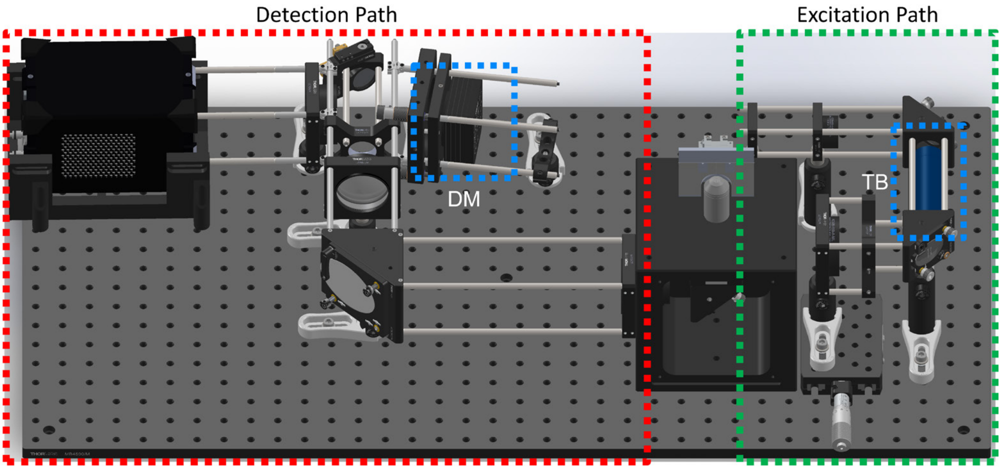

Figure 1.9. Illustration of the enhanced miCube open framework. The excitation path (green dotted rectangle) features a top hat beam shaper (TB, highlighted in blue) to transform the Gaussian laser beam intensity distribution into a uniform flat-field profile. The detection path (red dotted rectangle) integrates a DM (highlighted in blue) for aberration correction and 3D SMLM PSF engineering.

1.10 Aim and outline of this thesis

A main methodological bottleneck in understanding the physical and chemical stability of food emulsions is the non-invasive assessment of protein spatial distribution at emulsion interfaces with molecular specificity and submicron precision. This thesis introduces advanced microscopy techniques tailored to directly localize proteins at the interface of oil droplets within turbid food emulsions. Objectives are to develop the methods for extracting and quantifying interfacial protein distribution and to demonstrate these methods in challenging model emulsions. **Figure 1.10** provides the schematic outline of this thesis. The first two chapters detail the development of microscopic methodologies for the assessment of proteins at droplet interfaces and quantifying heterogeneity of droplet coverage. In the subsequent chapters, the applications of these methodologies are demonstrated on model systems mimicking the complexity of mayonnaise. Lastly, a general discussion of the findings and an outlook on future research will be presented.

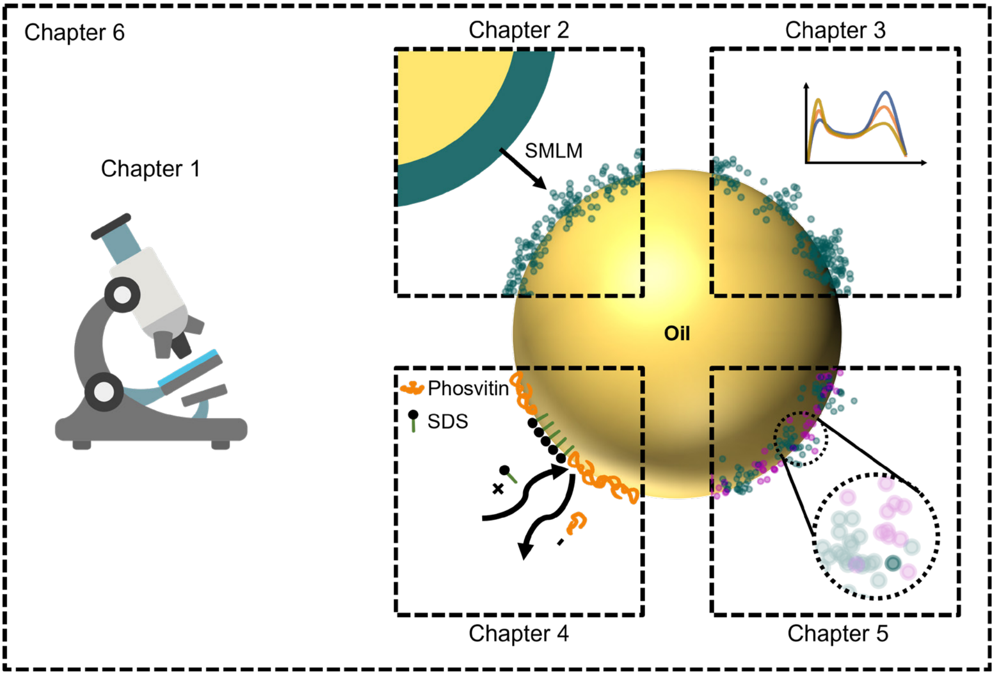

Figure 1.10. Schematic overview of this thesis. Chapters 2 and 3 focus on methodology development; Chapter 2 presents the upgraded miCube, a custom-built microscope with enhancements for aberration correction within opaque food emulsion samples. Chapter 3 introduces the RPD method for quantitative analysis of protein distribution at the interface of oil-in-water emulsions. Chapters 4 and 5 apply these methodologies to model systems; Chapter 4 delves into the competition between proteins and surfactants for adsorbing at the interface. Chapter 5 investigates the co-localization of proteins and radical formation in the early stages of oxidation at the interface. Chapter 6 provides a discussion of the findings and prospects for future research.

Chapter 2 describes the fluorescence-based imaging of oil/water interfaces in turbid food samples, where traditional imaging methods are limited by the diffraction of light. An upgraded custom-built miCube microscope will be presented, featuring adaptive optics and flat-top beam excitation. These enhancements aim to tackle optical aberrations in complex emulsions and open the door to 3D SMLM through PSF engineering and advanced quantitative. The chapter also introduces a first model system for mayonnaise.

Chapter 3 presents a new method for quantitatively analyzing the distribution of proteins at the interface of oil-in-water emulsions. This analytical approach aims to answer whether the distribution of emulsifiers at these interfaces is homo- or heterogeneous.

Chapter 4 employs the methodology from Chapters 2 and 3 to assess intra- and inter-droplet heterogeneity in the distribution of proteins at droplet interfaces. This chapter further explores the specificity of antibodies for phosvitin and examines their efficacy in relation to affimers, which are small proteins- engineered as alternatives to antibodies for specific target recognition.

Chapter 5 explores a model system encompassing a model emulsion developed using egg yolk as an emulsifier. The chapter seeks to answer the question: how does protein surface coverage relate to local co-oxidation? A water-soluble, fluorescently labeled spin trap (CAMPO-AFDye647) [54] will be used for detecting early radical formation, enabling co-localization of protein and radical formation. This analysis will aim to compare which protein is more susceptible to co-oxidation compared to the other.

Chapter 6 provides a comprehensive discussion of the findings presented in this thesis, along with an outlook on potential avenues for future research.

References

1 *Principles of Colloid and Surface Chemistry, Revised and Expanded*, 0 ed.; Hiemenz, P. C., Rajagopalan, R., Eds.; CRC Press, 2016. https://doi.org/10.1201/9781315274287.

2 Brady, J. W. *Introductory Food Chemistry*; Comstock Pub. Associates: Ithaca, 2013.

3 Kasapis, S.; Norton, I. T.; Ubbink, J. B. *Modern Biopolymer Science: Bridging the Divide between Fundamental Treatise and Industrial Application*; Academic Press, 2009.

4 Stephen, A. M. *Food Polysaccharides and Their Applications*; CRC Press, 1995.

5 Ozturk, B.; McClements, D. J. Progress in Natural Emulsifiers for Utilization in Food Emulsions. *Current Opinion in Food Science* **2016**, *7*, 1–6. https://doi.org/10.1016/j.cofs.2015.07.008.

6 Kralova, I.; Sjöblom, J. Surfactants Used in Food Industry: A Review. *Journal of Dispersion Science and Technology* **2009**, *30* (9), 1363–1383. https://doi.org/10.1080/01932690902735561.

7 Urban, K.; Wagner, G.; Schaffner, D.; Röglin, D.; Ulrich, J. Rotor-Stator and Disc Systems for Emulsification Processes. *Chem. Eng. Technol.* **2006**, *29* (1), 24–31. https://doi.org/10.1002/ceat.200500304.

8 Hall, S.; Cooke, M.; El-Hamouz, A.; Kowalski, A. J. Droplet Break-up by in-Line Silverson Rotor–Stator Mixer. *Chemical Engineering Science* **2011**, *66* (10), 2068–2079. https://doi.org/10.1016/j.ces.2011.01.054.

9 Perrier-Cornet, J. M.; Marie, P.; Gervais, P. Comparison of Emulsification Efficiency of Protein-Stabilized Oil-in-Water Emulsions Using Jet, High Pressure and Colloid Mill Homogenization. *Journal of Food Engineering* **2005**, *66* (2), 211–217. https://doi.org/10.1016/j.jfoodeng.2004.03.008.

10 Santana, R. C.; Perrechil, F. A.; Cunha, R. L. High- and Low-Energy Emulsifications for Food Applications: A Focus on Process Parameters. *Food Eng Rev* **2013**, *5* (2), 107–122. https://doi.org/10.1007/s12393-013-9065-4.

11 Qian, C.; McClements, D. J. Formation of Nanoemulsions Stabilized by Model Food-Grade Emulsifiers Using High-Pressure Homogenization: Factors Affecting Particle Size. *Food Hydrocolloids* **2011**, *25* (5), 1000–1008. https://doi.org/10.1016/j.foodhyd.2010.09.017.

12 Leong, T. S. H.; Wooster, T. J.; Kentish, S. E.; Ashokkumar, M. Minimising Oil Droplet Size Using Ultrasonic Emulsification. *Ultrasonics Sonochemistry* **2009**, *16* (6), 721–727. https://doi.org/10.1016/j.ultsonch.2009.02.008.

13 Abbas, S.; Hayat, K.; Karangwa, E.; Bashari, M.; Zhang, X. An Overview of Ultrasound-Assisted Food-Grade Nanoemulsions. *Food Eng Rev* **2013**, *5* (3), 139–157. https://doi.org/10.1007/s12393-013-9066-3.

14 Jabermoradi, A.; Yang, S.; Gobes, M. I.; van Duynhoven, J. P. M.; Hohlbein, J. Enabling Single-Molecule Localization Microscopy in Turbid Food Emulsions. *Phil. Trans. R. Soc. A.* **2022**, *380* (2220), 20200164. https://doi.org/10.1098/rsta.2020.0164.

15 McClements, D. J.; Jafari, S. M. Improving Emulsion Formation, Stability and Performance Using Mixed Emulsifiers: A Review. *Advances in Colloid and Interface Science* **2018**, *251*, 55–79. https://doi.org/10.1016/j.cis.2017.12.001.

16 Robins, M. M.; Watson, A. D.; Wilde, P. J. Emulsions—Creaming and Rheology. *Current Opinion in Colloid & Interface Science* **2002**, *7* (5–6), 419–425. https://doi.org/10.1016/S1359-0294(02)00089-4.

17 Shao, P.; Feng, J.; Sun, P.; Xiang, N.; Lu, B.; Qiu, D. Recent Advances in Improving Stability of Food Emulsion by Plant Polysaccharides. *Food Research International* **2020**, *137*, 109376. https://doi.org/10.1016/j.foodres.2020.109376.

18 Dickinson, E. Hydrocolloids as Emulsifiers and Emulsion Stabilizers. *Food Hydrocolloids* **2009**, *23* (6), 1473–1482. https://doi.org/10.1016/j.foodhyd.2008.08.005.

19 Tcholakova, S.; Denkov, N. D.; Lips, A. Comparison of Solid Particles, Globular Proteins and Surfactants as Emulsifiers. *Phys. Chem. Chem. Phys.* **2008**, *10* (12), 1608. https://doi.org/10.1039/b715933c.

20 McClements, D. J. *Food Emulsions: Principles, Practices, and Techniques*, Third edition.; CRC Press, Taylor & Francis Group: Boca Raton, 2016.

21 Leal-Calderon, F.; Bibette, J.; Schmitt, V. *Emulsion Science: Basic Principles*; Springer New York: New York, NY, 2007. https://doi.org/10.1007/978-0-387-39683-5.

22 Li, Y.; Le Maux, S.; Xiao, H.; McClements, D. J. Emulsion-Based Delivery Systems for Tributyrin, a Potential Colon Cancer Preventative Agent. *J. Agric. Food Chem.* **2009**, *57* (19), 9243–9249. https://doi.org/10.1021/jf901836f.

23 *Food Emulsifiers and Their Applications*; Hasenhuettl, G. L., Hartel, R. W., Eds.; Springer International Publishing: Cham, 2019. https://doi.org/10.1007/978-3-030-29187-7.

24 Murray, B. S.; Durga, K.; Yusoff, A.; Stoyanov, S. D. Stabilization of Foams and Emulsions by Mixtures of Surface Active Food-Grade Particles and Proteins. *Food Hydrocolloids* **2011**, *25* (4), 627–638. https://doi.org/10.1016/j.foodhyd.2010.07.025.

25 Felderhof, B. U. Effect of Surface Elasticity on the Motion of a Droplet in a Viscous Fluid. *The Journal of Chemical Physics* **2006**, *125* (12), 124904. https://doi.org/10.1063/1.2352757.

26 Laguerre, M.; Tenon, M.; Bily, A.; Birtić, S. Toward a Spatiotemporal Model of Oxidation in Lipid Dispersions: A Hypothesis-Driven Review. *European Journal of Lipid Science and Technology* **2020**, *122* (3), 1900209. https://doi.org/10.1002/ejlt.201900209.

27 Berton-Carabin, C. C.; Ropers, M.-H.; Genot, C. Lipid Oxidation in Oil-in-Water Emulsions: Involvement of the Interfacial Layer: Lipid Oxidation: An Interface Outlook…. *Comprehensive Reviews in Food Science and Food Safety* **2014**, *13* (5), 945–977. https://doi.org/10.1111/1541-4337.12097.

28 McClements, D. J.; Decker, E. Interfacial Antioxidants: A Review of Natural and Synthetic Emulsifiers and Coemulsifiers That Can Inhibit Lipid Oxidation. *J. Agric. Food Chem.* **2018**, *66* (1), 20–35. https://doi.org/10.1021/acs.jafc.7b05066.

29 Waraho, T.; McClements, D. J.; Decker, E. A. Mechanisms of Lipid Oxidation in Food Dispersions. *Trends in Food Science & Technology* **2011**, *22* (1), 3–13. https://doi.org/10.1016/j.tifs.2010.11.003.

30 Rampon, V.; Lethuaut, L.; Mouhous-Riou, N.; Genot, C. Interface Characterization and Aging of Bovine Serum Albumin Stabilized Oil-in-Water Emulsions As Revealed by Front-Surface Fluorescence. *J. Agric. Food Chem.* **2001**, *49* (8), 4046–4051. https://doi.org/10.1021/jf001170y.

31 Chen, J.; Li, X.; Cao, C.; Kong, B.; Wang, H.; Zhang, H.; Liu, Q. Effects of Different PH Conditions on Interfacial Composition and Protein-Lipid Co-Oxidation of Whey Protein Isolate-Stabilised O/W Emulsions. *Food Hydrocolloids* **2022**, *131*, 107752. https://doi.org/10.1016/j.foodhyd.2022.107752.

32 Laguerre, M.; Tenon, M.; Bily, A.; Birtić, S. Toward a Spatiotemporal Model of Oxidation in Lipid Dispersions: A Hypothesis-Driven Review. *European Journal of Lipid Science and Technology* **2020**, *122* (3), 1900209. https://doi.org/10.1002/ejlt.201900209.

33 Anton, M. Egg Yolk: Structures, Functionalities and Processes: Egg Yolk: Structures, Functionalities and Processes. *J. Sci. Food Agric.* **2013**, *93* (12), 2871–2880. https://doi.org/10.1002/jsfa.6247.

34 *Bioactive Egg Compounds*; Huopalahti, R., López-Fandiño, R., Anton, M., Schade, R., Eds.; Springer: Berlin, Heidelberg, 2007. https://doi.org/10.1007/978-3-540-37885-3.

35 Byrne, B. M.; Van Het Schip, A. D.; Van De Klundert, J. A. M.; Arnberg, A. C.; Gruber, M.; Ab, G. Amino Acid Sequence of Phosvitin Derived from the Nucleotide Sequence of Part of the Chicken Vitellogenin Gene. *Biochemistry* **1984**, *23* (19), 4275–4279. https://doi.org/10.1021/bi00314a003.

36 Taborsky, G. Optical Rotatory Dispersion and Circular Dichroism of Phosvitin at Low PH: Reversible Transition between Unordered Conformation and β Structure. *Journal of Biological Chemistry* **1968**, *243* (22), 6014–6020. https://doi.org/10.1016/S0021-9258(18)94521-7.

37 Damodaran, S.; Xu, S. The Role of Electrostatic Forces in Anomalous Adsorption Behavior of Phosvitin at the Air/Water Interface. *Journal of Colloid and Interface Science* **1996**, *178* (2), 426–435. https://doi.org/10.1006/jcis.1996.0137.

38 Yilmaz, B.; Ağagündüz, D. Bioactivities of Hen's Egg Yolk Phosvitin and Its Functional Phosphopeptides in Food Industry and Health. *Journal of Food Science* **2020**, *85* (10), 2969–2976. https://doi.org/10.1111/1750-3841.15447.

39 Castellani, O.; Belhomme, C.; David-Briand, E.; Guérin-Dubiard, C.; Anton, M. Oil-in-Water Emulsion Properties and Interfacial Characteristics of Hen Egg Yolk Phosvitin. *Food Hydrocolloids* **2006**, *20* (1), 35–43. https://doi.org/10.1016/j.foodhyd.2005.02.010.

40 Lee, S. k.; Han, J. h.; Decker, E. a. Antioxidant Activity of Phosvitin in Phosphatidylcholine Liposomes and Meat Model Systems. *Journal of Food Science* **2002**, *67* (1), 37–41. https://doi.org/10.1111/j.1365-2621.2002.tb11355.x.

41 Duan, X.; Li, M.; Ma, H.; Xu, X.; Jin, Z.; Liu, X. Physicochemical Properties and Antioxidant Potential of Phosvitin–Resveratrol Complexes in Emulsion System. *Food Chemistry* **2016**, *206*, 102–109. https://doi.org/10.1016/j.foodchem.2016.03.055.

42 Takeuchi, M.; Mashima, T.; Sztucki, M.; Petukhov, A. V.; Vis, M.; Friedrich, H.; Tuinier, R. Characterization of Hen Phosvitin in Aqueous Salt Solutions: Size, Structure, and Aggregation. *Food Hydrocolloids* **2022**, *129*, 107545. https://doi.org/10.1016/j.foodhyd.2022.107545.

43 Merkx, D. W. H.; Delić, F.; Wierenga, P. A.; Hennebelle, M.; van Duynhoven, J. P. M. 31P NMR Assessment of the Phosvitin-Iron Complex in Mayonnaise. *Magnetic Resonance in Chemistry* **2019**, *57* (9), 540–547. https://doi.org/10.1002/mrc.4808.

44 McCully, K. A.; Mok, C.-C.; Common, R. H. Paper Elegtrophoretic Characterization of Proteins and Lipoproteins of Hen's Egg Yolk. *Can. J. Biochem. Physiol.* **1962**, *40* (7), 937–952. https://doi.org/10.1139/o62-105.

45 Chang, C. M.; Powrie, W. D.; Fennema, O. Microstructure of Egg Yolk. *Journal of Food Science* **1977**, *42* (5), 1193–1200. https://doi.org/10.1111/j.1365-2621.1977.tb14458.x.

46 Moussa, M.; Martinet, V.; Trimeche, A.; Tainturier, D.; Anton, M. Low Density Lipoproteins Extracted from Hen Egg Yolk by an Easy Method: Cryoprotective Effect on Frozen–Thawed Bull Semen. *Theriogenology* **2002**, *57* (6), 1695–1706. https://doi.org/10.1016/S0093-691X(02)00682-9.

47 Jolivet, P.; Boulard, C.; Beaumal, V.; Chardot, T.; Anton, M. Protein Components of Low-Density Lipoproteins Purified from Hen Egg Yolk. *J. Agric. Food Chem.* **2006**, *54* (12), 4424–4429. https://doi.org/10.1021/jf0531398.

48 Saari, A.; Powrie, W. D.; Fennema, O. Isolation and Characterization of Low-Density Lipoproteins in Native Egg Yolk Plasma. *Journal of Food Science* **1964**, *29* (3), 307–315. https://doi.org/10.1111/j.1365-2621.1964.tb01736.x.

49 Cook, W. H.; Martin, W. G. *Chapter 8 in:" Structural and Functional Aspects of Lipoproteins in Living Systems", Eds. E. Tria and AM Scanu*; Academic Press, London, 1969.

50 Tria, E.; Scanu, A. M. Structural and Functional Aspects of Lipoproteins in Living Systems. *Structural and functional aspects of lipoproteins in living systems.* **1969**.

51 Mine, Y. Emulsifying Characterization of Hens Egg Yolk Proteins in Oil-in-Water Emulsions. *Food Hydrocolloids* **1998**, *12* (4), 409–415. https://doi.org/10.1016/S0268-005X(98)00054-X.

52 Koller, E.; Quehenberger, O.; Jürgens, G.; Wolfbeis, O. S.; Esterbauer, H. Investigation of Human Plasma Low Density Lipoprotein by Three-Dimensional Fluorescence Spectroscopy. *FEBS Lett* **1986**, *198* (2), 229–234. https://doi.org/10.1016/0014-5793(86)80411-2.

53 Pinchuk, I.; Lichtenberg, D. Analysis of the Kinetics of Lipid Peroxidation in Terms of Characteristic Time-Points. *Chem Phys Lipids* **2014**, *178*, 63–76. https://doi.org/10.1016/j.chemphyslip.2013.12.001.

54 Yang, S.; Takeuchi, M.; Friedrich, H.; van Duynhoven, J. P. M.; Hohlbein, J. Unravelling Mechanisms of Protein and Lipid Oxidation in Mayonnaise at Multiple Length Scales. *Food Chemistry* **2023**, *402*, 134417. https://doi.org/10.1016/j.foodchem.2022.134417.

55 Dickinson, E. Mixed Biopolymers at Interfaces: Competitive Adsorption and Multilayer Structures. *Food Hydrocolloids* **2011**, *25* (8), 1966–1983. https://doi.org/10.1016/j.foodhyd.2010.12.001.

56 Hinderink, E. B. A.; Münch, K.; Sagis, L.; Schroën, K.; Berton-Carabin, C. C. Synergistic Stabilisation of Emulsions by Blends of Dairy and Soluble Pea Proteins: Contribution of the Interfacial Composition. *Food Hydrocolloids* **2019**, *97*, 105206. https://doi.org/10.1016/j.foodhyd.2019.105206.

57 Dickinson, E.; Rolfe, S. E.; Dalgleish, D. G. Competitive Adsorption in Oil-in-Water Emulsions Containing α-Lactalbumin and β-Lactoglobulin. *Food Hydrocolloids* **1989**, *3* (3), 193–203. https://doi.org/10.1016/S0268-005X(89)80003-7.

58 Hinderink, E. B. A.; Meinders, M. B. J.; Miller, R.; Sagis, L.; Schroën, K.; Berton-Carabin, C. C. Interfacial Protein-Protein Displacement at Fluid Interfaces. *Advances in Colloid and Interface Science* **2022**, *305*, 102691. https://doi.org/10.1016/j.cis.2022.102691.

59 Hu, Y.-T.; Ting, Y.; Hu, J.-Y.; Hsieh, S.-C. Techniques and Methods to Study Functional Characteristics of Emulsion Systems. *Journal of Food and Drug Analysis* **2017**, *25* (1), 16–26. https://doi.org/10.1016/j.jfda.2016.10.021.

60 Javadi, A.; Mucic, N.; Karbaschi, M.; Won, J. Y.; Lotfi, M.; Dan, A.; Ulaganathan, V.; Gochev, G.; Makievski, A. V.; Kovalchuk, V. I.; Kovalchuk, N. M.; Krägel, J.; Miller, R. Characterization Methods for Liquid Interfacial Layers. *Eur. Phys. J. Spec. Top.* **2013**, *222* (1), 7–29. https://doi.org/10.1140/epjst/e2013-01822-3.

61 Murray, B. S. Rheological Properties of Protein Films. *Current Opinion in Colloid & Interface Science* **2011**, *16* (1), 27–35. https://doi.org/10.1016/j.cocis.2010.06.005.

62 Rampon, V.; Genot, C.; Riaublanc, A.; Anton, M.; Axelos, M. A. V.; McClements, D. J. Front-Face Fluorescence Spectroscopy Study of Globular Proteins in Emulsions: Displacement of BSA by a Nonionic Surfactant. *J. Agric. Food Chem.* **2003**, *51* (9), 2482–2489. https://doi.org/10.1021/jf026168g.

63 Chantrapornchai, W.; Clydesdale, F.; McClements, D. J. Influence of Droplet Size and Concentration on the Color of Oil-in-Water Emulsions. *J. Agric. Food Chem.* **1998**, *46* (8), 2914–2920. https://doi.org/10.1021/jf980278z.

64 Melik, D. H.; Fogler, H. S. Turbidimetric Determination of Particle Size Distributions of Colloidal Systems. *Journal of Colloid and Interface Science* **1983**, *92* (1), 161–180. https://doi.org/10.1016/0021-9797(83)90125-X.

65 Martens, K. J. A.; van Beljouw, S. P. B.; van der Els, S.; Vink, J. N. A.; Baas, S.; Vogelaar, G. A.; Brouns, S. J. J.; van Baarlen, P.; Kleerebezem, M.; Hohlbein, J. Visualisation of DCas9 Target Search in Vivo Using an Open-Microscopy Framework. *Nat Commun* **2019**, *10* (1), 3552. https://doi.org/10.1038/s41467-019-11514-0.

66 Born, M.; Wolf, E.; Bhatia, A. B.; Clemmow, P. C.; Gabor, D.; Stokes, A. R.; Taylor, A. M.; Wayman, P. A.; Wilcock, W. L. *Principles of Optics: Electromagnetic Theory of Propagation, Interference and Diffraction of Light*, 7th ed.; Cambridge University Press, 1999. https://doi.org/10.1017/CBO9781139644181.

67 Abbe, E. Beiträge zur Theorie des Mikroskops und der mikroskopischen Wahrnehmung. *Archiv f. mikrosk. Anatomie* **1873**, *9* (1), 413–468. https://doi.org/10.1007/BF02956173.

68 Pawley, J. B.; Pawley, J. B. *Handbook of Biological Confocal Microscopy*, 3rd ed.; Springer: New York, NY, 2006.

69 Luca, G. M. R. D.; Breedijk, R. M. P.; Brandt, R. A. J.; Zeelenberg, C. H. C.; Jong, B. E. de; Timmermans, W.; Azar, L. N.; Hoebe, R. A.; Stallinga, S.; Manders, E. M. M. Re-Scan Confocal Microscopy: Scanning Twice for Better Resolution. *Biomed. Opt. Express, BOE* **2013**, *4* (11), 2644–2656. https://doi.org/10.1364/BOE.4.002644.

70 De Luca, G. M. R.; Breedijk, R. M. P.; Brandt, R. A. J.; Zeelenberg, C. H. C.; de Jong, B. E.; Timmermans, W.; Azar, L. N.; Hoebe, R. A.; Stallinga, S.; Manders, E. M. M. Re-Scan Confocal Microscopy: Scanning Twice for Better Resolution. *Biomed. Opt. Express* **2013**, *4* (11), 2644. https://doi.org/10.1364/BOE.4.002644.

71 Hohlbein, J. Single-Molecule Localization Microscopy as an Emerging Tool to Probe Multiscale Food Structures. *Food Structure* **2021**, *30*, 100236. https://doi.org/10.1016/j.foostr.2021.100236.

72 Gallegos-Cerda, S. D.; Hernández-Varela, J. D.; Chanona-Pérez, J. J.; Arredondo Tamayo, B.; Méndez Méndez, J. V. Super-Resolution Microscopy and Their Applications in Food Materials: Beyond the Resolution Limits of Fluorescence Microscopy. *Food Bioprocess Technol* **2023**, *16* (2), 268–288. https://doi.org/10.1007/s11947-022-02883-4.

73 Dyba, M.; Jakobs, S.; Hell, S. W. Immunofluorescence Stimulated Emission Depletion Microscopy. *Nat Biotechnol* **2003**, *21* (11), 1303–1304. https://doi.org/10.1038/nbt897.

74 Weber, M.; Leutenegger, M.; Stoldt, S.; Jakobs, S.; Mihaila, T. S.; Butkevich, A. N.; Hell, S. W. MINSTED Fluorescence Localization and Nanoscopy. *Nat. Photonics* **2021**, *15* (5), 361–366. https://doi.org/10.1038/s41566-021-00774-2.

75 Wang, S.; Ding, M.; Chen, X.; Chang, L.; Sun, Y. Development of Bimolecular Fluorescence Complementation Using RsEGFP2 for Detection and Super-Resolution Imaging of Protein-Protein Interactions in Live Cells. *Biomed. Opt. Express* **2017**, *8* (6), 3119. https://doi.org/10.1364/BOE.8.003119.

76 Balzarotti, F.; Eilers, Y.; Gwosch, K. C.; Gynnå, A. H.; Westphal, V.; Stefani, F. D.; Elf, J.; Hell, S. W. Nanometer Resolution Imaging and Tracking of Fluorescent Molecules with Minimal Photon Fluxes. *Science* **2017**, *355* (6325), 606–612. https://doi.org/10.1126/science.aak9913.

77 Rust, M. J.; Bates, M.; Zhuang, X. Sub-Diffraction-Limit Imaging by Stochastic Optical Reconstruction Microscopy (STORM). *Nat Methods* **2006**, *3* (10), 793–796. https://doi.org/10.1038/nmeth929.

78 Betzig, E.; Patterson, G. H.; Sougrat, R.; Lindwasser, O. W.; Olenych, S.; Bonifacino, J. S.; Davidson, M. W.; Lippincott-Schwartz, J.; Hess, H. F. Imaging Intracellular Fluorescent Proteins at Nanometer Resolution. *Science* **2006**, *313* (5793), 1642–1645. https://doi.org/10.1126/science.1127344.

79 Sharonov, A.; Hochstrasser, R. M. Wide-Field Subdiffraction Imaging by Accumulated Binding of Diffusing Probes. *Proc. Natl. Acad. Sci. U.S.A.* **2006**, *103* (50), 18911–18916. https://doi.org/10.1073/pnas.0609643104.

80 Heilemann, M.; van de Linde, S.; Schüttpelz, M.; Kasper, R.; Seefeldt, B.; Mukherjee, A.; Tinnefeld, P.; Sauer, M. Subdiffraction-Resolution Fluorescence Imaging with Conventional Fluorescent Probes. *Angew. Chem. Int. Ed.* **2008**, *47* (33), 6172–6176. https://doi.org/10.1002/anie.200802376.

81 Jungmann, R.; Steinhauer, C.; Scheible, M.; Kuzyk, A.; Tinnefeld, P.; Simmel, F. C. Single-Molecule Kinetics and Super-Resolution Microscopy by Fluorescence Imaging of Transient Binding on DNA Origami. *Nano Lett.* **2010**, *10* (11), 4756–4761. https://doi.org/10.1021/nl103427w.

82 Small, A.; Stahlheber, S. Fluorophore Localization Algorithms for Super-Resolution Microscopy. *Nat Methods* **2014**, *11* (3), 267–279. https://doi.org/10.1038/nmeth.2844.

83 Henriques, R.; Lelek, M.; Fornasiero, E. F.; Valtorta, F.; Zimmer, C.; Mhlanga, M. M. QuickPALM: 3D Real-Time Photoactivation Nanoscopy Image Processing in ImageJ. *Nat Methods* **2010**, *7* (5), 339–340. https://doi.org/10.1038/nmeth0510-339.

84 Parthasarathy, R. Rapid, Accurate Particle Tracking by Calculation of Radial Symmetry Centers. *Nat Methods* **2012**, *9* (7), 724–726. https://doi.org/10.1038/nmeth.2071.

85 Babcock, H. P.; Zhuang, X. Analyzing Single Molecule Localization Microscopy Data Using Cubic Splines. *Sci Rep* **2017**, *7* (1), 552. https://doi.org/10.1038/s41598-017-00622-w.

86 Martens, K. J. A.; Bader, A. N.; Baas, S.; Rieger, B.; Hohlbein, J. Phasor Based Single-Molecule Localization Microscopy in 3D (PSMLM-3D): An Algorithm for MHz Localization Rates Using Standard CPUs. *The Journal of Chemical Physics* **2018**, *148* (12), 123311. https://doi.org/10.1063/1.5005899.

87 Deschout, H.; Zanacchi, F. C.; Mlodzianoski, M.; Diaspro, A.; Bewersdorf, J.; Hess, S. T.; Braeckmans, K. Precisely and Accurately Localizing Single Emitters in Fluorescence Microscopy. *Nat Methods* **2014**, *11* (3), 253–266. https://doi.org/10.1038/nmeth.2843.

88 Špelda, D. The Role of the Telescope and Microscope in the Constitution of the Idea of Scientific Progress. *The Seventeenth Century* **2019**, *34* (1), 107–126. https://doi.org/10.1080/0268117X.2017.1356743.

89 Hardy, J. W. *Adaptive Optics for Astronomical Telescopes*; Oxford series in optical and imaging sciences; Oxford University Press: New York, 1998.

90 Schwertner, M.; Booth, M. J.; Wilson, T. Characterizing Specimen Induced Aberrations for High NA Adaptive Optical Microscopy. *Opt. Express* **2004**, *12* (26), 6540. https://doi.org/10.1364/OPEX.12.006540.

91 Vellekoop, I. M.; Aegerter, C. M. Scattered Light Fluorescence Microscopy: Imaging through Turbid Layers. *Opt. Lett.* **2010**, *35* (8), 1245. https://doi.org/10.1364/OL.35.001245.

92 Tyson, R. *Principles of Adaptive Optics*, 0 ed.; CRC Press, 2010. https://doi.org/10.1201/EBK1439808580.

93 Claflin, E. S.; Bareket, N. Configuring an Electrostatic Membrane Mirror by Least-Squares Fitting with Analytically Derived Influence Functions. *J. Opt. Soc. Am. A* **1986**, *3* (11), 1833. https://doi.org/10.1364/JOSAA.3.001833.

94 Steinhaus, E.; Lipson, S. G. Bimorph Piezoelectric Flexible Mirror. *J. Opt. Soc. Am.* **1979**, *69* (3), 478. https://doi.org/10.1364/JOSA.69.000478.

95 Ealey, M. A. Deformable Mirrors At Litton/Itek: A Historical Perspective; Vukobratovich, D., Ed.; San Diego, 1989; p 48. https://doi.org/10.1117/12.962929.

96 Ealey, M. A. Continuous Facesheet Low Voltage Deformable Mirrors. *Opt. Eng.* **1990**, *29* (10), 1191. https://doi.org/10.1117/12.55715.

97 Booth, M. J. Adaptive Optics in Microscopy. *Phil. Trans. R. Soc. A.* **2007**, *365* (1861), 2829–2843. https://doi.org/10.1098/rsta.2007.0013.

98 Booth, M. J. Adaptive Optical Microscopy: The Ongoing Quest for a Perfect Image. *Light Sci Appl* **2014**, *3* (4), e165–e165. https://doi.org/10.1038/lsa.2014.46.

99 Li, C.; Xian, H.; Rao, C.; Jiang, W. Field-of-View Shifted Shack-Hartmann Wavefront Sensor for Daytime Adaptive Optics System. *Opt. Lett.* **2006**, *31* (19), 2821. https://doi.org/10.1364/OL.31.002821.

100 Tao, X.; Fernandez, B.; Azucena, O.; Fu, M.; Garcia, D.; Zuo, Y.; Chen, D. C.; Kubby, J. Adaptive Optics Confocal Microscopy Using Direct Wavefront Sensing. *Opt. Lett.* **2011**, *36* (7), 1062. https://doi.org/10.1364/OL.36.001062.

101 Johnson, P. A.; Trissel, R. G.; Cuellar, E. L.; Arnold, R. L.; Sandler, D. G. Real-Time Wavefront Reconstruction for a 512 Subaperture Adaptive Optical System; Ealey, M. A., Ed.; San Diego, CA, 1992; p 460. https://doi.org/10.1117/12.51201.

102 Sandler, D. G.; Cuellar, L.; Lefebvre, M.; Barrett, T.; Arnold, R.; Johnson, P.; Rego, A.; Smith, G.; Taylor, G.; Spivey, B. Shearing Interferometry for Laser-Guide-Star Atmospheric Correction at Large D/R_0. *J. Opt. Soc. Am. A* **1994**, *11* (2), 858. https://doi.org/10.1364/JOSAA.11.000858.

103 Roddier, C.; Roddier, F.; Demarcq, J. Compact Rotational Shearing Interferometer For Astronomical Applications. *Opt. Eng* **1989**, *28* (1). https://doi.org/10.1117/12.7976903.

104 Bonaglia, M. Design of the Wavefront Sensor Unit of ARGOS, the LBT Laser Guide Star System. **2012**. https://doi.org/10.48550/ARXIV.1203.5081.

105 Huang, B.; Wang, W.; Bates, M.; Zhuang, X. Three-Dimensional Super-Resolution Imaging by Stochastic Optical Reconstruction Microscopy. *Science* **2008**, *319* (5864), 810–813. https://doi.org/10.1126/science.1153529.

106 Burke, D.; Patton, B.; Huang, F.; Bewersdorf, J.; Booth, M. J. Adaptive Optics Correction of Specimen-Induced Aberrations in Single-Molecule Switching Microscopy. *Optica* **2015**, *2* (2), 177. https://doi.org/10.1364/OPTICA.2.000177.

107 Tehrani, K. F.; Zhang, Y.; Shen, P.; Kner, P. Adaptive Optics Stochastic Optical Reconstruction Microscopy (AO-STORM) by Particle Swarm Optimization. *Biomed. Opt. Express* **2017**, *8* (11), 5087. https://doi.org/10.1364/BOE.8.005087.

108 Hess, S. T.; Girirajan, T. P. K.; Mason, M. D. Ultra-High Resolution Imaging by Fluorescence Photoactivation Localization Microscopy. *Biophysical Journal* **2006**, *91* (11), 4258–4272. https://doi.org/10.1529/biophysj.106.091116.

109 Burke, D.; Patton, B.; Huang, F.; Bewersdorf, J.; Booth, M. J. Adaptive Optics Correction of Specimen-Induced Aberrations in Single-Molecule Switching Microscopy. *Optica* **2015**, *2* (2), 177. https://doi.org/10.1364/OPTICA.2.000177.

110 Zernike, F.; Stratton, F. J. M. Diffraction Theory of the Knife-Edge Test and Its Improved Form, The Phase-Contrast Method. *Monthly Notices of the Royal Astronomical Society* **1934**, *94* (5), 377–384. https://doi.org/10.1093/mnras/94.5.377.

111 Siemons, M. E.; Hanemaaijer, N. A. K.; Kole, M. H. P.; Kapitein, L. C. Robust Adaptive Optics for Localization Microscopy Deep in Complex Tissue. *Nat Commun* **2021**, *12* (1), 3407. https://doi.org/10.1038/s41467-021-23647-2.

112 Shechtman, Y.; Sahl, S. J.; Backer, A. S.; Moerner, W. E. Optimal Point Spread Function Design for 3D Imaging. *Phys. Rev. Lett.* **2014**, *113* (13), 133902. https://doi.org/10.1103/PhysRevLett.113.133902.

113 Zhou, Y.; Carles, G. Precise 3D Particle Localization over Large Axial Ranges Using Secondary Astigmatism. *Opt. Lett.* **2020**, *45* (8), 2466. https://doi.org/10.1364/OL.388695.

114 Quirin, S.; Pavani, S. R. P.; Piestun, R. Optimal 3D Single-Molecule Localization for Superresolution Microscopy with Aberrations and Engineered Point Spread Functions. *Proceedings of the National Academy of Sciences* **2012**, *109* (3), 675–679. https://doi.org/10.1073/pnas.1109011108.

115 King, S. V.; Doblas, A.; Patwary, N.; Saavedra, G.; Martínez-Corral, M.; Preza, C. Implementation of PSF Engineering in High-Resolution 3D Microscopy Imaging with a LCoS (Reflective) SLM. In *Three-Dimensional and Multidimensional Microscopy: Image Acquisition and Processing XXI*; SPIE, 2014; Vol. 8949, pp 174–180. https://doi.org/10.1117/12.2040723.

116 Pavani, S. R. P.; Thompson, M. A.; Biteen, J. S.; Lord, S. J.; Liu, N.; Twieg, R. J.; Piestun, R.; Moerner, W. E. Three-Dimensional, Single-Molecule Fluorescence Imaging beyond the Diffraction Limit by Using a Double-

Helix Point Spread Function. *Proc. Natl. Acad. Sci. U.S.A.* **2009**, *106* (9), 2995–2999. https://doi.org/10.1073/pnas.0900245106.

117 Aristov, A.; Lelandais, B.; Rensen, E.; Zimmer, C. ZOLA-3D Allows Flexible 3D Localization Microscopy over an Adjustable Axial Range. *Nat Commun* **2018**, *9* (1), 2409. https://doi.org/10.1038/s41467-018-04709-4.

118 York, A. G.; Ghitani, A.; Vaziri, A.; Davidson, M. W.; Shroff, H. Confined Activation and Subdiffractive Localization Enables Whole-Cell PALM with Genetically Expressed Probes. *Nat Methods* **2011**, *8* (4), 327–333. https://doi.org/10.1038/nmeth.1571.

119 Petrov, P. N.; Shechtman, Y.; Moerner, W. E. Measurement-Based Estimation of Global Pupil Functions in 3D Localization Microscopy. *Opt. Express* **2017**, *25* (7), 7945. https://doi.org/10.1364/OE.25.007945.

120 Li, Y.; Mund, M.; Hoess, P.; Deschamps, J.; Matti, U.; Nijmeijer, B.; Sabinina, V. J.; Ellenberg, J.; Schoen, I.; Ries, J. Real-Time 3D Single-Molecule Localization Using Experimental Point Spread Functions. *Nat Methods* **2018**, *15* (5), 367–369. https://doi.org/10.1038/nmeth.4661.

121 Martens, K. J. A.; Jabermoradi, A.; Yang, S.; Hohlbein, J. Integrating Engineered Point Spread Functions into the Phasor-Based Single-Molecule Localization Microscopy Framework. *Methods* **2021**, *193*, 107–115. https://doi.org/10.1016/j.ymeth.2020.07.010.

122 Douglass, K. M.; Sieben, C.; Archetti, A.; Lambert, A.; Manley, S. Super-Resolution Imaging of Multiple Cells by Optimized Flat-Field Epi-Illumination. *Nature Photon* **2016**, *10* (11), 705–708. https://doi.org/10.1038/nphoton.2016.200.

123 Deschamps, J.; Rowald, A.; Ries, J. Efficient Homogeneous Illumination and Optical Sectioning for Quantitative Single-Molecule Localization Microscopy. *Opt. Express* **2016**, *24* (24), 28080. https://doi.org/10.1364/OE.24.028080.

124 Ma, H.; Fu, R.; Xu, J.; Liu, Y. A Simple and Cost-Effective Setup for Super-Resolution Localization Microscopy. *Sci Rep* **2017**, *7* (1), 1542. https://doi.org/10.1038/s41598-017-01606-6.

125 Mau, A.; Friedl, K.; Leterrier, C.; Bourg, N.; Lévêque-Fort, S. *Fast Scanned Widefield Scheme Provides Tunable and Uniform Illumination for Optimized SMLM on Large Fields of View*; preprint; Bioengineering, 2020. https://doi.org/10.1101/2020.05.08.083774.

126 Khaw, I.; Croop, B.; Tang, J.; Möhl, A.; Fuchs, U.; Han, K. Y. Flat-Field Illumination for Quantitative Fluorescence Imaging. *Opt. Express* **2018**, *26* (12), 15276. https://doi.org/10.1364/OE.26.015276.

127 Stehr, F.; Stein, J.; Schueder, F.; Schwille, P.; Jungmann, R. Flat-Top TIRF Illumination Boosts DNA-PAINT Imaging and Quantification. *Nat Commun* **2019**, *10* (1), 1268. https://doi.org/10.1038/s41467-019-09064-6.

2

Enabling single-molecule localization microscopy in turbid food emulsions

A version of this chapter has been published as:

Abbas Jabermoradi, Suyeon Yang, Martijn Gobes, John P.M. van Duynhoven, Johannes Hohlbein. Enabling single-molecule localization microscopy in turbid food emulsions. Philosophical Transactions of the Royal Society A, 380 (2020)

Abstract

Turbidity poses a major challenge for the microscopic characterization of food systems. Local mismatches in refractive indices, for example, lead to significant image deterioration along sample depth. To mitigate the issue of turbidity and to increase the accessible optical resolution in food microscopy, we added adaptive optics (AO) and flat-field illumination to our previously published open microscopy framework, the miCube. In the detection path, we implemented AO via a deformable mirror to compensate aberrations and to modulate the emission wavefront enabling the engineering of point spread functions (PSFs) for single-molecule localization microscopy (SMLM) in three dimensions. As a model system for a non-transparent food colloid such as mayonnaise, we designed an oil-in-water emulsion containing the ferric ion binding protein phosvitin commonly present in egg yolk. We targeted phosvitin with fluorescently labelled primary antibodies and used PSF engineering to obtain two- and three-dimensional images of phosvitin covered oil droplets with sub 100 nm resolution. Our data indicated that phosvitin is homogeneously distributed at the interface. With the possibility to obtain super-resolved images in depth, our work paves the way for localizing biomacromolecules at heterogeneous colloidal interfaces in food emulsions.

2.1 Introduction

In turbid media, optical imaging can be compromised by the presence of ingredients or phases bearing different refractive indices. In food emulsions such as mayonnaise, for example, the presence of oil droplets in the aqueous phase will disturb incoming and outgoing wavefronts of light. With an increasing depth of imaging, more and more photons will be reflected, absorbed, or scattered leading to aberrated images that suffer from decreased resolution, blurriness and distortions[1,2]. To correct aberrations, the concept of adaptive optics (AO) was developed in which active controllable elements such as deformable mirrors or spatial light modulators allow to modulate the wavefronts before the light reaches the photon detecting camera[3]. First developed for astronomical telescopes[4], AO is increasingly finding applications in fluorescence microscopy such as a super resolution[5], light-sheet[6], confocal[7,8] or multiphoton[9] microscopy. AO can be implemented using direct or indirect wavefront sensing[10]. In the direct sensing mode, an additional wavefront sensor (e.g. Shack–Hartmann wavefront sensor) is required to send instantaneous feedback to the optical element that can modulate the wavefront[11]. However, operation in direct mode reduces the number of photons available for image formation, hampering especially applications in super-resolution localization microscopy (SMLM)[12,13]. Using indirect sensing, the wavefront is obtained from analyzing a sequence of images allowing more photons to reach the main camera and simplifying the experimental layout. A common implementation of indirect sensing AO uses a deformable mirror in reflecting mode to compensate aberrations that can be described by Zernike polynomials[14].

In SMLM, individual emitters, whose distance to each other is below the diffraction limit of optical microscopy, can be distinguished from each other, if conditions are achieved that allow separation of the emission of each fluorophore in time. In the dSTORM (direct stochastic optical reconstruction microscopy) variant, this requirement is achieved by using blinking fluorophores that switch between fluorescent and non-fluorescent states[15,16]. Originally a two-dimensional imaging technique, three-dimensional resolution in SMLM can be achieved by breaking the axial symmetry of the imaged point spread function (PSF) using astigmatism[17,18] or further PSF engineering via phase masks or AO enabling saddle point, tetrapod[19] and double helix[20] PSFs. Our recent work introduced a method called circular-tangent phasor-based SMLM (ct-pSMLM) that enables fast and accurate localization of emitters after PSFs engineering on standard CPUs[21].

SMLM has not yet found widespread use to study food systems[22]. We therefore decided to update the previously published miCube microscopy framework[23] on several aspects to showcase SMLM in food-related turbid media. Quantitative SMLM measurements are often compromised by inhomogeneous illumination due to a Gaussian intensity distribution of the exciting laser beam. To overcome this issue, several approaches have been introduced to achieve illumination with a constant intensity over the entire field of view. Examples include the use of a pair of micro lenses array consisting of identical spherical lenslets[24,25], the use of multimode optical fibers (MMF)[26] for illumination in combination with speckle reducers[27] or rotating diffusers[28] with the latter being less suitable for total internal reflection fluorescence (TIRF) microscopy due to the degradation of spatial coherence that prevents diffraction limited focusing. Recent work further demonstrated flat field illumination over variable field sizes using two galvanometer scanning mirrors placed in a plane conjugated to the back focal plane of the microscope objective in epifluorescence or TIRF mode[29]. In our implementation, we added a top-hat beam shaper in the excitation path that converts the Gaussian shaped intensity distribution of the excitation beam into a homogeneous flat field profile (top hat) enabling quantitative microscopy[30,31]. Moreover, we equipped the miCube with a deformable mirror placed in the detection pathway to compensate aberrations coming from in-depth imaging of opaque samples with spatial variations of refractive indices and for enabling PSF engineering. In particular, we adapted an approach called robust and effective adaptive optics in localization microscopy (REALM) that was recently developed to compensate aberrations in depth of complex biological samples[32]. REALM uses the image quality metric derived from a weighted sum of Fourier transforms of raw images of emitters to estimate the aberrations. REALM then compensates the aberrations of different Zernike modes based on the metric values and biases of the mirror.

In a recent study using conventional multi-colour confocal microscopy, we found evidence that the distribution of oxidized proteins in the water phase and the oil/water interface of mayonnaise is not homogeneous[33]. Mayonnaise is a highly turbid food emulsion containing up to 80% of oil, in which egg yolk acts as an emulsifier[34]. For the previous oxidation study, we saw structural features too small to be resolved, motivating us to implement SMLM. To demonstrate the applicability of SMLM, we will here use a dilute oil-in-water model emulsion that was emulsified with phosvitin[35]. Phosvitin is a protein contained in egg yolk that has a binding capacity for ferric ions[36]. Ferric/ferrous ions can catalyze lipid oxidation at the oil–water interface, which can be detrimental to the sensorial and nutritional quality of food emulsions. Visualization of phosvitin at oil–water interfaces in food emulsions is therefore relevant to understand lipid oxidation mechanisms and design anti-oxidant strategies[37]. For our model emulsion, we opted for a 15% v/v oil concentration to obtain small droplets (approx. 1 µm diameter) with a large surface area available for phosvitin. We then used a phosvitin antibody conjugated with the fluorophore Alexa Fluor 647 to map phosvitin at the droplet interface and to obtain the three-dimensional distribution of phosvitins. With the demonstration of SMLM supported by adaptive optics, PSF engineering and a flat-field illumination scheme, our work paves the way for quantitative characterization of food systems under ambient environmental conditions.

2.2 Material and methods

2.2.1 The miCube excitation path

For laser excitation, we used two options. The first option features a standard laser combiner (Omicron Lighthub, Germany) equipped with 4 lasers operating at 405 nm, 488 nm, 561 nm, and 642 nm that were coupled into a single mode fiber. As a second option, we used two low-cost diode lasers equipped with simple beam shaping optics. The lasers operate at 635 nm (PD-01287, 200 mW, Standard Module, Lasertack, Germany) and 520 nm (PD-01298, 100 mW, Standard Module, Lasertack, Germany) and are controlled via a home-built Arduino powered laser control engine (**https://hohlbeinlab.github.io/miCube/LaserTrack_Arduino.html**). After combining the laser light with a dichroic mirror (RGB Beam Splitter-Combiner – Lasertack, Germany), the light was coupled into a single-mode fiber (P3-460B-FC-2, Thorlabs) using a 10x objective (RMS10X - 10X Olympus Plan Achromat Objective, Japan). The coupling efficiencies of the 635 nm and 520 nm diode lasers to single-mode fiber were 56% and 42%, respectively. For collimating the laser light after the fiber, we used an achromatic lens (CL) of either 30 mm or 60 mm focal length (AC254-030-A-ML and AC254-060-A-ML, Thorlabs). Collimation was checked with a shear plate (SI050, Thorlabs). The laser light was then reflected by an elliptical mirror (M1, BBE1-E02, Thorlabs) mounted to a right-angle kinematic cage mount (KCB1E/M, Thorlabs), towards the top-hat beam shaper (TSM25-10-D-D-355, Top Shape, Asphericon GmbH, Germany) to create a homogeneous distribution of illumination intensity. The ideal input beam size for the beam shaper is between 9.2 mm and 10.8 mm (1/e2). Using the 60 mm collimating lens, the input beam size is approximately 10.2 mm. After the beam shaping, the laser beam was reflected with another mirror (M2, BBE1-E02, Thorlabs) towards an iris (Iris, SM1D12D, Thorlabs) that allows the area of illumination in the sample plane to be controlled. The laser light was then focused into the back focal plane (BFP) of the microscope objective using an achromatic lens (TR, f = 150 mm, AC508-150-A-ML, Thorlabs) mounted on a translational stage (XR25C/M, Thorlabs) used to change the position of the focus in the BFP.

2.2.2 The miCube main block

The main block itself is similar to the one reported previously[23]. The laser beam focused by the TIRF lens is reflected by a polychroic mirror (DiM, ZT532/640rpc or ZT405/488/561/640rpcv2, Chroma) into the back focal plane of the objective lens (OL, CFI Plan Apo Lambda 100× Oil NA 1.45, Nikon). The sample was placed on a three-dimensional printed coverslip sample holder and secured in place with small magnets. We used a stick–slip piezo XYZ stage (SLS-3232, SmarAct GmbH, Germany) for sample scanning. The stage has a footprint of 32 mm by 32 mm and offers a travel range of 21 mm in each direction with 1 nm closed-loop resolvable position resolution. The stage is able to handle payloads of up to 1.5 N. The light emitted from the sample was collected with the same microscope objective and, after passing the polychroic mirror, further cleaned up with a bandpass filter (F, ZET532/640m-TRF, Chroma) located at the bottom of the dichroic cage holder (DFM1/M, Thorlabs) to block remaining back-reflected laser light from entering the emission path. Subsequently, emitted light was reflected using a 90° mirror (M3, BBE1-E02, Thorlabs) towards the tube lens.

2.2.3 The miCube emission path

A tube lens TuL (MXA20696, Nikon) with 200 mm effective focal length is used to form an image in the first image plane. An elliptical mirror M4 (BBE1-E02, Thorlabs) steers the light towards a 4f system of lenses. The first lens L1 (AC508-100-A-ML, Thorlabs) was positioned to collimate the light from the first image plane. As the angle between incident and reflected light from the deformable mirror should stay below 30°, we used mirror M5 (PF10-03-P01, Protected Silver Mirror, Thorlabs) mounted to a precision kinematic mirror holder (KS1, Thorlabs), placed in front of the deformable mirror to control this angle. For modifying the incoming wave front and to compensate the aberrations, we placed the deformable mirror DM (DMP40/M-P01, 40- Actuator Piezo Deformable Mirror, Thorlabs) in the Fourier plane of L1 (one focal distance). The deformable mirror consists of a 40-actuator array with three bimorph benders for ±2.0 mrad Tip/Tilt actuation and was mounted on a XZ linear stage (XR25C/M, Thorlabs) to simplify the alignment of the mirror in respect to the emission light. The light reflected from the deformable mirror was conducted to lens L2 (AC508-100-A-ML, Thorlabs), which focused the light on the camera (Prime 95B sCMOS, Photometrics) having a maximum quantum yield of 95% QE and featuring a 11 µm by 11 µm pixel size. The camera was mounted on a custom three-dimensional printed stand to adjust the height and position on the optical table.

2.2.4 Re-scan confocal microscopy

We updated the previous miCube microscope with a re-scan confocal microscopy (RCM) module (Confocal.nl, Amsterdam, The Netherlands)[38]. The RCM has a separate fiber input for and allows scanning of the collimated laser beam across the sample. The emitted light from the specimen is then rescanned with a second mirror with twice the sweep length as the excitation scanning mirror, leading to a 43 nm pixel size on the sCMOS chip. The RCM is capable of achieving a $\sqrt{2}$ times increase in resolution compared to classical confocal laser scanning microscopes.

2.2.5 Deformable mirror for adaptive optics and PSF engineering

The mirror (DM, DMP40/M-P01, 40-Actuator Piezo Deformable Mirror, Thorlabs) consists of 40 individual actuators and three arms for tip/tilt. Each actuator and each arm can be controlled by applying voltages between 0 V and 200 V. In combination, the voltages determine the curvature of the mirror. To correct the flatness of the mirror and later for modulating the PSFs, we implemented REALM (**https://github.com/MSiemons/REALM**)[32], which allows for corrections without requiring an additional sensor to monitor the incoming wavefront. We further wrote a plugin for Micromanager to connect REALM to the deformable mirror used in our study (**https://github.com/HohlbeinLab/Thorlabs_DM_Device_Adapter**)[21].

2.2.6 Data acquisition, visualization and image analysis of SMLM data

If not stated otherwise, we used the 642 nm laser for excitation of Alexa Fluor 647 and the 405 nm laser for photo-reactivation. Movies were recorded for 10,000 frames with a frame time of 20 ms. The raw data were analysed with ThunderSTORM[39] plugin in ImageJ/Fiji[40] based on the phasor-based localization algorithm[41]. After obtaining the localizations, we performed two-dimensional cross-correlation drift correction (settings in ThunderSTORM: 10 bins and 5× magnification). The localizations were visualized using the average shifted histogram options, with the magnification set to 5. Moreover, no lateral shifts were added and cyan was chosen for the lookup table. A rewritten ImageJ plugin was used to remove constant fluorescence background by means of a temporal median filter[42] (see **github.com/HohlbeinLab/FTM2 for the ImageJ/Fiji plugin**). To determine the histogram of droplet sizes, we first manually encircled droplets in the field of view based on the ring-shaped presence and absence of fluorescence. We then applied the Hough circle transform[43] function in MATLAB (Mathworks, UK) to obtain the radii of all circles using 0.2 μm as the minimum and 2 μm as the maximum search radius for oil droplets. For measuring the resolution of super resolved images, we further used Fourier ring correlation (FRC) as implemented in the software package SMAP[44].

2.2.7 Isolation and purification of phosvitin

Our procedure of isolating and purifying phosvitin follows previous work[36]. Briefly, fresh hen eggs were purchased from the domestic market. To remove egg white and chalazas, the yolks were rolled on a filter paper. The temperature of the following steps was kept at 4◦C. An equal amount of distilled water was added to the yolk. The diluted solution was centrifuged at 12,000 g for 10 min (Avanti j-25, Beckman). The precipitate was collected and homogenized with an equal mass of a 0.17 M NaCl solution and centrifuged again at 12,000 g for 10 min. The granules were dissolved in a 10% w/v of a 1.74 M NaCl solution. The pH was adjusted to 8.0 with 1 mM NaOH solution and homogenized with 4% PEG6000 w/w and centrifuged at 12,000 g for another 10 min. The supernatant was dialyzed against distilled water for 48 h and subsequently centrifuged at 12,000 g for 10 min. The supernatant was collected and lyophilized using a lyophilizer from either Christ, Germany or Labconco, USA.

2.2.8 Phosvitin based model emulsion

In total, 6 mg ml−1 of lyophilized phosvitin was added to 0.05 M of 2-N-porpholino ethane sulfonic acid (MES) buffer at pH 6.6. The solution was centrifuged at 4,000 g for 20 min and the supernatant was extracted to remove the undissolved particle from the solution. We then added 0.15% w/v of sodium dodecyl sulfate (SDS) to the solution to obtain a stable model emulsion. A 15% oil in water mixture was prepared with 7.5 mL of rapeseed oil and 42.5 mL of the phosvitin containing solution. The emulsion was premixed with an 18 mm diameter head disperser at 18,000 r.p.m. for 2 min (T 18 digital ULTRA-TURRAX, IKA, Germany). Next, the 15% oil in water model emulsion was obtained by emulsifying the premix at 70 bar for 20 min with a flow rate of 80 mL min^{-1} using a high-pressure homogenizer (Delta Instruments LAB Homogenizer).

2.2.9 Sample preparation

For the rescan-confocal microscopy measurements on mayonnaise, 1% w/w of 1 mg mL^{-1} Nile blue (Sigma, ref. N0766) solution was gently stirred into the mayonnaise. Nile blue was excited at 642 nm. For correcting the deformable mirror, we used fluorescent beads (FluoSpheresTM Carboxylate-Modified Microspheres, 28 nm diameter, dark red fluorescent (660/680), Thermo Fisher). First, we diluted the provided solution 1 : 100,000 and added 4 mL of the dilution to a coverslip (no. 1.5, Thermo Scientific Menzel Gläser). We then used a second coverslip used on top of the first one to have homogeneous distribution of beads on the field of view. To measure the drift characteristics in x, y and z, we prepared a sample as described but using 50 nm fluorescent beads (560 nm peak emission wavelength) instead. For dSTORM measurements, the phosvitin antibody conjugated with Alexa Fluor 647 stock solution was first diluted 50 times in TRIS buffer. Here 40 µL of the diluted antibodies were then added to 400 µL of the 15% oil-inwater model emulsion. In order to stall self-diffusion of droplets, we further added 0.5% w/v of guar gum (Sigma, ref. G4129). The specimen was then dripped into a well of a silicon gasket. 1.5 µL of the STORM buffer containing 50 mM TRIS pH 8, 10 mM NaCl, 10% glucose, 140 mM 2-mercaptoethanol, 68 µg mL^{-1} catalase and 200 µg ml^{-1} glucose oxidase[45] was mixed into 15 µL of sample, before we sealed the gasket. We note that although we effectively used a 10- fold reduced concentration of a standard STORM buffer in our sample, sufficient blinking was achieved. Using a 10× increased concentration of BME did not lead to improvements in blinking and achievable resolution.

2.3 Results and discussion

2.3.1 Turbidity compromises the image quality in oil-in-water emulsions

We first imaged a mayonnaise sample containing Nile blue using a stack of confocal images to demonstrate the challenges of optical imaging in turbid media (**Figure 2.1A**). The expected loss of optical resolution in depth of the sample is seen in the cross-sectional view; an increase of imaging depth coincides with increased blurriness (**Figure 2.1B, C**). To obtain a model emulsion suitable for SMLM, we prepared a low (15%) oil-in-water model emulsion emulsified with phosvitin. We decided to start with a simple model system consisting of phosvitin as the main emulsifier to develop and refine the required microscopy framework. The main restriction of using real mayonnaise is its compositional complexity: egg yolk, used as emulsifier in mayonnaise, consists of many different proteins (e.g., phosvitin, LDL, apoB) making an attribution of the individual contributions difficult. Owing to the lower oil content of the model emulsion, the packing of droplets is less dense leading to self-diffusion of droplets. We therefore added guar gum to the emulsion which increased the viscosity leading to an effective immobilization of the droplets (**Figure 2.1D, E**). The rescan-confocal laser scanning images showed that the high shear during emulsification resulted in smaller droplet sizes (approx. 0.5 µm radius) compared to typical mayonnaises (2– 2.5 µm radius; **Figure 2.1E, F**). Similar to imaging in mayonnaise, we observed a loss of resolution and signal-to-noise ratio with increasing depth (**Figure 2.1G, H**). We note that larger areas are void of droplets and are likely occupied with guar gum networks (**Figure 2.1B, E**: xz and xy sectional views).

2.3.2 Adapting the miCube for SMLM in turbid media

We modified the miCube microscopy framework[23] at various positions to address the challenges imposed by super-resolution measurements in turbid media and to provide users with additional hardware options (**Figure 2.2**). In the excitation path, we included an option to use cheaper laser diodes as light sources rather than a scientific-grade multicolor laser engine. To enable simplified quantitative analysis of super-resolution data, we added a top-hat beam shaper providing an even illumination profile over the field of view[24,30,31]. We compared the resulting illumination profile in the field of view with one obtained using conventional Gaussian distributed laser excitation (**Figure 2.2B–D**). To this end, we placed a droplet of 1 µM Cy3B dye solution (Cytiva) on the coverslip and used a second coverslip on top to obtain a homogeneous spatial distribution of fluorophores. The fluorescence intensity profiles of the Gaussian and flattop epi-illumination were obtained by exciting the sample with the 561 nm laser set to 26 mW. Using a collimating lens with a focal length of CL = 30 mm and 60 mm (for their position, see **Figure 2.2**), we achieved a full width at 90% of the maximum intensity (FW90M) for these two lenses in the Gaussian illumination mode of 27 µm and 28 µm and for

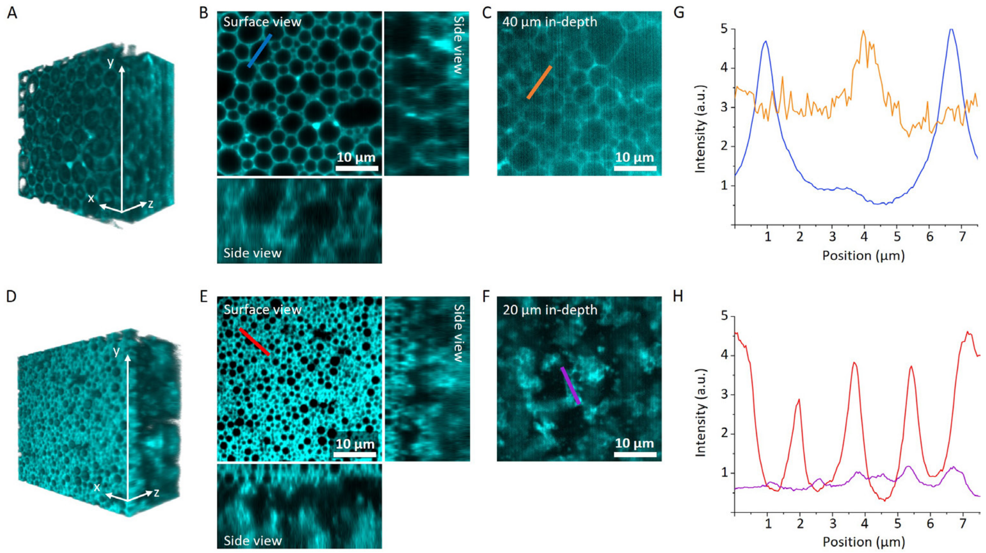

Figure 2.1. Rescan-confocal images of mayonnaise and the model emulsion labelled with Nile blue. (A) Three-dimensional volume rendering image of 40 µm by 40 µm by 20 µm taken with a 1 µm step size along the optical z-axis. (B, C) Cross sectional views in different planes of xy-xz-yz shows in a slice of 20 µm thickness (B) and in the xy plane located in 40 µm depth in the sample (C). (D) Three-dimensional volume rendering of 40 µm by 40 µm by 20 µm stabilized by guar gum, taken with 1 µm step size. (E, F) Cross-sectional views in different planes of xy-xz-yz starting at the surface close to the coverslip (E) and in the xy plane located in 20 µm depth in the sample (F). Void areas in the model emulsion are caused by the guar gum network. (G) Line plots of fluorescence intensity (blue line in B) representing the achievable signal to noise of droplets close to the glass interface and (orange line in C) in 40 µm depth. (H) Line plots of fluorescence intensity (red line in E) representing the achievable signal to noise of droplets close to the glass interface and (purple line in F) in 20 µm depth.

flat illumination of 116 µm and 128 µm, respectively (**Figure 2.2D**). The flat field leads to laser intensity of 0.19 kW cm^{-2}. For the main cube, we opted for a sample scanning stage that offers nanometer resolution over a 21 mm scanning range in all three directions and working in closed loop mode to compensate the thermal drift of the stage (**Supplementary Figure 2.1**). In the detection path, we implemented a deformable mirror to correct the aberrations induced by either the sample or by other optical elements in the detection pathway and enable PSF engineering that allow us to have higher z range in three dimensions. We noted, however, that the deformable mirror itself introduces additional aberrations to the system requiring corrections. Using the standard setting of all actuators set to 100 V, we observed asymmetrically elongated PSFs (**Figure 2.2E**) rather than the expected symmetrical and circular PSFs when imaging fluorescent latex beads of 28 nm diameter. To correct the flatness of the mirror and later for modulating the PSFs, we implemented REALM[32]. Using REALM, each Zernike aberration mode was individually corrected by sequentially optimizing the image metric (**Figure 2.2F**). The software evaluated 11 biases ranging from −100 nm to 100 nm for the mirror setting for each of the nine tested Zernike modes. By using three correction rounds, a total of 297 images were acquired. A Gaussian function was fitted to the metric values of each bias. The position of the maximum of the fitted function was taken as the required correction amplitude for that specific mode. After correcting the mirror, the expected circular symmetry of the PSF is restored (**Figure 2.2G**) and we found the correction settings to be stable for several months.

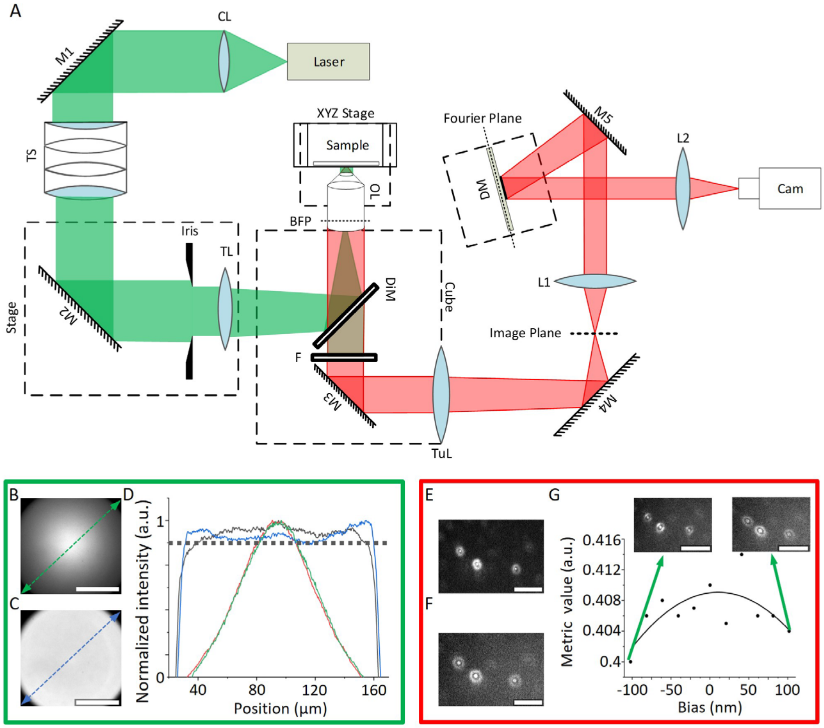

Figure 2.2. (A) Schematic of the optical pathway. The excitation path (left, green) and the detection path (right, red) are highlighted. Components include a collimating lens(CL), mirrors(M), top-hat beam shaper(TS), TIRF lens(TL), polychroicmirror (DiM), objective lens (OL), back focal plane (BFP), bandpass filter (F), tube lens (TuL), lenses (L), deformable mirror (DM), and a camera (Cam). (B–D) Characterization of the intensity profile in the field of view. Two collimating lenses (CL) were compared with either 30 mm or 60 mm focal length and with or without top-hat beam shaper. (B) Intensity profile after using the 30 mm lens. (C) Intensity profile after using the 60 mm lens with added top-hat beam shaper. Scale bars in (B, C) represent 50 µm. (D) The line profiles of B (green line) and C (blue line) are plotted and compared to using the 30 mm collimation lens with (black line) and without the top-hat beam shaper (red line). (E, F) Corrections of aberrations using adaptive optics in the emission path. (E) Fluorescent beads (28 nm diameter) were immobilized on a cover slip and imaged. Here, the asymmetrical shape of the PSF is induced by the deformable mirror itself. (F) A specific Zernike mode, oblique secondary astigmatism, Z_{-2}^{4}, was selected and the correction procedure was performed providing a Gaussian fit of the obtained metric values and biases. (G) The expected symmetrical shape of the PSF is restored after correcting the deformable mirror for all Zernike modes using REALM. We note that the beads are slightly out of focus to exemplify the symmetry. Scale bars in (E–G) represent 10 µm.

2.3.3 Super-resolution microscopy in turbid media

Phosvitin is an egg yolk protein that has a binding capacity for ferric ions[36] which can catalyze lipid oxidation at oil-water interface in food emulsions. Here, we aimed at visualizing phosvitin at the oil-water interfaces of a model emulsion to explore the potential spatial heterogeneity of phosvitin that could provide clues to design strategies combating lipid oxidation. In our 15% oil-in-water model emulsion, phosvitin took the role as the main emulsifier. We further added SDS to increase the stability of the emulsion (**Figure 2.3A**). To localize phosvitin at the oil-water interface, we added fluorescently labelled antibodies against phosvitin.

To demonstrate the effect of adaptive optics, we first recorded data in 8 μm depth without aberration correction in addition to the flat-mirror correction with REALM (**Figure 2.3B, D**) for 5 min. Then, the sample was imaged with the depth correction setting applied. The outlines of the oil droplets representing labelled antibodies bound to phosvitin are clearly visible. We performed control experiments with phalloidin antibodies conjugated with Alexa Fluor 647 to verify the specificity of the phosvitin antibodies. As expected, a noisy background was observed without clear outlines of droplets being visible (**Supplementary Figure 2.2**). Before any further analysis of the raw data, we minimized the influence of background fluorescence by applying a temporal median filter (see Material and methods). To compare the datasets with and without aberration correction, we first summed up the intensities of all 10,000 frames pixel by pixel to mimic diffraction-limited resolution (**Figure 2.3B, C**). With correction, more droplets are visible showing a clear circular shape with better signal-to-noise ratio. We then analyzed the individual point spread functions frame by frame to demonstrate the increase in resolution obtainable in SMLM (**Figure 2.3E, G**). As indicated in the histograms, more localizations per movie frame can be obtained after correction with AO due to a better signal-to-noise ratio (**Figure 2.3F, G**).

For a more quantitative analysis, we then imaged a new sample in a plane close to the surface (a few 100 nm deep) and plotted a line profile over an isolated droplet (**Figure 2.4A**) indicating a radii of approximately 0.65 μm. Further, analyzing the profile of the droplet using a Gaussian fit and calculating the FWHM of the intensity profile around the droplets revealed a thickness of 74 nm (**Supplementary Figure 2.3**) thereby representing a convolution of the localization precision and the expected geometrical averaging due to projecting a three dimensional cut-out of a sphere onto a two-dimensional imaging plane. We obtained an imaging resolution of 71 nm using FRC[42,44,46] (**Supplementary Figure 2.4**). In total, we found 284 droplets with radii between 0.2 μm and 1.2 μm with a number averaged mean radius of 0.46 μm (**Figure 2.4C** and **Supplementary Figure 2.5**). We note that these are apparent radii due to the

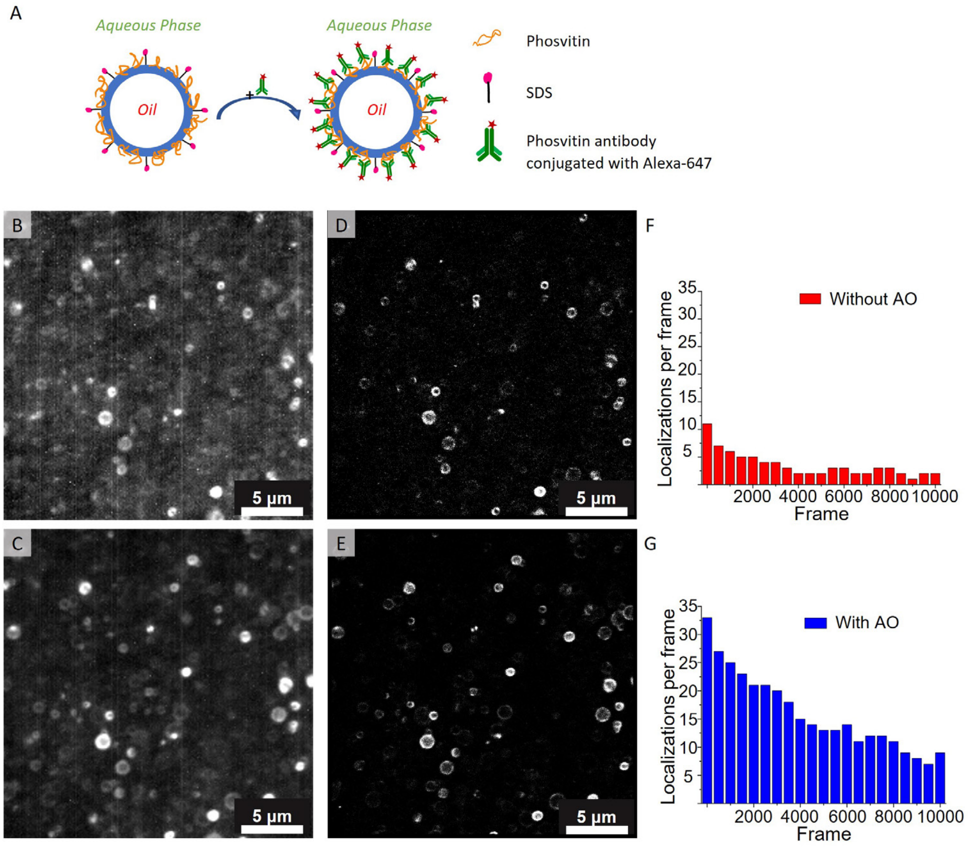

Figure 2.3. From diffraction limited to super-resolved imaging of fluorescently labelled antibodies bound to phosvitin present at the oil–water interface of a model food emulsion. (A) Schematic diagram of an oil-in-water emulsion droplet in the model emulsion. Phosvitin and SDS jointly stabilize the oil–water interface. We then added antibodies against phosvitin that are fluorescently labelled (Alexa Fluor 647) to localize phosvitin at the interface using dSTORM. (B–E) Comparing diffraction limited and super-resolved images with and without adaptive optics. (B, C) The accumulated fluorescence intensity over 10,000 frames each in the same field of view in 8 µm sample depth first measured without (B) and then with AO enabled (C). (D, E) The corresponding super-resolved images of the same stack in 8 µm sample depth without (D) and with AO enabled (E). (F, G) The number of localizations in the field of view per 500 frames without (F) and with AO (G).

error introduced by the imaging plane not crossing all droplets at the center[47]. We then recorded data in 4 µm depth (**Figure 2.4D**) after applying the aberration corrections obtained with REALM. At this depth, the PSFs of individual fluorophore emitters are slightly aberrated such that they could be directly used to obtain the correction coefficients. We again enlarged a droplet and obtained a radius of 0.75 µm. In this plane, we obtained 79 nm for the FWHM of the intensity profile around the droplet (**Supplementary Figure 2.3**). We counted 134 droplets with a different radius between 0.2 µm and 1.8 µm and a number averaged mean of 0.55 µm (**Figure 2.4F** and **Supplementary Figure 2.5**). At 15 µm sample depth we had to first correct the PSFs using embedded fluorescent latex beads. We further had to increase the laser excitation power twofold to obtain a sufficient number of photons per localization (**Figure 2.4G**). As we measured deeper into the sample, we noticed a decrease in the number of droplets present likely induced by the guar gum used to reduce the mobility of droplets in the sample. We achieved super resolved images in 15 µm depth indicated by resolving two droplets with approximately 0.45 µm radius. Using FRC, we calculated the resolution of the image to be approximately 124 nm (**Figure 2.4H**). As expected, the number of droplets per field of view reduced to 27 with an averaged mean radius of 0.43 µm and mostly those droplets distributed between 0.35 µm and 0.48 µm. We note that the operational range offered by SMLM is not accessible by conventional laser scanning microscopy, which typically has a lower limit of 0.5 µm for determining the radii of droplets[48].

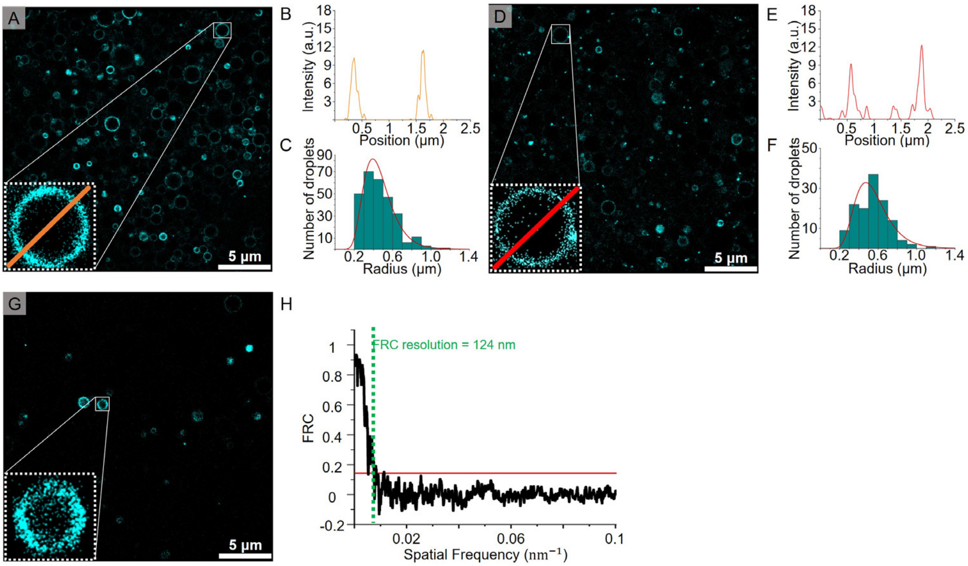

Figure 2.4. Super-resolved imaging in various depths of a turbid model food emulsion. (A, D, G) 25 µm by 25 µm field of view of the super-resolved droplets (A) close (less than 1 µm) to the surface, (D) 4 µm in-depth and, (G) 15 µm in-depth. Line profile of an enlarged droplet from the sample with a radius of (B) approximately 0.65 µm and (E) approximately 0.75 µm. Apparent size distributions presented as histograms for a 15% model emulsion stabilized with phosvitin for the plane close to the surface (C) and, the plane 4 µm in-depth (F). (H) The FRC calculation to determine the resolution of super resolved image in 15 µm depth.

2.3.4 Obtaining 3D image of oil droplets using PSF engineering

To show the capability of three-dimensional imaging using adaptive optics, we recorded engineered PSFs using the deformable mirror. Various PSFs such as astigmatism, saddle point and tetrapod can be engineered using the deformable mirror. To access a 2–2.5 µm z-range, we employed vertical astigmatism and vertical secondary astigmatism Zernike coefficients (Saddle point PSF). We recorded 40,000 frames with 30 ms frame time (**Figure 2.5**). We visualized the cross-sectional view of three-dimensional distribution in xz- and yz-planes, showing that the full volume of a droplet can be covered and further indicating that phosvitin is homogeneously distributed at oil droplet interfaces. Vertical and horizontal dashed lines in **Figure 2.5** indicate the corresponding xz and yz sections. We note that further analysis of the homogeneity will critically depend on the surface coverage of the droplets with phosvitin and the matching, fluorescently labelled antibody.

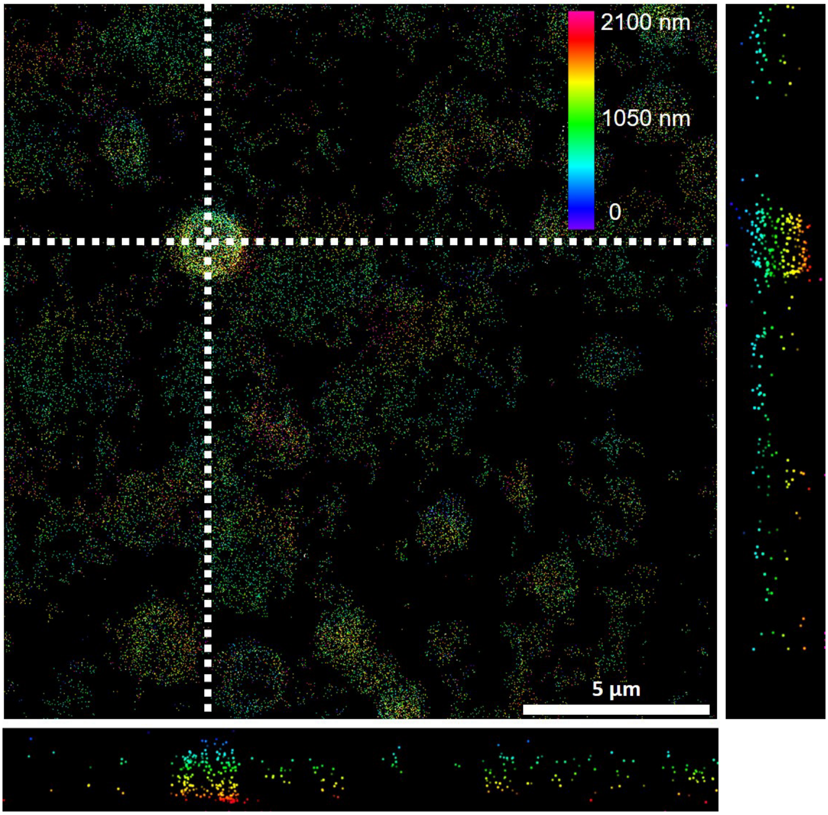

Figure 2.5. 20 µm × 20 µm image of the oil-in-water model emulsion droplets in 4 µm depth with the saddle point PSF setting providing a 2.1 µm z-range. The cross-sectional views show the distribution of protein in the xz- and xy-plane. Saddle point PSFs were introduced by applying vertical astigmatism and vertical secondary astigmatism Zernike modes to the deformable mirror.

2.4 Conclusions

In this study, we presented an updated design of the miCube open-source microscope featuring flat-field illumination and adaptive optics for PSF engineering. Together, these updates enable 3D-SMLM in both standard samples and samples compromised by inherent turbidity. As a first model system we used a dilute oil-in-water emulsion in which we imaged the iron-binding protein phosvitin at the droplet interface using a primary phosvitin antibody conjugated with Alexa Fluor 647. Flat-field illumination enables homogeneous excitation intensities over areas surpassing 30 µm by 30 µm indicating that phosvitin is homogeneously distributed over the droplet interfaces. Droplets with radii as small as 0.2 µm can be discerned and localization of phosvitin in extended sample depths is possible. Using the deformable mirror to engineer PSFs, we demonstrated that extended z-ranges can be accessed with SMLM without moving the focus of the objective in the sample plane. Our work showed the ability of the open miCube platform to perform SMLM techniques for localizing biomacromolecules in both two and three dimensions at colloidal interfaces in complex and oxidation-sensitive food emulsions.

References

1 Schwertner, M.; Booth, M. J.; Wilson, T. Characterizing Specimen Induced Aberrations for High NA Adaptive Optical Microscopy. *Opt. Express, OE* **2004**, *12* (26), 6540–6552. https://doi.org/10.1364/OPEX.12.006540.

2 Vellekoop, I. M.; Aegerter, C. M. Scattered Light Fluorescence Microscopy: Imaging through Turbid Layers. *Opt. Lett., OL* **2010**, *35* (8), 1245–1247. https://doi.org/10.1364/OL.35.001245.

3 Girkin, J. M.; Poland, S.; Wright, A. J. Adaptive Optics for Deeper Imaging of Biological Samples. *Current Opinion in Biotechnology* **2009**, *20* (1), 106–110. https://doi.org/10.1016/j.copbio.2009.02.009.

4 Hardy, J. W. *Adaptive Optics for Astronomical Telescopes*; Oxford University Press, 1998.

5 Booth, M.; Andrade, D.; Burke, D.; Patton, B.; Zurauskas, M. Aberrations and Adaptive Optics in Super-Resolution Microscopy. *Microscopy (Oxf)* **2015**, *64* (4), 251–261. https://doi.org/10.1093/jmicro/dfv033.

6 Dalgarno, H. I. C.; Čižmár, T.; Vettenburg, T.; Nylk, J.; Gunn-Moore, F. J.; Dholakia, K. Wavefront Corrected Light Sheet Microscopy in Turbid Media. *Appl. Phys. Lett.* **2012**, *100* (19), 191108. https://doi.org/10.1063/1.4710527.

7 Hell, S.; Reiner, G.; Cremer, C.; Stelzer, E. H. K. Aberrations in Confocal Fluorescence Microscopy Induced by Mismatches in Refractive Index. *Journal of Microscopy* **1993**, *169* (3), 391–405. https://doi.org/10.1111/j.1365-2818.1993.tb03315.x.

8 Ji, N.; Sato, T. R.; Betzig, E. Characterization and Adaptive Optical Correction of Aberrations during in Vivo Imaging in the Mouse Cortex. *PNAS* **2012**, *109* (1), 22–27. https://doi.org/10.1073/pnas.1109202108.

9 Dong, C.-Y.; Koenig, K.; So, P. T. C. Characterizing Point Spread Functions of Two-Photon Fluorescence Microscopy in Turbid Medium. *JBO* **2003**, *8* (3), 450–459. https://doi.org/10.1117/1.1578644.

10 Booth, M. J. Adaptive Optical Microscopy: The Ongoing Quest for a Perfect Image. *Light Sci Appl* **2014**, *3* (4), e165–e165. https://doi.org/10.1038/lsa.2014.46.

11 Tao, X.; Fernandez, B.; Azucena, O.; Fu, M.; Garcia, D.; Zuo, Y.; Chen, D. C.; Kubby, J. Adaptive Optics Confocal Microscopy Using Direct Wavefront Sensing. *Opt. Lett., OL* **2011**, *36* (7), 1062–1064. https://doi.org/10.1364/OL.36.001062.

12 Betzig, E.; Patterson, G. H.; Sougrat, R.; Lindwasser, O. W.; Olenych, S.; Bonifacino, J. S.; Davidson, M. W.; Lippincott-Schwartz, J.; Hess, H. F. Imaging Intracellular Fluorescent Proteins at Nanometer Resolution. *Science* **2006**, *313* (5793), 1642–1645. https://doi.org/10.1126/science.1127344.

13 Hess, S. T.; Girirajan, T. P. K.; Mason, M. D. Ultra-High Resolution Imaging by Fluorescence Photoactivation Localization Microscopy. *Biophysical Journal* **2006**, *91* (11), 4258–4272. https://doi.org/10.1529/biophysj.106.091116.

14 Madec, P.-Y. Overview of Deformable Mirror Technologies for Adaptive Optics and Astronomy. In *Adaptive Optics Systems III*; International Society for Optics and Photonics, 2012; Vol. 8447, p 844705. https://doi.org/10.1117/12.924892.

15 Heilemann, M.; van de Linde, S.; Schüttpelz, M.; Kasper, R.; Seefeldt, B.; Mukherjee, A.; Tinnefeld, P.; Sauer, M. Subdiffraction-Resolution Fluorescence Imaging with Conventional Fluorescent Probes. *Angew. Chem. Int. Ed.* **2008**, *47* (33), 6172–6176. https://doi.org/10.1002/anie.200802376.

16 Rust, M. J.; Bates, M.; Zhuang, X. Stochastic Optical Reconstruction Microscopy (STORM) Provides Sub-Diffraction-Limit Image Resolution. *Nat Methods* **2006**, *3* (10), 793–795. https://doi.org/10.1038/nmeth929.

17 Huang, B.; Wang, W.; Bates, M.; Zhuang, X. Three-Dimensional Super-Resolution Imaging by Stochastic Optical Reconstruction Microscopy. *Science* **2008**, *319* (5864), 810–813. https://doi.org/10.1126/science.1153529.

18 Holtzer, L.; Meckel, T.; Schmidt, T. Nanometric Three-Dimensional Tracking of Individual Quantum Dots in Cells. *Appl. Phys. Lett.* **2007**, *90* (5), 053902. https://doi.org/10.1063/1.2437066.

19 Aristov, A.; Lelandais, B.; Rensen, E.; Zimmer, C. ZOLA-3D Allows Flexible 3D Localization Microscopy over an Adjustable Axial Range. *Nature Communications* **2018**, *9* (1), 2409. https://doi.org/10.1038/s41467-018-04709-4.

20 Pavani, S. R. P.; Thompson, M. A.; Biteen, J. S.; Lord, S. J.; Liu, N.; Twieg, R. J.; Piestun, R.; Moerner, W. E. Three-Dimensional, Single-Molecule Fluorescence Imaging beyond the Diffraction Limit by Using a Double-Helix Point Spread Function. *PNAS* **2009**, *106* (9), 2995–2999. https://doi.org/10.1073/pnas.0900245106.

21 Martens, K. J. A.; Jabermoradi, A.; Yang, S.; Hohlbein, J. Integrating Engineered Point Spread Functions into the Phasor-Based Single-Molecule Localization Microscopy Framework. *Methods* **2020**. https://doi.org/10.1016/j.ymeth.2020.07.010.

22 Hohlbein, J. Single-Molecule Localization Microscopy as an Emerging Tool to Probe Multiscale Food Structures. *Food Structure* **2021**, *30*, 100236. https://doi.org/10.1016/j.foostr.2021.100236.

23 Martens, K. J. A.; van Beljouw, S. P. B.; van der Els, S.; Vink, J. N. A.; Baas, S.; Vogelaar, G. A.; Brouns, S. J. J.; van Baarlen, P.; Kleerebezem, M.; Hohlbein, J. Visualisation of DCas9 Target Search in Vivo Using an

Open-Microscopy Framework. *Nature Communications* **2019**, *10* (1), 3552. https://doi.org/10.1038/s41467-019-11514-0.

24 Douglass, K. M.; Sieben, C.; Archetti, A.; Lambert, A.; Manley, S. Super-Resolution Imaging of Multiple Cells by Optimized Flat-Field Epi-Illumination. *Nature Photonics* **2016**, *10* (11), 705–708. https://doi.org/10.1038/nphoton.2016.200.

25 Scholtens, T. M.; Schreuder, F.; Ligthart, S. T.; Swennenhuis, J. F.; Tibbe, A. G. J.; Greve, J.; Terstappen, L. W. M. M. CellTracks TDI: An Image Cytometer for Cell Characterization. *Cytometry Part A* **2011**, *79A* (3), 203–213. https://doi.org/10.1002/cyto.a.21024.

26 Deschamps, J.; Rowald, A.; Ries, J. Efficient Homogeneous Illumination and Optical Sectioning for Quantitative Single-Molecule Localization Microscopy. *Optics Express* **2016**, *24* (24), 28080–28090. https://doi.org/10.1364/OE.24.028080.

27 Kwakwa, K.; Savell, A.; Davies, T.; Munro, I.; Parrinello, S.; Purbhoo, M. A.; Dunsby, C.; Neil, M. A. A.; French, P. M. W. EasySTORM: A Robust, Lower-Cost Approach to Localisation and TIRF Microscopy. *Journal of Biophotonics* **2016**, *9* (9), 948–957. https://doi.org/10.1002/jbio.201500324.

28 Ma, H.; Fu, R.; Xu, J.; Liu, Y. A Simple and Cost-Effective Setup for Super-Resolution Localization Microscopy. *Scientific Reports* **2017**, *7* (1), 1542. https://doi.org/10.1038/s41598-017-01606-6.

29 Mau, A.; Friedl, K.; Leterrier, C.; Bourg, N.; Lévêque-Fort, S. Fast Scanned Widefield Scheme Provides Tunable and Uniform Illumination for Optimized SMLM on Large Fields of View. *bioRxiv* **2020**, 2020.05.08.083774. https://doi.org/10.1101/2020.05.08.083774.

30 Khaw, I.; Croop, B.; Tang, J.; Möhl, A.; Fuchs, U.; Han, K. Y. Flat-Field Illumination for Quantitative Fluorescence Imaging. *Optics Express* **2018**, *26* (12), 15276–15288. https://doi.org/10.1364/OE.26.015276.

31 Stehr, F.; Stein, J.; Schueder, F.; Schwille, P.; Jungmann, R. Flat-Top TIRF Illumination Boosts DNA-PAINT Imaging and Quantification. *Nature Communications* **2019**, *10* (1), 1268. https://doi.org/10.1038/s41467-019-09064-6.

32 Siemons, M. E.; Hanemaaijer, N. A. K.; Kole, M. H. P.; Kapitein, L. C. Robust Adaptive Optics for Localization Microscopy Deep in Complex Tissue. *Nature Communications* **2021**, *12* (1), 3407. https://doi.org/10.1038/s41467-021-23647-2.

33 Yang, S.; Verhoeff, A. A.; Merkx, D. W. H.; van Duynhoven, J. P. M.; Hohlbein, J. Quantitative Spatiotemporal Mapping of Lipid and Protein Oxidation in Mayonnaise. *Antioxidants* **2020**, *9* (12), 1278. https://doi.org/10.3390/antiox9121278.

34 Depree, J. A.; Savage, G. P. Physical and Flavour Stability of Mayonnaise. *Trends in Food Science & Technology* **2001**, *12* (5), 157–163. https://doi.org/10.1016/S0924-2244(01)00079-6.

35 Castellani, O.; Belhomme, C.; David-Briand, E.; Guérin-Dubiard, C.; Anton, M. Oil-in-Water Emulsion Properties and Interfacial Characteristics of Hen Egg Yolk Phosvitin. *Food Hydrocolloids* **2006**, *20* (1), 35–43. https://doi.org/10.1016/j.foodhyd.2005.02.010.

36 Zhang, X.; Qiu, N.; Geng, F.; Ma, M. Simply and Effectively Preparing High-Purity Phosvitin Using Polyethylene Glycol and Anion-Exchange Chromatography. *Journal of Separation Science* **2011**, *34* (22), 3295–3301. https://doi.org/10.1002/jssc.201100601.

37 Berton-Carabin, C. C.; Ropers, M.-H.; Genot, C. Lipid Oxidation in Oil-in-Water Emulsions: Involvement of the Interfacial Layer. *Comprehensive Reviews in Food Science and Food Safety* **2014**, *13* (5), 945–977. https://doi.org/10.1111/1541-4337.12097.

38 Luca, G. M. R. D.; Breedijk, R. M. P.; Brandt, R. A. J.; Zeelenberg, C. H. C.; Jong, B. E. de; Timmermans, W.; Azar, L. N.; Hoebe, R. A.; Stallinga, S.; Manders, E. M. M. Re-Scan Confocal Microscopy: Scanning Twice for Better Resolution. *Biomed. Opt. Express, BOE* **2013**, *4* (11), 2644–2656. https://doi.org/10.1364/BOE.4.002644.

39 Ovesný, M.; Křížek, P.; Borkovec, J.; Švindrych, Z.; Hagen, G. M. ThunderSTORM: A Comprehensive ImageJ Plug-in for PALM and STORM Data Analysis and Super-Resolution Imaging. *Bioinformatics* **2014**, *30* (16), 2389–2390. https://doi.org/10.1093/bioinformatics/btu202.

40 Schindelin, J.; Arganda-Carreras, I.; Frise, E.; Kaynig, V.; Longair, M.; Pietzsch, T.; Preibisch, S.; Rueden, C.; Saalfeld, S.; Schmid, B.; Tinevez, J.-Y.; White, D. J.; Hartenstein, V.; Eliceiri, K.; Tomancak, P.; Cardona, A. Fiji: An Open-Source Platform for Biological-Image Analysis. *Nature Methods* **2012**, *9* (7), 676–682. https://doi.org/10.1038/nmeth.2019.

41 Martens, K. J. A.; Bader, A. N.; Baas, S.; Rieger, B.; Hohlbein, J. Phasor Based Single-Molecule Localization Microscopy in 3D (PSMLM-3D): An Algorithm for MHz Localization Rates Using Standard CPUs. *The Journal of Chemical Physics* **2018**, *148* (12), 123311. https://doi.org/10.1063/1.5005899.

42 Nieuwenhuizen, R. P. J.; Lidke, K. A.; Bates, M.; Puig, D. L.; Grünwald, D.; Stallinga, S.; Rieger, B. Measuring Image Resolution in Optical Nanoscopy. *Nature Methods* **2013**, *10* (6), 557–562. https://doi.org/10.1038/nmeth.2448.

43 Yuen, H. K.; Princen, J.; Dlingworth, J.; Kittler, J. A Comparative Study of Hough Transform Methods for Circle Finding. In *Procedings of the Alvey Vision Conference 1989*; Alvey Vision Club: Reading, 1989; p 29.1–29.6. https://doi.org/10.5244/C.3.29.

44 Ries, J. SMAP: A Modular Super-Resolution Microscopy Analysis Platform for SMLM Data. *Nature Methods* **2020**, *17* (9), 870–872. https://doi.org/10.1038/s41592-020-0938-1.

45 Jimenez, A.; Friedl, K.; Leterrier, C. About Samples, Giving Examples: Optimized Single Molecule Localization Microscopy. *Methods* **2020**, *174*, 100–114. https://doi.org/10.1016/j.ymeth.2019.05.008.

46 Banterle, N.; Bui, K. H.; Lemke, E. A.; Beck, M. Fourier Ring Correlation as a Resolution Criterion for Super-Resolution Microscopy. *Journal of Structural Biology* **2013**, *183* (3), 363–367. https://doi.org/10.1016/j.jsb.2013.05.004.

47 Schuster, S.; Bernewitz, R.; Guthausen, G.; Zapp, J.; Greiner, A. M.; Köhler, K.; Schuchmann, H. P. Analysis of W1/O/W2 Double Emulsions with CLSM: Statistical Image Processing for Droplet Size Distribution. *Chemical Engineering Science* **2012**, *81*, 84–90. https://doi.org/10.1016/j.ces.2012.06.059.

48 Duynhoven, J. P. M. van; Goudappel, G. J. W.; Dalen, G. van; Bruggen, P. C. van; Blonk, J. C. G.; Eijkelenboom, A. P. a. M. Scope of Droplet Size Measurements in Food Emulsions by Pulsed Field Gradient NMR at Low Field. *Magnetic Resonance in Chemistry* **2002**, *40* (13), S51–S59. https://doi.org/10.1002/mrc.1115.

2.5 Supplementary materials

Supplementary Figure 2.1. To measure the drift characteristics, we recorded 10,000 frames of 50 ms each using 50 nm diameter beads sample excited at 561 nm laser wavelength. We engineered the PSF to represent a saddle-point PSF by changing the Zernike modes Z_{-2}^{2} and Z_{2}^{4} by applying a proper voltage from the flat mirror and recorded 3D raw data for determining the drift in the x, y, and z direction. We analyzed the data using the SMALL LABS combined with phasor analysis. We performed 3D drift-correction using the cross-correlation function in SMALL LABS. Our data show that we have less than 200 nm drift in the lateral plane during the 500 s long measurement (SFig 2.1).

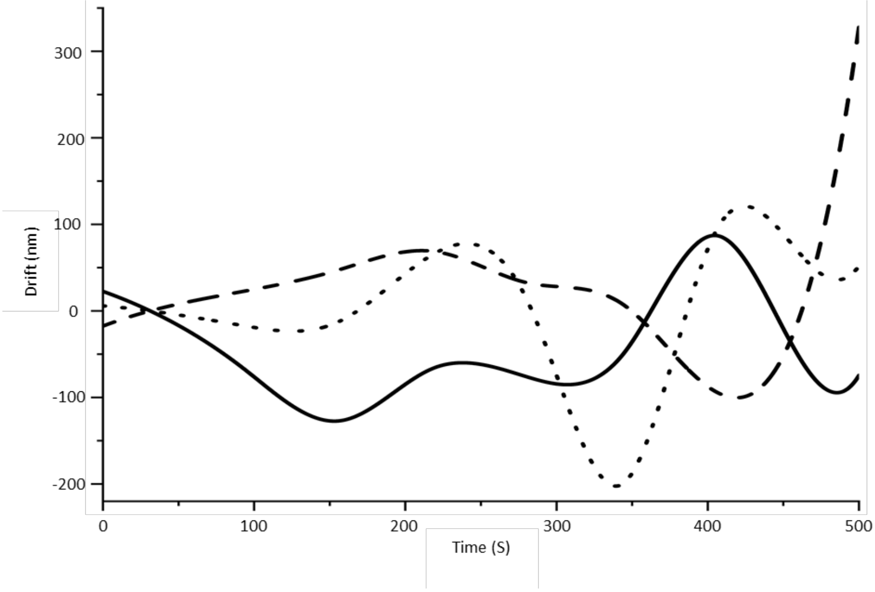

SFig 2.1. 500 seconds movie recording using 50 ms frame time and a 50 nm diameter bead sample. To measure the drift in three dimensions, we used a saddle point PSF enabled by the deformable mirror. The figure shows the tracked position of the bead in X (straight line), Y (dotted line), and Z (dashed line) direction.

Supplementary Figure 2.2. We used phalloidin antibody conjugated with Alexa-647 for a control experiment to see whether these antibodies attach to phosvitins at droplets or not. Raw data were obtained by recording 10,000 frames with a 10 ms frame time. After analyzing the raw data and finding the localizations we achieved a noisy super-resolved image (SFig 2.2A). A single frame from raw data is extracted to demonstrate, the blinking presents not only on the droplets but all over the field of view (SFig 2.2B).

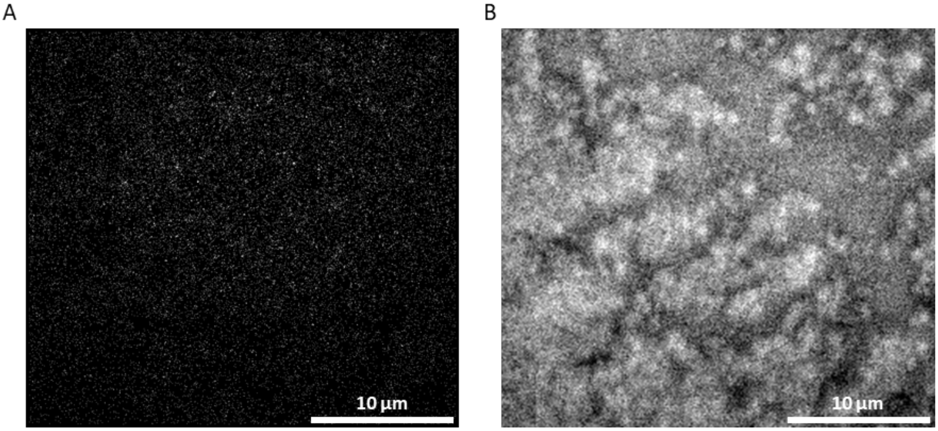

Figure S2.2. The control experiment using phalloidin antibody conjugated with Alexa-647. A Super resolved image after processing the raw data from model emulsion with phalloidin antibody. B A single frame from raw data to show the interaction of control antibody with droplets covered by phosvitins.

Supplementary Figure 2.3. To measure the thickness of droplets, a gaussian fitted to the line profiles of droplets at a different depth. For the plane close to the surface we measured full width at half maximum of 71 nm with considering the average of both sides of the droplet (SFig 2.3A). with the same procedure we fitted also for the plane 4 µm (SFig 2.3B).

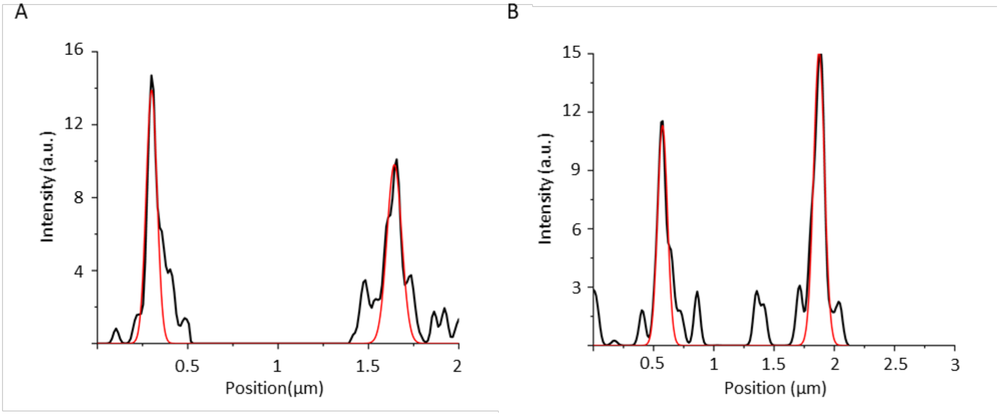

Figure S2.3. A Gaussian function was fitted to the droplets to calculate the thickness of droplets in different depths, A Close to the surface and, B 4 µm in depth.

Supplementary Figure 2.4. To determine the resolution of super-resolved images from our model emulsion, we used the Fourier ring correlation method. The localization list was used in the SMAP software to compute the resolution from FRC. FRC curve shows the decay of the correlation with spatial frequency and when it goes below the threshold, the resolution will be calculated by taking the spatial frequency inverse at that point. For the droplets close to the surface we achieved 71 nm resolution (SFig 2.4A) and for the plane 15 µm in depth 124 nm was achieved (SFig 2.4B).

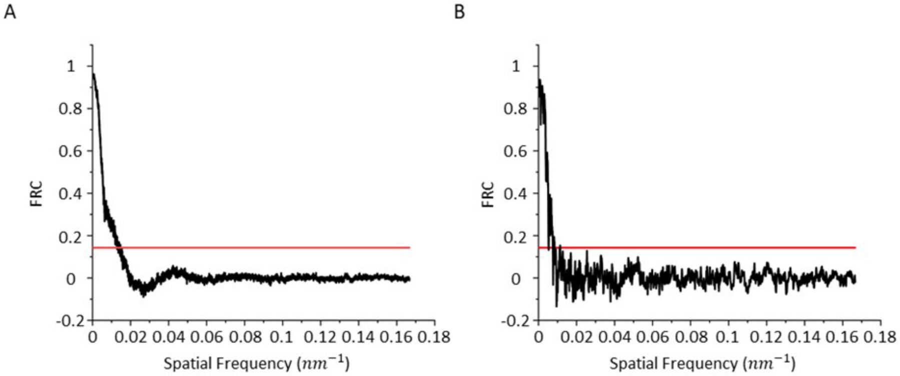

Figure S2.4. The data shows the FRC versus spatial frequency in which we can calculate the resolution of the images (A) close to the surface and, (B) 4 µm in depth.

Supplementary Figure 2.5. Droplet distribution sizes were quantified using visual inspection and Hough circle transform. First, the droplets visually inspected based on the presence and absence of fluorescents. Consecutively, we used Hough circle transform for circles in the range between 0.2 µm to 2.0 µm in which the circles with radius lower than 0.2 µm and higher than 2.0 µm removed from quantification analysis. We used this approach for the image plane close to the surface (SFig 2.5A) and 4 µm in-depth (SFig 2.5B).

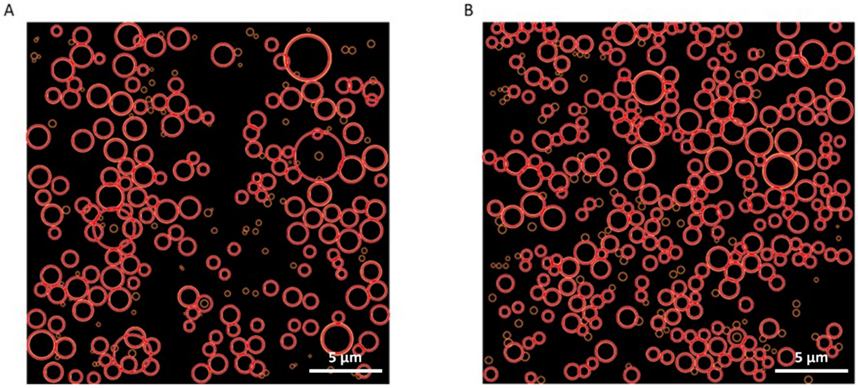

Figure S2.5. Analyzed field of view for droplet distribution. Orange circles show the visually inspected droplets and, red circles show detected droplets by Hough circle transformation for (A) close to the surface and, (B) 4 µm in-depth.

3

Quantifying the distribution of proteins at the interface of oil-in-water food emulsions

Manuscript in preparation for submission:

Abbas Jabermoradi, John P.M. van Duynhoven, Johannes Hohlbein.

Abstract

Emulsifiers play an essential role in ensuring the physiochemical stability of food emulsions. In the case of mayonnaise, proteins contained in egg yolk act as emulsifiers. Here, we employed stochastic optical reconstruction microscopy (STORM) to localize proteins at the oil/water droplet interface using fluorescently labeled protein antibodies. To quantitatively analyze the distribution of proteins at the droplet interface, we first simulated droplets with homogeneously and heterogeneously distributed proteins. We implemented the relative position distribution (RPD) analysis to extract the histogram of relative distances between all neighboring localizations. By analyzing the local maxima of the histogram, we could classify distributions at droplet interfaces as homogeneous, partially heterogeneous, and heterogeneous. The model fitting over the RPD histogram using a 2D probability function further provided a localization precision amplitude consistent with the analysis of the local maxima. As a model system for mayonnaise, we used emulsions prepared with combinations of phosvitin, phospholipids, apolipoprotein B (apoB), and sodium dodecyl sulfate (SDS) as emulsifiers. The binary phosvitin/SDS model emulsion showed a partially heterogeneous distribution of phosvitin around the droplets. The ternary phosvitin/phospholipid/SDS and apoB/phospholipid/SDS emulsions showed increased heterogeneity of phosvitin and apoB at the droplet interfaces. Quantification of heterogeneity at droplet interfaces may provide insights in factors determining the physical and chemical stability of emulsions.

3.1 Introduction

In food emulsions, the underlying immiscibility of vegetable oil and water causes thermodynamic instability and a tendency to phase-separate. Mechanisms such as coalescence, flocculation, creaming, and Ostwald ripening reduce the free energy of the system, thereby effectively leading to an increase in the size of droplets before complete phase separation occurs[1]. To keep emulsions stable, the use of emulsifiers that lower the interfacial tension is essential. These emulsifiers adsorb at the oil/water interface during homogenization and can form an effective barrier against the degradation of the emulsion. Depending on the physicochemical properties of the aqueous phase, emulsifiers bearing a charge, for example, exert electrostatic interactions that prevent droplets from aggregation. Interfacial composition and structure have been postulated to play a critical role in the physical[2,3] and chemical stability[4,5] of food emulsions.

Existing methods to assess interfacial structure, such as droplet tensiometry or atomic force microscopy (AFM) cannot be directly applied in the soft matter environment of food emulsions or are not yet adapted for quantitative assessments[6]. This lack of suitable tools hampers the rational design of formulations and processing routes. In this study, we will introduce a fluorescence imaging-based approach to quantitatively assess both composition and spatial distribution of proteins at the droplet interface of mayonnaise model emulsions, in which egg yolk is the main source of emulsifiers. Egg yolk represents a complex system of functional ingredients that can be separated into plasma (78%) and granules (22% of dry yolk matter)[7]. The plasma comprises 85% low-density lipoprotein (LDL) particles and 15% livetin. The granules consist of 70% high-density lipoprotein (HDL) particles, 12% LDL, 16% phosvitin, and 2% ash[8]. Both LDL and HDL particles contain apoproteins and phospholipids, with the latter being primarily present as phosphatidylcholine (PC). Together with apoproteins and the phospholipids, phosvitin adsorbs at the oil/water interface, where it has been associated with pro-oxidant activity[9]. Phosvitin is a highly phosphorylated protein consisting of phosphoserine clusters capable of binding ferric ions. When released, these ferric ions can engage in redox cycling and thus catalyze lipid oxidation, which induces a loss of sensory and nutritional quality[10]. The most abundant apoprotein in egg yolk is apolipoprotein B (apoB)[11]. ApoB shows stronger interfacial adsorption compared to phosvitin due to its flexible structure and higher surface hydrophobicity[12]. It has been demonstrated that both oxidation of lipoprotein particles in the continuous phase[13] and lipid oxidation in the droplet phase[14,15] can induce oxidation of apoB at the interface. Multiscale microscopic imaging techniques have provided insights into localizing the chemical events at play in lipid oxidation in mayonnaise[14]. Yet the interplay between interfacial composition, structure, and physical and chemical stability remains to be established experimentally.

Brightfield microscopy has been widely used to characterize properties such as flocculation, coalescence, and size distributions of droplets in food emulsions[16,17] but does lack target specificity to provide additional insights in interfacial structure. Fluorescence-based confocal laser scanning microscopy (CLSM), on the other hand, provides good background suppression and some target specificity by using, for example, auto-fluorescence of proteins or dyes that report on the surrounding chemical environment, and was recently used to map lipid and protein oxidation in mayonnaise[14] Despite the progress, finding and applying the right protein-specific marker has remained challenging[3] and the spatial resolution achievable with CLSM of around 200 nm limits our ability to visualize interfacial structure[18,19]. Electron microscopy techniques provide better spatial resolution, but resolving the droplet interfacial composition within an emulsion like mayonnaise involves cumbersome and invasive sample preparation steps, and only limited progress has been made[14,20]. Single-molecule localization microscopy (SMLM) allows us to overcome the so-called diffraction limit of fluorescence microscopy such as CLSM. The core idea is switching fluorophores between a fluorescent and non-fluorescent state so that single emitters can be identified and fitted with a 2D Gaussian function to localize the emitter with higher precision and accuracy. One particular implementation of SMLM is stochastic optical reconstruction microscopy (STORM), in which the induced blinking of standard fluorescent probes attached to targets of interest allows achieving sub-25 nm resolution[19,21–23]. We recently applied STORM to localize fluorescently labelled phosvitin at the interface of turbid oil-in-water model emulsions[24].

To evaluate and quantify the homogeneity of localizations of proteins at the interface, we introduce a quantitative analysis framework based on calculating the relative position distribution (RPD), which represents a histogram of distances between all super-resolved localization coordinates within a specific object[25–27]. In a recent application of RPD called pattern extraction from relative positions of localizations (PERPL), the authors analyzed the expected 8-fold symmetry of nuclear pore complexes[27]. We extend RPD and PERPL to assess the level of heterogeneity of randomly adsorbed proteins at interfaces. In particular, we quantify distributions obtained in the presence of phosvitin and additional protein emulsifiers. For this purpose, we prepared binary and ternary model systems of mayonnaise. The binary model system comprised isolated phosvitin and SDS, and the ternary systems were stabilized by phospholipids, SDS and either isolated phosvitin or apoB introduced via LDL. In the ternary phospholipids/SDS/phosvitin emulsion, the phospholipid was added in the form of phosphatidylcholine (PC). In the ternary phospholipid/apoB/SDS emulsions, LDL was used as a vehicle to introduce both apoB and phospholipids, that latter also mainly in the form of PC.

3.2 Materials and methods

3.2.1 Isolation and purification of LDL and phosvitin

Fresh hen eggs were purchased from a domestic market to isolate LDL, as a source of apoB and phospholipids, and phosvitin using protocols adapted from[28,29]. Briefly, egg yolks were rolled on filter paper to remove the chalazas. An equal amount of distilled water was added to the yolk at 4°C. The obtained solution was centrifuged at 12,000 g for 45 min (Avanti j-25, Beckman). To isolate LDL, the plasma fraction was moved to a new centrifuge tube and centrifuged again to obliterate the granules. Then, plasma was mixed with 40% ammonium sulfate for 1 hour to precipitate livetin. Next, the pH was adjusted to 8.7 using a 420 mM NaOH stock solution. The solution was centrifuged at 12,000 g for 45 min. The semisolid yellow supernatant was separated and dialyzed using a 7 kDa pore-size tube. The dialysis continued overnight to remove the ammonium sulfate. The dialyzed solution was then centrifuged at 12,000 g for 45 min. The floated residue was collected and lyophilized using a freeze-dryer from either (Christ, Germany) or (Labconco, United States of America). The granule fraction for isolating phosvitin was collected and homogenized with an equal mass of a 0.17 M NaCl solution and centrifuged again at 12,000 g for 15 min. The granules were dissolved in a 1.74 M NaCl solution (1:10 w/v). Further, the solution was homogenized with 4% w/w of PEG6000 and centrifuged at 12,000 g for 15 min. The supernatant was dialyzed against distilled water for 24 hours at 4°C and subsequently centrifuged at 12,000 g for 15 min. The supernatant was collected and lyophilized using a freeze-dryer.

3.2.2 Preparation of oil-water model emulsions

The binary phosvitin/SDS model emulsion was prepared using 6 mg/mL of lyophilized phosvitin in 0.05 M acetate buffer at pH 3.8. The solution was centrifuged at 4,000 g for 20 min, and the supernatant was transferred to a new aliquot. We then added 0.15% w/v of sodium dodecyl sulfate (SDS) to the solution to obtain a stable model emulsion. The solution was then premixed using an 18 mm diameter head disperser at 18,000 rpm for 2 min (T 18 digital ULTRA-TURRAX, IKA, Germany) to obtain a coarsely homogenized emulsion. Following that procedure, the coarse emulsion was further homogenized at 70 bar using a high-pressure homogenizer (HPH) (Delta Instruments LAB Homogenizer) for 20 min.

For the ternary phosvitin/phospholipid/SDS emulsion, we first prepared the oil phase by dissolving 10 mg/mL of L-α-lecithin powder, which contains >94% phosphatidylcholine (429415, Sigma-Aldrich) in the oil before continuing with the steps outlined for the phosvitin emulsion. For the ternary apoB/phospholipid/SDS emulsion, we dissolved 10 mg/mL of lyophilized LDL into the oil phase using a magnetic stirrer. Here, LDL particles were used as carriers to deliver both apoB and phospholipids to the droplet interface. Subsequently, SDS was added to the aqueous phase of both model systems.

3.2.3 Single-molecule localization microscopy

For acquiring SMLM data, we used the same modalities reported previously[24]. In short, the laser beam entered the excitation path of the microscope via a fiber-coupled laser engine (Omicron, Germany). After the fiber, the laser beam was collimated using a 60 mm achromatic lens (AC254-060-A-ML, Thorlabs) and reflected by a kinematic mirror (BBE1-E02, Thorlabs) into a top hat beam shaper (Asphericon GmbH). Then, the beam was focused by a 150 mm lens (AC508-150-A-ML, Thorlabs) into the back focal plane of a 100x oil immersion objective (NA = 1.45, Nikon) through a polychroic mirror (ZT405/488/561/640rpcv2, Chroma). The emitted signal from a sample is collected with the same objective and passes an emission filter (ZET405/488/561/640m-TRF, Chroma). The signal was further reflected by a kinematic mirror and focused through a tube lens (MXA20696, Nikon) into a focal plane of the first lens (AC508-100-A-ML, Thorlabs) of a 4f system. Then, the emitted light was reflected by another mirror before arriving at a deformable mirror (DMP40/M – P01, Thorlabs) positioned in the Fourier plane of the 4f imaging system. The light was then focused via a second lens (AC508-100-A-ML, Thorlabs) on a sCMOS camera (Prime 95B, Photometerics) with an effective pixel size of 112 nm.

3.2.4 Sample preparations and image acquisition

To localize phosvitin, a primary phosvitin antibody conjugated with Alexa Fluor 647 (sc-46681, Santa Cruz Biotechnology) stock solution was diluted 50 times in PBS buffer. 10% v/v of the diluted solution was added to 400 µL of the phosvitin containing model emulsion. For staining apoB in the ternary apoB/phospholipid/SDS model emulsion, we first diluted 22.6 µL of the primary human apoB mouse antibody from the 8.85 mg/mL of stock solution (MBS530791, MyBioSource) in PBS buffer in a 1 mL final volume to obtain 200 µg/mL concentration. Then, a secondary anti-mouse antibody conjugated to Alexa 555 (ab150118, Abcam) was diluted 10 times from the 2 mg/mL stock solution into the same solution and incubated at ambient temperature for an hour. Further, the mixture of the antibodies was diluted 50 times in PBS buffer (4 µg/mL), and 40 µL of the diluted solution was added to 360 µL of the LDL-based emulsion.

The labeled emulsions were centrifuged at 4,000 g for 5 min to obtain the cream phase. In this phase, droplets are prevented from diffusing in the water phase during image acquisition. 2 µL of the cream phase was attentively pipetted into a silicone gasket's well (Grace Bio-Labs). Further, to increase the number of fluorophores blinking events, 25 µL of STORM buffer containing 50 mM TRIS pH 8, 10 mM NaCl, 10% glucose, 140 mM 2-mercaptoethanol, 68 µg/mL catalase, and 200 µg/mL glucose oxidase was added[30]. A second cover glass was put on the well to prevent new oxygen from getting into the sample. We recorded 10,000 frames with a 30 ms frame time for all samples. The samples containing phosvitin and apoB were excited using 640 nm (15 mW) and 561 nm (٢٠ mW) laser wavelengths, respectively.

3.2.5 Simulation of protein interfacial distributions

A simple Monte Carlo simulation was written in Python to analyze the protein distribution at the oil/water interface. First, virtual fluorescently tagged proteins were randomly placed on rings representing 2D cross-sections of oil/water droplet interfaces. In the next step, each fluorophore was allowed to blink to generate several localizations per protein. To enable a quantitative analysis of the experimental localizations at the interface, we simulated homogeneous and heterogeneous distributions of proteins around $N = 100$ non-overlapping droplets in a 30 µm by 30 µm field of view. The homogeneous distribution was simulated using an even distribution ranging from 0 to 2π, representing the Φ value in polar coordinates. The radius r of each droplet in the simulation was randomly chosen from a normal distribution with a mean of 750 nm and a standard deviation of 200 nm. To determine the number of proteins present at the interface of each droplet, we take into account the droplet's circumference, the size of the protein ($d = 22$ nm diameter), and a quantity we define as the density ρ of proteins adsorbed at the interface. We multiply the droplet's cross-sectional circumference by the protein density ρ divided by the protein size to calculate the number of proteins occupying a specific perimeter. The value of ρ can vary between 0 and 1, with 0 indicating no proteins present and 1 indicating that proteins occupy the entire interface (a circle in our two-dimensional representation). For example, a droplet with a radius of 500 nm diameter and a protein density ρ of 0.5 would have 71 proteins distributed ($71 = 2\pi\ 500[nm]\ \rho /d$). The ground truth position r_{gt} of each protein relative to the droplet's interface is set by the polar coordinate Φ, the radius of the simulated droplet, and an additional sigma error in x and y representing the finite localization accuracy σ_{ac} of 30 nm for each position. Moreover, the position of each fluorophore (localization) was calculated using the positions of each protein and an additional sigma error representing the finite localization precision σ_{lp} of 50 nm unless otherwise specified. To model the number of localizations for each protein, a random number is generated from an exponential distribution with a mean of 5. Together with assuming an average of five localizations per protein, this will lead to a total number of 355 localisations for this simulated droplet.

To simulate a *heterogeneous* protein distribution at the interface, we placed the first protein randomly on the interface as outlined for the homogeneous case. Each additional protein was given an aggregation probability β to any previously placed protein, thereby potentially overwriting its initially calculated position. If aggregation occurred, the new position was randomly chosen either to the left or right side of the protein or the existing chain of proteins to which it aggregates. Consequently, the continuing aggregation will lead to one-dimensional clusters of proteins at the droplet interface. This course of action is repeated over all simulated proteins per droplet (**Supplementary Figure 3.1**). Jupyter notebooks are provided with the manuscript and are available online:

https://github.com/HohlbeinLab/Protein_distribution_analyzer.

3.2.6 Image visualization and data analysis

For analyzing the experimental raw data, we first removed the constant fluorescence background using a temporal median filter based on a rewritten ImageJ plugin (**https://github.com/HohlbeinLab/FTM2**)[24,31]. Then, we obtained the positions of the fluorophores with sub-pixel localization precision using a phasor-based localization algorithm[32] implemented in ThunderSTORM[33] available for ImageJ/Fiji[34]. The 2D cross-correlation drift correction was applied (ThunderSTORM settings: 10 bins and 5x magnification). The localizations were visualized using the average shifted histogram option with the magnification set to 5. For the lookup table, we chose magenta and green for the labeled proteins phosvitin and apoB, respectively.

The droplets in the field of view were segmented using StarDist to extract the position of each droplet[35,36] after training our segmentation model on multiple data sets using QuPath (**Supplementary Note 3.1**)[37]. We quantitatively analyzed the protein distributions using the relative position distribution (RPD) method[25–27]. In RPD, all distances between all localizations attributed to each single droplet were calculated, and the normalized distance distributions were plotted in a histogram.

Further, to quantitatively analyze the protein distribution, we obtained the local maxima present in the averaged RPD distribution. Additionally, we implemented a model fitting using the 2D probability function of distance distribution to the histogram data.

3.3 Results and discussion

3.3.1 Quantitative analysis of fluorophore distributions around droplet interfaces

To establish our framework for quantifying the heterogeneity of localisations at droplet interfaces, we first placed 100 neighboring but non-overlapping droplets of different diameters in a box and simulated a homogeneous distribution of proteins on each droplet (**Figure 3.1A**). We then separated each droplet based on the known ground truth (**Figure 3.1B**) and calculated the relative position distribution for each droplet. The histograms of two selected droplets show a local maximum for small distances representing a convolution of the localization precision σ_{lp}

and the localization accuracy σ_{ac} and a local maximum for large distances defined by the diameter of the droplet, further discussed below (**Figure 3.1C**). Normalizing the distance distributions over all droplets showed a smooth distribution with the local maxima identified earlier in the individual droplets (**Figure 3.1D**). The normalized histogram presents a fingerprint of expected distances.

For the simulations of the heterogeneously covered interfaces, we added a simple aggregation probability to the model that prioritizes aggregation of proteins over a random distribution of individual proteins over the interface. Indeed, the simulated droplets show a more heterogeneous distribution of localisations, with the normalized histogram of relative distances showing suppressed occurrences and lower amplitudes of large-distance correlations (**Figure 3.1E-H**). The higher we set the aggregation probability, the more the large-distance correlations were suppressed, and consequently, the first peak became dominant, thereby deviating from the 'fingerprint' of the homogeneous distribution.

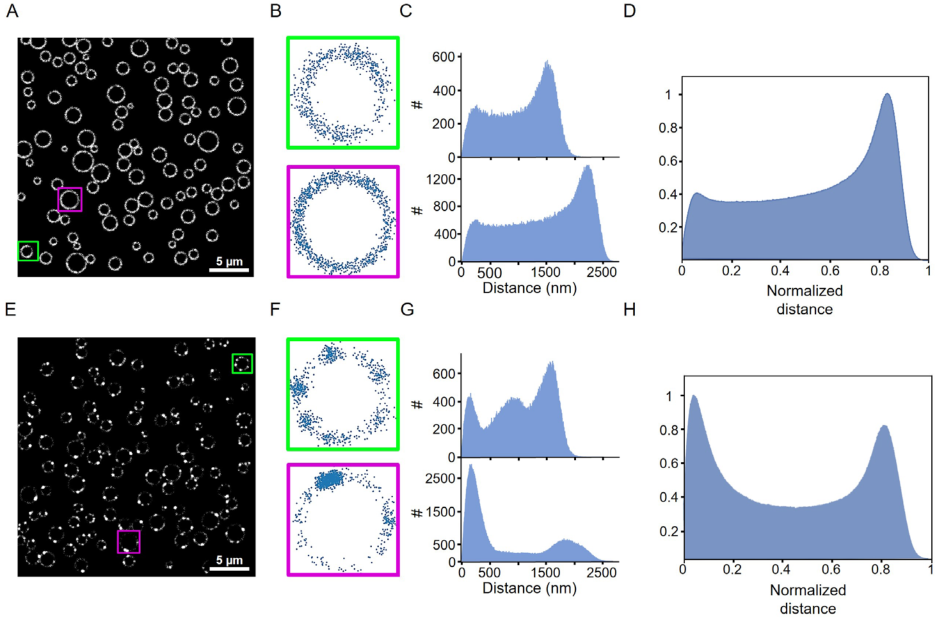

Figure 3.1. Simulation of homogeneous and heterogeneous distributions of fluorescently labeled proteins at droplet interfaces. (A) Homogeneous distribution with 100 droplets placed in a 30 µm by 30 µm field of view. A protein density of ρ = 0.5 and a protein size of d = 22 nm was chosen (B) Zoom-in of two droplets from (A). (C) Histogram showing the relative distance distribution (RPD) of all distances between localisations at the interface of the droplets selected in (B). (D) Averaged distribution over the distances normalized to each respective droplet in the entire field of view. (E-H) as in A-D but after simulating a heterogeneous distribution with a molecular aggregation probability β of 0.65.

To show the variation of the peaks, we simulated data with aggregation probabilities β ranging from 0.1 to 0.99 and plotted the resulting images and RPD histograms (**Figure 3.2**). The first local maximum in each histogram increased its relative amplitude with increasing aggregation. From an aggregation probability β of around 0.65, the amplitude of the first maximum is higher than the amplitude of the second maximum.

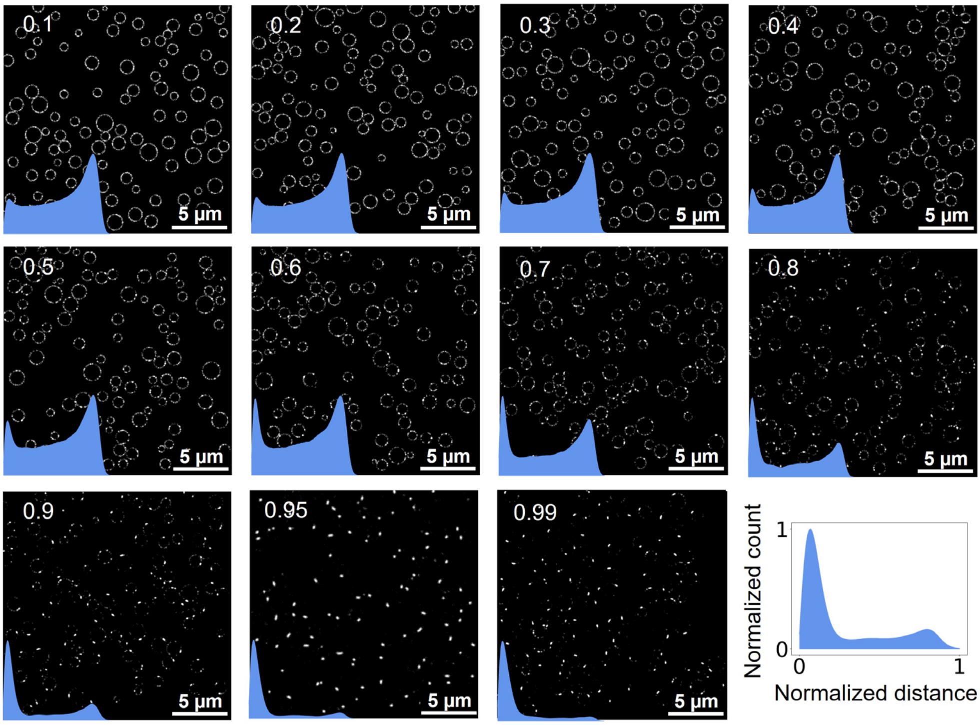

Figure 3.2. Simulations of heterogeneous distributions. We simulated 100 droplets in the field of view with aggregation probabilities β ranging from 0.1 to 0.99. Inserted graphs represent RPD histograms showing the changes in the relative peak amplitudes of the first and the second peak with changing aggregation probabilities.

We employed a composite model fitting approach to analyze the simulated data, allowing us to validate the matching between the input parameters used in the simulation and the values obtained through the fitting process (**Supplementary Figure 3.2**)[27]. The composite model is built from several distinct components, each of which contributes to the overall distribution of pairwise distances between localizations at the droplet interface. The composite model is composed of parts describing the rotational symmetry, repeated localizations, and arrangement of proteins. The rotational symmetry component represents the isotropic distribution of proteins at the circular droplet interface. The localization precision component represents the influence of localizing the same protein. The arrangement of proteins component accounts for proteins that are adsorbed closely, causing the protein localizations to become unresolvable in the clusters.

The rotational symmetry component involves three parameters, the 'radius of averaged droplets' (RR) and 'RPD broadening' (RB) describe the spread in the pairwise distances between the proteins around a droplet. The 'amplitude of RPD broadening' (ARB) determines the amplitude of the pairwise distances between the proteins. The localization precision component involves two parameters LP and ALP. The 'localization precision' (LP, denoted as σ_{lp}) represents the uncertainty in the repeated localizations of the same protein. The 'amplitude of localization precision' (ALP) determines the amplitude of the pairwise distances between the localizations belonging to the same protein. The arrangement of proteins involves two additional parameters; the 'arrangement of proteins broadening' (AB) describes the spread associated with the pairwise distances of localizations within a cluster. The 'amplitude of arrangement of proteins broadening' (AAB) determines the amplitude of the pairwise distances between the localizations in the clusters (**Supplementary Figure 3.3**).

To quantify the heterogeneity of the experimental data, we first plotted the RPD histograms for aggregation probabilities β of 0, 0.6, and 0.95 (**Figure 3.3A-C**). We have shown earlier (**Figure 3.1**) that the relative amplitude of the first maximum increases while the amplitude of the second peak decreases with increasing aggregation probability. To obtain a more quantitative readout, we defined a relative peak amplitude A_{rel} as the first peak amplitude divided by the sum of the amplitudes of the first and the second peak. We obtained relative peaks amplitude A_{rel} of 0.29, 0.49, and 0.93 and localization precision amplitudes (ALP) of 1.73, 6.75, and 12.18, respectively. We then determined the amplitudes of the local maxima e for the simulated data sets with aggregation probabilities β from 0 to 0.99 from **Figure 3.2** and determined the amplitudes of the local maxima. (**Figure 3.3D**). The resulting graph shows A_{rel} being constant around 0.25 for an aggregation probability $0 < \beta < 0.3$. For $0.3 <= \beta < 0.6$, A_{rel} slightly increases to around 0.4. For $\beta > 0.6$ A_{rel} increases, ultimately approaching unity. Moreover, when fitting over the RPD histograms, the green triangled line representing the amplitude of localization precision (ALP) variation of the RPD histograms show a similar trend as the relative peak amplitude (**Supplementary Table 3.1**).

To quantitatively describe the degree of heterogeneity, we suggest defining a relative peak amplitude below 0.32 as homogeneous, 0.32 – 0.4 as partially heterogeneous, and the relative peak larger than 0.4 as heterogeneous. To further analyze the shape of the normalized histograms, we simulated 100 homogeneous droplets with a radius of 1000 nm and three different localization precisions σ_{lp} of 250 nm, 100 nm, and 40 nm. For this simulation, we set the localization accuracy σ_{ac} to 30 nm to see the contribution of the σ_{lp} to the RPD histogram's

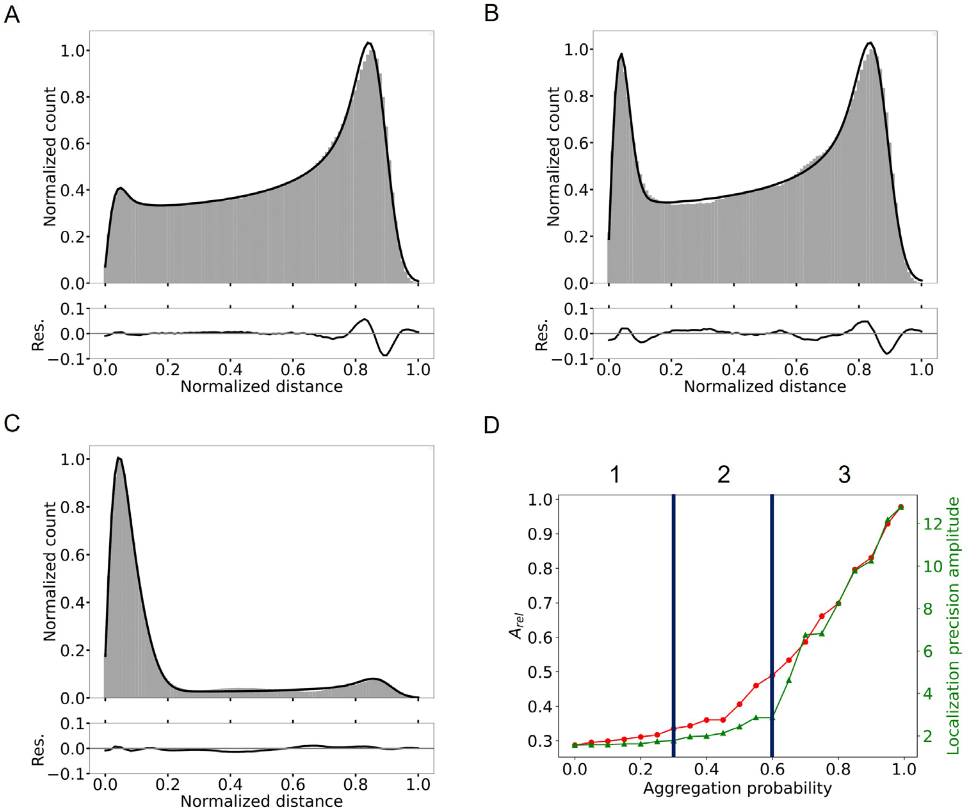

Figure 3.3. Quantification of heterogeneity using the distribution of relative distances. For the simulation, a protein density of ρ = 0.5 and a protein size of d = 22 nm was chosen. (A-C) The data (gray bars) is simulated with β = 0 representing a homogeneous distribution, (A) and 0.6 and 0.95 representing heterogeneous distributions, respectively (B and C) fitted the composite model (black line). (D) Relative peak amplitude values A_{rel}, (red circles) are obtained for different aggregation probabilities β by dividing the amplitude of the first peak by the sum of the first and the second amplitudes. The triangles line (green) represents the amplitude of the localization precision obtained from fitting all different aggregation probabilities. Vertical lines demarcate the regions that we define as representing homogeneous coverage of droplets (1) partially heterogeneous coverage (2), and heterogeneous coverage (3).

first peak. For σ_{lp} of 250 nm, we obtained two broad peaks in the RPD histogram (**Figure 3.4A**). Decreasing σ_{lp} to 100 nm and 40 nm, respectively, led to an increasingly clear separation between the local maxima and the narrowing of both peak widths (**Figure 3.4B, C**). To validate the simulation results, we performed fitting on the data. The fitted values are normalized against the maximum distance and resulted in σ_{lp} values (LP) of 42 ± 3 nm, 103 ± 5 nm, and 257 ± 5 nm for the small, medium, and large σ_{lp}, respectively.

We note that the residues between the simulated data and the fit show some systematic deviations, especially around the peak locations. This deviation is attributed to the fact that we have normalized over different max distances of the droplets in the field of view, which affects the characteristics of the peak position in the pattern and lead to a shift of the local maxima in the averaged droplet pattern. As the diameter size of the droplets is varied, the number of proteins, localizations per droplet, and maximum distance are affected, resulting in slightly different RPD broadening and peak locations. We neither observe systematic deviations in the residuals of single droplets and fits nor in a field of view with an identical radius of droplets (**Supplementary Figure 3.4**, **Figure 3.4**). Therefore, we consider the averaging effects as not being critical for the conclusions drawn in our study.

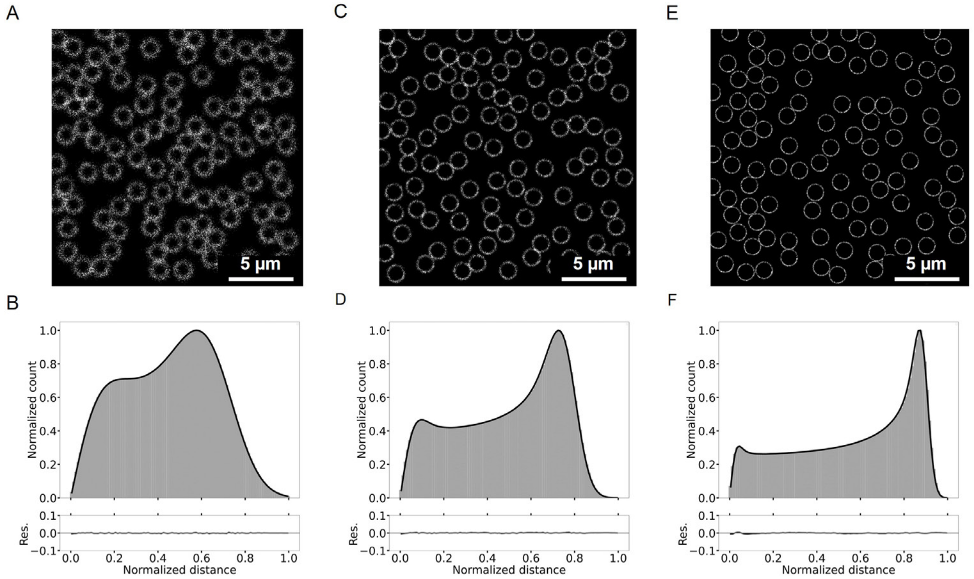

Figure 3.4. Dependency of the peak positions of the local maxima on the localization precision. Simulations with a protein density of ρ = 0.25 and protein dimension of 22 nm, a 1000 nm radius and aggregation probability of β = 0. Simulated field of view and RPD histogram with σ_{ac} = 30 nm and (A, B) σ_{lp} = 250 nm, (C, D) σ_{lp} = 100 nm, and (E, F) σ_{lp} = 40 nm. The fit of the data using the composite model returned localisation precision (LP) of σ_{lp} = 257 ± 5 nm, 103 ± 5 nm, and 42 ± 3 nm for B, D, and F, respectively.

3.3.2 The interfacial distribution of phosvitin in binary, high-pressure homogenized model emulsions is partially heterogeneous

We first prepared a binary phosvitin/SDS model emulsion with a high-pressure homogenizer and captured a brightfield image showing the distribution of oil droplets (**Figure 3.5A**). We then determined the distribution of the fluorescently labeled phosvitin antibody using STORM microscopy and overlayed the bright field and super-resolved images (**Figures 3.5B**, **C**). The data show that phosvitin does not cover all droplets, indicating a competition between phosvitin and the SDS emulsifier at the interface. Interestingly, most phosvitin localizations at the interface visually appear to be homogeneously distributed (**Figure 3.5B**). To perform further quantitative analysis, we require all localizations to be attributed to individual droplets. To this end, we used the trained model from StarDist to obtain a segmentation mask of droplets that we overlayed with the super-resolved image (**Figure 3.5D**). StarDist attributes the localizations from overlapping droplet regions twice, once for each droplet. We note that this behavior does not affect the extracted RPD histogram from the localizations (**Supplementary Figure 3.5**). We then calculated the experimental RPD for each droplet and plotted the sum of all distance-normalized distributions (**Figure 3.5E**). We calculated a A_{rel} of 0.36 for the binary phosvitin/SDS model emulsion. Following our previous classification, the value indicates a partially heterogeneous distribution of phosvitin around the oil droplets. Furthermore, fitting the distribution gives the amplitude of the localization precision of 2.77, which follows the results with the relative peak values indicating partial heterogeneity.

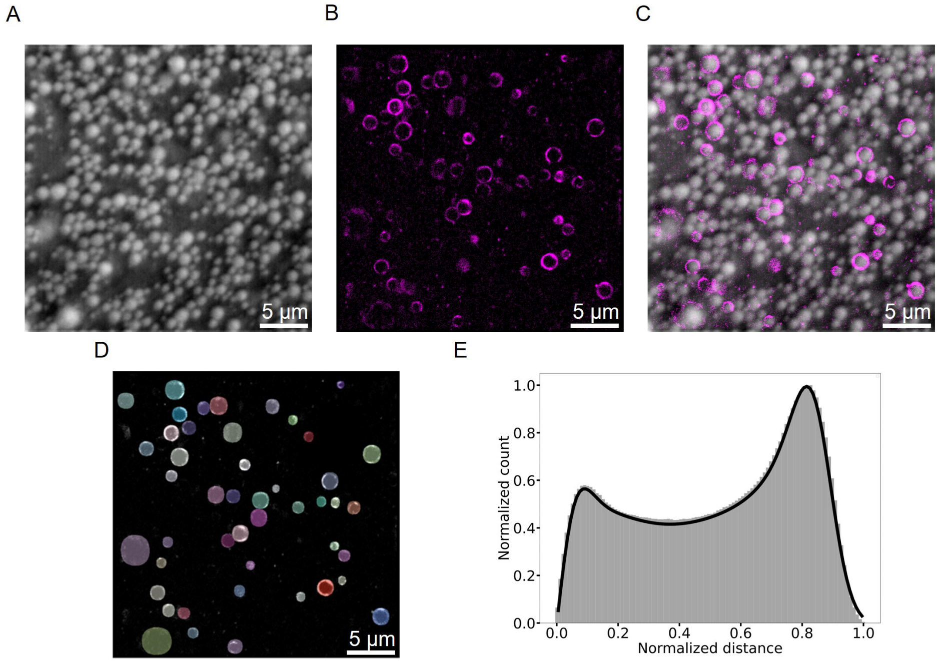

Figure 3.5. Images for a binary SDS/phosvitin model emulsion labeled with phosvitin primary antibodies conjugated to Alexa-647. (A) Brightfield image (B) Super resolved image based on localizing the emission of single fluorophores with STORM. (C) Image showing the merging of brightfield and super-resolved data (A+B). (D) Segmented image based on the StarDist applied to the super-resolved image in (B). (E) Extracted histogram of distances (gray bar chart), the fit over the data (blue line), and the peak analysis lines (dashed vertical lines). We calculated the relative peak amplitude of 0.36 and localization precision amplitude of 2.77, which indicates that the phosvitin distribution at the interface is partially heterogeneous.

3.3.3 The distribution of phosvitin and apoB in ternary, high-pressure homogenized model emulsions is heterogeneous

We proceeded by testing how the presence of three emulsifiers would change the protein distribution at the droplet interfaces in model emulsions prepared with a high-pressure homogenizer. In the first experiment, we added phospholipids in addition to phosvitin and SDS to observe their impact on the spatial distribution of phosvitin. Again, phosvitin was labeled with a phosvitin antibody conjugated with Alexa Fluor 647. In this experiment, the absence of dyes at the interface of many droplets indicates the presence of either phospholipids or SDS that outcompete phosvitin at the droplet interface. Visual inspection of the super-resolved image of the sample qualitatively showed a more heterogeneous distribution of phosvitin at the interface of those droplets that had phosvitin present (**Figure 3.6A**). To assess the distribution quantitatively, we applied the segmentation to isolate all droplets' localizations in the field of view (**Figure 3.6B**) and calculated the RPD over all droplets. The peak analysis indicated a A_{rel} value of 0.43; thus, we consider the phosvitin distribution at the interface in the presence of phospholipids and SDS as heterogeneous. This is also reflected in the RPD histogram, which shows a clear deviation from the fingerprint of a homogeneous distribution (**Figure 3.1**).

Next, we prepared a ternary model emulsion based on SDS, phospholipid and apoB. Since apoB is poorly water soluble, we used LDL as a vehicle introduce this protein to the interphase. During homogenization, the LDL particles disintegrate, and the contained apoBs and phospholipids adsorb at the interface of droplets[7]. We labeled the apoB using a secondary apoB antibody conjugated with Alexa Fluor 555. We note that we used an antibody against human apoB, which this however strongly resembling apoB present in egg yolk[11]. **Figure 3.6D** indeed shows that this antibody is specific for egg yolk apoB present at droplet interfaces. In the SDS, phospholipid and apoB ternary emulsion a slightly more heterogeneous distribution could be observed compared to the ternary emulsion with phosvitin/phospholipids/SDS at the interface (**Figure 3.6D).** We again applied segmentation to obtain localizations for each droplet in the field of view (**Figure 3.6E**). The analysis of the peaks gave a A_{rel} value of 0.47, indicative of a heterogeneous apoB distribution. In this methodological work, the use of the A_{rel} value to classify model emulsions as homogeneous, partially heterogeneous and heterogeneous is based on the visual assessment of protein distributions at the droplet interfaces. We suggest to use A_{rel} value for quantitative modelling of the effect of protein interfacial heterogeneity on physical and chemical stability of food emulsions.

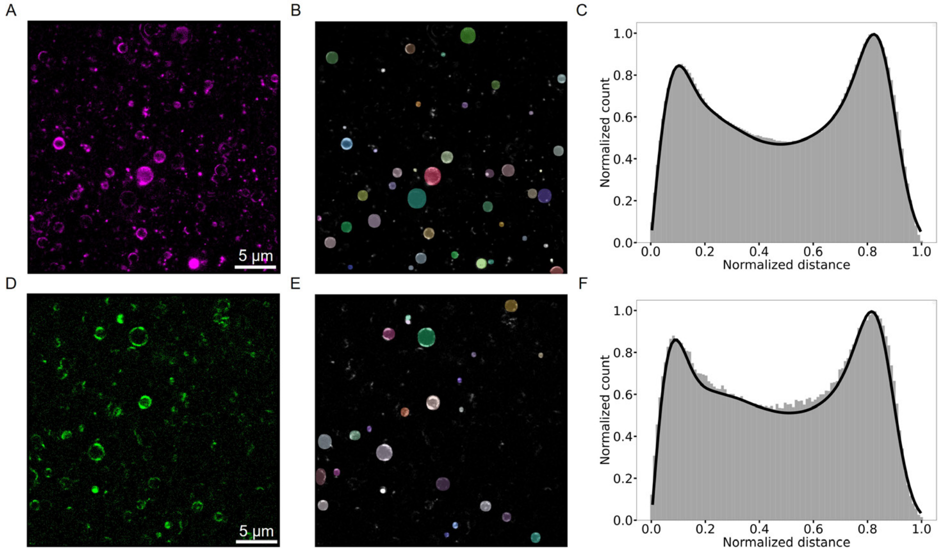

Figure 3.6. Assessment of heterogeneity in ternary model emulsions. (A) Super-resolved images of a phosvitin/phospholipid/SDS model emulsion. (B) Segmented droplets in the field of view, (C) Distribution of distances (gray bar chart), fitting function (blue line), and the peak analysis lines (dashed vertical lines). We obtained the relative peak amplitude of 0.43, which indicates a heterogeneous distribution of phosvitin in the presence of phospholipids. (D-F) as in (A-C) but for an apoB/phospholipid/SDS model emulsion. We labeled the apoB with a secondary antibody conjugated to Alexa Fluor 555. We obtained a relative peak amplitude of 0.47, which suggests again a heterogeneous distribution of apoBs at the interface.

3.4 Conclusions

In this study, we introduced a quantitative method to analyze the heterogeneity of particles adsorbed at droplet interfaces. In our specific case, we analyzed oil/water interfaces in binary and ternary oil-in-water, high-pressure homogenized food emulsions that can be considered as models for mayonnaise. Using simulations of homogeneously and heterogeneously distributed labeled proteins, we showed that the distribution of distances on a droplet interface could be used as a measure to quantify the degree of heterogeneity.

Using STORM, we could perform single-molecule localization of antibodies bound to protein emulsifiers (phosvitin and apoB) present at the droplet interfaces in mayonnaise model emulsions. The binary phosvitin/SDS model emulsion showed a partial heterogeneous phosvitin distribution at the interfaces of the droplets. In our ternary model emulsions, based on SDS/phospholipids, we showed that adding a third protein emulsifier (phospholipid or apoB) resulted in heterogeneous distributions at the droplet interface. Our proposed method will enable quantifying the effect of formulation and processing on protein emulsifier distribution at droplet interfaces and ultimately on physical and chemical food emulsion stability.

References

1 Capek, I. Degradation of Kinetically-Stable o/w Emulsions. *Advances in Colloid and Interface Science* **2004**, *107* (2–3), 125–155. https://doi.org/10.1016/S0001-8686(03)00115-5.

2 Berton-Carabin, C.; Schroën, K. Towards New Food Emulsions: Designing the Interface and Beyond. *Current Opinion in Food Science* **2019**, *27*, 74–81. https://doi.org/10.1016/j.cofs.2019.06.006.

3 Hinderink, E. B. A.; Meinders, M. B. J.; Miller, R.; Sagis, L.; Schroën, K.; Berton-Carabin, C. C. Interfacial Protein-Protein Displacement at Fluid Interfaces. *Advances in Colloid and Interface Science* **2022**, *305*, 102691. https://doi.org/10.1016/j.cis.2022.102691.

4 Berton-Carabin, C. C.; Ropers, M.-H.; Genot, C. Lipid Oxidation in Oil-in-Water Emulsions: Involvement of the Interfacial Layer: Lipid Oxidation: An Interface Outlook…. *Comprehensive Reviews in Food Science and Food Safety* **2014**, *13* (5), 945–977. https://doi.org/10.1111/1541-4337.12097.

5 Mcclements, D. J.; Decker, E. A. Lipid Oxidation in Oil-in-Water Emulsions: Impact of Molecular Environment on Chemical Reactions in Heterogeneous Food Systems. *J Food Science* **2000**, *65* (8), 1270–1282. https://doi.org/10.1111/j.1365-2621.2000.tb10596.x.

6 Berton-Carabin, C. C.; Sagis, L.; Schroën, K. Formation, Structure, and Functionality of Interfacial Layers in Food Emulsions. *Annu. Rev. Food Sci. Technol.* **2018**, *9* (1), 551–587. https://doi.org/10.1146/annurev-food-030117-012405.

7 Anton, M. Egg Yolk: Structures, Functionalities and Processes: Egg Yolk: Structures, Functionalities and Processes. *J. Sci. Food Agric.* **2013**, *93* (12), 2871–2880. https://doi.org/10.1002/jsfa.6247.

8 McCully, K. A.; Mok, C.-C.; Common, R. H. PAPER ELEGTROPHORETIC CHARACTERIZATION OF PROTEINS AND LIPOPROTEINS OF HEN’S EGG YOLK. *Can. J. Biochem. Physiol.* **1962**, *40* (7), 937–952. https://doi.org/10.1139/o62-105.

9 Jacobsen, C.; Hartvigsen, K.; Thomsen, M. K.; Hansen, L. F.; Lund, P.; Skibsted, L. H.; Hølmer, G.; Adler-Nissen, J.; Meyer, A. S. Lipid Oxidation in Fish Oil Enriched Mayonnaise: Calcium Disodium Ethylenediaminetetraacetate, but Not Gallic Acid, Strongly Inhibited Oxidative Deterioration. *J. Agric. Food Chem.* **2001**, *49* (2), 1009–1019. https://doi.org/10.1021/jf000729r.

10 Takeuchi, M.; Mashima, T.; Sztucki, M.; Petukhov, A. V.; Vis, M.; Friedrich, H.; Tuinier, R. Characterization of Hen Phosvitin in Aqueous Salt Solutions: Size, Structure, and Aggregation. *Food Hydrocolloids* **2022**, *129*, 107545. https://doi.org/10.1016/j.foodhyd.2022.107545.

11 Jolivet, P.; Boulard, C.; Beaumal, V.; Chardot, T.; Anton, M. Protein Components of Low-Density Lipoproteins Purified from Hen Egg Yolk. *J. Agric. Food Chem.* **2006**, *54* (12), 4424–4429. https://doi.org/10.1021/jf0531398.

12 Mine, Y. Emulsifying Characterization of Hens Egg Yolk Proteins in Oil-in-Water Emulsions. *Food Hydrocolloids* **1998**, *12* (4), 409–415. https://doi.org/10.1016/S0268-005X(98)00054-X.

13 Aidyraliev, R. K.; Azizova, O. A.; Vakhrusheva, T. V.; Lopukhin, Yu. M.; Mirrakhimov, M. M. Autofluorescence of Low-Density Lipoproteins Modified as a Result of Autooxidation. *Bull Exp Biol Med* **2006**, *142* (4), 433–436. https://doi.org/10.1007/s10517-006-0385-8.

14 Yang, S.; Verhoeff, A. A.; Merkx, D. W. H.; van Duynhoven, J. P. M.; Hohlbein, J. Quantitative Spatiotemporal Mapping of Lipid and Protein Oxidation in Mayonnaise. *Antioxidants* **2020**, *9* (12), 1278. https://doi.org/10.3390/antiox9121278.

15 Yang, S.; Takeuchi, M.; Friedrich, H.; van Duynhoven, J. P. M.; Hohlbein, J. Unravelling Mechanisms of Protein and Lipid Oxidation in Mayonnaise at Multiple Length Scales. *Food Chemistry* **2023**, *402*, 134417. https://doi.org/10.1016/j.foodchem.2022.134417.

16 Mcclements, D. J. Critical Review of Techniques and Methodologies for Characterization of Emulsion Stability. *Critical Reviews in Food Science and Nutrition* **2007**, *47* (7), 611–649. https://doi.org/10.1080/10408390701289292.

17 Hu, Y.-T.; Ting, Y.; Hu, J.-Y.; Hsieh, S.-C. Techniques and Methods to Study Functional Characteristics of Emulsion Systems. *Journal of Food and Drug Analysis* **2017**, *25* (1), 16–26. https://doi.org/10.1016/j.jfda.2016.10.021.

18 Gallegos-Cerda, S. D.; Hernández-Varela, J. D.; Chanona-Pérez, J. J.; Arredondo Tamayo, B.; Méndez Méndez, J. V. Super-Resolution Microscopy and Their Applications in Food Materials: Beyond the Resolution Limits of Fluorescence Microscopy. *Food Bioprocess Technol* **2022**. https://doi.org/10.1007/s11947-022-02883-4.

19 Hohlbein, J. Single-Molecule Localization Microscopy as an Emerging Tool to Probe Multiscale Food Structures. *Food Structure* **2021**, *30*, 100236. https://doi.org/10.1016/j.foostr.2021.100236.

20 ten Klooster, S.; Boerkamp, V.; Lazaridi, E.; Yang, S.; Takeuchi, M.; Berton-Carabin, C.; Schroën, K.; Janssen, H.-G.; Friedrich, H.; Hohlbein, J.; van Duynhoven, J.; Hennebelle, M. Lipid Oxidation in Food Emulsions: Analytical Challenges and Recent Developments. In *Lipid Oxidation in Food and Biological Systems*; Bravo-

Diaz, C., Ed.; Springer International Publishing: Cham, 2022; pp 3–29. https://doi.org/10.1007/978-3-030-87222-9_1.

21 Rust, M. J.; Bates, M.; Zhuang, X. Sub-Diffraction-Limit Imaging by Stochastic Optical Reconstruction Microscopy (STORM). *Nat Methods* **2006**, *3* (10), 793–796. https://doi.org/10.1038/nmeth929.

22 Heilemann, M.; van de Linde, S.; Schüttpelz, M.; Kasper, R.; Seefeldt, B.; Mukherjee, A.; Tinnefeld, P.; Sauer, M. Subdiffraction-Resolution Fluorescence Imaging with Conventional Fluorescent Probes. *Angew. Chem. Int. Ed.* **2008**, *47* (33), 6172–6176. https://doi.org/10.1002/anie.200802376.

23 Masullo, L. A.; Szalai, A. M.; Lopez, L. F.; Stefani, F. D. Fluorescence Nanoscopy at the Sub-10 Nm Scale. *Biophys Rev* **2021**, *13* (6), 1101–1112. https://doi.org/10.1007/s12551-021-00864-z.

24 Jabermoradi, A.; Yang, S.; Gobes, M. I.; van Duynhoven, J. P. M.; Hohlbein, J. Enabling Single-Molecule Localization Microscopy in Turbid Food Emulsions. *Phil. Trans. R. Soc. A.* **2022**, *380* (2220), 20200164. https://doi.org/10.1098/rsta.2020.0164.

25 Schnitzbauer, J.; Wang, Y.; Zhao, S.; Bakalar, M.; Nuwal, T.; Chen, B.; Huang, B. Correlation Analysis Framework for Localization-Based Superresolution Microscopy. *Proc. Natl. Acad. Sci. U.S.A.* **2018**, *115* (13), 3219–3224. https://doi.org/10.1073/pnas.1711314115.

26 Sengupta, P.; Jovanovic-Talisman, T.; Skoko, D.; Renz, M.; Veatch, S. L.; Lippincott-Schwartz, J. Probing Protein Heterogeneity in the Plasma Membrane Using PALM and Pair Correlation Analysis. *Nat Methods* **2011**, *8* (11), 969–975. https://doi.org/10.1038/nmeth.1704.

27 Curd, A. P.; Leng, J.; Hughes, R. E.; Cleasby, A. J.; Rogers, B.; Trinh, C. H.; Baird, M. A.; Takagi, Y.; Tiede, C.; Sieben, C.; Manley, S.; Schlichthaerle, T.; Jungmann, R.; Ries, J.; Shroff, H.; Peckham, M. Nanoscale Pattern Extraction from Relative Positions of Sparse 3D Localizations. *Nano Lett.* **2021**, *21* (3), 1213–1220. https://doi.org/10.1021/acs.nanolett.0c03332.

28 Moussa, M.; Martinet, V.; Trimeche, A.; Tainturier, D.; Anton, M. Low Density Lipoproteins Extracted from Hen Egg Yolk by an Easy Method: Cryoprotective Effect on Frozen–Thawed Bull Semen. *Theriogenology* **2002**, *57* (6), 1695–1706. https://doi.org/10.1016/S0093-691X(02)00682-9.

29 Zhang, X.; Qiu, N.; Geng, F.; Ma, M. Simply and Effectively Preparing High-Purity Phosvitin Using Polyethylene Glycol and Anion-Exchange Chromatography. *J. Sep. Science* **2011**, *34* (22), 3295–3301. https://doi.org/10.1002/jssc.201100601.

30 Jimenez, A.; Friedl, K.; Leterrier, C. About Samples, Giving Examples: Optimized Single Molecule Localization Microscopy. *Methods* **2020**, *174*, 100–114. https://doi.org/10.1016/j.ymeth.2019.05.008.

31 Nieuwenhuizen, R. P. J.; Lidke, K. A.; Bates, M.; Puig, D. L.; Grünwald, D.; Stallinga, S.; Rieger, B. Measuring Image Resolution in Optical Nanoscopy. *Nat Methods* **2013**, *10* (6), 557–562. https://doi.org/10.1038/nmeth.2448.

32 Martens, K. J. A.; van Beljouw, S. P. B.; van der Els, S.; Vink, J. N. A.; Baas, S.; Vogelaar, G. A.; Brouns, S. J. J.; van Baarlen, P.; Kleerebezem, M.; Hohlbein, J. Visualisation of DCas9 Target Search in Vivo Using an Open-Microscopy Framework. *Nat Commun* **2019**, *10* (1), 3552. https://doi.org/10.1038/s41467-019-11514-0.

33 Ovesný, M.; Křížek, P.; Borkovec, J.; Švindrych, Z.; Hagen, G. M. ThunderSTORM: A Comprehensive ImageJ Plug-in for PALM and STORM Data Analysis and Super-Resolution Imaging. *Bioinformatics* **2014**, *30* (16), 2389–2390. https://doi.org/10.1093/bioinformatics/btu202.

34 Schindelin, J.; Arganda-Carreras, I.; Frise, E.; Kaynig, V.; Longair, M.; Pietzsch, T.; Preibisch, S.; Rueden, C.; Saalfeld, S.; Schmid, B.; Tinevez, J.-Y.; White, D. J.; Hartenstein, V.; Eliceiri, K.; Tomancak, P.; Cardona, A. Fiji: An Open-Source Platform for Biological-Image Analysis. *Nat Methods* **2012**, *9* (7), 676–682. https://doi.org/10.1038/nmeth.2019.

35 Schmidt, U.; Weigert, M.; Broaddus, C.; Myers, G. Cell Detection with Star-Convex Polygons. **2018**. https://doi.org/10.48550/ARXIV.1806.03535.

36 Weigert, M.; Schmidt, U.; Haase, R.; Sugawara, K.; Myers, G. Star-Convex Polyhedra for 3D Object Detection and Segmentation in Microscopy. In *2020 IEEE Winter Conference on Applications of Computer Vision (WACV)*; IEEE: Snowmass Village, CO, USA, 2020; pp 3655–3662. https://doi.org/10.1109/WACV45572.2020.9093435.

37 Bankhead, P.; Loughrey, M. B.; Fernández, J. A.; Dombrowski, Y.; McArt, D. G.; Dunne, P. D.; McQuaid, S.; Gray, R. T.; Murray, L. J.; Coleman, H. G.; James, J. A.; Salto-Tellez, M.; Hamilton, P. W. QuPath: Open Source Software for Digital Pathology Image Analysis. *Sci Rep* **2017**, *7* (1), 16878. https://doi.org/10.1038/s41598-017-17204-5.

3.5 Supplementary materials

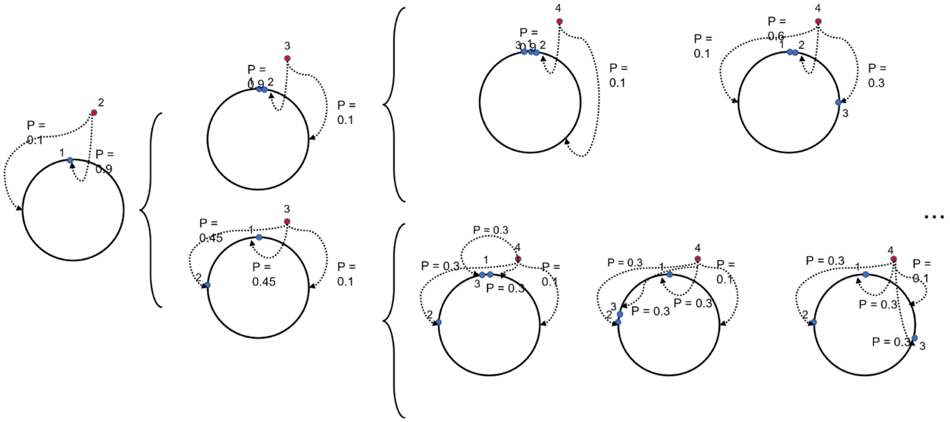

Supplementary Figure 3.1. For simulating heterogeneous distributions of proteins, we used a simple algorithm for placing new proteins at the droplet interface that already contains at least one protein. We defined a probability for the aggregation of new proteins ranging between 0 and 1. For a probability of 0, our algorithm will lead to an entirely homogeneous distribution. For a probability of 1, each new protein will be placed next to the previous one considering a 5 nm distance between proteins. If the aggregation probability is, for example, 0.9 and if we consider the first protein adsorbed at the interface, there are two options for the second protein: there is a 10% chance that the protein adsorbs as an independent protein at the interface and a 90% chance that the protein aggregates with the first protein. Subsequently, the probabilities of placing the third protein will be divided based on the placing of the second protein. The schematic below shows the different probabilities for the second and third proteins for the simulation. The succeeding proteins follow the same approach as the second and third proteins.

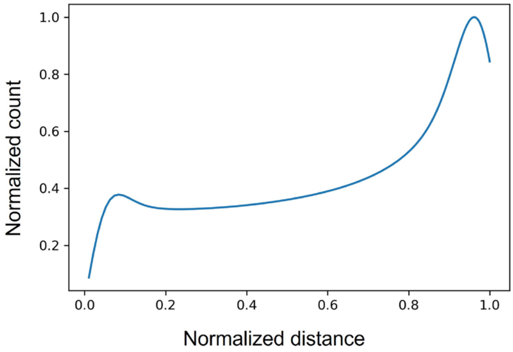

Supplementary Figure 3.2. We plotted the rotational symmetry component from the composite model by incorporating the 2D probability non-gaussian distance distribution function 27 which assumes a homogeneous distribution of emitters around a circle. This model provides the distribution of protein pair distances using only three parameters: the radius of averaged droplets (RR), the RPD broadening (RB), and the amplitude of RPD broadening (ARB). The model RPD was generated using 200 proteins, each with, on average, five localizations. We plotted the generated 2D probability function based on a droplet of 1000 nm diameter and 60 nm RB. Similar to Figure 3.4, increasing the localization precision will lead to moving the position of peaks towards each other.

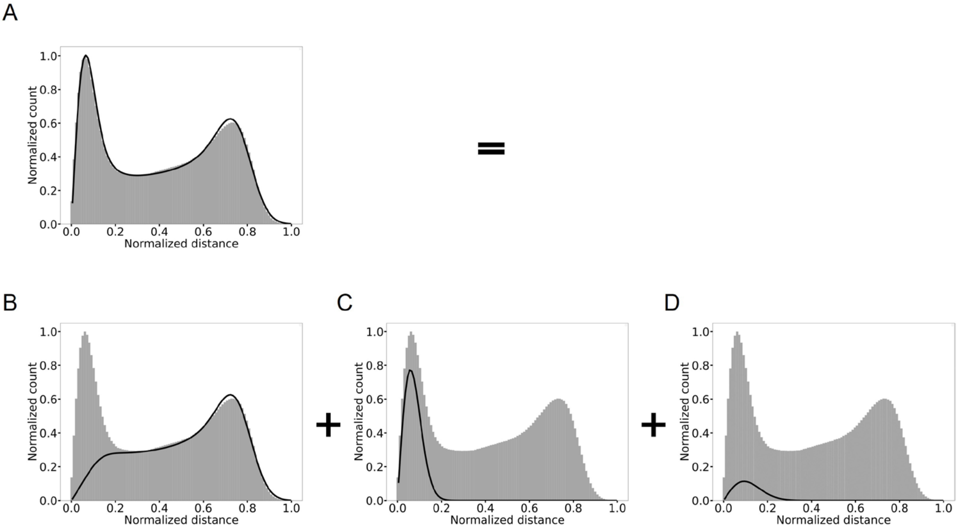

Supplementary Figure 3.3. (A) The contribution of the fitting parameters for an RPD histogram with an aggregation probability β of 0.8. (B) The first three fit parameters were obtained using the rotational symmetry component to acquire the radius of the averaged droplets (RR = 0.95 D), the RPD broadening (RB = 0.07 D), and the amplitude of RPD broadening (ARB = 0.05). (C) The following two fit parameters belong to the localization precision broadening (LP = 0.048 D) and the amplitude (ALP = 8.25) contribution. (D) The last two parameters of the fit belong to the component describing the arrangement of proteins broadening (AB = 0.08 D) and its amplitude (AAB = 2.45).

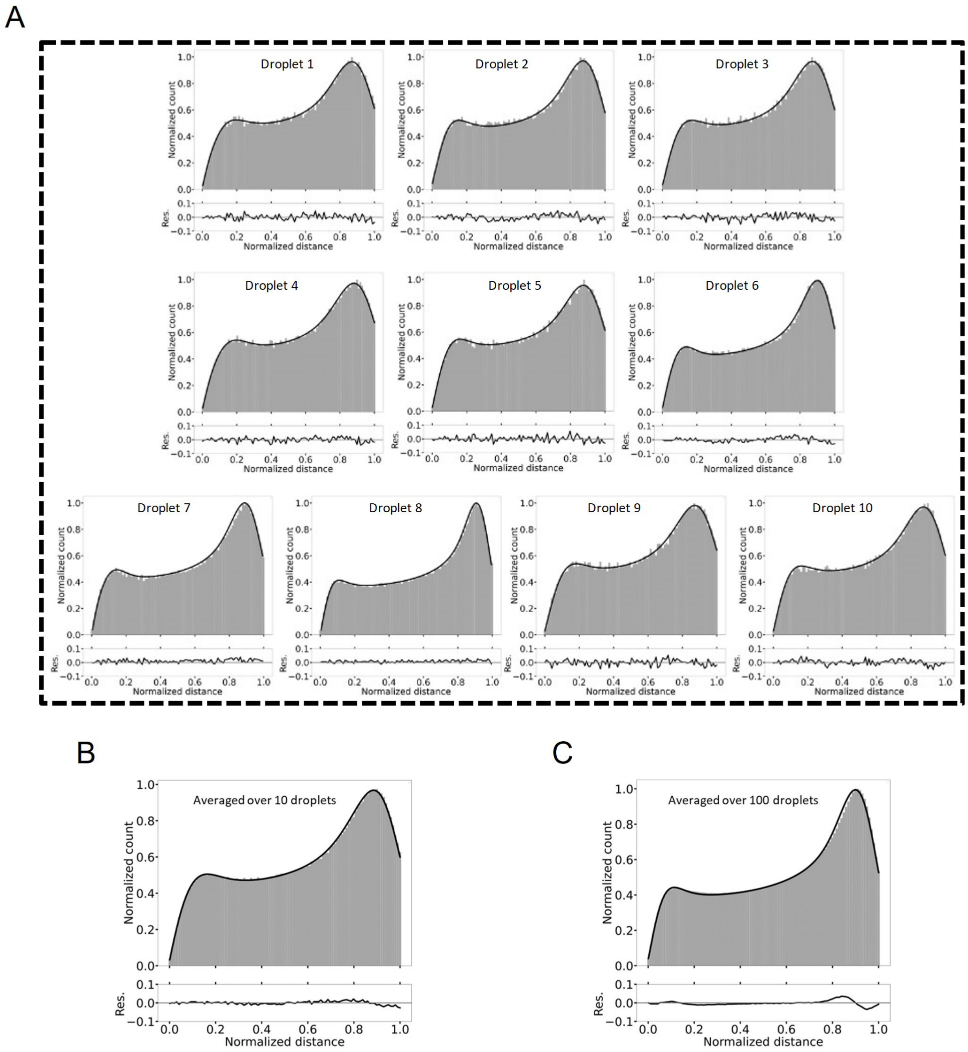

Supplementary Figure 3.4. The fit over an averaged relative position distribution (RPD) histogram of all droplets in a field of view shows small deviations around the peaks in the residues in which droplets differed in their radius (from a normal distribution with a mean of 700 nm and a standard deviation of 200 nm). This bias arises due to variations in peak positions among individual droplets. Each droplet exhibits a distinct radius and a unique distribution of proteins at the interface. Consequently, this leads to non-identical peak positions and varying maximum distances of localizations. In the figure below, subfigure (A) shows fits of ten randomly selected, homogeneous droplets in a field of view (The radii of droplets 1 to 10 are 573 nm, 545 nm, 558 nm, 566 nm, 634 nm, 705 nm, 716 nm, 908 nm, 517 nm, 587 nm, respectively). The residues between fit and the RPDs show an unbiased behavior for individual droplets. Subfigure (B) shows a fit over an averaged RPD histogram of the ten droplets in the field of view, where the residues start to show a bias around the peak positions of the RPD histogram. Subfigure C shows a fit over an averaged RPD histogram of 100 droplets.

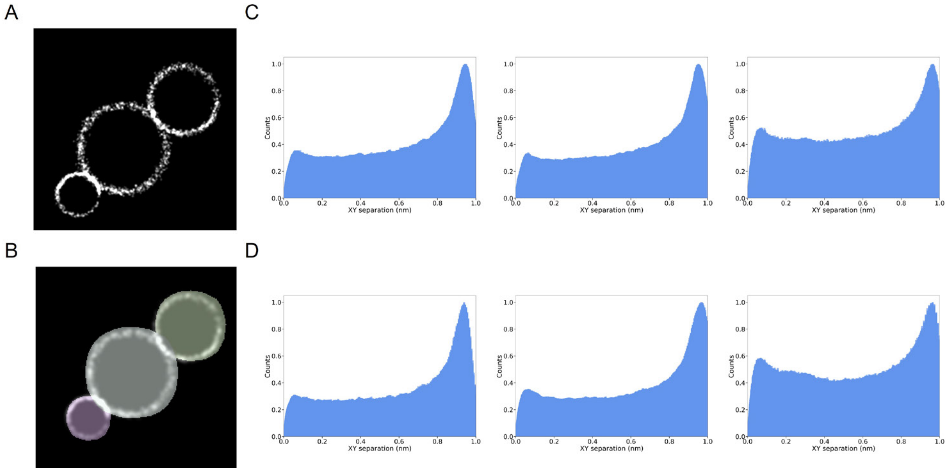

Supplementary Figure 3.5. In the experimental data, droplets often partially overlap. The overlapping localizations were counted twice when StarDist was used to segment the data. To investigate the overlapping effect on the extracted pattern, we simulated three neighboring homogeneous droplets with a radius of 900 nm, 1100 nm, and 500 nm (A) and calculated their individual RPD distributions based on the known ground truth (C). We then used StarDist to segment the simulated droplets (B). The segmented droplets were processed and plotted for all three droplet localizations containing overlapped localizations (D). The processed data indicates no major difference between the pattern extracted from the ground truth data and the segmented droplets.

Supplementary Note 3.1. The workflow of droplet segmentation using StarDist follows three steps: (1) generation and annotating of raw images, (2) training a model using Qupath, and (3) predicting segmentation.

(1) First, we require ground-truth annotated images of droplets featuring ring structure (protein at the interface) to train a model. Therefore, we prepared four experimental and two simulated data sets. The simulated data sets contain homogeneous and heterogeneous (with an aggregation probability of β = 0.8) droplets images. Further, we cropped our raw images into six different 500 pixels by 500 pixels sub-images to increase the number of input images. In total, we annotated 30 images for training.

(2) We used Qupath to prepare ground-truth annotated images where all pixels of a droplet, including the interface, are labeled for all droplets in a field of view. Moreover, we considered using the augmentation mode of the training program to increase the number of raw images even higher by applying random rotations, flips, and intensity changes on each cropped image. Afterward, we used the ground-truth annotated images in the StarDist python training code to obtain our model. The figure below shows a matching metric between the ground truth and the predicted droplets in the field of view that validated the segmentation performance. The metric shows an accuracy of 0.8 and a precision of 0.9 for the intersection over union (IoU) threshold of 0.5 used in our training model.

(3) In the final step, we used our trained model to segment the droplets.

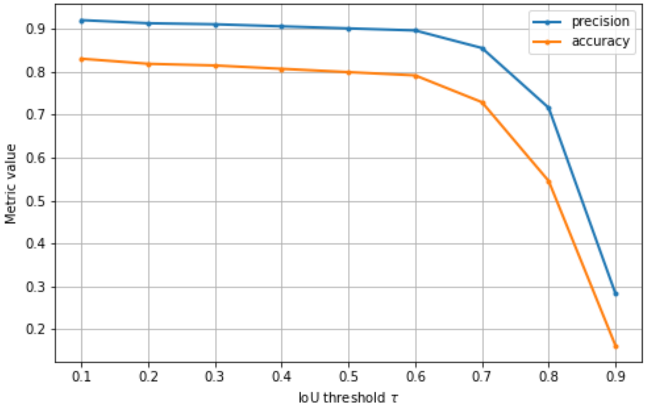

Supplementary Table 3.1. Fitting parameters of the simulated data, values are calculated for normalized droplets. Abbreviations used are RPD (relative position distribution),RR (radius of averaged droplets), RB (RPD broadening), ARB (amplitude of RPD broadening), LP (localization precision), ALP (amplitude of localization precision), AB (arrangement of proteins broadening), and AAB (amplitude of arrangement of proteins broadening).

Aggregation Probability	RR	RB	ARB	LP	ALP	AB	AAB
0.00	0.87 D	0.04 D	0.08	0.026 D	1.56	0.0 D	0.0
0.05	0.87 D	0.04 D	0.08	0.026 D	1.60	0.01 D	0.01
0.10	0.87 D	0.05 D	0.08	0.028 D	1.58	0.01 D	0.03
0.15	0.87 D	0.04 D	0.08	0.027 D	1.62	0.01 D	0.11
0.20	0.87 D	0.04 D	0.08	0.028 D	1.62	0.02 D	0.25
0.25	0.88 D	0.04 D	0.08	0.027 D	1.74	0.02 D	0.37
0.30	0.87 D	0.05 D	0.08	0.027 D	1.77	0.02 D	0.39
0.35	0.87 D	0.04 D	0.08	0.027 D	1.99	0.02 D	0.42
0.40	0.87 D	0.04 D	0.08	0.028 D	1.99	0.02 D	0.45
0.45	0.88 D	0.04 D	0.08	0.026 D	2.13	0.03 D	0.48
0.50	0.87 D	0.04 D	0.08	0.027 D	2.43	0.02 D	0.60
0.55	0.88 D	0.04 D	0.08	0.024 D	2.86	0.04 D	1.89
0.60	0.87D	0.05 D	0.08	0.025 D	2.86	0.03 D	3.17
0.65	0.87 D	0.04 D	0.07	0.026 D	4.62	0.03 D	4.32
0.70	0.88 D	0.04 D	0.06	0.026 D	6.75	0.03 D	3.65
0.75	0.87 D	0.05 D	0.03	0.028 D	6.82	0.04 D	4.72
0.80	0.88 D	0.04 D	0.03	0.027 D	8.25	0.04 D	5.06
0.85	0.88 D	0.04 D	0.02	0.028 D	9.79	0.04 D	5.15
0.90	0.87 D	0.04 D	0.01	0.029 D	10.2	0.05 D	5.89
0.95	0.87 D	0.04 D	0.00	0.027 D	10.2	0.06 D	6.81
0.99	0.87 D	0.04 D	0.00	0.028 D	10.18	0.06 D	7.28

4

Super-resolution imaging reveals heterogeneity in the coverage of oil-in-water food emulsions

Manuscript in preparation for submission:

Abbas Jabermoradi, Sanam Foroutanparsa, Ilja K. Voets, Jo Janssen, John P.M. van Duynhoven, Johannes Hohlbein.

Abstract

Super-resolution imaging was applied to reveal the distribution of phosvitin on the droplet interfaces of binary SDS/phosvitin model emulsions manufactured by high-pressure homogenization (HPH). For this purpose, phosvitin-binding primary antibodies were used to localize phosvitin at droplet interfaces. Re-scan confocal microscopy (RCM) revealed that for HPH manufactured O/W model emulsions, a bimodal droplet size distribution was obtained in which small droplets were covered by SDS and large droplets by phosvitin, respectively. This inter-droplet heterogeneity in droplet coverage was in line with expected kinetics of emulsifier coverage of droplet interfaces during HPH. Stochastic optical reconstruction microscopy (STORM) indicated that the concentration of phosvitin did not affect the intra-droplet distribution at the droplet interface. STORM further provided a direct visualization of the redistribution of phosvitin in the HPH prepared emulsions upon prolonged low shear treatment, resulting in diffusion-assisted exchange of SDS and phosvitin between droplet interfaces and the continuous aqueous phase. Our RCM- and STORM-based approaches allow a direct and quantitative view on the intricate balance between kinetic and thermodynamic forces governing the inter- and intra-droplet interfacial distribution of proteins.

4.1 Introduction

Food emulsions are intricately structured systems comprising two immiscible liquid phases, usually oil and water, that are effectively stabilized by emulsifiers and mixtures thereof[1]. Many of these mixtures contain both proteins and low molecular weight (LMW) surfactants. The adsorption of emulsifying proteins at an oil/water interface is influenced by the protein's inherent physical and chemical properties, such as size, charge, conformation, and amino acid composition, as well as environmental conditions like the type of interface (e.g., oil-water, air-water), pH, temperature, and presence of other substances[2]. When these proteins adsorb, they stabilize the emulsion through self-interaction, resulting in a viscoelastic layer that resists local deformation[3]. On the other hand, LMW surfactants are small molecules, each having a hydrophilic head group and one or more hydrophobic tails. When these surfactants are present at an interface, they orient themselves such that the hydrophilic head faces the water phase while the hydrophobic tails align with the oil phase. Their high mobility allows them to quickly coat the newly formed oil-water interface following the emulsification process[4]. Unlike proteins, LMW surfactants form a fluid layer due to the absence of strong intermolecular bonds[5]. Moreover, LMW surfactants diffuse laterally towards areas of high surface tension, known as the Marangoni effect[6]. Although the viscoelastic mechanism associated with protein adsorption and the Marangoni mechanism linked to LMW surfactant adsorption both serve to stabilize emulsions, they might not always complement each other and can be mutually unfavorable[7]. Formulating protein/LMW emulsifier mixtures has been identified as a route for designing food emulsions with desired physical[8] and chemical[9] stability.

Interfacial composition has been identified as a key determinant of the properties of food emulsions[10] and is typically determined by indirect methods[11,12]. Interfacial rheology, for example, can be applied on model films or hanging droplets[13], but does not allow to study the effects of food emulsification routes[14]. In food emulsions, the assessment of surface load via the (centrifuged) serum or cream phases is a common and straightforward method to assess interfacial composition. This method is, however, invasive and destructive, and cannot be generally applied to all types of food emulsions[12]. Spectroscopic methods can be applied to assess conformational changes of proteins at droplet interfaces and their displacement by LMW surfactants, but do usually not provide spatial information[15]. Fluorescence microscopy has been identified as a method to assess surface morphology in food emulsions, but so far, this method lacked the capability of resolving protein composition at droplet interfaces[12]. In this work, we will outline an approach based on fluorescence imaging to visualize and quantify surfactant composition at the single-droplet level. We will use a model system for mayonnaise to demonstrate our approach.

To localize proteins and surfactants, the correct choice of fluorescent probes for imaging is critical. In the life sciences, primary or secondary antibodies labeled with fluorescent markers are being widely deployed due to their inherent capability to localize specific biomacromolecules and bind to various targets[16]. There are challenges with their use, however, including long and unpredictable production timelines, inconsistencies across different production batches that can undermine their effectiveness[17], and their large size (approximately 150 kDa) that may limit their ability to penetrate densely packed structures like tissues[18,19]. Affimers, small protein scaffolds of about 100 amino acids, present a viable alternative[20]. They possess a well-defined structure featuring one or two target-specific loops, enhancing localization accuracy by positioning the probe closer to the target[21]. Affimers are selected through a process known as phage biopanning, which is relatively rapid and effectively minimizes variations between production batches[19]. Affimers can be produced via bacterial expression systems thereby circumventing the expensive and time-consuming traditional routes to obtain antibodies. Together, these features have expanded the use of affimers as specific ligands in bioassays[20,22]. Their use as ligands that specifically bind to biomolecular targets has also been exploited within the bioimaging field[20,21,23], yet their application in food emulsion studies is unexplored, presenting an exciting area for future investigation.

Mayonnaise is a food emulsion that relies on egg yolk as an emulsifier mixture to maintain its physical and chemical stability[23]. Egg yolk is composed of several constituents, including low-density lipoproteins (LDL), high-density lipoproteins (HDL), phosvitin, and livetin. Upon emulsification, the lipoprotein particles disintegrate, liberating apoproteins and phospholipids as emulsifiers[24]. Phosvitin is a highly phosphorylated protein with unique emulsifying, metal-chelating, and pro-oxidant properties among the proteins found in egg yolk[25]. In this work we will focus on studying the interaction of phosvitin and SDS, as a model LMW surfactant, at the oil-water interface in emulsions[26]. Here, we build on our previous work in which we used super-resolution microscopy techniques to localize proteins in model emulsions for mayonnaise[26]. In particular, we use stochastic optical reconstruction microscopy (STORM)[27] to surpass the diffraction limit of traditional fluorescence microscopy and localize phosvitin with molecular specificity at droplet interfaces in binary O/W model emulsions prepared with SDS. Additionally, re-scan confocal microscopy (RCM) is employed providing higher resolution than conventional confocal microscopy technique thereby enabling us to resolve smaller droplets. We will first benchmark different strategies to localize phosvitin at droplet interfaces. We will compare the performance of affimer- and antibody-based labelling strategies, and benchmark these against an approach in which phosvitin was labelled covalently with a fluorophore. Next, we will prepare binary emulsions with different phosvitin/SDS ratios with a high-pressure homogenizer (HPH). HPH is a common emulsification method in food processing, known to have an effect on the composition of the droplet surface[28]. Further, we will employ RCM to investigate the effect of the formulated phosvitin/SDS ratio on the heterogeneity of phosvitin surface coverage. With STORM we will investigate the impact of the phosvitin/SDS ratio on the phosvitin surface coverage at the intra-droplet level. Furthermore, we will investigate the effect of prolonged low shear rate treatment[29,30] on the model emulsion. Under such low shear conditions, diffusion-assisted exchange of SDS and phosvitin between the droplet interface and the continuous aqueous phase will enable a transition towards a more thermodynamically favorable state which implies an interfacial composition that yields minimized interfacial.

4.2 Materials and Method

4.2.1 Isolation and purification of phosvitin

Phosvitin was isolated from fresh egg yolk according to the protocol described by Zhang et al.[31]. Fresh hen eggs were obtained from the local market. Egg yolks were separated and rolled on filter paper to remove the chalazas. An equal amount of distilled water was added to the yolk at 4°C, and the obtained solution was centrifuged at 12,000 g for 15 min (Avanti j-25, Beckman). The precipitate was collected and homogenized with an equal mass of a 0:17M NaCl solution, followed by another centrifugation at 12,000 g for 15 min. The granules were dissolved in 10% (w/v) of a 1.74 M NaCl solution. Further, the solution was homogenized with 4% w/w of PEG6000 and centrifuged at 12,000 g for 15 min. The supernatant was dialyzed against distilled water for 24 hours at 4°C and subsequently centrifuged at 12,000 g for 15 min. The supernatant was collected and lyophilized using a freeze-dryer from either Christ, Germany or Labconco, United States of America.

4.2.2 Preparation of binary emulsions

To prepare the binary emulsions, we dissolved lyophilized phosvitin in 0.05 M acetate buffer at pH 3.8 to obtain concentrations of 3, 6, 9 and 12 mg/mL. Each solution was centrifuged at 4,000 g for 20 min, and the supernatants were transferred to new aliquots to remove any impurities. We then added 0.15% w/v of sodium dodecyl sulfate (SDS) to each solution to stabilize the emulsion and investigate the competition between SDS and phosvitin. Next, we added rapeseed oil, 15% of the final volume, into each of these solutions to prepare the model emulsions. The mixtures were coarsely homogenized using an 18 mm diameter head disperser at 18,000 rpm for 2 min, followed by further homogenization at 70 bar using a high-pressure homogenizer (HPH) (Niro Soavi – PandaPLUS 2000, GEA) for ten cycles.

4.2.2.1 Low shear treatment

To investigate the impact of low shear treatment on the competition between phosvitin and SDS, we gently stirred 20 mL of the emulsion prepared with the phosvitin concentration of 6 mg/mL using a magnetic stirrer at a speed of 500 rpm for 3 days.

4.2.3 Confocal and single-molecule localization microscopy

For the confocal RCM measurements, we used a Nikon A1R HD25 upright confocal microscope body equipped with an RCM module (Confocal.nl, Amsterdam, Netherlands)[32]. The microscope was equipped with a CCD camera (Tucsen, FL 20BW) and four laser lines (405 nm, 488 nm, 561 nm, and 640 nm, Oxxius, France). Images were captured using a 60x Plan Apo objective lens with a numerical aperture of 1.4. All images were captured in 16-bit format with a resolution of 1024 x 1024 pixels. Micromanager 1.4[33], an open-source software for microscope control and image acquisition, was used to acquire RCM images at room temperature. We used the following settings for acquisition: 2.8 mW of 488 nm laser for the oil droplets channel, and 4.6 mW of 647 nm laser for the phosvitin channel.

For the measurements of covalent/non-covalent labelled phosvitin, we used a confocal mode of STED microscope (Abberior Instruments) equipped with a UPlanSApo 100x/1.40 Oil [infinity]/0.17/FN26.5 objective (Olympus), a Katana-08 HP laser (Onefive), and multiple laser lines at 405 nm, 488 nm, 561 nm, 640 nm, and pulsed lasers at 595 nm and 775 nm (power = 3 W). The images were typically acquired with a pixel size of 60 nm and a pixel dwell time of 10 µs around 2 µm above the coverslip. The Inspector 0.14.13919 software was used for image acquisition, and the pinhole was set at 1.00 AU at 100x.

For STORM data acquisition we employed techniques similar to those previously reported[26]. A fiber-coupled laser engine (Omicron, Germany) delivered the laser beam to the microscope's excitation path. The beam was collimated using a 60 mm achromatic lens (AC254-060-A-ML, Thorlabs), then deflected by a kinematic mirror (BBE1-E02, Thorlabs) into a top hat beam shaper (Asphericon GmbH). The beam was next focused by a 150 mm lens (AC508-150-A-ML, Thorlabs) into the back focal plane of a 100x oil immersion objective (NA = 1.45, Nikon) via a polychroic mirror (ZT405/488/561/640rpcv2, Chroma). The emitted signal from the sample was collected through the same objective and passed through an emission filter (ZET405/488/561/640m-TRF, Chroma). After being reflected by a kinematic mirror, the signal was focused through a tube lens (MXA20696, Nikon) and into the first lens (AC508-100-A-ML, Thorlabs) of a 4f system. The light was then directed by another mirror to a deformable mirror (DMP40/M – P01, Thorlabs) located in the Fourier plane of the 4f imaging system. Finally, the emitted light was focused via a second lens (AC508-100-A-ML, Thorlabs) onto an sCMOS camera (Prime 95B, Photometerics), with an effective pixel size of 112 nm per pixel. We recorded a total of 10,000 frames per field of view at a rate of 40 ms per frame (25 Hz).

4.2.4 Conjugation of phosvitin with fluorescein isothiocyanate (FITC) and emulsion preparation

To enable direct fluorescence imaging of phosvitin, we employed a FITC labeling strategy that targeted the primary amines of phosvitin. First, we prepared a solution of phosvitin at a concentration of 6 mg/mL in 0.05 M MES buffer at pH 6.6. Then, we added a freshly prepared solution of 5 mg/mL FITC in DMSO to achieve a final concentration of 0.5 mM. The reaction mixture was stirred for 2 hours and subsequently dialyzed for four days using an 8 kDa cutoff dialysis bag (Sigma-Aldrich, Cat. No. D9527). To ensure the complete removal of free dyes, the dialyzed solution was filtered and concentrated using an Amicon® Ultra-15 centrifugal filter with a 3 kDa cut-off (Millipore, Cat. No. C7715). The degree of labeling was then determined by measuring the absorbance of the protein and FITC using a Nanodrop spectrophotometer. The degree of labeling was calculated to be approximately 10%, assuming that phosvitin has a molecular weight of 35 kD and absorbance (A280 nm) at 0.1% (1 g/L) of 0.32 +/- 0.02 (L/g.cm)[34]. Using this covalently labeled phosvitin solution, we immediately prepared an oil-in-water emulsion by dissolving 0.15% w/v SDS and adding 15% (v/v) rapeseed oil. We then proceeded by making a coarse emulsion using an 18 mm diameter dispersing head at 7,000 rpm for 2 min (T 18 digital ULTRA-TURRAX, IKA, Germany). We subsequently homogenized the coarse emulsion at 70 bar using a high-pressure homogenizer (HPH) (Delta Instruments LAB Homogenizer) for 20 min and stored the resulting emulsions at 4°C overnight for further use.

4.2.5 Sample preparation and image acquisition

For RCM, 5 µL of BODIPY 493/503 (TCI America, ref. D4341) 1 mg/mL in DMSO was added to 495 µL of the emulsion. After a quick vortex, the emulsion was mixed with 100 µL of phosvitin primary antibody conjugated with Alexa Fluor 647 (sc-46681, Santa Cruz Biotechnology) at a concentration of 20 µg/mL diluted in PBS buffer. For CLSM, 100 µL of phosvitin antibody conjugated with Alexa Fluor 647 (20 µg/mL diluted in PBS) was added to 500 µL of the covalently labeled phosvitin-FITC emulsion. For STORM, the phosvitin antibody conjugated with Alexa 647 (sc-46681, Santa Cruz Biotechnology) stock solution was diluted 50 times in PBS buffer. 10% v/v of the diluted solution was added to 400 µL of the phosvitin-containing model emulsion. After a 15-minute incubation at room temperature, all labeled emulsions were centrifuged at 4,000 g for 5 min, and the cream layer on top was harvested for imaging. In this cream phase, droplets are prevented from diffusing in the water phase during image acquisition. 2 µL of the cream phase was attentively pipetted into a silicone gasket's well (Grace Bio-Labs). Further, to increase the number of fluorophore blinking events, 25 µL of STORM buffer containing 50 mM TRIS pH 8, 10 mM NaCl, 10% glucose, 140 mM 2-mercaptoethanol, 68 µg/mL catalase, and 200 µg/mL glucose oxidase was added [35]. A second cover glass was put on the well to prevent new oxygen from getting into the sample. For each sample we acquired a total of five different field of views.

4.2.6 Image visualization and data analysis

To analyze the confocal microscope images, we first normalized the contrast of the images from different channels using ImageJ/Fiji[36]. Next, we used StarDist segmentation[37,38] to extract the positions of individual droplets within the field of view after training the model on multiple datasets using QuPath[39]. For the phosvitin antibody channel (Magenta), the image was subtracted from the BODIPY channel (green) to eliminate background interference. We then compared the number of droplets covered with phosvitin to the total number of droplets in the field of view. To assess emulsifier adsorption in relation to droplet size, we computed the Sauter mean diameter, $D_{3,2}$, for all samples within each channel. To specify the width of the droplet size distribution, we took its standard deviation. To analyze the dSTORM raw data, we first removed the constant fluorescence background using a temporal median filter[26] available at GitHub (**https://github.com/HohlbeinLab/FTM2**). Next, we used a phasor-based localization algorithm[40] implemented in ThunderSTORM[41], a software plugin for ImageJ/Fiji, to determine the positions of the fluorophores with sub-pixel localization precision. For image background filtering in ThunderSTORM, a β-spline wavelet filter with order 2 and scale 3 was used. We applied 2D cross-correlation drift correction with ThunderSTORM settings of 10 bins and 5x magnification. The localizations were then visualized using the "average shifted histogram" option, with the magnification set to 5 and the labeled protein phosvitin represented in magenta. To analyze the distribution of proteins at the interface of individual droplets, we applied droplet segmentation to extract the localizations for each droplet. This allowed us to apply relative position distribution (RPD) analysis[42] to quantify the spatial heterogeneity of localizations within droplets, which we previously reported in chapter 3.

4.3 Results and discussion

4.3.1 Localization of phosvitin at droplet interfaces using covalent and non-covalent labeling

First, we evaluated the use of affimers to target phosvitin at droplet interfaces. A main advantage of affimer ligands is that they can be generated from libraries in a combinatorial approach, thus avoiding expensive and time-consuming procedures to generate antibodies. Being small peptide sequences of only around 100 amino acids that can be expressed and harvested in bacteria, affimers may offer a spatially tighter interaction with the target protein and thereby improved localization accuracy. However, the phosvitin-binding affimers that we specifically raised against phosvitin in a phage display, were positively charged at pH 6 and lacked the required specificity for phosvitin. Instead, the affimers non-specifically interacted with any negatively charged component, including both phosvitin and SDS. As a result, the affimers uniformly accumulated in the continuous water phase and showed accumulation at droplet interfaces, regardless of the presence or absence of phosvitin. This non-specific binding pattern was also evident for the control affimer, which is also positively charged at pH 6. In this control affimer, the recognition sequence identified for phosvitin was replaced with alanine residues (**Supplementary Figure 4.1**), suggesting that the interactions between affimers and phosvitin were primarily driven by electrostatic forces rather than specific recognition of phosvitin (**Supplementary Figure 4.2**, **4.3**). By contrast, phosvitin-binding antibodies exhibited higher selectivity, targeting specific regions of phosvitin (**Supplementary Figure 4.4**). Consequently, we chose commercially available phosvitin antibodies for our subsequent RCM and STORM investigations of droplet surface coverage. We confirmed the specificity of the primary phosvitin antibodies by comparing the localization of phosvitin tagged covalently labeled with fluorescein isothiocyanate (FITC) (**Figure 4.1A**) and phosvitin tagged non-covalently through the phosvitin antibody conjugated to Alexa 647 (**Figure 4.1B**). The overlay image showed that the antibodies targeted the oil droplets that had covalently labeled phosvitin at their interface (**Figure 4.1C**). Among all oil droplets in the FOV only a fraction was covered with covalent and non-covalently labelled phosvitin (**Supplementary Figure 4.5**). In the non-covalent case, we observed a non-uniform distribution of phosvitin on the oil droplet interfaces, as evidenced by the larger variations in fluorescence intensity of phosvitin-binding antibodies around the droplets (**Figure 4.1D**). This contrasted with the uniform distribution observed in the covalent case, suggesting that the degree of labeling with the antibody affects the distribution of phosvitin on the droplet interfaces.

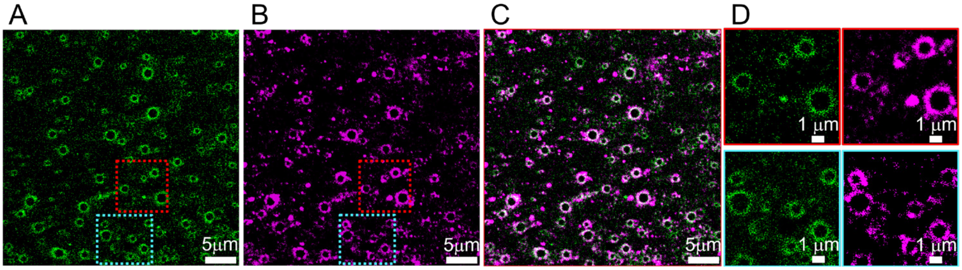

Figure 4.1. Dual-color CLSM imaging of a model emulsion stabilized with 0.15% w/v SDS and FITC-conjugated phosvitin. (A) Phosvitin covalently labeled with FITC (green channel), (B) Phosvitin antibody covalently labeled with Alexa Fluor 647 (magenta channel), (C) Overlay image (green: phosvitin-FITC, magenta: phosvitin antibody, white: co-localization of phosvitin-FITC and phosvitin antibody), and (D) The zoomed-in areas of the square region.

4.3.2 Effect of phosvitin/SDS concentration ratio on the surface coverage of droplets

As phosvitin alone is a poor emulsifying agent[43,44], achieving a stable emulsion required the addition of SDS. To obtain insights in the competition and interactions between phosvitin and SDS, we stained the oil droplets with BODIPY 493/503 and kept the concentration of SDS fixed at 1.5 mg/ml (5.2 mM). We then changed the concentration of phosvitin from 3 mg/mL to 12 mg/mL (0.09 to 0.34 mM) (**Figure 4.2**). The chosen concentrations for SDS and the lowest considered concentration of phosvitin were selected to ensure full potential coverage of the surface of all oil droplets (**Supplementary Note 4.1**). Whereas the Bodipy (green channel) stains the oil droplets homogeneously (**Figure 4.2**, first column), the fluorescence measured

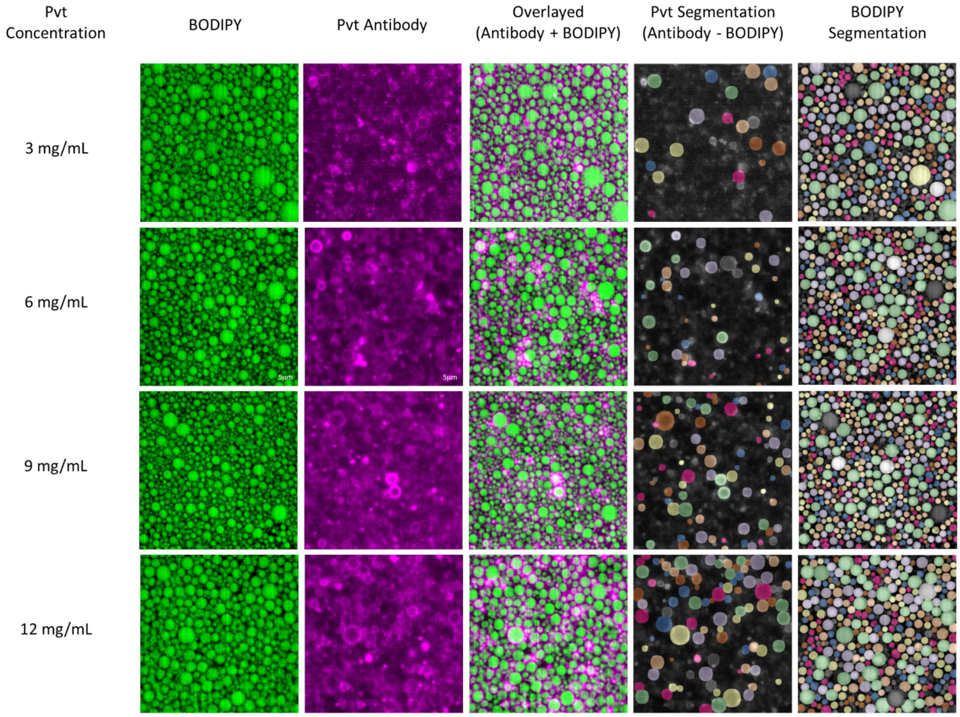

Figure 4.2. Visualization and quantification of phosvitin-covered droplets in low-oil-content emulsions. Re-scan confocal microscopy (RCM) was used to visualize phosvitin-coated droplets in emulsions with varying phosvitin concentrations and a constant SDS concentration (1.5 mg/mL). The BODIPY column visualizes all oil droplets labeled by BODIPY 493/503 (represented in the green channel), while the antibody column visualizes phosvitin-coated droplets (shown in the magenta channel) that were identified using Alexa Fluor 647-labeled primary phosvitin antibodies. The Merged column shows the overlay of the Antibody and BODIPY columns. The Pvt Segmentation column demonstrates the result of subtracting the Antibody column from the BODIPY column, a step necessary for the segmentation of phosvitin-covered droplets due to the noise present in the Antibody channel. The BODIPY Segmentation column presents the segmentation of all droplets using the BODIPY column. As demonstrated, the number of identified droplets covered by phosvitin increases with increasing concentrations of phosvitin.

from the phosvitin antibody (magenta channel) is not confined to the interface of the droplets (**Figure 4.2**, second column). In fact, we observe a rather hazy intensity distribution, which we attribute to (1) the presence of phosvitin in the water phase, (2) droplets that are either below or above the imaged volume, and (3) the high number of the droplets in the field of view. Merging both channels reveals that some oil droplets in the green channel are encircled by magenta rings, indicating their coverage by phosvitin (**Figure 4.2**, third column). Importantly, in this system, where only phosvitin and SDS serve as emulsifying agents, droplets that are devoid of phosvitin coverage can be inferred to be coated by SDS. Coverage by SDS is supported by the long-term physical stability of the binary SDS/phosvitin emulsions, which can only be achieved by coverage with an emulsifier. Droplets not visibly covered by phosvitin will henceforth be referred to as SDS-covered droplets. We employed the segmentation tool StarDist[37,38] to segment the droplets in both the green (Bodipy) and magenta (phosvitin) channels. We employed the green channel as a reference to subtract the magenta channel. We achieved a reliable segmentation of the phosvitin-coated droplets (**Figure 4.2**, fourth column) and the droplets in the Bodipy channel (**Figure 4.2**, fifth column). Decreasing concentrations of phosvitin (from top to bottom) are accompanied by decreasing numbers of phosvitin coated droplets in the field of view. In the next section we will quantify the heterogeneity in the coverage of the droplets at the inter- and intra-droplet level.

4.3.3 Inter-droplet surface heterogeneity

Utilizing the results from the previous section, we analyzed the size distribution for droplets predominantly covered by SDS or phosvitin. Histograms with the comparative droplet size distributions for SDS and phosvitin coated droplets show that as the concentration of phosvitin increased, the number of droplets covered by phosvitin increased, whereas the number of SDS droplets declined (**Figure 4.3**). The overall data indicate that phosvitin tends to adsorb at larger droplets. SDS on the other hand, consistently coated smaller droplets across all samples. This indicates that phosvitin prefers covering larger droplets. We computed the surface volume mean diameter (Sauter mean diameter, $D_{3,2}$) for the emulsions depicted in **Figure 4.2** and **4.3**. This metric quantified the tendencies observed visually in the histogram (**Figure 4.4A**). For all concentrations of phosvitin, we obtained $D_{3,2}$ values between 2.08 and 2.28 ± 0.7 µm, and for SDS $D_{3,2}$ between 1.52 and 1.59 ± 0.5 µm. The larger $D_{3,2}$ values for phosvitin confirm the protein's tendency to associate with larger droplets, and the $D_{3,2}$ for SDS align with the surfactant's observed preference for smaller droplets. For both phosvitin and SDS droplets, the $D_{3,2}$ values do not vary with concentration, indicating that regardless of the concentration of the emulsifiers, they adsorb to specific droplet sizes ranges (**Figure 4.4A**).

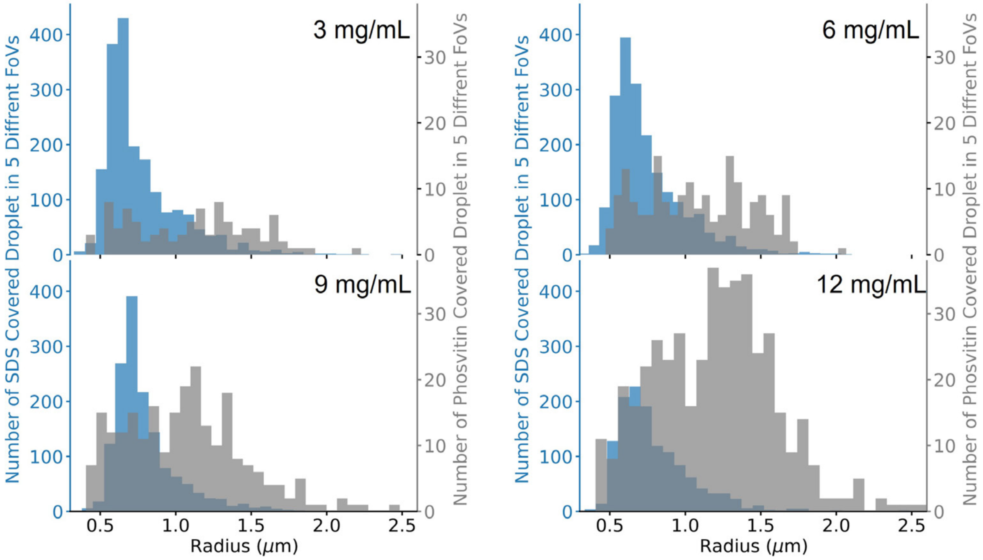

Figure 4.3. Assessment of inter-droplet heterogeneity and the impact of various phosvitin concentrations, with a constant SDS concentration (1.5 mg/mL), on droplet size distribution post-segmentation as obtained from RCM images. The histograms display the relative distribution of SDS-covered droplets (blue bars) versus phosvitin-covered droplets (gray bars). Note that phosvitin covered droplets were identified directly in the RCM images, non-covered droplet stained with Bodipy were assumed to be covered with SDS only (see text). For clearer comparisons, droplet counts were adjusted to a reference: maximum observed counts of 450 for SDS droplets in the 3 mg/mL sample and 40 for phosvitin droplets in the 12 mg/mL sample. Increasing the phosvitin concentrations from 3 mg/mL to 12 mg/mL led to a corresponding rise in the proportion of droplets covered by phosvitin, from 10% (38 out of a total of 400 droplets) to 14% (54/390), 19% (71/373), and 25% (89/358), respectively; The reported droplet counts are based on observations from five different fields of view (FOVs).

An explanation of these results lies in the events occurring during the HPH process. In our binary model emulsion, both SDS and phosvitin are present in the aqueous phase from the outset of the coarse homogenization step using a high-shear mixer. The coarse droplets are likely stabilized by a mix of SDS and phosvitin. Subsequently, these pre-homogenized coarse droplets are processed using a high-pressure homogenizer (HPH), which fragments them into smaller ones. This then leads to a very rapid and massive increase of the total surface area, which needs to be stabilized by emulsifiers. Immediately after their formation, the fine droplets have virtually bare interfaces, and will coalesce, while the emulsifier coverage builds up due to adsorption from the bulk solution. Moreover, the coalescence itself will contribute to the increase of interfacial coverage because the coarsening implies a reduction in interfacial area. Since the adsorption kinetics of SDS is much faster than that of phosvitin, the smallest droplets in the size distribution will soon get stabilized by SDS before much phosvitin has adsorbed. On the other hand, larger droplets from the initial coarse distribution coalesce more slowly, allowing time for protein adsorption. As these droplets coalesce, their mixed interfaces of phosvitin and SDS become denser. However, while protein adsorption is quasi-irreversible[45], SDS dynamically exchanges with the bulk, leading to the detachment of surplus SDS as the protein concentration increases. This process yields larger droplets, predominantly covered by proteins. Consequentially, in oil water emulsions with SDS and phosvitin, phosvitin plays a more dominant role in the stabilization of larger droplets. The competition between SDS and phosvitin is shown in **Figure 4.4B**, which depicts the SDS area coverage against the concentrations of phosvitin. At the lowest concentration of phosvitin, 91% of the surface area was covered by SDS. However, as the concentration of phosvitin increased, the proportion of droplet surface area covered by SDS consistently decreased. It is important to note that both SDS and phosvitin were present a sufficiently high concentrations to cover all droplets (**Supplementary Note 4.1**). The observed decrease in SDS droplet surface coverage with increasing phosvitin concentration indicates an inherent competition between these emulsifiers for covering droplet interfaces within the binary emulsion.

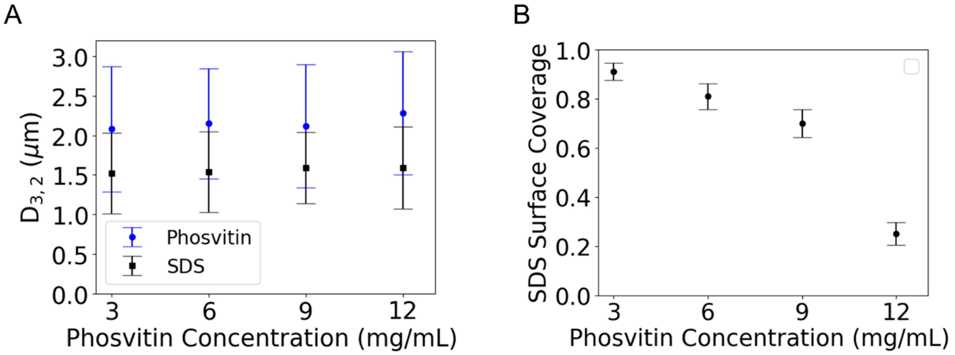

Figure 4.4. (A) Plot of the surface volume mean diameter $D_{3,2}$ for emulsion samples with varying phosvitin concentrations with a constant SDS concentration (1.5 mg/mL). The circle marker represents the $D_{3,2}$ for phosvitin, the square marker indicates the $D_{3,2}$ for SDS. The larger mean $D_{3,2}$ of phosvitin compared to SDS indicates a tendency of phosvitin to associate with larger droplets. (B) Plot illustrating the SDS area coverage across various phosvitin concentrations with a constant SDS concentration (1.5 mg/mL).

4.3.4 Intra-droplet surface heterogeneity

Next, we proceeded with STORM to further quantify the intra-droplet distribution of phosvitin. The STORM images in **Figure 4.5A** show that an increase in phosvitin results in an increased number of large droplets covered. This experiment validates the findings from the RCM experiment that also showed an increase in the number of droplets covered by phosvitin with increasing concentration of phosvitin. The enhanced spatial resolution of STORM allowed assessment of the intra-droplet surface heterogeneity of droplets that were at least partially covered with phosvitin. We quantified the spatial heterogeneity of phosvitin localizations at the surface of single droplets with the methodology outlined in **Chapter 3**. This approach leads to

RPD histograms that provide a fingerprint of intra-droplet heterogeneity of interfacial coverage. We calculated RPD histograms for droplet sizes below and above the average $D_{3,2}$ value and these appeared similar. For the two droplet populations, the relative peak amplitudes A_{rel} - a metric representing the ratio of the first peak's amplitude to the sum of the first and second peaks (see **Chapter 3**) - were all approximately 0.39, indicating a partially heterogeneous distribution of phosvitin (**Supplementary Figure 4.6**). The values for the two droplet populations did not differ within experimental error. There was no significant influence of phosvitin concentration on A_{rel} either (**Figure 4.5B**). We conclude that neither droplet size nor phosvitin concentration affected the heterogeneity of the distribution of phosvitin on droplet interfaces in HPH prepared SDS/phosvitin based emulsions.

4.3.5 Impact of low shear treatment

We further investigated the impact of low-shear treatment, which allows for diffusion-assisted exchange of SDS and phosvitin between droplet interfaces and with the continuous aqueous phase. For this purpose, we selected the binary SDS/phosvitin emulsion with a phosvitin concentration of 6 mg/mL. This emulsion was subjected to low shear using a roller shaker for a duration of 3 days. To assess the influence of this processing step on the emulsion, we employed STORM before and after low-shear treatment (**Figure 4.6A**).

After the low shear treatment, we see a clear reduction of the number of phosvitin-covered droplets (**Figure 4.6B**). The redistribution of SDS over the droplet surface is visualized in the histograms in **Figure 4.6C, D**. Post low-shear treatment, the histogram (**Figure 4.6D**) showed that the distribution of SDS-covered droplets remained constant. However, the number of phosvitin-covered droplets diminished, indicating that phosvitin was displaced by SDS from the droplet interfaces. To verify whether droplet coalescence played a role, we calculated the $D_{3,2}$, which remained constant at approximately 1.73 ± 0.56 µm and 1.72 ± 0.61 µm before and after low-shear treatment, respectively. Thus, droplet coalescence can be excluded to play a role during the low shear treatment. We therefore attribute the replacement of phosvitin by SDS to a slow equilibration to a more thermodynamically favorable state in which droplet interfaces are solely covered by SDS. To ensure that the observed decrease in phosvitin coverage was not due to aging of the emulsion, we also measured a control sample from the same stock kept at room temperature that had not been sheared for three days. Upon imaging the control sample, we observed results consistent with **Figure 4.6A**, indicating that aging without shear treatment did not cause a decrease in phosvitin coverage (**Supplementary Figure 4.7**).

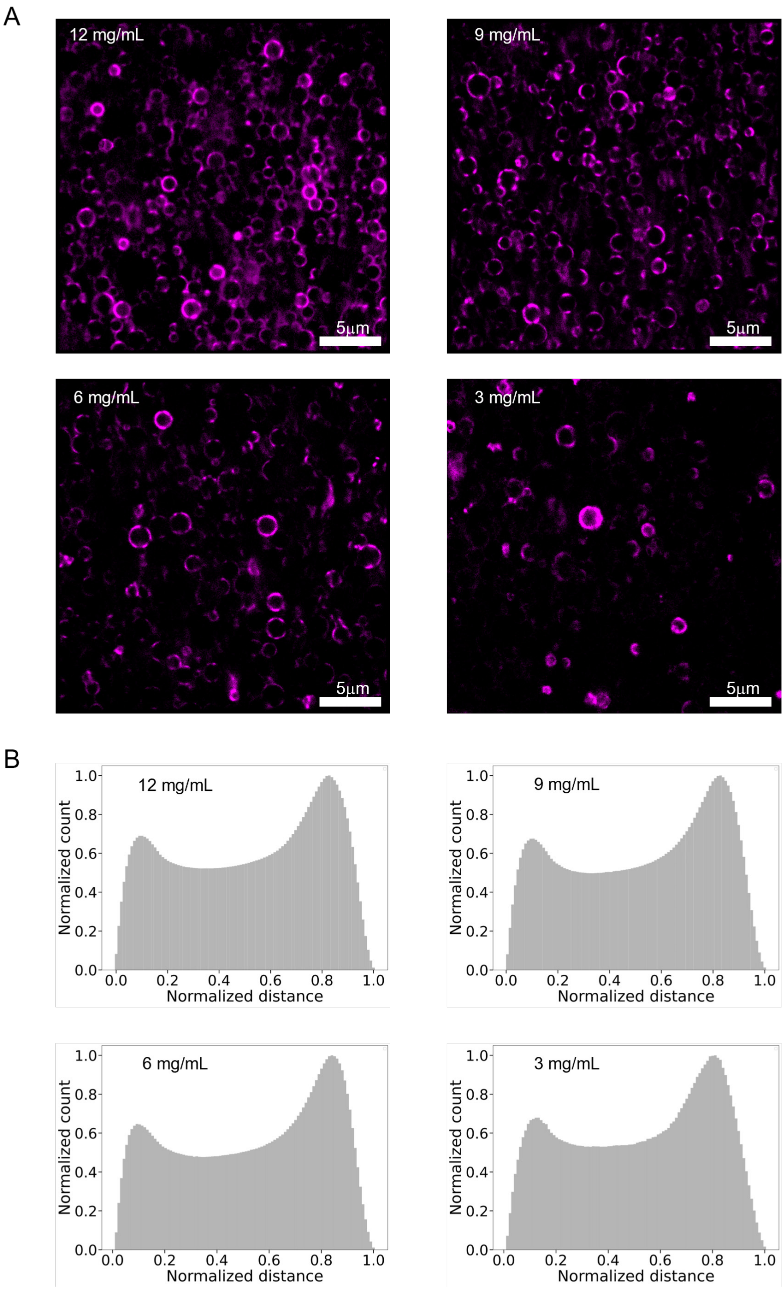

Figure 4.5. Analyzing the intra-droplet heterogeneity of the distribution of phosvitin at droplet interfaces. (A) STORM microscopy images of phosvitin at droplet interfaces at different concentrations. (B) Histograms of normalized relative position distances (RPD) were used to analyze the intra-droplet heterogeneity of the phosvitin distribution. RPD distances were normalized and averaged across all droplets for each concentration.

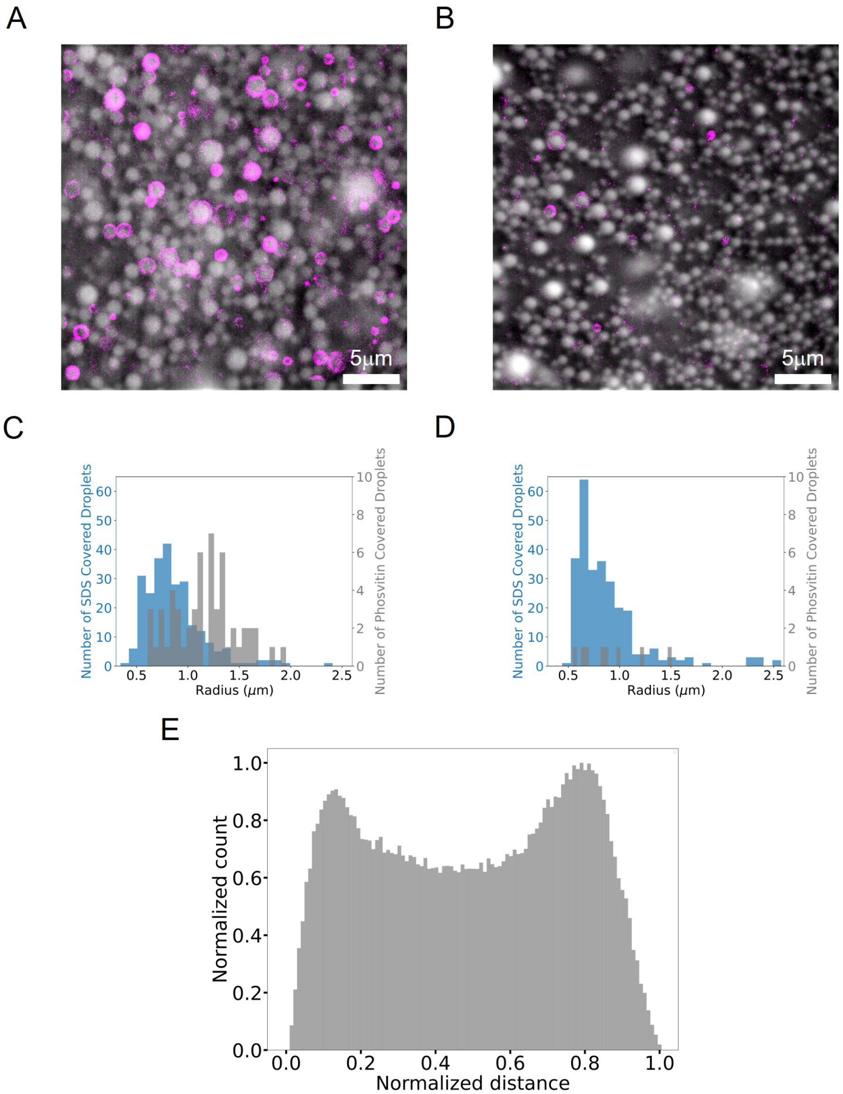

Figure 4.6. Impact of low shear treatment (A, B before; B, D, E after) on phosvitin droplet surface coverage relative to SDS, obtained from a single field of view (FOV). Note that phosvitin covered droplets can be identified directly in STORM images, non-covered droplets are assumed to be covered with SDS (see text). (A) Merge of the STORM image (Magenta channel) and the bright field of the emulsion sample before low shear treatment. The total number of droplets covered by SDS is 256. (B) Same as in A with a total of 273 droplets covered by SDS, but after low shear treatment. The histograms display the relative distribution of SDS-covered droplets (blue bars) versus phosvitin-covered droplets (gray bars) (C) Before low shear treatment, and (D) After low shear treatment. (E) Histograms of the normalized RPD to examine the heterogeneity of phosvitin distribution post low-shear treatment. RPD distances were normalized and averaged across all droplets within the field of view. The relative peak amplitude, Arel for droplets after the treatment is 0.48 which is not significantly different from the Arel of 0.39 obtained before the low-shear treatment.

We then quantified the intra-droplet phosvitin distribution at the interface for all droplets within the field of view post low-shear treatment (**Figure 6E**). The relative peak amplitude, A_{rel} for droplet with sizes below and above $D_{3,2}$were respectively 0,47 and 0.49. These values are not significantly different from each other, and also not from the A_{rel} obtained before the low-shear treatment. Our results are in line with previous findings that in O/W emulsions droplet coverage with low molecular weight surfactants is thermodynamically favored over coverage with proteins[4,46]. This effect was also observed for full mayonnaise subjected to a prolonged low shear treatment[29]. These previous findings were, however, mostly underpinned with indirect measurements of droplet surfactant coverage, whereas our super-resolution approach provides direct visualization with inter- and intra-droplet resolution.

4.4 Conclusions

Phosvitin-binding affimers that were specifically raised against phosvitin in a phage display, did not show sufficient specificity for phosvitin at the at the oil-water interface of HPH manufactured SDS/phosvitin model emulsions. In contrast, phosvitin-binding antibodies showed the required high specificity for localization at droplet interfaces. Re-scan confocal microscopy revealed that for HPH manufactured O/W model emulsions a bimodal droplet size was obtained wherein small droplets were covered by SDS and large droplets by phosvitin. This inter-droplet heterogeneity in the coverage of droplets was in line with the time-evolution of the emulsifier coverage of droplet interfaces during HPH. STORM indicated that the concentration of phosvitin did not affect the intra-droplet distribution at the droplet interface. STORM also provided a direct visualization of the redistribution of phosvitin upon low shear treatment, which hitherto could only be inferred from indirect measurements. Our RCM- and STORM-based approaches allow a direct and quantitative view on the intricate balance between kinetic and thermodynamic forces governing the intra- and inter-droplet interfacial distribution of proteins, paving the way for new studies in the realm of research on food emulsions.

References

1 McClements, D. J.; Jafari, S. M. Improving Emulsion Formation, Stability and Performance Using Mixed Emulsifiers: A Review. *Advances in Colloid and Interface Science* **2018**, *251*, 55–79. https://doi.org/10.1016/j.cis.2017.12.001.

2 Rodríguez Patino, J. M.; Pilosof, A. M. R. Protein–Polysaccharide Interactions at Fluid Interfaces. *Food Hydrocolloids* **2011**, *25* (8), 1925–1937. https://doi.org/10.1016/j.foodhyd.2011.02.023.

3 van Aken, G. A. Competitive Adsorption of Protein and Surfactants in Highly Concentrated Emulsions: Effect on Coalescence Mechanisms. *Colloids and Surfaces A: Physicochemical and Engineering Aspects* **2003**, *213* (2–3), 209–219. https://doi.org/10.1016/S0927-7757(02)00514-9.

4 Pugnaloni, L. A.; Dickinson, E.; Ettelaie, R.; Mackie, A. R.; Wilde, P. J. Competitive Adsorption of Proteins and Low-Molecular-Weight Surfactants: Computer Simulation and Microscopic Imaging. *Advances in Colloid and Interface Science* **2004**, *107* (1), 27–49. https://doi.org/10.1016/j.cis.2003.08.003.

5 Wilde, P.; Mackie, A.; Husband, F.; Gunning, P.; Morris, V. Proteins and Emulsifiers at Liquid Interfaces. *Advances in Colloid and Interface Science* **2004**, *108–109*, 63–71. https://doi.org/10.1016/j.cis.2003.10.011.

6 Ewers, W.; Sutherland, K. The Role of Surface Transport in the Stability and Breakdown of Foams. *Aust. J. Chem.* **1952**, *5* (4), 697. https://doi.org/10.1071/CH9520697.

7 Cornec, M.; Wilde, P. J.; Gunning, P. A.; Mackie, A. R.; Husband, F. A.; Parker, M. L.; Clark, D. C. Emulsion Stability as Affected by Competitive Adsorption Between an Oil-Soluble Emulsifier and Milk Proteins at the Interface. *J Food Science* **1998**, *63* (1), 39–43. https://doi.org/10.1111/j.1365-2621.1998.tb15671.x.

8 McClements, D. J. *Food Emulsions: Principles, Practices, and Techniques, Third Edition*, 0 ed.; CRC Press, 2015. https://doi.org/10.1201/b18868.

9 Berton-Carabin, C.; Villeneuve, P. Targeting Interfacial Location of Phenolic Antioxidants in Emulsions: Strategies and Benefits. *Annu. Rev. Food Sci. Technol.* **2023**, *14* (1), 63–83. https://doi.org/10.1146/annurev-food-060721-021636.

10 Ravera, F.; Dziza, K.; Santini, E.; Cristofolini, L.; Liggieri, L. Emulsification and Emulsion Stability: The Role of the Interfacial Properties. *Advances in Colloid and Interface Science* **2021**, *288*, 102344. https://doi.org/10.1016/j.cis.2020.102344.

11 Niu, H.; Wang, W.; Dou, Z.; Chen, X.; Chen, X.; Chen, H.; Fu, X. Multiscale Combined Techniques for Evaluating Emulsion Stability: A Critical Review. *Advances in Colloid and Interface Science* **2023**, *311*, 102813. https://doi.org/10.1016/j.cis.2022.102813.

12 Hinderink, E. B. A.; Meinders, M. B. J.; Miller, R.; Sagis, L.; Schroën, K.; Berton-Carabin, C. C. Interfacial Protein-Protein Displacement at Fluid Interfaces. *Advances in Colloid and Interface Science* **2022**, *305*, 102691. https://doi.org/10.1016/j.cis.2022.102691.

13 Maldonado-Valderrama, J.; Patino, J. M. R. Interfacial Rheology of Protein–Surfactant Mixtures. *Current Opinion in Colloid & Interface Science* **2010**, *15* (4), 271–282. https://doi.org/10.1016/j.cocis.2009.12.004.

14 Javadi, A.; Dowlati, S.; Shourni, S.; Miller, R.; Kraume, M.; Kopka, K.; Eckert, K. Experimental Techniques to Study Protein–Surfactant Interactions: New Insights into Competitive Adsorptions via Drop Subphase and Interface Exchange. *Advances in Colloid and Interface Science* **2022**, *301*, 102601. https://doi.org/10.1016/j.cis.2022.102601.

15 Rampon, V.; Genot, C.; Riaublanc, A.; Anton, M.; Axelos, M. A. V.; McClements, D. J. Front-Face Fluorescence Spectroscopy Study of Globular Proteins in Emulsions: Displacement of BSA by a Nonionic Surfactant. *J. Agric. Food Chem.* **2003**, *51* (9), 2482–2489. https://doi.org/10.1021/jf026168g.

16 Voskuil, J. Commercial Antibodies and Their Validation. *F1000Res* **2014**, *3*, 232. https://doi.org/10.12688/f1000research.4966.2.

17 *Reproducibility: Standardize antibodies used in research | Nature*. https://www.nature.com/articles/518027a (accessed 2023-07-28).

18 Orlova, A.; Magnusson, M.; Eriksson, T. L. J.; Nilsson, M.; Larsson, B.; Höidén-Guthenberg, I.; Widström, C.; Carlsson, J.; Tolmachev, V.; Ståhl, S.; Nilsson, F. Y. Tumor Imaging Using a Picomolar Affinity HER2 Binding Affibody Molecule. *Cancer Research* **2006**, *66* (8), 4339–4348. https://doi.org/10.1158/0008-5472.CAN-05-3521.

19 Banta, S.; Dooley, K.; Shur, O. Replacing Antibodies: Engineering New Binding Proteins. *Annual Review of Biomedical Engineering* **2013**, *15* (1), 93–113. https://doi.org/10.1146/annurev-bioeng-071812-152412.

20 Tiede, C.; Bedford, R.; Heseltine, S. J.; Smith, G.; Wijetunga, I.; Ross, R.; AlQallaf, D.; Roberts, A. P.; Balls, A.; Curd, A.; Hughes, R. E.; Martin, H.; Needham, S. R.; Zanetti-Domingues, L. C.; Sadigh, Y.; Peacock, T. P.; Tang, A. A.; Gibson, N.; Kyle, H.; Platt, G. W.; Ingram, N.; Taylor, T.; Coletta, L. P.; Manfield, I.; Knowles, M.; Bell, S.; Esteves, F.; Maqbool, A.; Prasad, R. K.; Drinkhill, M.; Bon, R. S.; Patel, V.; Goodchild, S. A.; Martin-Fernandez, M.; Owens, R. J.; Nettleship, J. E.; Webb, M. E.; Harrison, M.; Lippiat, J. D.; Ponnambalam,

S.; Peckham, M.; Smith, A.; Ferrigno, P. K.; Johnson, M.; McPherson, M. J.; Tomlinson, D. C. Affimer Proteins Are Versatile and Renewable Affinity Reagents. *eLife* **2017**, *6*, e24903. https://doi.org/10.7554/eLife.24903.

21 Schlichthaerle, T.; Eklund, A. S.; Schueder, F.; Strauss, M. T.; Tiede, C.; Curd, A.; Ries, J.; Peckham, M.; Tomlinson, D. C.; Jungmann, R. Site-Specific Labeling of Affimers for DNA-PAINT Microscopy. *Angewandte Chemie International Edition* **2018**, *57* (34), 11060–11063. https://doi.org/10.1002/anie.201804020.

22 Tans, R.; van Rijswijck, D. M. H.; Davidson, A.; Hannam, R.; Ricketts, B.; Tack, C. J.; Wessels, H. J. C. T.; Gloerich, J.; van Gool, A. J. Affimers as an Alternative to Antibodies for Protein Biomarker Enrichment. *Protein Expression and Purification* **2020**, *174*, 105677. https://doi.org/10.1016/j.pep.2020.105677.

23 *Food Emulsifiers and Their Applications*; Hasenhuettl, G. L., Hartel, R. W., Eds.; Springer International Publishing: Cham, 2019. https://doi.org/10.1007/978-3-030-29187-7.

24 Anton, M. Egg Yolk: Structures, Functionalities and Processes: Egg Yolk: Structures, Functionalities and Processes. *J. Sci. Food Agric.* **2013**, *93* (12), 2871–2880. https://doi.org/10.1002/jsfa.6247.

25 Marcet, I.; Sáez-Orviz, S.; Rendueles, M.; Díaz, M. Egg Yolk Granules and Phosvitin. Recent Advances in Food Technology and Applications. *LWT* **2022**, *153*, 112442. https://doi.org/10.1016/j.lwt.2021.112442.

26 Jabermoradi, A.; Yang, S.; Gobes, M. I.; van Duynhoven, J. P. M.; Hohlbein, J. Enabling Single-Molecule Localization Microscopy in Turbid Food Emulsions. *Phil. Trans. R. Soc. A.* **2022**, *380* (2220), 20200164. https://doi.org/10.1098/rsta.2020.0164.

27 Rust, M. J.; Bates, M.; Zhuang, X. Sub-Diffraction-Limit Imaging by Stochastic Optical Reconstruction Microscopy (STORM). *Nat Methods* **2006**, *3* (10), 793–796. https://doi.org/10.1038/nmeth929.

28 Taisne, L.; Walstra, P.; Cabane, B. Transfer of Oil between Emulsion Droplets. *Journal of Colloid and Interface Science* **1996**, *184* (2), 378–390. https://doi.org/10.1006/jcis.1996.0632.

29 Serial, M. R.; Arnaudov, L. N.; Stoyanov, S.; Dijksman, J. A.; Terenzi, C.; van Duynhoven, J. P. M. Non-Invasive Rheo-MRI Study of Egg Yolk-Stabilized Emulsions: Yield Stress Decay and Protein Release. *Molecules* **2022**, *27* (10), 3070. https://doi.org/10.3390/molecules27103070.

30 Kokini, J.; Aken, G. van. Discussion Session on Food Emulsions and Foams. *Food Hydrocolloids* **2006**, *20* (4), 438–445. https://doi.org/10.1016/j.foodhyd.2005.10.003.

31 Zhang, X.; Qiu, N.; Geng, F.; Ma, M. Simply and Effectively Preparing High-Purity Phosvitin Using Polyethylene Glycol and Anion-Exchange Chromatography. *J. Sep. Science* **2011**, *34* (22), 3295–3301. https://doi.org/10.1002/jssc.201100601.

32 De Luca, G. M. R.; Breedijk, R. M. P.; Brandt, R. A. J.; Zeelenberg, C. H. C.; de Jong, B. E.; Timmermans, W.; Azar, L. N.; Hoebe, R. A.; Stallinga, S.; Manders, E. M. M. Re-Scan Confocal Microscopy: Scanning Twice for Better Resolution. *Biomedical Optics Express* **2013**, *4* (11), 2644. https://doi.org/10.1364/BOE.4.002644.

33 Stuurman, N.; Amdodaj, N.; Vale, R. MManager: Open Source Software for Light Microscope Imaging. *Microscopy Today* **2007**, *15* (3), 42–43. https://doi.org/10.1017/S1551929500055541.

34 Castellani, O.; Martinet, V.; David-Briand, E.; Guérin-Dubiard, C.; Anton, M. Egg Yolk Phosvitin: Preparation of Metal-Free Purified Protein by Fast Protein Liquid Chromatography Using Aqueous Solvents. *Journal of Chromatography B* **2003**, *791* (1–2), 273–284. https://doi.org/10.1016/S1570-0232(03)00230-7.

35 Jimenez, A.; Friedl, K.; Leterrier, C. About Samples, Giving Examples: Optimized Single Molecule Localization Microscopy. *Methods* **2020**, *174*, 100–114. https://doi.org/10.1016/j.ymeth.2019.05.008.

36 Schindelin, J.; Arganda-Carreras, I.; Frise, E.; Kaynig, V.; Longair, M.; Pietzsch, T.; Preibisch, S.; Rueden, C.; Saalfeld, S.; Schmid, B.; Tinevez, J.-Y.; White, D. J.; Hartenstein, V.; Eliceiri, K.; Tomancak, P.; Cardona, A. Fiji: An Open-Source Platform for Biological-Image Analysis. *Nat Methods* **2012**, *9* (7), 676–682. https://doi.org/10.1038/nmeth.2019.

37 Schmidt, U.; Weigert, M.; Broaddus, C.; Myers, G. Cell Detection with Star-Convex Polygons. In *Medical Image Computing and Computer Assisted Intervention – MICCAI 2018*; Frangi, A. F., Schnabel, J. A., Davatzikos, C., Alberola-López, C., Fichtinger, G., Eds.; Lecture Notes in Computer Science; Springer International Publishing: Cham, 2018; Vol. 11071, pp 265–273. https://doi.org/10.1007/978-3-030-00934-2_30.

38 Weigert, M.; Schmidt, U.; Haase, R.; Sugawara, K.; Myers, G. Star-Convex Polyhedra for 3D Object Detection and Segmentation in Microscopy. In *2020 IEEE Winter Conference on Applications of Computer Vision (WACV)*; IEEE: Snowmass Village, CO, USA, 2020; pp 3655–3662. https://doi.org/10.1109/WACV45572.2020.9093435.

39 Bankhead, P.; Loughrey, M. B.; Fernández, J. A.; Dombrowski, Y.; McArt, D. G.; Dunne, P. D.; McQuaid, S.; Gray, R. T.; Murray, L. J.; Coleman, H. G.; James, J. A.; Salto-Tellez, M.; Hamilton, P. W. QuPath: Open Source Software for Digital Pathology Image Analysis. *Sci Rep* **2017**, *7* (1), 16878. https://doi.org/10.1038/s41598-017-17204-5.

40 Martens, K. J. A.; Bader, A. N.; Baas, S.; Rieger, B.; Hohlbein, J. Phasor Based Single-Molecule Localization Microscopy in 3D (PSMLM-3D): An Algorithm for MHz Localization Rates Using Standard CPUs. *The Journal of Chemical Physics* **2018**, *148* (12), 123311. https://doi.org/10.1063/1.5005899.

41 Ovesný, M.; Křížek, P.; Borkovec, J.; Švindrych, Z.; Hagen, G. M. ThunderSTORM: A Comprehensive ImageJ Plug-in for PALM and STORM Data Analysis and Super-Resolution Imaging. *Bioinformatics* **2014**, *30* (16), 2389–2390. https://doi.org/10.1093/bioinformatics/btu202.

42 Curd, A. P.; Leng, J.; Hughes, R. E.; Cleasby, A. J.; Rogers, B.; Trinh, C. H.; Baird, M. A.; Takagi, Y.; Tiede, C.; Sieben, C.; Manley, S.; Schlichthaerle, T.; Jungmann, R.; Ries, J.; Shroff, H.; Peckham, M. Nanoscale Pattern Extraction from Relative Positions of Sparse 3D Localizations. *Nano Lett.* **2021**, *21* (3), 1213–1220. https://doi.org/10.1021/acs.nanolett.0c03332.

43 Castellani, O.; Belhomme, C.; David-Briand, E.; Guérin-Dubiard, C.; Anton, M. Oil-in-Water Emulsion Properties and Interfacial Characteristics of Hen Egg Yolk Phosvitin. *Food Hydrocolloids* **2006**, *20* (1), 35–43. https://doi.org/10.1016/j.foodhyd.2005.02.010.

44 Dickinson, E.; Hunt, J. A.; Dalgleish, D. G. Competitive Adsorption of Phosvitin with Milk Proteins in Oil-in-Water Emulsions. *Food Hydrocolloids* **1991**, *4* (5), 403–414. https://doi.org/10.1016/S0268-005X(09)80135-5.

45 Jafari, S. M.; Assadpoor, E.; He, Y.; Bhandari, B. Re-Coalescence of Emulsion Droplets during High-Energy Emulsification. *Food Hydrocolloids* **2008**, *22* (7), 1191–1202. https://doi.org/10.1016/j.foodhyd.2007.09.006.

46 Nylander, T.; Arnebrant, T.; Cárdenas, M.; Bos, M.; Wilde, P. Protein/Emulsifier Interactions. In *Food Emulsifiers and Their Applications*; Hasenhuettl, G. L., Hartel, R. W., Eds.; Springer International Publishing: Cham, 2019; pp 101–192. https://doi.org/10.1007/978-3-030-29187-7_5.

47 Takeuchi, M.; Mashima, T.; Sztucki, M.; Petukhov, A. V.; Vis, M.; Friedrich, H.; Tuinier, R. Characterization of Hen Phosvitin in Aqueous Salt Solutions: Size, Structure, and Aggregation. *Food Hydrocolloids* **2022**, *129*, 107545. https://doi.org/10.1016/j.foodhyd.2022.107545.

48 de Aguiar, H. B.; Strader, M. L.; de Beer, A. G. F.; Roke, S. Surface Structure of Sodium Dodecyl Sulfate Surfactant and Oil at the Oil-in-Water Droplet Liquid/Liquid Interface: A Manifestation of a Nonequilibrium Surface State. *J. Phys. Chem. B* **2011**, *115* (12), 2970–2978. https://doi.org/10.1021/jp200536k.

4.5 Supplementary materials

Supplementary note 4.1

To demonstrate that the sodium dodecyl sulfate (SDS) and phosvitin concentrations were in excess of covering available droplet surface we provide the following estimates:

Calculation of Surface Area per Unit Volume

For phosvitin droplets, assuming an oil volume fraction ($\emptyset$) of 0.15 and oil droplet radius (R) of 1.2 µm (1.2×10^{-6} m), the surface area per unit volume (A) was calculated as $A = 3\emptyset/R$ yielding $A = 3.75 \times 10^{5}$ 1/m. For SDS, with the same oil volume fraction but a droplet radius (R) of 0.5 µm (0.5×10^{-6} m), the surface area per unit volume was found to be $A = 9 \times 10^{5}$ 1/m We note that in binary emulsions these values are to be considered as maximum values.

Conversion of Saturation Adsorption Γ_{sa} for Phosvitin

The saturation adsorption Γ_{sa} of phosvitin, taken as equivalent to that of ovalbumin due to comparable size, is 1.8 mg/m^2 at pH 3.4 This was converted into µmol/m^2 for consistency with the following calculations using the molecular weight of Phosvitin (35 kDa or 35000 g/mol): Γ_{sa} (phosvitin) = 0.0514 µmol/m^2. This value is in line with the recently reported value of the effective diameter $d_{eff} < 8$ nm for phosvitin in solution at pH <7[47], which would give Γ_{sa} (phosvitin) < 0.08 µmol/m^2.

Calculation of Phosvitin/SDS Required Concentration

The amount of phosvitin required per unit volume, given its saturation adsorption of 0.0514 µmol/m^2, was found to be: 0.0514 µmol/m^2 $\times 3.75 \times 10^{5}$ 1/m = 19.275×10^{3} µmol/m^3 . Subsequently, the concentration of phosvitin become 0.0193 µM. The amount of SDS required per unit volume, given Γ_{sa} (SDS) =3 µmol/m^2 [48], was found to be: 3 µmol/m^2 $\times$ 9 $\times 10^{5}$ 1/m $= 2.7 \times 10^{6}$ µmol/m^3. Likewise, concentration of SDS become 2.7 mM.

Based on these calculations, summarized in Table 4.1, the lowest concentrations of emulsifiers that were used in the experiments are in excess of what would be needed to fully cover all droplets.

	Average droplet size [µm]	Surface area per unit volume $[10^5 \frac{1}{m}]$	Γ_{sa} $[\frac{\mu mol}{m^2}]$	Required concentration to cover droplets [µM]	Range used in this study [µM]	Range used in this study $[\frac{mg}{ml}]$
SDS	0.5	9	3	2.7 x 10^3	5.2 x 10^3	1.5
Phosvitin	1.2	3.8	0.051	0.02	0.09 - 0.34	3-12

Table 4.1 Overview of surface area per unit volume, saturation adsorption Γ_{sa} and required concentrations to fully cover droplets in an emulsion with an oil volume fraction (φ) of 0.15. We note that these estimates are made of single-emulsifier emulsions, hence values for surface area per unit volume and Γ_{sa} should be considered as upper limits in binary emulsions. As a consequence, the required concentrations to cover all droplets in a binary emulsion are also upper (estimated) limits.

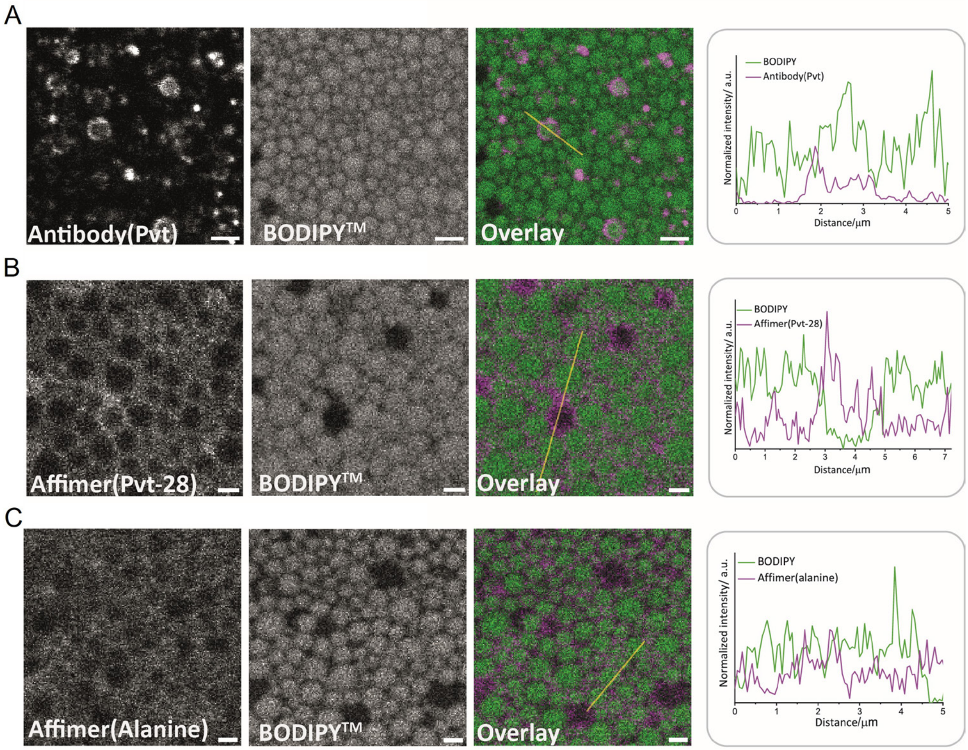

Supplementary Figure 4.1. Comparison of the specificity of antibody and affimer in Confocal laser scanning microscopy (CLSM) images of an emulsion stabilized by phosvitin and SDS, with an accompanying oil droplet line intensity profile. The line intensity profile of the highlighted yellow line in the overlay image is depicted in the right panels. In these profiles, green represents the intensity of oil droplets stained with BODIPY 493/503 dye, while magenta indicates the line intensity of affimers/antibodies at the interface: (A) CLSM image showing oil droplets with phosvitin antibody conjugated to Alexa Fluor 647. This reveals the accumulation of phosvitin-binding antibodies in the interfacial region of certain oil droplets, with discernible variations in magenta and green line intensity. (B) Image of the emulsion with Cy5-conjugated affimer (Pvt-28). Pvt-28, along with Pvt-7 and Pvt-33, comes from a phage display library containing 1.3 × 10^{10} randomized protein scaffold clones. From 48 potential affimer clones identified post-biopanning, three (Pvt-7, 28, and 33) were selected due to their binding proficiency as assessed by phage ELISA. Subsequent engineering introduced cysteines for enhanced labeling. Images show that Pvt-28 uniformly accumulates throughout the continuous water phase. (C) Cy5-conjugated control affimer (alanine) as a control labelling which lacks phosvitin-specific regions. Results show alanine accumulated in the continuous phase. Scale bar in the CLSM images is 1 μm. Images were acquired using the same settings and are shown at the same brightness scale.

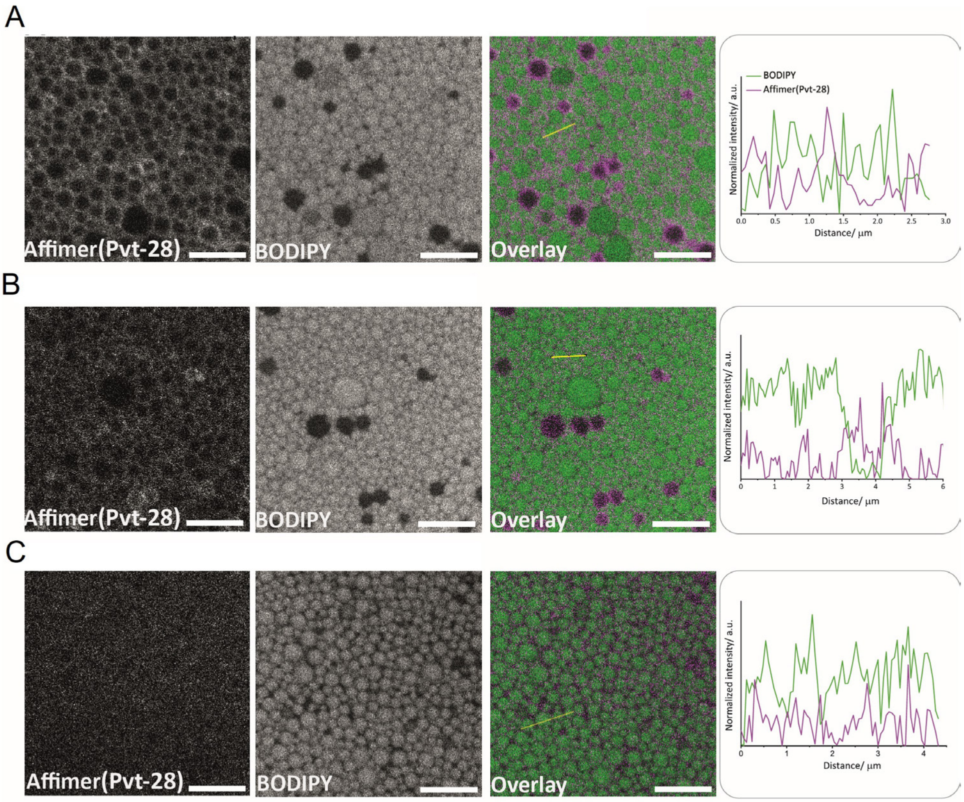

Supplementary Figure 4.2. Comparing the specificity of Affimer (Pvt-28) in emulsions with different compositions. Representative CLSM images of emulsions (pH 6.6) stained with Cy5-conjugated affimer (Pvt-28) and BODIPY 493/503 with an accompanying oil droplet line intensity profile. The line intensity profile of the highlighted yellow line in the overlay image is depicted in the right panels. In these profiles, green represents the intensity of oil droplets stained with BODIPY 493/503 dye, while magenta indicates the line intensity of affimers at the interface. The emulsions are stabilized with: (A) SDS (anionic emulsifier) and phosvitin. (B) SDS (anionic emulsifier) as control emulsion. The images shows even though there is no phosvitin in the system that the affimer (Pvt-28) accumulated in the continuous water phase of the emulsion. (C) Tween20 (neutral emulsifier). The results show the nonspecific signal from the presence of affimer (Pvt-28) in the continuous phase was less pronounced and indistinguishable from the signal coming from the oil phase. Overall, all phosvitin-binding affimers showed a lower signal when the model emulsion was stabilized with the Tween20 (neutral emulsifier) than the control emulsion stabilized with only SDS (anionic emulsifier). This result suggests that electrostatic interactions play a role in the ligand binding of affimers to the interface and that the composition of the variable region may have less influence. Scale bars in all panels are 5 µm. Images were acquired using the same settings and are shown at the same brightness scale.

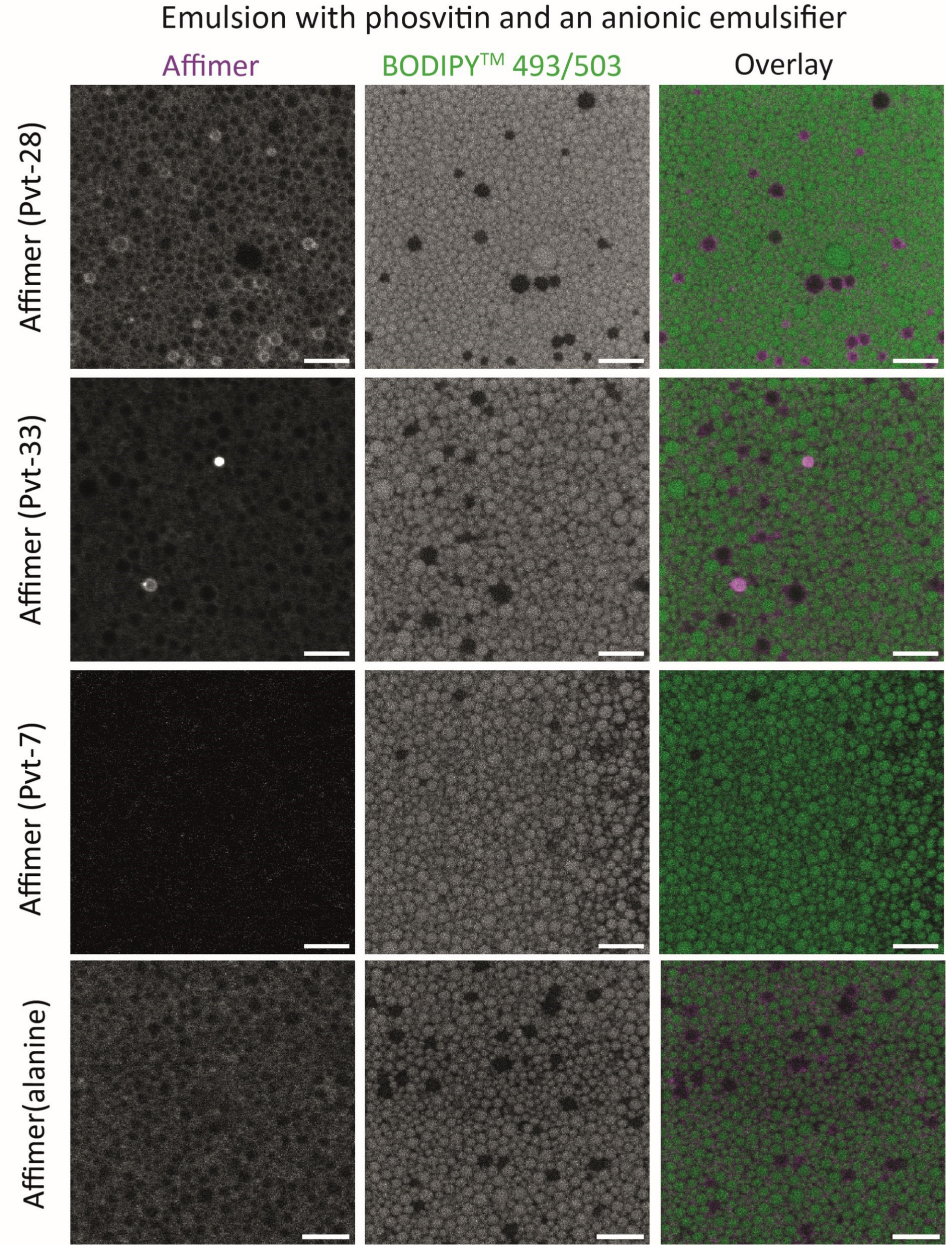

Supplementary Figure 4.3. Comparing the specificity of Affimers in CLSM images of emulsion (pH 6.6) containing SDS (anionic emulsifier) and phosvitin stained with Cy5-conjugated Affimers and BODIPY 493/503: (from up to down) (Pvt-1), (Pvt-7), (Pvt-28), (Pvt-33) and (alanine). All phosvitin-binding affimers accumulated in the continuous phase of emulsions with SDS (anionic emulsifier), regardless of the presence of phosvitin. Scale bars in all panels are 5 μm.

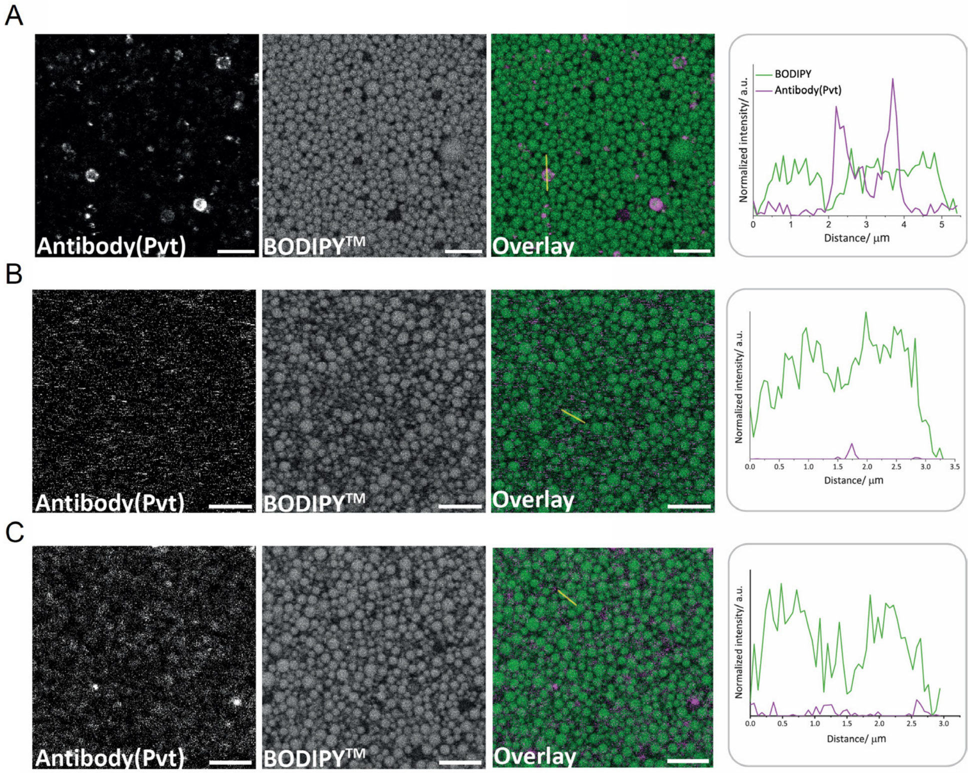

Supplementary Figure 4.4. Validating the specificity of phosvitin binding antibody in representative CLSM images of model emulsions stained with BODIPY and phosvitin antibody conjugated to Alexa Fluor 647 with an accompanying oil droplet line intensity profile. The line intensity profile of the highlighted yellow line in the overlay image is depicted in the right panels. In these profiles, green represents the intensity of oil droplets stained with BODIPY 493/503 dye, while magenta indicates the line intensity of antibodies at the interface. The emulsions stabilized with: (A) SDS (anionic emulsifier) and phosvitin. (B) SDS (anionic emulsifier), phosvitin-binding antibodies did not accumulate in the interfacial region of oil droplets in this control emulsion. (C) Tween20 (neutral emulsifier), phosvitin-binding antibodies did not accumulate in the interfacial region of oil droplets in this control emulsion as well. This suggesting that the monoclonal antibodies showed higher selectivity for phosvitin than affimers. Scale bars in all panels are 5 µm. Images were acquired with the same settings and are shown with the same brightness scale.

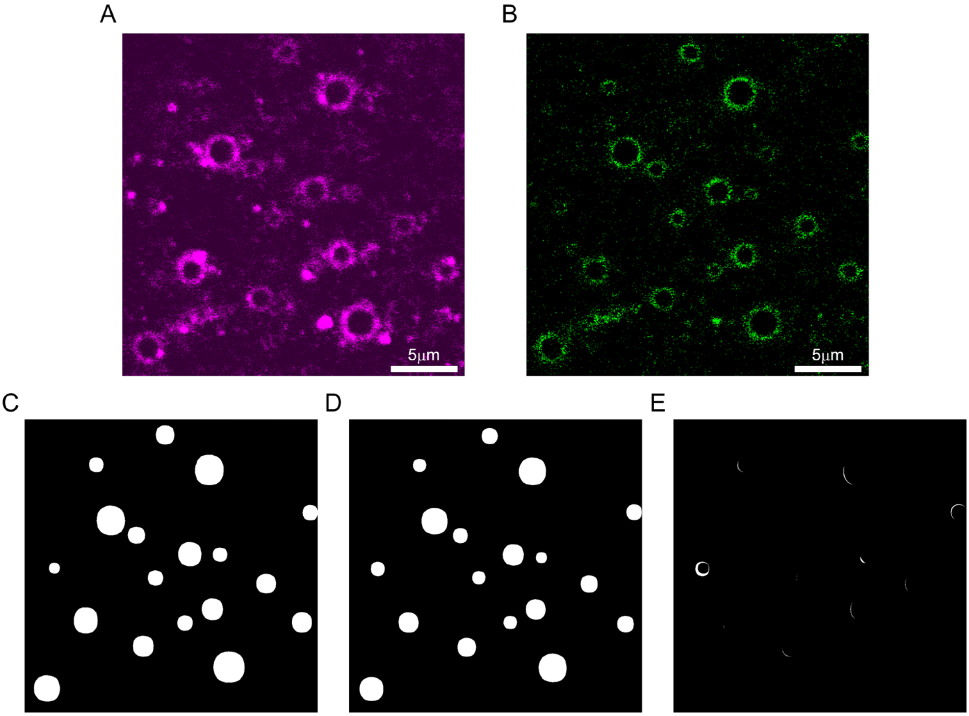

Supplementary Figure 4.5. Verification of the specificity of phosvitin antibody using fluorescent labeling. (A) Antibody targeting phosvitin, labeled with Alexa Fluor 647, visualized in the magenta channel. (B) Direct visualization of phosvitin covalently stained with FITC, shown in the green channel. Both A and B show that only a fraction of the oil droplet interfaces were covered with covalently and non-covalently labeled phosvitin (C) Segmentation mask of droplets derived from the magenta channel, detecting 18 droplets. (D) Segmentation mask based on the green channel, where 18 droplets were detected. (E) Resultant image post-subtraction of the phosvitin antibody mask (A) from the FITC-stained phosvitin mask (B) showed no droplets. The absence of droplets in the subtracted image confirms that droplets visualized in the magenta channel are also present in the green channel, indicating a match between droplets covered by phosvitin covalently stained with FITC and those recognized by the phosvitin antibody.

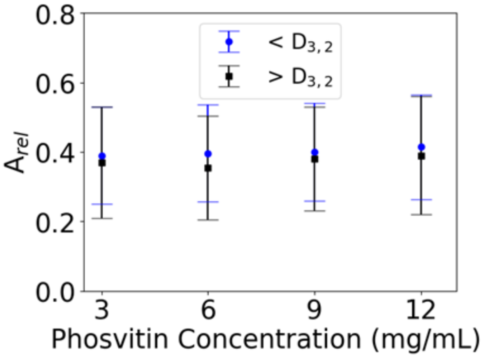

Supplementary Figure 4.6. Amplitude ratios for droplet size smaller or larger than $D_{3,2}$ for different formulated phosvitin concentrations.

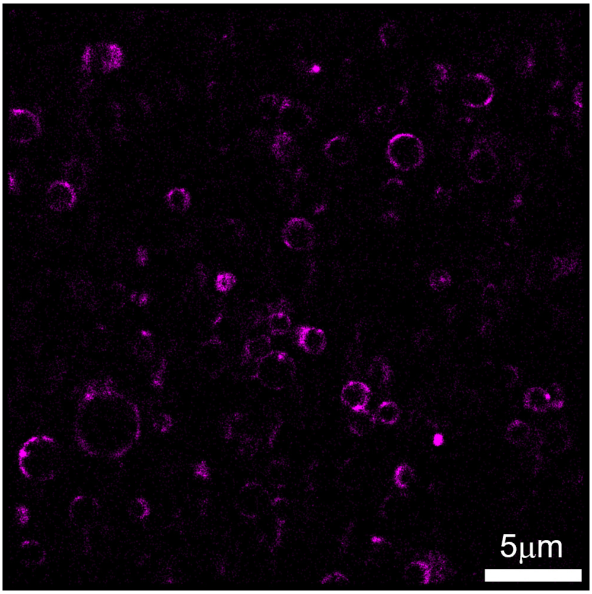

Supplementary Figure 4.7. STORM imaging of a non-sheared sample with a phosvitin concentration of 6 mg/mL, stored at room temperature for three days. The image identified 46 droplets covered by phosvitin, illustrating that the reduction in phosvitin coverage observed in the main study (Figure 4.6B) was specifically due to the low-shear treatment and not merely the aging of the sample.

5

Co-localization analysis of egg yolk proteins and formation of radicals at the interface of oil droplets in a mayonnaise model emulsion

Manuscript in preparation for submission:

Abbas Jabermoradi, Suyeon Yang, John P.M. van Duynhoven, Johannes Hohlbein

Abstract

The interfacial properties of oil droplets in food emulsions modulate both the physical and oxidative stability of lipids and proteins. Here, we analyze the co-localization behavior and spatial heterogeneity of two egg yolk proteins, phosvitin and apolipoprotein B (apoB), and oxidative protein radical formation at the oil droplet interfaces in model emulsions. We employed stochastic optical reconstruction microscopy (STORM) to achieve sub-100 nm localization precision of these proteins and their radicals. To assess the effects of oxidation, we employed a three-color detection strategy, including fluorescently labelled antibodies and the fluorescent spin trap CAMPO-AFDye647 as a marker for protein radicals. Relative-position-distribution analysis showed that phosvitin and apoB were heterogeneously distributed at the droplet surfaces. This heterogeneity was not droplet size dependent and not affected by protein oxidation. Small oil droplets were preferentially covered with phospholipids, which was reflected in lower formation of radicals. Co-localization analysis showed that apoB is more susceptible to radical formation than phosvitin. Our presented methodology provides us with a direct view of the distribution of protein emulsifiers at droplet surfaces and enables a better understanding and prediction of the physical and chemical stability of complex emulsions.

5.1 Introduction

Mayonnaise is a widely consumed food emulsion. The physical stability of mayonnaise can be largely attributed to egg yolk, which provides a range of high and low molecular weight emulsifiers. Egg yolk primarily consists of plasma (78%) and granules (22%)[1]. The plasma contains predominantly low-density lipoprotein (LDL) particles (85%) and some livetin (15%). The granules are a mixture of high-density lipoprotein (HDL) particles (70%), LDL (12%), phosvitin (16%), and ash (2%)[2]. Both LDL and HDL exhibit structural similarities despite having varying amounts of cholesterol, phospholipids and apoprotein, with apolipoprotein B (apoB) being the most abundant one[3]. In oil-in-water emulsions, adsorption of proteins and phospholipids from egg yolk is primarily driven by hydrophobic interactions[4] Specifically apoB's surface hydrophobicity and structural flexibility leads to strong interfacial adsorption[5]. Phosvitin, which is rich in phosphoserine clusters, also adsorbs at the oil/water interface, with an ability to bind ferric ions. In a neutral pH environment, phosvitin is a strong binder of ferric ions. However, under the acidic conditions of mayonnaise, its affinity for ferric ions decreases, which can then form a redox couple with ferrous ions[6]. These ferrous and ferric ions are potent catalysts for the radical formation of hydroperoxides[7]. These radicals can then generate lipid radicals that consume oxygen in their reaction to hydroperoxides. In this chain reaction, the formation of hydroperoxides is propagated by the redox cycling of iron ions introduced by phosvitin at the droplet interface[8].

In mayonnaise, protein oxidation at the interface can be induced by both oxidation of lipoprotein particles in the continuous phase[9] as well as lipid oxidation at the droplet interface[10]. The potential anti-oxidant role of proteins at droplet surfaces remains unclear. Similarly, the extent to which heterogeneity of droplet coverage by pro- and anti-oxidant proteins modulates lipid oxidation behavior is yet to be fully understood. Indications for a modulating role of surface heterogeneity are provided by indirect measurements in model emulsions and on reconstituted monolayers[11,12]. These indirect methods did, however, not allow for identification of the involved proteins.

In this work, we quantify the co-localization of specific egg yolk proteins, phosvitin and apolipoprotein B (apoB), and monitor the formation of protein radicals at the droplet surfaces in a mayonnaise model emulsion. This endeavor first necessitates the precise observation and quantification of protein co-localization. A particular challenge lies in discerning whether two protein targets co-localize on the same spot at the interface are part of separate entities. To address these limitations, the advent of super-resolution microscopy techniques has significantly elevated our capability to probe protein distributions at sub-100 nm resolution[13,14]. Single-molecule localization microscopy (SMLM) techniques such as photoactivated localization microscopy (PALM)[15,16], stochastic optical reconstruction microscopy (STORM)[17,18], point accumulation for imaging in nanoscale topography (PAINT)[19] and MINFLUX[20], have proven to be particularly potent, achieving spatial resolutions from tens of nanometers down to a few nanometers. At the sub-diffraction scale, the organization of proteins adsorbed at the interface of oil droplets has been investigated with molecular specificity using protein antibodies[21]. Here, we will rely on STORM, where individual fluorophores are stochastically activated, allowing image acquisition of isolated emission events[22]. These events gathered over 10,000 frames, can then be localized using computational fitting routines or a phasor-based method[23,24], thereby determining the position of single molecules with nanometer precision. These localizations are subsequently used to construct a super-resolved image, offering an approximately 10-fold improvement in spatial resolution in comparison to traditional, diffraction-limited images. Hence, STORM images, essentially constructed from a list of molecular coordinates, offer unique opportunities to quantitatively analyze the spatial distribution of proteins at the interface of oil droplets in food emulsions.

To co-localize different proteins and protein radicals, we will deploy multi-color fluorescence microscopy. Traditional co-localization methodologies hinge on the intensity correlation analysis of signals emitted in two or more channels, often separated by different fluorescence emission wavelengths of the labels[25,26]. These methodologies are commonly known as pixel-based methods. When it comes to analyzing STORM data, the intensity correlation-based methods for co-localization analysis are compromised by a potential loss of information during image reconstruction namely binning as the user's choice of binning size directly affects the spatial resolution of the data. As a consequence, variations in binning sizes can result in different estimates of co-localization for the same sample, as they alter the area of overlap between the analyzed entities[27]. Another implementation of pixel based methods for co-localization analysis are object-based methods[28]. In this context, an 'object' refers to either a molecule or a patch of molecules. These objects are identified and segmented, and their spatial distribution and overlap are then analyzed[28–30]. One of the object-based methods is the nearest-neighbor distance method, which calculates the distance between the centers of mass of two objects. If the distance is less than a predefined threshold, the objects are considered to be co-localized. The object-based methods are independent of object size. Thus, particularly suited for analyzing objects smaller than the diffraction limit of light, such as those obtained in single-molecule localization microscopy. Here, we will adopt an object-based method that only relies on coordinates of localizations obtained from super-resolution microscopy and their respective localization precisions (**Supplementary Note 5.1**) to analyze the spatial arrangement of targets at the droplets interface[31].

We will examine protein (co-) localization in a model emulsion stabilized by egg yolk. We will deploy a primary antibody conjugated with Alexa 488 to localize phosvitin at the oil-water interface (**Figure 5.1A**). Similarly, localization of apoB will be achieved using a secondary antibody conjugated with Alexa 555 (**Figure 5.1B**). To localize protein radicals in oxidizing emulsions, we will employ the CAMPO-AFDye647 spin trap (**Figure 5.1C**). This compound is composed of the fluorophore AFDye 647 and CAMPO, a derivative of the water-soluble DMPO spin trap[10]. Using multi-color detection, we aim to discern the spatial relationship between phosvitin, apoB, and oxidized proteins to infer their relative susceptibilities to lipid radical attacks at the interface.

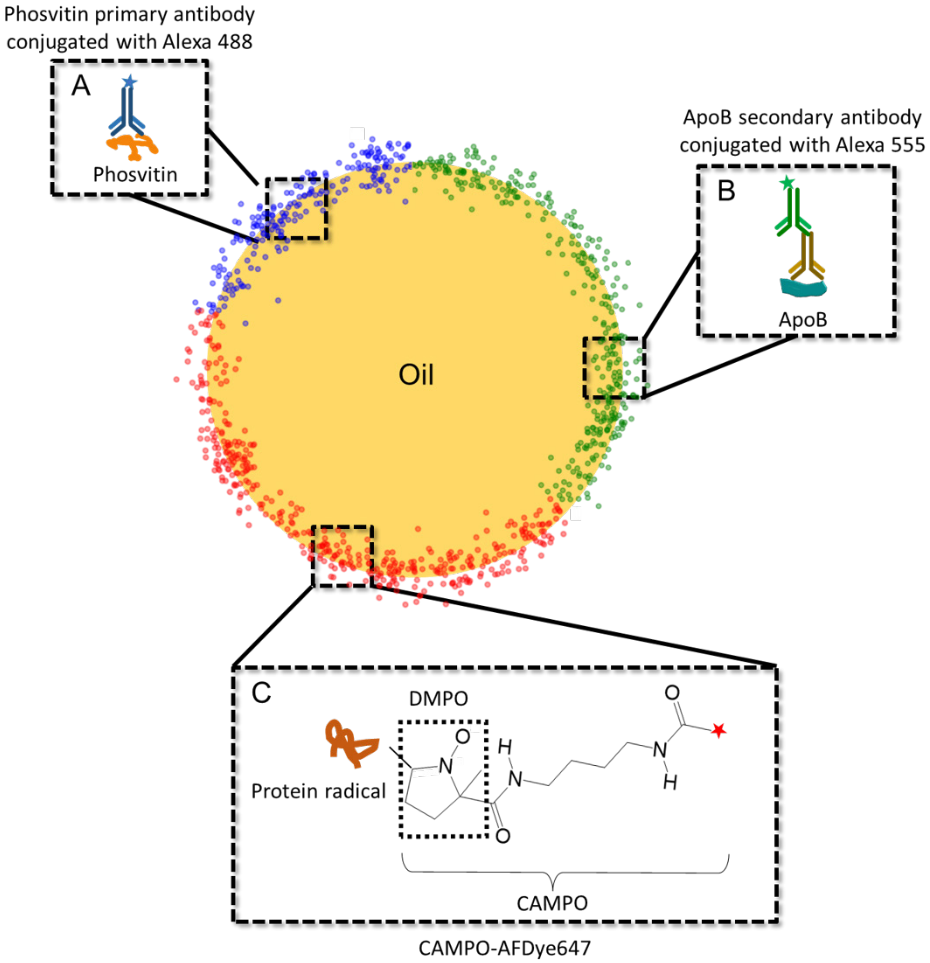

Figure 5.1. Schematic illustration of our approach to examine protein localization at the oil-water interface of a mayonnaise model emulsion stabilized by egg yolk. Phosvitin (A), apoB (B), and trapped protein radicals (C) are schematically presented.

5.2 Materials and methods

5.2.1 Preparation of oil-water model emulsion using egg yolk

An acetate buffer solution (0.05 M, pH 3.8) was prepared by dissolving sodium acetate (0.6 g) and acetic acid (2.6 g) in one liter of ultrapure water. To prepare the continuous water phase, a 1 w/w% solution of egg yolk was prepared using the buffer. Next, soybean oil was stripped of impurities and lipid-soluble anti-oxidants using alumina powder[32]. The procedure involved mixing the oil and powder in a 2:1 volume ratio in Falcon tubes and then agitating the tubes for 24 hours. The resulting mixture was centrifuged at 2,000 g for 20 min. The collected oil underwent a subsequent round of centrifugation under identical conditions to ensure the complete removal of alumina powder. To generate a coarse emulsion, we used 15 wt.% of stripped soybean oil in the continuous phase. Mixing was followed by homogenization at 11,000 rpm for 2 min using an Ultra-Turrax IKA T18 basic rotor-stator homogenizer (Germany). Finally, the coarse emulsion was subjected to further processing using a high-pressure homogenizer (HPH) at 70 bar (Niro Soavi – PandaPLUS 2000, GEA). This procedure was repeated for a total of ten cycles, resulting in a fine emulsion.

5.2.2 Stochastic optical reconstruction microscopy

For the acquisition of STORM data, we used the experimental setup previously described[13]. Briefly, we utilized a fiber-coupled laser engine (Omicron, Germany) to introduce the laser beam into the excitation path of the microscope. The laser beam was collimated using a 60 mm achromatic lens (AC254-060-A-ML, Thorlabs) and directed by a kinematic mirror (BBE1-E02, Thorlabs) into a top hat beam shaper from Asphericon GmbH. Subsequently, the beam was focused through a 150 mm lens (AC508-150-A-ML, Thorlabs) into the back focal plane of a 100x oil immersion objective (NA = 1.45, Nikon) after passing through a polychroic mirror (ZT405/488/561/640rpcv2, Chroma). The emitted signal from the sample was collected using the same objective and transmitted through an emission filter (ZET405/488/561/640m-TRF, Chroma). The collected signal was then reflected by a kinematic mirror and focused through a tube lens (MXA20696, Nikon) onto the focal plane of the first lens (AC508-100-A-ML, Thorlabs) within a 4f imaging system. A mirror positioned in the Fourier plane of the 4f imaging system directed the light towards a deformable mirror (DMP40/M – P01, Thorlabs). The deformable mirror was modulated to correct for the aberrations induced by the microscope itself. The light then passed through a second lens (AC508-100-A-ML, Thorlabs) before being focused onto a sCMOS camera (Prime 95B, Photometrics) with an effective pixel size of 112 nm. During the measurement, the deformable mirror was modulated again to compensate for the aberrations introduced by the sample. These deformable corrections were calculated and applied using the REALM method[33].

5.2.3 Sample preparation and image acquisition

Phosvitin was labeled using a primary antibody conjugated with Alexa 488 (sc-46681, Santa Cruz Biotechnology). For apoB labeling, 22.6 µL of the primary human apoB mouse antibody was diluted from an 8.85 mg/mL stock solution (MBS530791, MyBioSource) in PBS buffer to a 1 mL final volume, achieving a concentration of 200 µg/mL. Then, an anti-mouse secondary antibody conjugated to Alexa 555 (ab150118, Abcam) was diluted tenfold from a 2 mg/mL stock solution and added to the same solution. The mixture was incubated at room temperature for an hour. For localizing protein radicals at the interface, CAMPO conjugated to AFDye 647 (SyMO-Chem B.V.) was used. This CAMPO-AFDye 647 spin trap, with a molecular weight of 1068.30 g/mol, was dissolved in dimethyl sulfoxide (DMSO) to prepare a 0.01 g/L stock solution. The staining procedure started with targeting the phosvitin. The phosvitin primary antibody conjugated with Alexa-488 stock solution was diluted 50-fold in PBS buffer, and 10% v/v of the resultant solution was added to 400 µL of the egg yolk model emulsion. After incubating at room temperature for 15 min, the apoB staining process was performed. The secondary antibody conjugated with Alexa 555 was then diluted 50-fold in PBS buffer (final concentration 4 µg/mL), and 10% v/v of this diluted solution was added to the phosvitin-stained egg yolk model emulsion. Protein radicals were then trapped with CAMPO-AFDye647 stock solution added to the continuous phase samples and mayonnaise to attain a final concentration of 1 µM. The labeled model emulsion was centrifuged at 4,000 g for 5 min. The creamy top layer was harvested for imaging to prevent droplet diffusion in the water phase during image acquisition. Carefully, 2 µL of this cream phase was pipetted into a well in a silicone gasket (Grace Bio-Labs). To enhance the frequency of fluorophore blinking events, 25 µL of STORM buffer containing 50 mM TRIS pH 8, 10 mM NaCl, 10% glucose, 140 mM 2-mercaptoethanol, 68 µg/mL catalase, and 200 µg/mL glucose oxidase was added[34]. Lastly, a second cover glass was placed on the well to prevent new oxygen from infiltrating the sample. For image acquisition, we employed three different laser wavelengths for sample excitation within a 20 µm by 20 µm field of view. Initially, 10,000 frames were captured using a 488 nm laser at 15 mW to localize the phosvitin. Subsequently, 10,000 frames were acquired using a 561 nm laser with 20 mW power to localize the apoB. Finally, 10,000 frames were captured using a 648 nm laser at 15 mW to localize the trapped CAMPO-AFDye647.

5.2.4 Image visualization co-localization analysis

To analyze the raw data, we first removed the constant fluorescence background using a temporal median filter available at GitHub (**https://github.com/HohlbeinLab/FTM2**)[13]. Next, we used an integrated Gaussian method with maximum likelihood estimation (MLE)[35] implemented in ThunderSTORM[23], a software plugin for ImageJ/Fiji[36], to determine the positions of the fluorophores with sub-pixel localization precision. For localization in

ThunderSTORM, we used a β-spline wavelet filter with order 2 and scale 3, a fitting radius of 3 pixels, and an initial sigma of 1.6 pixels. After performing the localization, we applied 2D cross-correlation drift correction with ThunderSTORM settings of 10 bins and 10x magnification. The localizations were then visualized using the "average shifted histogram" option, with the magnification set to 5 and the labeled protein phosvitin represented in magenta.

To determine the positions of individual droplets within the field of view, we first trained a model on multiple datasets using QuPath[37] before using StarDist segmentation[38,39] to determine the positions of individual droplets within the field of view. The adsorption of emulsifiers in relation to droplet size was assessed by computing the Sauter mean diameter, $D_{3,2}$[40], for all samples within each of the three detection channels. To specify the width of the droplet size distribution, we calculated the standard deviation over all diameters. Next, for each droplet, we extracted all localizations and performed relative position distribution (RPD) analysis[41] to quantify the spatial heterogeneity of proteins at the interface of individual droplets as described in **Chapter 3**. Further, using a coordinate-based co-localization method on each droplet localization[31], we analyzed the spatial relations between phosvitin, apoB, and the protein radicals. Since we used three different detection channels in our multi-color experiment, chromatic aberration was observed. We initially based our segmentation of the STORM data on the green channel. As these droplets appear in three different channels, however, circles were fitted over the individual droplets in all channels independently. Then, utilizing the green channel as a reference and we compared the centers of droplets from the red and blue channels to obtain transformation matrices. These matrices were subsequently applied to the respective channels, enabling positional adjustments to compensate the chromatic aberration.

5.2.5 Computational analysis of emulsifier surface coverage

A Python script was written to analyze the coverage of adsorbed emulsifiers on segmented droplets. The program computes the fraction of each droplet's circumference covered by an emulsifier. To model the droplet's circumference, first, the radius and the center of the droplets were determined by fitting a circle to all localizations. Then, the droplet was divided into segments, each representing an arc of 0.72°, effectively slicing the droplet into $N = 500$ segments. Each array element corresponds to a discrete segment of the droplet's ring, serving as a marker that can be flagged when emulsifiers are localized within that segment. For each localization of each emulsifier, its position was projected onto the droplet's circumference. The occupied regions were subsequently plotted and overlaps between phosvitin and apoB channels were explicitly marked.

5.2.6 Simulating co-localization analysis based on single emitters

The simulation models a geometrically well-defined distribution of two sets of proteins, each representing a different detection channel (green and magenta), located at the interface of oil-water droplets. We distributed ten proteins in the green channel centered at 0° in a polar coordinate system with a spread of the proteins determined by a standard deviation of 2.8° (π/64 radians) on the droplet interface. The simulated droplet had a radius of 500 nm. Similarly, the initial positions of proteins for the magenta channel were generated with their initial distribution centered at -22.5°. For each protein 50 localizations were simulated by adding a normally distributed distance with a standard deviation of 30 nm. The standard deviation represents here a convolution of the distribution of targeted proteins and the experimentally achievable localization precision and accuracy. This process resulted in a dataset of 500 localizations for each channel. The position of the green distribution marked a reference point at 0°. The magenta distribution was initially positioned to the right of the green distribution at -22.5° before being gradually rotated to sweep over the green distribution with a step size of π/32 radians (≈ 5.6°) until reaching + 22.5°. To test a scenario in which localizations exhibit different precision, we simulated distribution of localizations in the second channel with a 20 nm standard deviation.

5.2.7 Statistical analysis

The Shapiro-Wilk test was employed to assess the normality of the distribution of co-localization indices. For non-normal distributions, the Wilcoxon signed-rank test, a non-parametric method, was utilized to test for differences between populations[42]. The level of significance was set at 0.05. The statistical analysis was conducted using the scipy.stats module in Python.

5.3 Results and discussion

5.3.1 Simultaneous detection of phosvitin, apoB, and protein radicals at droplet surfaces using multicolour STORM

We prepared a model emulsion of mayonnaise using egg yolk to introduce both phosvitin and apoB as protein emulsifiers. Phosvitin was localized using a primary antibody conjugated to Alexa Fluor 488 and visualized in the blue channel (**Figure 5.2A**). Further, apoB was localized using a primary mouse antibody against apoB and a secondary anti-mouse antibody conjugated to Alexa Fluor 555, depicted in the green channel (**Figure 5.2A**). The STORM images indicate that both phosvitin and apoB are present at the oil droplet interface but are not uniformly distributed. Further, to ensure the specificity of our oxidative marker, we conducted a control experiment using fresh emulsion samples. We applied the CAMPO-AFDye647 spin trap to these samples and, as expected, observed no signal in the CAMPO channel, confirming the absence of radical formation in the fresh emulsion. Additionally, to investigate the impact of oxidation on the interfacial properties of oil droplets, we subjected a freshly prepared emulsion to incubation at 30°C for a duration of five days. Notably, the emulsion remained physically stable throughout this period (**Figure 5.2B**). In addition to the antibodies against phosvitin and apoB, we used CAMPO-AFDye647 to localize protein radicals visualized in the red channel (**Figure 5.2B**). For visual examination of co-localization, we further plotted the fields of view as a composite featuring pairs of channels: phosvitin/apoB, apoB/protein radical, and phosvitin/protein radical (**Figure 5.2C**).

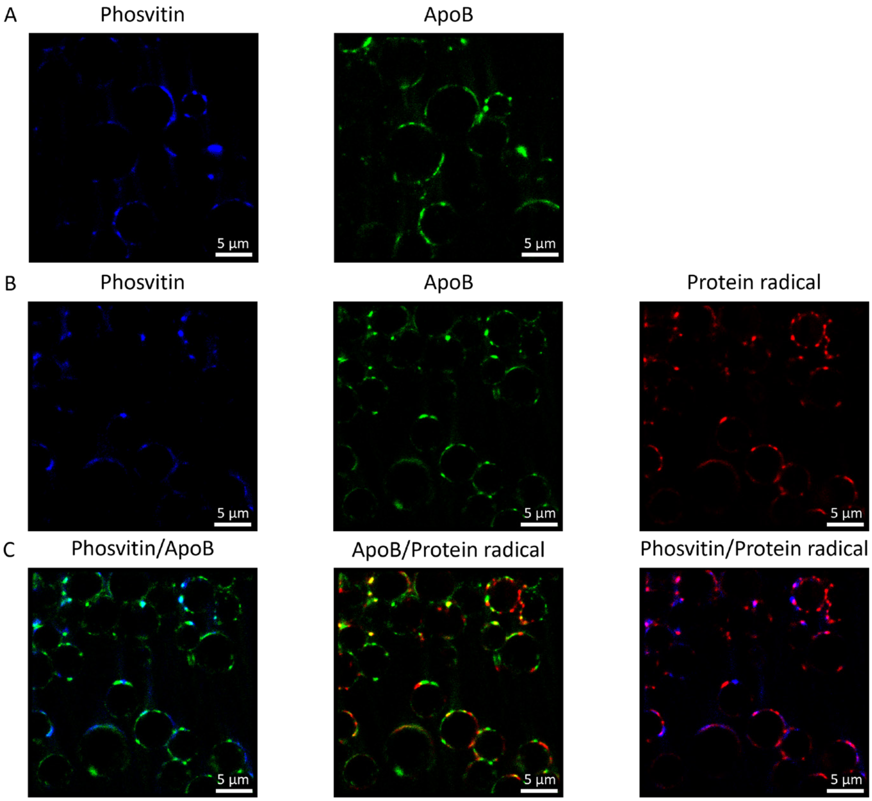

Figure 5.2. Comparative STORM image analysis between fresh and oxidized emulsions. (A) In a fresh emulsion, the localization of phosvitin and apoB is distinctly visualized in the blue and green channels respectively, facilitated by a primary antibody conjugated with Alexa Fluor 488 for phosvitin, and a secondary antibody conjugated to Alexa Fluor 555 for apoB. We note that protein radical detection using CAMPO-AFDye647 did not lead to any detectable signal in the red channel. (B) Three-colour detection elucidating the spatial arrangement of phosvitin, apoB, and protein radicals in an oxidized emulsion. Phosvitin is visualized in the blue channel, and apoB in the green channel, while detection of protein radicals in the red channel is enabled by spin trapping with CAMPO- AFDye647. (C) Composite images of the FOV shown in (B) reveal paired channel overlaps among phosvitin/apoB (overlap in cyan), apoB/protein radical (overlap in yellow), and phosvitin/protein radical (overlap in magenta).

5.3.2 Inter-droplet heterogeneity of protein surface coverage

We first focused on analyzing the localization of phosvitin and apoB at the droplet interface in respect to their respective surface coverage. We projected the localizations of phosvitin and apoB onto the droplet circumference (**Figure 5.3A** for apoB; **Figure 5.3B** for phosvitin). The union coverage of apoB and phosvitin was illustrated in dark cyan, corresponding to the part of the interface that is covered by phosvitin, or apoB (**Figure 5.3C**). Furthermore, uncolored regions indicate the absence of both phosvitin and apoB. The long-term stability of such small droplets not fully covered by proteins indicates coverage by another emulsifier. Given our findings in **Chapter 4** showing that low molecular weight emulsifiers preferentially adsorb at smaller droplets, phospholipids from the egg yolk emerge as a likely candidate. Regions not covered by phosvitin or apoB will henceforth be referred to as phospholipid covered. The approach to quantify droplet surface coverage allowed the construction of a droplet size distribution histogram (**Figure 5.3D**). In this figure, we plotted a histogram representing the size distribution of droplets, with a with a mean Sauter diameter, $D_{3,2}$, of 2.36 µm and a size distribution width of +/- 0.67 µm. For each bin, we calculated the average coverage of either proteins or phospholipids at the droplet interface and presented these averages using a normalized bar plot. As the droplet size increases, the average coverage with proteins increases. We attribute this shift in droplet surface coverage to the mechanism at play during high-pressure homogenization (HPH), which favors coverage of small droplets by a low molecular weight surfactant over coverage by proteins (**Chapter 4**). We utilized the same droplet distribution and evaluated the average coverage with protein radicals (**Figure 5.3E**). Although smaller droplets are expected to undergo more oxidation due to their higher interfacial area per droplet volume with the water phase, our results indicate that larger droplets have a higher coverage with protein radicals. Our current data do not allow for a conclusion whether this to a pro- or anti-oxidant effect. The most straightforward explanation is however scavenging of lipid radicals formed within the droplets. This effect will be more pronounced for larger droplets which are more abundantly covered with proteins than the smaller ones. This finding suggests that droplet size is not the sole factor influencing lipid oxidation rates; the relative abundance of proteins adsorbed at the interface must also be considered. Additionally, we analyzed the correlation between the co-coverage of phosvitin/apoB and the radius of droplets using Pearson correlation. We obtained a low correlation coefficient, indicating that our data is insufficient to draw meaningful conclusions about this relationship (**Supplementary Figure 5.1**).

5.3.3 Intra-droplet surface heterogeneity

To quantify the protein distribution at the interface, we employed the relative peak distribution (RPD) analysis as we described in **Chapter 3**. Specifically, we used the relative peak amplitudes

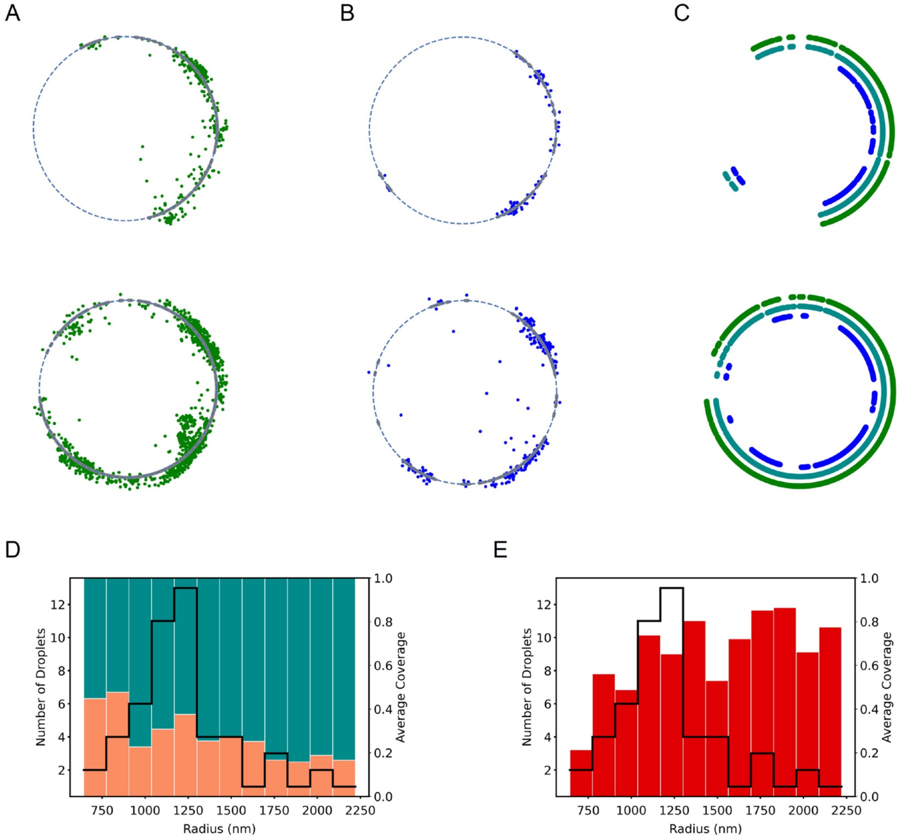

Figure 5.3. Quantitative analysis of phospholipid, apoB and phosvitin coverage on oil droplets. (A-C) Experimental data from two single droplets (diameter 1.2 µm and 1.8 µm, respectively). (A) ApoB localizations (shown as green dots) projected onto the circumference of the droplets (shown as gray areas at the dashed interface), indicating 44% and 83% coverage, respectively. (B) Corresponding projection for phosvitin (shown as blue dots), indicating 25% and 44% coverage, respectively. (C) Co-coverage analysis demonstrates correlated apoB and phosvitin localizations, with 23% and 40% co-localized coverage in the respective channels. Non-co-localized coverage accounts for 21% apoB and 0% phosvitin in the first droplet, and 42% apoB and 3% phosvitin in the second. Color key: green for apoB, blue for phosvitin, cyan for co-coverage regions, empty regions are assumed to be covered by phospholipids (see text). (D) Histograms display droplet size distribution (black line) alongside corresponding apparent phospholipid coverage (orange) and total protein coverage (turquoise), normalized to 1. (E) Histograms display droplet size distribution (black line) alongside corresponding protein radical coverage (red).

A_{rel}, defined as the ratio of the amplitude of the first peak to the sum of the first and the second peak. For the phosvitin channel, we averaged RPDs over all droplets and obtained a value of A_{rel} = 0.56 +/- 0.17, indicating a heterogeneous distribution of phosvitin at the interface (**Figure 5.4A** – blue histogram). Likewise, the A_{rel} for the apoB was calculated to be 0.51 +/- 0.14, also indicative for a heterogeneous distribution of apoB at the interface (**Figure 5.4A** –

green histogram). To elucidate the potential effects of oxidation on protein distribution at the oil droplet interface, we calculated A_{rel} for phosvitin, apoB, and protein radicals in the oxidized emulsion. The A_{rel} value for phosvitin (**Figure 5.4B** – blue histogram) was found to be 0.64+/- 0.15, and for apoB (**Figure 5.4B** – green histogram) 0.58+/- 0.15 both displaying a similar level of heterogeneity as observed in the untreated, fresh sample considering the uncertainty. These values collectively suggest that the distribution of phosvitin and apoB at the interface remains consistent over the course of incubation and oxidation. Further, we extended our analysis to the distribution of protein radicals at the interface. The A_{rel} for protein radicals (**Figure 5.4B** – red histogram) was calculated to be 0.62+/- 0.14, aligned with our expectations of heterogeneous distribution, given the expected associated localizations of protein radicals with phosvitin and apoB.

.

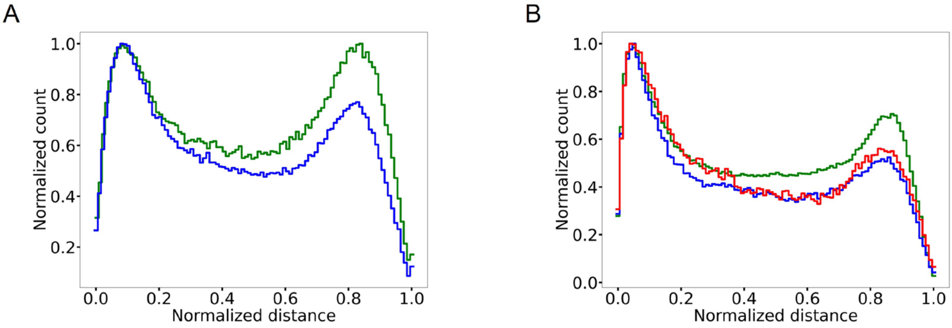

Figure 5.4. Comparative analysis of protein emulsifiers phosvitin and apoB at oil droplet interfaces in both fresh and oxidized model emulsions stabilized by egg yolk. (A) Graph of Relative Positional Distribution (RPD) histogram for phosvitin (blue) and apoB (green) in fresh emulsion. A_{rel} values of 0.56 for phosvitin and 0.51 for apoB indicate heterogeneous distributions at the interface. (B) Histograms representing the distribution of apoB (green), phosvitin (blue), and protein radicals (red). The A_{rel} values for phosvitin (0.62), apoB (0.58), and protein radicals (0.64) indicate heterogeneous distributions.

5.3.4 Coordinate-based co-localization index methodology at oil droplet interfaces

To analyze the spatial arrangements commonly observed in food emulsions, we performed simulations involving two-channel localizations on a ring-like structure, representing the interface of an oil droplet when visualizing emulsifiers. We assessed the co-localization index (**Supplementary note 5.1**) using two sets of proteins by gradually rotating the second channel (represented in magenta) over the first channel (shown in green), thereby altering the overlapping area between the two channels. Both channels were simulated with 500 localizations per channel as explained in the material and methods section (**Figure 5.5A**). Initially, starting without any overlap, the second channel was rotated by π/32 radians per step, gradually increasing the overlap with the first channel. As expected, the co-localization index increased with the growing overlap, approaching 1 at a 0° rotation due to the complete overlap of localizations (**Figure 5.5B**), and then decreasing again, nearing zero at a +22.5° rotation as the overlap diminished. A subsequent simulation retained the same number of localizations but used a decreased standard deviation of 20 nm for the magenta channel to feature two differently sized objects on the ring structure (**Figure 5.5C**). Starting with no overlap between the two channels, we noted that as the overlap increased, the co-localization index for the magenta channel reached 1.6, exceeding the value of 1 as the tighter localized localizations in the magenta channel fall entirely within the localizations simulated for the green channel. For the green channel calculated against the magenta channel, however, the co-localization index was only 0.5, as the localizations in the magenta channel did not fully cover those in the green channel (**Figure 5.5D**). Upon rotating the magenta channel, there was a sharper decrease in its co-localization index compared to the more gradual decline for the green channel. This demonstrates that even if the structure and number of localizations are consistent, variances in the distributions of localizations can significantly influence the co-localization indices across channels.

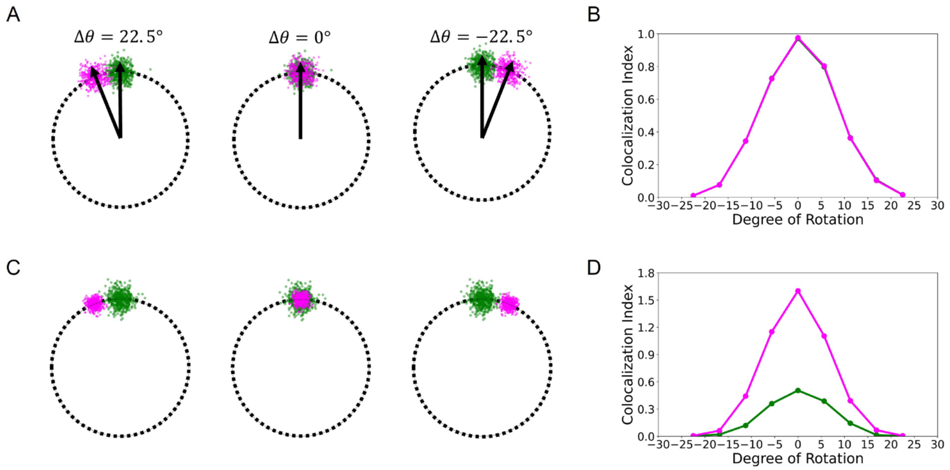

.

Figure 5.5. Simulations of emulsifiers in different channels at an oil droplet interface with a radius of 500 nm to assess the co-localization index using a coordinate-based method. (A) Simulation with both channels (green and magenta) having identical settings: 500 localizations and 50 nm localization precision. In this scenario, the magenta channel rotates from 22.5° to + 22.5°. (B) The co-localization index calculated as a function of the sweeping angle of the magenta over the green channel. (C) Simulation with the same number of localizations but a lower localization precision of 25 nm for the magenta channel. (D) Co-localization index derived from the simulation in part (C) showing that if the if one distribution of proteins is engulfed by another one, the co-localization index can exceed 1.

Additionally, we conducted a separate simulation to explore the impact of varying the number of localizations per protein in the channels (**Supplementary Figure 5.2**). For this, we halved the number of localizations in the magenta channel while keeping all other settings identical to our initial conditions. Interestingly, the results remained consistent with our initial findings, demonstrating that the number of localizations per protein (distribution) at the interface does not impact the co-localization calculation. We then applied the coordinate-based co-localization index method to assess the spatial relationship between phosvitin and apoB channels in oxidized emulsion (**Supplementary Figure 5.3**). The swarm plots indicates that there is no clear trend concerning the co-localization indices across the entire set of droplets. The degree of co-localization varies from droplet to droplet, ranging from none to full co-localization, and even co-clustering in some instances. This variability in the co-localization indices indicates random adsorption of phosvitin and apoB. As also inferred in **Chapter 4**, this randomness stems from the use of HPH for emulsion production, which leads to the formation of droplets where emulsifier adsorption is kinetically driven. The Shapiro-Wilk test, applied to the co-localization indices for apoB and phosvitin, confirmed their non-normal distributions. Further analysis revealed median co-localization indices of 0.38 for apoB/phosvitin and 0.51 for phosvitin/apoB. Since the concentrations of phosvitin and apoB are different, we refrained from testing whether the distributions of co-localization indices of the apoB/phosvitin and phosvitin/apoB are different. For the co-localization of apoB and phosvitin with radical formation via the CAMPO-AFDye647 channel we are, however, not limited by this complication. Whenever there is an apoB or phosvitin present, a radical can be formed, and we can test whether the distributions of the co-localization indices of these proteins with the CAMPO-AFDye647 and vice versa are different. Analysis of the co-localization indices for apoB/CAMPO-AFDye647 and CAMPO-AFDye647/apoB revealed median co-localization indices of 0.24 and 0.32, respectively (**Figures 5.6A**). In contrast, the median co-localization indices for phosvitin/CAMPO-AFDye647 CAMPO-AFDye647/phosvitin are 0.20 and 0.22, respectively (**Figures 5.6B**. These co-localization indices showed a non-normal distribution according to the Shapiro-Wilk normality test in all four distributions of co-localization indices depicted in Figure 6. We therefore used the Wilcoxon signed-rank metric to test for differences between each co-localization pair of apoB and CAMPO-AFDye647 and phosvitin and CAMPO-AFDye647. For apoB/CAMPO-AFDye647, the Wilcoxon test yielded a p-value of 0.0083, indicating a statistically significant association beyond random chance at the set threshold of 0.05. Conversely, phosvitin/CAMPO-AFDye647 produced a p-value of 0.884, suggesting a random association at the interface. On the one hand, phosvitin has a weak affinity for pro-oxidant iron ions under the acidic conditions of the model emulsion and is thus close to lipid radical formation at the droplet surfaces. On the other hand, phosvitin primarily consists of phosphoserine residues, which are less prone to scavenge lipid radicals compared to the amino acids found in apoB[43], thus explaining the stronger association of apoB with protein radical formation. We note that the sizes of phosvitin and apoB patches at the droplet surfaces are well with in the distance that lipid peroxide radicals can travel in the aqueous continuous phase[44].

We note that our measurements were conducted using the HILO mode of the microscope. Due to the inclined angle of light illumination, certain angular sections of the droplets might receive more excitation light than others. This can lead to an uneven distribution of detected signals across the droplet's surface. To assess this potential source of bias, we performed a comparative analysis between the angular distribution of protein localizations observed experimentally and those from a homogenized simulated droplet. The results substantiate that our experimental data indeed show a bias of detection at specific angles (**Supplementary Figure 5.4**). This might affect the accuracy of our co-localization analysis between experimental data in different channels. However, the co-localization method analysis employed is independent of localization density, which may mitigate potential concerns regarding the observed bias. Nonetheless, follow up studies should explore alternative microscopy modalities by using rotating focused laser beams azimuthally in the back focal plane of the objective lens[45].

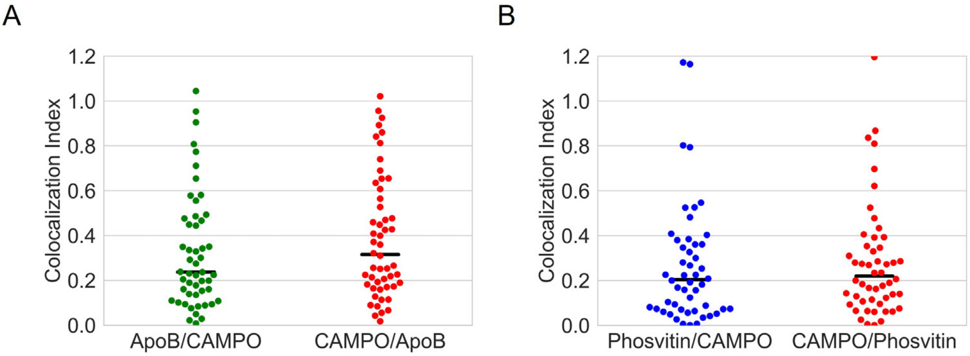

Figure 5.6. Evaluation of spatial relationships and co-localization indices among phosvitin/ apoB, and protein radicals measured via CAMPO-AFDye 647 detection at individual droplet interfaces in oxidized emulsions as presented in Figure 5.2. (A) Co-localization indices between apoB/CAMPO-AFDye 647, and CAMPO-AFDye 647/apoB with median values of 0.24, and 0.32, respectively. (B) Co-localization indices between phosvitin/ CAMPO-AFDye 647, and CAMPO-AFDye 647/phosvitin with median values of 0.20, and 0.22, respectively.

5.4 Conclusions

In this study, we employed STORM in combination with specific antibodies to unveil the spatial distribution and co-localization of two egg yolk proteins, phosvitin, and apoB, at the oil droplet interfaces of a model emulsion for mayonnaise. At the inter-droplet level these proteins preferentially cover larger droplets, with smaller ones assumed to be covered primarily by phospholipids. This droplet size dependency can be attributed to the dynamics of droplet surface stabilization during high-pressure homogenization. Further, using RPD analysis revealed a heterogeneous distribution for both apoB and phosvitin. Applying the coordinate-based co-localization index allowed us to quantify the co-localization of these proteins. The use of STORM with the fluorescent spin trap CAMPO-AfDye647 facilitated the co-localization of proteins and protein radicals likely formed by scavenging lipid radicals near the droplet interface. We observed that pro-oxidant, iron-binding phosvitin was less prone to radical formation compared to apoB.

References

1 Anton, M. Egg Yolk: Structures, Functionalities and Processes: Egg Yolk: Structures, Functionalities and Processes. *J. Sci. Food Agric.* **2013**, *93* (12), 2871–2880. https://doi.org/10.1002/jsfa.6247.

2 McCully, K. A.; Mok, C.-C.; Common, R. H. PAPER ELEGTROPHORETIC CHARACTERIZATION OF PROTEINS AND LIPOPROTEINS OF HEN'S EGG YOLK. *Can. J. Biochem. Physiol.* **1962**, *40* (7), 937–952. https://doi.org/10.1139/o62-105.

3 Jolivet, P.; Boulard, C.; Beaumal, V.; Chardot, T.; Anton, M. Protein Components of Low-Density Lipoproteins Purified from Hen Egg Yolk. *J. Agric. Food Chem.* **2006**, *54* (12), 4424–4429. https://doi.org/10.1021/jf0531398.

4 Bergenståhl, B.; Claesson, P. M. Surface Forces in Emulsions; Marcel Dekker, 1997; pp 57–109.

5 Mine, Y. Emulsifying Characterization of Hens Egg Yolk Proteins in Oil-in-Water Emulsions. *Food Hydrocolloids* **1998**, *12* (4), 409–415. https://doi.org/10.1016/S0268-005X(98)00054-X.

6 Laguerre, M.; Tenon, M.; Bily, A.; Birtić, S. Toward a Spatiotemporal Model of Oxidation in Lipid Dispersions: A Hypothesis-Driven Review. *European Journal of Lipid Science and Technology* **2020**, *122* (3), 1900209. https://doi.org/10.1002/ejlt.201900209.

7 Schaich, K. M. Thinking Outside the Classical Chain Reaction Box of Lipid Oxidation. *Lipid Technology* **2012**, *24* (3), 55–58. https://doi.org/10.1002/lite.201200170.

8 Berton, C.; Ropers, M.-H.; Guibert, D.; Solé, V.; Genot, C. Modifications of Interfacial Proteins in Oil-in-Water Emulsions Prior to and During Lipid Oxidation. *J. Agric. Food Chem.* **2012**, *60* (35), 8659–8671. https://doi.org/10.1021/jf300490w.

9 Aidyraliev, R. K.; Azizova, O. A.; Vakhrusheva, T. V.; Lopukhin, Yu. M.; Mirrakhimov, M. M. Autofluorescence of Low-Density Lipoproteins Modified as a Result of Autooxidation. *Bull Exp Biol Med* **2006**, *142* (4), 433–436. https://doi.org/10.1007/s10517-006-0385-8.

10 Yang, S.; Takeuchi, M.; Friedrich, H.; van Duynhoven, J. P. M.; Hohlbein, J. Unravelling Mechanisms of Protein and Lipid Oxidation in Mayonnaise at Multiple Length Scales. *Food Chemistry* **2023**, *402*, 134417. https://doi.org/10.1016/j.foodchem.2022.134417.

11 Berton, C.; Genot, C.; Guibert, D.; Ropers, M.-H. Effect of Lateral Heterogeneity in Mixed Surfactant-Stabilized Interfaces on the Oxidation of Unsaturated Lipids in Oil-in-Water Emulsions. *Journal of Colloid and Interface Science* **2012**, *377* (1), 244–250. https://doi.org/10.1016/j.jcis.2012.03.084.

12 Berton-Carabin, C.; Genot, C.; Gaillard, C.; Guibert, D.; Ropers, M. H. Design of Interfacial Films to Control Lipid Oxidation in Oil-in-Water Emulsions. *Food Hydrocolloids* **2013**, *33* (1), 99–105. https://doi.org/10.1016/j.foodhyd.2013.02.021.

13 *Enabling single-molecule localization microscopy in turbid food emulsions | Philosophical Transactions of the Royal Society A: Mathematical, Physical and Engineering Sciences*. https://royalsocietypublishing.org/doi/abs/10.1098/rsta.2020.0164 (accessed 2023-07-30).

14 Schermelleh, L.; Ferrand, A.; Huser, T.; Eggeling, C.; Sauer, M.; Biehlmaier, O.; Drummen, G. P. C. Super-Resolution Microscopy Demystified. *Nat Cell Biol* **2019**, *21* (1), 72–84. https://doi.org/10.1038/s41556-018-0251-8.

15 Betzig, E.; Patterson, G. H.; Sougrat, R.; Lindwasser, O. W.; Olenych, S.; Bonifacino, J. S.; Davidson, M. W.; Lippincott-Schwartz, J.; Hess, H. F. Imaging Intracellular Fluorescent Proteins at Nanometer Resolution. *Science* **2006**, *313* (5793), 1642–1645. https://doi.org/10.1126/science.1127344.

16 Hess, S. T.; Girirajan, T. P. K.; Mason, M. D. Ultra-High Resolution Imaging by Fluorescence Photoactivation Localization Microscopy. *Biophysical Journal* **2006**, *91* (11), 4258–4272. https://doi.org/10.1529/biophysj.106.091116.

17 Heilemann, M.; van de Linde, S.; Schüttpelz, M.; Kasper, R.; Seefeldt, B.; Mukherjee, A.; Tinnefeld, P.; Sauer, M. Subdiffraction-Resolution Fluorescence Imaging with Conventional Fluorescent Probes. *Angewandte Chemie International Edition* **2008**, *47* (33), 6172–6176. https://doi.org/10.1002/anie.200802376.

18 Rust, M. J.; Bates, M.; Zhuang, X. Sub-Diffraction-Limit Imaging by Stochastic Optical Reconstruction Microscopy (STORM). *Nat Methods* **2006**, *3* (10), 793–796. https://doi.org/10.1038/nmeth929.

19 Jungmann, R.; Avendaño, M. S.; Woehrstein, J. B.; Dai, M.; Shih, W. M.; Yin, P. Multiplexed 3D Cellular Super-Resolution Imaging with DNA-PAINT and Exchange-PAINT. *Nat Methods* **2014**, *11* (3), 313–318. https://doi.org/10.1038/nmeth.2835.

20 Balzarotti, F.; Eilers, Y.; Gwosch, K. C.; Gynnå, A. H.; Westphal, V.; Stefani, F. D.; Elf, J.; Hell, S. W. Nanometer Resolution Imaging and Tracking of Fluorescent Molecules with Minimal Photon Fluxes. *Science* **2017**, *355* (6325), 606–612. https://doi.org/10.1126/science.aak9913.

21 Jabermoradi, A.; Yang, S.; Gobes, M. I.; van Duynhoven, J. P. M.; Hohlbein, J. Enabling Single-Molecule Localization Microscopy in Turbid Food Emulsions. *Philosophical Transactions of the Royal Society A:*

Mathematical, Physical and Engineering Sciences **2022**, *380* (2220), 20200164. https://doi.org/10.1098/rsta.2020.0164.

22 Samanta, S.; Gong, W.; Li, W.; Sharma, A.; Shim, I.; Zhang, W.; Das, P.; Pan, W.; Liu, L.; Yang, Z.; Qu, J.; Kim, J. S. Organic Fluorescent Probes for Stochastic Optical Reconstruction Microscopy (STORM): Recent Highlights and Future Possibilities. *Coordination Chemistry Reviews* **2019**, *380*, 17–34. https://doi.org/10.1016/j.ccr.2018.08.006.

23 Ovesný, M.; Křížek, P.; Borkovec, J.; Švindrych, Z.; Hagen, G. M. ThunderSTORM: A Comprehensive ImageJ Plug-in for PALM and STORM Data Analysis and Super-Resolution Imaging. *Bioinformatics* **2014**, *30* (16), 2389–2390. https://doi.org/10.1093/bioinformatics/btu202.

24 Martens, K. J. A.; Bader, A. N.; Baas, S.; Rieger, B.; Hohlbein, J. Phasor Based Single-Molecule Localization Microscopy in 3D (PSMLM-3D): An Algorithm for MHz Localization Rates Using Standard CPUs. *The Journal of Chemical Physics* **2017**, *148* (12), 123311. https://doi.org/10.1063/1.5005899.

25 Liang, F.; Hatanaka, Y.; Saito, H.; Yamamori, T.; Hashikawa, T. Differential Expression of γ-Aminobutyric Acid Type B Receptor-1a and -1b MRNA Variants in GABA and Non-GABAergic Neurons of the Rat Brain. *Journal of Comparative Neurology* **2000**, *416* (4), 475–495. https://doi.org/10.1002/(SICI)1096-9861(20000124)416:4<475::AID-CNE5>3.0.CO;2-V.

26 Manders, E. M. M.; Verbeek, F. J.; Aten, J. A. Measurement of Co-Localization of Objects in Dual-Colour Confocal Images. *Journal of Microscopy* **1993**, *169* (3), 375–382. https://doi.org/10.1111/j.1365-2818.1993.tb03313.x.

27 Demandolx, D.; Davoust, J. Multicolour Analysis and Local Image Correlation in Confocal Microscopy. *Journal of Microscopy* **1997**, *185* (1), 21–36. https://doi.org/10.1046/j.1365-2818.1997.1470704.x.

28 Lachmanovich, E.; Shvartsman, D. E.; Malka, Y.; Botvin, C.; Henis, Y. I.; Weiss, A. M. Co-Localization Analysis of Complex Formation among Membrane Proteins by Computerized Fluorescence Microscopy: Application to Immunofluorescence Co-Patching Studies. *Journal of Microscopy* **2003**, *212* (2), 122–131. https://doi.org/10.1046/j.1365-2818.2003.01239.x.

29 Prior, I. A.; Muncke, C.; Parton, R. G.; Hancock, J. F. Direct Visualization of Ras Proteins in Spatially Distinct Cell Surface Microdomains. *Journal of Cell Biology* **2003**, *160* (2), 165–170. https://doi.org/10.1083/jcb.200209091.

30 Zhang, B.; Chenouard, N.; Olivo-Marin, J.-C.; Meas-Yedid, V. Statistical Colocalization in Biological Imaging with False Discovery Control. In *2008 5th IEEE International Symposium on Biomedical Imaging: From Nano to Macro*; 2008; pp 1327–1330. https://doi.org/10.1109/ISBI.2008.4541249.

31 Willems, J.; MacGillavry, H. D. A Coordinate-Based Co-Localization Index to Quantify and Visualize Spatial Associations in Single-Molecule Localization Microscopy. *Sci Rep* **2022**, *12* (1), 4676. https://doi.org/10.1038/s41598-022-08746-4.

32 Berton, C.; Genot, C.; Ropers, M.-H. Quantification of Unadsorbed Protein and Surfactant Emulsifiers in Oil-in-Water Emulsions. *Journal of Colloid and Interface Science* **2011**, *354* (2), 739–748. https://doi.org/10.1016/j.jcis.2010.11.055.

33 Siemons, M. E.; Hanemaaijer, N. A. K.; Kole, M. H. P.; Kapitein, L. C. Robust Adaptive Optics for Localization Microscopy Deep in Complex Tissue. *Nat Commun* **2021**, *12* (1), 3407. https://doi.org/10.1038/s41467-021-23647-2.

34 Jimenez, A.; Friedl, K.; Leterrier, C. About Samples, Giving Examples: Optimized Single Molecule Localization Microscopy. *Methods* **2020**, *174*, 100–114. https://doi.org/10.1016/j.ymeth.2019.05.008.

35 Smith, C. S.; Joseph, N.; Rieger, B.; Lidke, K. A. Fast, Single-Molecule Localization That Achieves Theoretically Minimum Uncertainty. *Nat Methods* **2010**, *7* (5), 373–375. https://doi.org/10.1038/nmeth.1449.

36 Schindelin, J.; Arganda-Carreras, I.; Frise, E.; Kaynig, V.; Longair, M.; Pietzsch, T.; Preibisch, S.; Rueden, C.; Saalfeld, S.; Schmid, B.; Tinevez, J.-Y.; White, D. J.; Hartenstein, V.; Eliceiri, K.; Tomancak, P.; Cardona, A. Fiji: An Open-Source Platform for Biological-Image Analysis. *Nat Methods* **2012**, *9* (7), 676–682. https://doi.org/10.1038/nmeth.2019.

37 Bankhead, P.; Loughrey, M. B.; Fernández, J. A.; Dombrowski, Y.; McArt, D. G.; Dunne, P. D.; McQuaid, S.; Gray, R. T.; Murray, L. J.; Coleman, H. G.; James, J. A.; Salto-Tellez, M.; Hamilton, P. W. QuPath: Open Source Software for Digital Pathology Image Analysis. *Sci Rep* **2017**, *7* (1), 16878. https://doi.org/10.1038/s41598-017-17204-5.

38 Schmidt, U.; Weigert, M.; Broaddus, C.; Myers, G. Cell Detection with Star-Convex Polygons. In *Medical Image Computing and Computer Assisted Intervention – MICCAI 2018*; Frangi, A. F., Schnabel, J. A., Davatzikos, C., Alberola-López, C., Fichtinger, G., Eds.; Lecture Notes in Computer Science; Springer International Publishing: Cham, 2018; Vol. 11071, pp 265–273. https://doi.org/10.1007/978-3-030-00934-2_30.

39 Weigert, M.; Schmidt, U.; Haase, R.; Sugawara, K.; Myers, G. Star-Convex Polyhedra for 3D Object Detection and Segmentation in Microscopy. In *2020 IEEE Winter Conference on Applications of Computer Vision (WACV)*; IEEE: Snowmass Village, CO, USA, 2020; pp 3655–3662. https://doi.org/10.1109/WACV45572.2020.9093435.

40 Kowalczuk, P. B.; Drzymala, J. Physical Meaning of the Sauter Mean Diameter of Spherical Particulate Matter. *Particulate Science and Technology* **2016**, *34* (6), 645–647. https://doi.org/10.1080/02726351.2015.1099582.

41 Curd, A. P.; Leng, J.; Hughes, R. E.; Cleasby, A. J.; Rogers, B.; Trinh, C. H.; Baird, M. A.; Takagi, Y.; Tiede, C.; Sieben, C.; Manley, S.; Schlichthaerle, T.; Jungmann, R.; Ries, J.; Shroff, H.; Peckham, M. Nanoscale Pattern Extraction from Relative Positions of Sparse 3D Localizations. *Nano Lett.* **2021**, *21* (3), 1213–1220. https://doi.org/10.1021/acs.nanolett.0c03332.

42 Dodge, Y. *The Oxford Dictionary of Statistical Terms*; Oxford University Press, 2003.

43 Schaich, K. Schaich, K.M. 2008. Co-Oxidations of Oxidizing Lipids: Reactions with Proteins, in Lipid Oxidation Pathways, Chapter 8, Vol 2, Ed. Kamal-Eldin, A. and Min, D., AOCS Press, Pp. 183-274.; 2008; pp 183–274.

44 Laguerre, M.; Bily, A.; Roller, M.; Birtić, S. Mass Transport Phenomena in Lipid Oxidation and Antioxidation. *Annual Review of Food Science and Technology* **2017**, *8* (1), 391–411. https://doi.org/10.1146/annurev-food-030216-025812.

45 Lin, J.; Hoppe, A. D. Uniform Total Internal Reflection Fluorescence Illumination Enables Live Cell Fluorescence Resonance Energy Transfer Microscopy. *Microscopy and Microanalysis* **2013**, *19* (2), 350–359. https://doi.org/10.1017/S1431927612014420.

5.5 Supplementary materials

Supplementary Note 5.1

To calculate the co-localization index, we employed the same equation presented in reference[31]. First, the Nearest Neighbor Distance (NND) is computed for every point within a specified Region of Interest (ROI). By averaging the NND of all points, the Mean Nearest Neighbor Distance (MNND) is derived. Subsequently, the local density (*LD*) for every point is identified as the total number of points within a region whose radius is defined by the effective resolution *d*.

$$d = \sqrt{\mathrm{MNND}^2 + \varepsilon^2},$$

Here ε represents the localization precision. The co-localization Index for channel 1 (CI_{ij}^{1}) calculates how many localizations *i* from droplet *j*, in channel 2 (denoted by N_{1ij}^{2}) exist within a certain radius *d* around every point in channel 1.This CI_{ij}^{1} is then normalized on the average local density of localizations of droplet *j* in channel 2, represented as $\overline{LD}_{2j}$, where *d* is driven by the effective resolution of points in a droplet, in channel 2. This can be expressed as

$$CI_{ij}^{1} = \frac{N_{1ij}^{2}(d_2)}{\overline{LD}_{2j}}.$$

Subsequently for each localizations of droplet *j* in channel 2, the CI_{ij}^{2} values are computed as

$$CI_{ij}^{2} = \frac{N_{2ij}^{1}(d_1)}{\overline{LD}_{1j}}.$$

Averaged CI_j values for every single droplet *j* can be graphically represented in a co-localization swarm plot. By taking their average, a unified mean-CI value can be obtained for all droplets in the entire ROI across both channels.

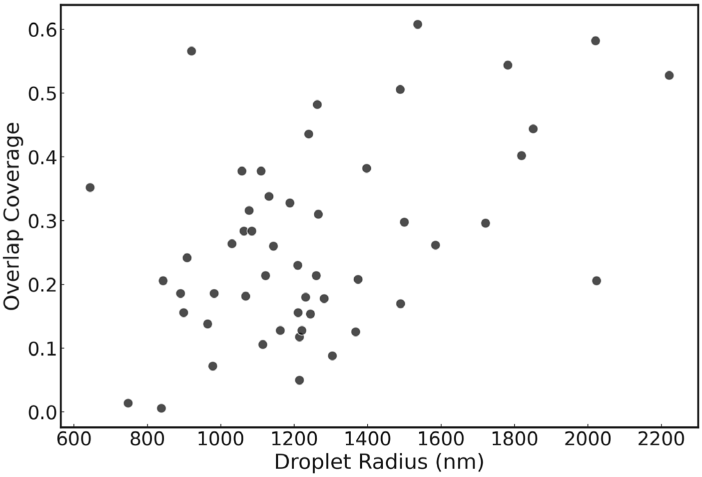

Supplementary Figure 5.1. Correlation between droplet radius and overlap coverage of apoB and phosvitin. The droplets are represented by black circular markers. The Pearson correlation, employed to analyze the correlation between the overlap coverage and radius, gives a coefficient of 0.41, indicating no significant correlation (p-value = 0.0025).

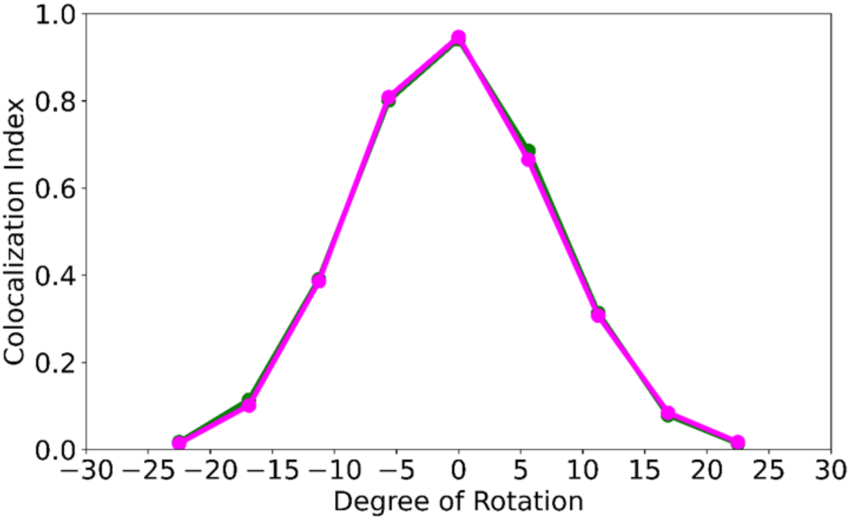

Supplementary Figure 5.2. Simulation exploring the effect of reducing the number of localizations in the magenta channel by half, while maintaining all other initial conditions in the simulation. Despite the alteration in the number of localizations, the co-localization index remained constant.

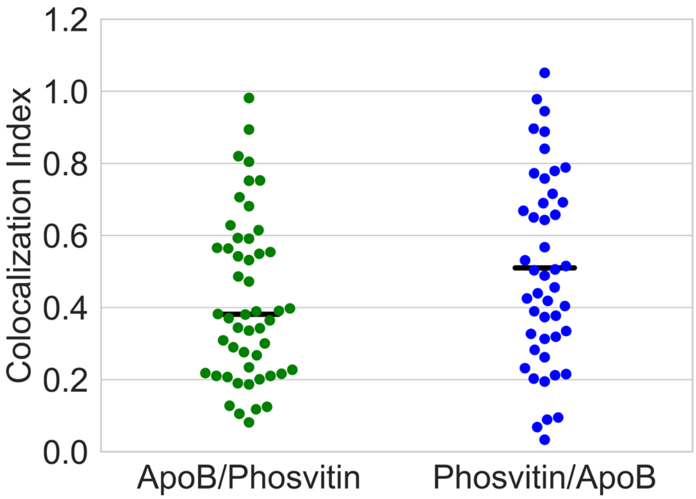

Supplementary Figure 5.3. Evaluation of spatial relationships and co-localization indices between phosvitin, and apoB, at individual droplet interfaces in oxidized emulsions. The swarm plot shows co-localization indices between apoB/phosvitin and phosvitin/apoB with median values of 0.38, and 0.51, respectively.

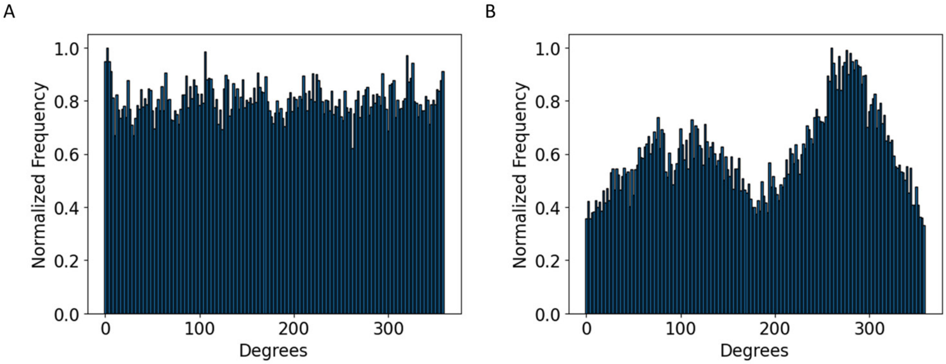

Supplementary Figure 5.4. Examination of the angular distribution of protein localizations between (A) 100 simulated droplets in which the proteins were homogeneously distributed and (B) experimentally observed data. We see a small bias introduced by the HILO mode of the microscope on the excitation/detection probability at certain angular orientations of the droplets.

6

General discussion

6.1 Overview and key outcomes: Nanoscale analysis of food emulsions

Super-resolution microscopy techniques have revolutionized the life sciences by transcending the diffraction limit of light, thereby facilitating the examination of specimens at the nanoscale. Extending super-resolution microscopy with adaptive optics makes it also useful for studying complex food emulsions. An example is mayonnaise in which the use of egg yolk adds a mixture of emulsifying agents[1]. This thesis focused on the localization of two key emulsifying egg yolk proteins found in mayonnaise: phosvitin, a metal-binding phosphoprotein with implications for oxidative food stability, and apolipoprotein B (apoB), which acts as a strong emulsifier[2].

In this thesis, super-resolution microscopy assays were developed to study model food emulsions[3]. First, adaptive optics and a homogeneous beam shaper were implemented into an existing microscopy framework. The main challenge was to overcome turbidity in emulsions where droplets averaged one micron in size[4] (**Chapter 2**). Subsequently, a quantitative analysis method was developed aimed at evaluating the spatial distribution of emulsifiers at the oil droplet interface (**Chapter 3**). To this end, the relative distances between all localizations around a single droplet were analyzed. Thereafter, the quantitative analysis of STORM data along with confocal images was employed to evaluate both inter- and intra-droplet heterogeneity of phosvitin in a binary model mayonnaise (**Chapter 4**). Finally, we transitioned to a more complex mayonnaise model system that used egg yolk as the emulsifying agent. We quantified the interfacial presence of phosvitin and apoB proteins while also analyzing their co-localization (**Chapter 5**). An overview of the thesis chapters is depicted in **Figure 6.1**. In this chapter, the challenges and bottlenecks faced in employing and developing super-resolution microscopy for food emulsions will be elaborated on. Future directions for improving the understanding of food emulsions will be outlined.

6.2 Super-resolution in foods: breaking the ground

6.2.1 Immobilization of oil droplets and efficient oxygen scavenging

Super-resolution microscopy has primarily been developed for applications in life sciences[5,6]. Adapting techniques like STORM for food emulsion samples presented several challenges. The first challenge was the immobilization of oil droplets. In low-oil-content model emulsions, the oil droplets were not stationary, making them unsuitable for STORM, which requires capturing thousands of steady frames. Initially, guar gum was employed to immobilize the oil droplets, forming a gel network to restrict droplet movement. While this approach was partially successful, as discussed below, it was noticed that with increasing depth, the number of observable oil droplets decreased. An attempt was made to use alternative ingredients, such as

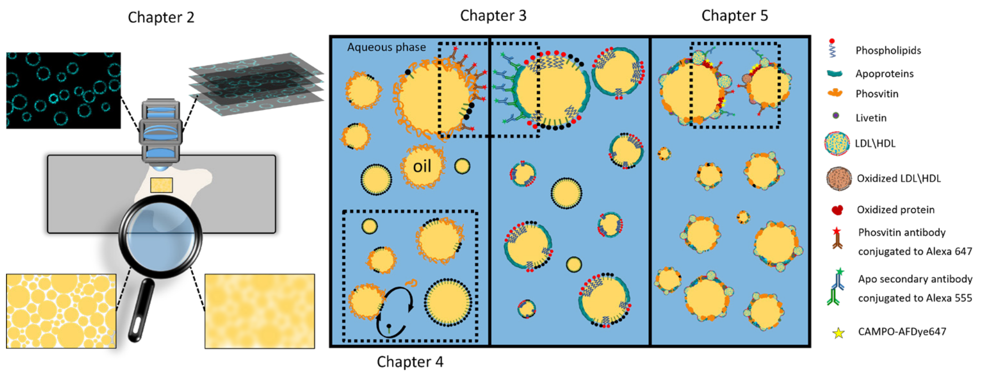

Figure 6.1. Overview of the work performed in this thesis. Chapter 2 advanced super-resolution microscopy for studying turbid food emulsions. Chapter 3 introduced quantitative emulsifier distribution analysis for emulsifiers at the interface. Chapter 4 applied the techniques developed in previous chapters to examine interfacial heterogeneity of phosvitin in a model emulsion. Chapter 5 extended the study to a complex mayonnaise model system with egg yolk, focusing on co-localization of proteins and protein radicals.

kappa-carrageenan—a negatively charged polysaccharide—to mitigate the void-forming effects of guar gum. However, this approach led to the sample becoming unstable, likely due to the negative charge, which in turn prevented meaningful fluorescence measurements. Additionally, sucrose and glycerol were employed to increase the emulsion's viscosity to immobilize the droplets. However, the addition did not enhance the viscosity to the level required for droplet immobilization. The droplets remained mobile, rendering this approach unsuccessful. To counteract the limitations of guar gum, low-speed centrifugation was utilized to separate the oil droplets from the aqueous phase. This approach packed the droplets closely together, mimicking a high-oil-content environment and allowing for stable placement of the sample on the cover slip during measurements. The effects of immobilization using guar gum (**Figure 6.2A**, adapted from **Chapter 2**) and centrifugation (**Figure 6.2B**, adapted from **Chapter 4**) on the distribution of emulsifiers at the surface of oil droplets were examined. The methods used included relative position displacement (RPD)[7] and relative peak amplitude analysis. These techniques were applied to a binary model emulsion, which contained phosvitin and sodium dodecyl sulfate (SDS) as emulsifiers (**Chapter 3**). Our results indicate no significant differences between the two methods, as demonstrated by comparable relative peak amplitudes of 0.4 +/- 0.14 for both methods (**Figure 6.2C** and **6.2D**).

Additional challenges arose in the context of oxygen scavenging for STORM experiments. STORM buffers, often incorporating oxygen scavenging systems, are essential for promoting frequent and stable blinking of fluorophores. This optimal environment ensures the intermittent and sparse activation of dyes, pivotal for achieving the characteristic high-resolution of STORM[8,9]. Most of the protocols and commercial STORM buffers were designed primarily for

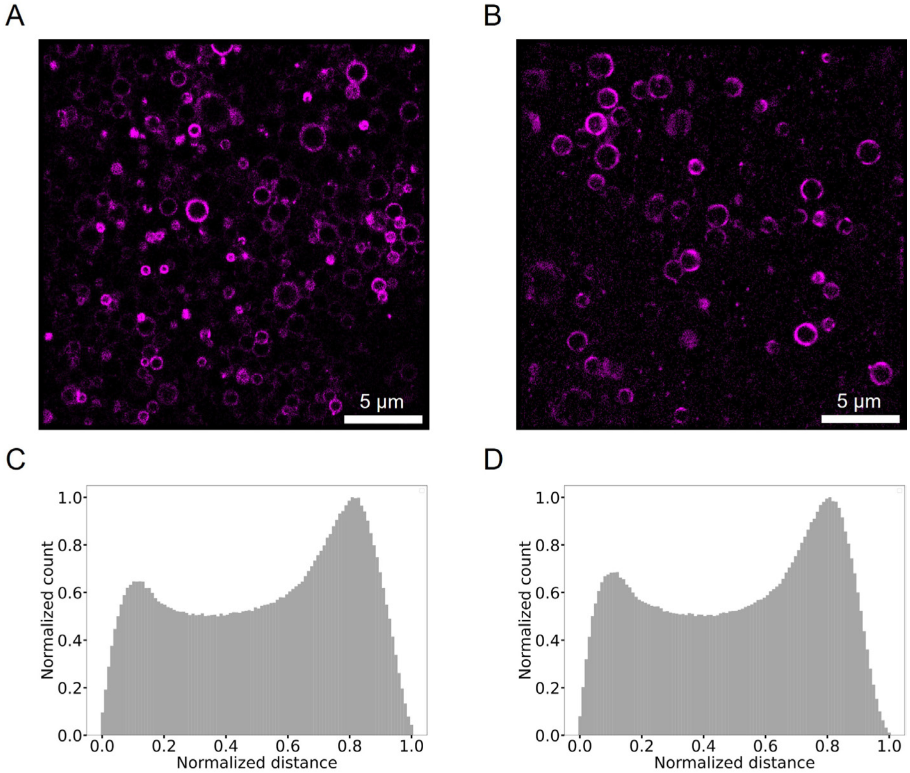

Figure 6.2. Comparative analysis of the distribution of emulsifiers (phosvitin/SDS) at the surface. Reconstructed images, obtained via STORM, showcase oil droplets immobilized with (A) guar gum (adapted from Chapter 2) and by (B) centrifugation (adapted from Chapter 4). Phosvitin was labeled using a primary antibody conjugated to Alexa Fluor 647. Relative Position Displacement (RPD) histogram for droplets immobilized with (C) guar gum and by (D) centrifugation. Both methods yielded comparable relative peak amplitude values of 0.4 +/- 0.14

applications in the life sciences and typically operate at a neutral pH of around 7. This posed a significant challenge for our low-pH model emulsions. Some buffers further lowered the pH of the sample[10]. These adverse pH changes had dual detrimental effects: they not only degraded the sample quality but also diminished the brightness of the dye used for imaging. Ultimately, a protocol described in[11] was adapted, identifying it as the most suitable oxygen scavenger buffer for our system. Further exploration of other oxygen-scavenging methods that claim to be capable of maintaining a stable pH during measurements did not work for our samples[12]. Another challenge faced in this thesis was the lack of existing methods for quantitative analysis of emulsifier localizations at the interface. Despite having a list of localizations from proteins for all observable droplets in a given field of view, this thesis recognized the need to develop new methodologies for quantitative image analysis of model emulsions. These methodologies will be reviewed in the next sections.

6.2.2 Imaging in depth

Food emulsions typically have droplet sizes in the microscale. These emulsions appear turbid, due to scattering and light aberrations especially when observed using optical microscopy (**Chapter 1**). To address this issue, adaptive optics utilizing a deformable mirror was employed, allowing penetration up to 15 μm into the emulsion samples, as described in **Chapter 2**. Initially, the aim was to compensate for aberrations arising from this depth, as we hypothesized that measurements taken close to the surface—particularly on a coverslip—could potentially influence the structure and characteristics of the sample. However, when images taken 8 μm deep were compared to those taken closer to the surface (see **Figures 6.3A**, and **6.3B** - adapted from **Chapter 2**), little variation was found in the distribution of emulsifiers among the oil droplets. To quantify this observation, the RPD analysis tool from **Chapter 3**, also further discussed below, was employed, and it was found that the relative peak amplitudes for samples close to the surface (**Figure 6.3C**) and 8 μm deep (**Figure 6.3D**) were with 0.38 and 0.36 very similar. These findings suggest that the surface proximity does not affect droplet coverage distribution. As such, there is no compelling reason to measure deep into the sample. However, it is worth noting that aberrations still exist in turbid samples close to the surface. For this reason, adaptive optics was used for all measurements in this thesis.

6.3 Methodological advances in studying the interface of droplets in food emulsions

In this thesis, the focus is on the often overlooked yet critical task of directly visualizing the interfacial composition of oil droplets in food emulsions[13]. Despite the interface's vital role in the stability and quality of emulsions, its surface characteristics have rarely been investigated with both molecular specificity and high spatial resolution[14–16]. To address this gap, we employed antibodies for targeted examination. Recognizing the need for quantitative, we introduced several methodological advances designed to examine this interface in more detail.

6.3.1 Assessing the heterogeneity of distribution of emulsifiers on oil droplet surfaces

To advance the quantitative analysis of the distribution of emulsifiers at the oil-water interface, the RPD pattern method was adopted, which was initially designed for nuclear pore structures[7]. By simulating diverse protein arrangements at the interface, we identified a correlation between the protein distribution and the RPD histogram patterns. Homogeneous distributions consistently generated similar RPD patterns, suggesting that RPD could serve as a 'fingerprint' for the degree of homogeneity. Deviations from this pattern indicated a heterogeneous distribution of emulsifiers. To quantify this distribution, a metric named the relative peak amplitude (A_{rel}) was

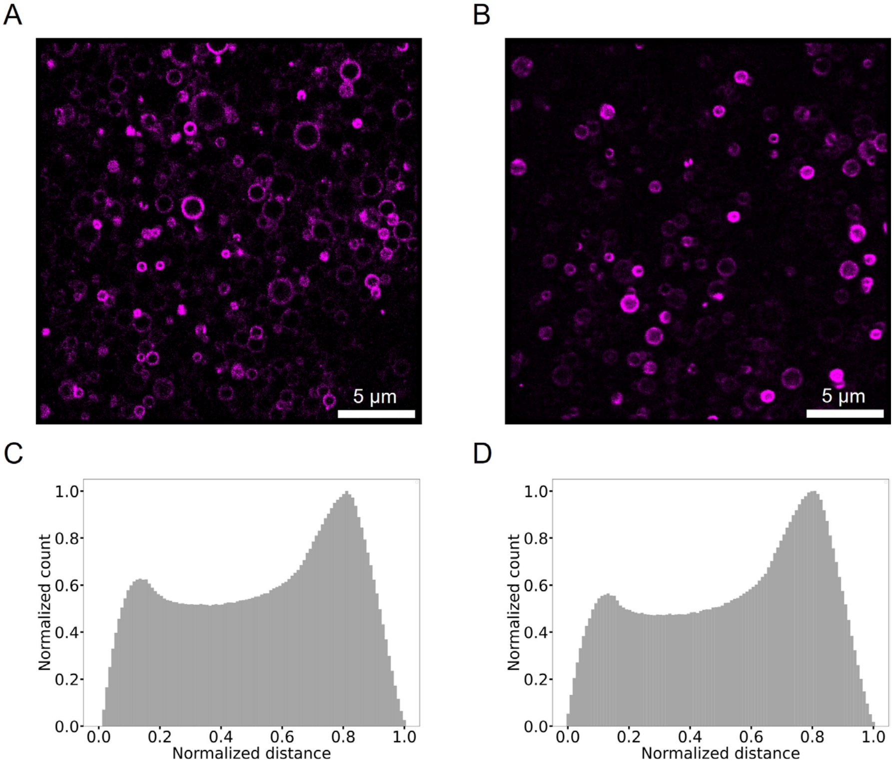

Figure 6.3. Comparative analysis of the distribution of emulsifiers at different sample depths using STORM. Labeling of phosvitin was performed using a primary phosvitin antibody conjugated to Alexa Fluor 647. (A) Reconstructed image of oil droplets close to the surface of the coverslip. (B) Reconstructed image of oil droplets taken at a sample depth of 8 µm. (C) Graph depicting the RPD histogram of the sample close to the surface, with a value of 0.38 +/- 0.14. (D) Graph depicting the RPD histogram of samples taken at a depth of 8 µm, with a value of 0.36 +/- 0.11.

introduced. A_{rel} is calculated by dividing the amplitude of the first peak by the sum of the amplitudes of both peaks appearing in the RPD histogram. In **Chapter 3**, we classify these distributions into three categories: homogeneous, partially heterogeneous, and heterogeneous. Although these categories are not rigidly defined, a higher A_{rel} value consistently indicated a more heterogeneous distribution. Utilizing this methodology not only enabled to distinguish between homogeneous and heterogeneous distribution of emulsifiers but also to quantify the degree of heterogeneity when comparing different emulsifiers.

6.3.2 Analyzing inter-droplet and intra-droplet heterogeneity

Building the methods for analyzing the single-droplet emulsifier distribution allowed to extend the scope to inter-droplet heterogeneity. The aim was to investigate whether specific emulsifiers preferentially adsorb to droplets of particular size. This approach is straightforward in binary model systems comprising a low-molecular-weight surfactant and a protein, as detailed in **Chapter 4**. However, the complexity increases when the system includes multiple ingredients and proteins that co-adsorb to the droplet surface. In **Chapter 5**, emulsions stabilized by egg yolk were examined, where proteins (apoB and phosvitin) and phospholipids adsorb at the oil-droplet interface. To facilitate the analysis of inter-droplet heterogeneity, a Python program capable of projecting the 2D localization of emulsifiers onto the surface of the oil droplets was developed. This method allows calculating the proportion of a droplet's circumference occupied by specific ingredients while assuming the unoccupied circumference to be filled with phospholipids. By correlating this data with droplet size, the extent of inter-droplet heterogeneity within the emulsions was assessed.

6.3.3 Advanced techniques for analyzing the co-localization of emulsifiers

Having established the methodologies for both intra-droplet and inter-droplet analyses, it was recognized that a more nuanced approach was necessary for assessing the spatial association of different emulsifiers and proteins. To address this, a coordinate-based co-localization index analysis method[17] was adopted. This approach calculates the spatial association between two channels irrespective of localization density and is not constrained by the bin size. Initially, the suitability of this methodology for studying the structure along the circumference of droplets through simulations was validated. Following verification, the method was applied to our egg yolk model system to assess co-localization indices between apoB and phosvitin. More importantly, this method allowed investigating the co-localization between proteins and protein radicals, with the surprising finding that for our model system both apoB and phosvitin had similar susceptibility to oxidation.

6.4 Outlook

6.4.1 From model emulsions to full mayonnaise: exploring the water-oil interface

In this thesis, the complexity of the model systems was successively increased. Initially, an elementary model system featuring only phosvitin as the sole emulsifier was chosen due to its structural properties and its capacity for binding iron. However, this unary model system was unstable. Therefore, SDS was added to obtain a stable emulsion at a 10% oil concentration. Subsequently, the complexity of the model was expanded by adding LDL, which is composed of apoB and phospholipids. Finally, we employed egg yolk as an emulsifying agent, mimicking the multi-component nature of emulsifiers found in real mayonnaise. The methodologies delineated in the initial chapters enabled our investigation of the egg-yolk containing model system. It should be noted that our studies are currently limited to a concentration of 1% egg yolk; in contrast, real mayonnaise typically contains around 5% egg yolk[18]. Hence, a relevant extension would be to examine the effects of varying egg yolk concentrations on both inter- and intra-droplet heterogeneity in relation to attenuation[19] or acceleration[20] of oxidation processes.

Moreover, it is worth mentioning that our model emulsions incorporated a low oil content and exhibited average droplet sizes of approximately 1 µm—parameters that diverge considerably from commercial mayonnaise, which typically features an oil concentration between 60-70% and droplet sizes ranging from 4 to 6 µm. Therefore, a future step is to apply the methods that were developed in this thesis to study interfaces of oil droplet in real mayonnaise systems.

6.4.2 Advanced probes and techniques for high-resolution imaging in food emulsions

In this thesis, antibodies were utilized to target egg yolk proteins for STORM experiments[21], an approach that has proven highly effective for localizing proteins. However, traditional antibodies present limitations due to their relatively large size, which can impede specimen penetration. In **Chapter 4**, affimers were evaluated as an alternative to phosvitin-specific antibodies. Unfortunately, these affimers exhibited low specificity, likely because their selection procedure was biases towards electrostatic interactions. As a recommended avenue for future research, I suggest the exploration of nanobodies[22] as potential probes for STORM measurements (**Figure 6.4**). Like relatively large antibodies (~150 kDa), nanobodies (~10-15 kDa) retain a specificity in antigen recognition comparable to that of larger antibodies[23–25]. Their smaller size enables better specimen penetration, making nanobodies an attractive option for STORM measurements in emulsions. Furthermore, the utilization of smaller targeting labels could potentially enhance the resolution of co-localization experiments. Specifically, higher localization accuracy could pave the way for improved analyses of co-localization between proteins, as well as between proteins and protein radicals.

Additionally, adopting the point accumulation for imaging in nanoscale topography (PAINT)[26] technique, specifically DNA-PAINT, could serve as a substitute for STORM. In DNA-PAINT[27], we suggest using docking strands conjugated to target-specific nanobodies, which, in our case, should be raised against phosvitin and apoB. Subsequently, the introduction of fluorescently-labeled imager strands allows for transient binding via DNA hybridization. This binding mechanism enables the precise localization of targets, in contrast to the on-off switching mechanism in STORM. For multi-labeling of different targets, orthogonal DNA strands will be employed, a feature especially valuable in complex systems[28]. This approach offers several advantages over STORM, including prolonged fluorophore association times and reduced photobleaching, which collectively results in improved localization precision and accuracy. This methodology has the potential to provide a robust platform for investigating early-stage oxidation processes (see **Figure 6.4**). However, traditional DNA-PAINT has two major disadvantages: the technical challenge of introducing freely diffusing DNA strands to the model emulsion and its more time-consuming data acquisition compared to STORM[29,30]. I recommend sequential imaging of specific fields of view using various fluorophores conjugated to different imager strands. An alternative approach involves the use of a single fluorophore for multiple orthogonal imager strands. However, this latter method requires washing the sample and reloading new imager strands for each target, adding complexity due to the challenges of re-locating the same field of view on the coverslip[31]. To verify the technique, I suggest using a simple model system. In this scenario, even though the model emulsion has a low oil concentration, the washing steps required in this method are applicable to the sample post-centrifugation for imaging.

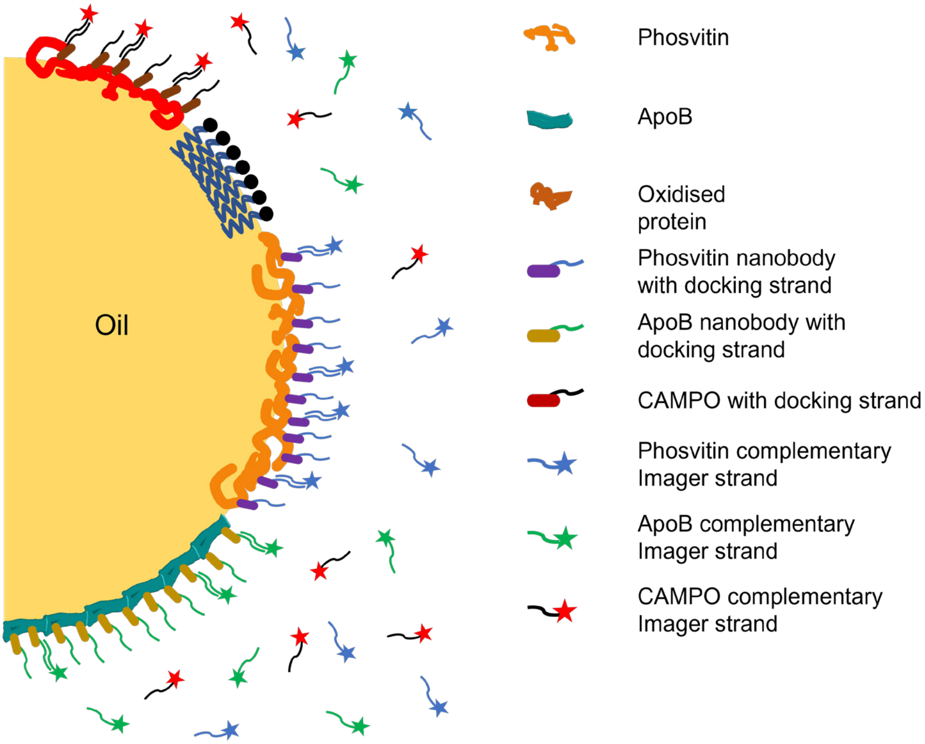

Figure 6.4. Schematic illustration of multicolor DNA-PAINT employing three orthogonal pairs of docking and imager strands. Target molecules—phosvitin, apoB, and protein radicals—are located on the surface of oil droplets and are labeled via nanobodies conjugated to their respective docking strands. Each imager strand can be conjugated to a distinct fluorophore for simultaneous multicolor imaging.

6.4.3 Improvements in simulations

To scrutinize and authenticate the efficacy of quantitative methods, simulations are invaluable tools. This thesis employed simulation techniques to conduct heterogeneity analysis of emulsifiers situated at the interface of oil droplets (**Chapter 3**). Moreover, these simulations were utilized to validate the utility of coordinate-based co-localization index analysis (**Chapter 5**). For the purpose of simulating localizations, certain factors were omitted, such as the effect of localizations originating from focal planes above or below the target region. With respect to the aggregation term introduced in **Chapter 3**, the analysis was constrained to one dimension along the circumference of the oil droplets. Nevertheless, preliminary efforts were undertaken to extend the aggregation term into a two-dimensional plane within the oil droplet structure. For the advancement of quantitative analysis, further developments of these simulations into a three-dimensional framework are recommended.

Now that the heterogeneity of emulsifiers can be mapped at oil droplet interfaces, a more verification of emulsifiers' behavior is possible. This involves integrating formalism for diffusion, local shear rate, protein aggregation, and convection. Into a simulation framework These advancements will deepen our insights into how emulsifiers interact with oil droplets during emulsification and how they distribute at the interface.

In summary, simulations offer a versatile platform for the validation and extension of quantitative methods in the analysis of spatial association and heterogeneity of emulsifiers. Further advancements in multi-dimensional and multi-component whole-body simulation frameworks are anticipated. These enhancements will adequately address the complexity food emulsions and thus provide new insights. This, in turn, will aid in the meticulous design of emulsions and the strategic application of antioxidant strategies.

6.4.4 New tools for studying food emulsions at the single droplet level

In this thesis, various techniques and methods have been developed to study food emulsions and, specifically, the interface of oil droplets. These approaches enable the investigation of the modulating effect of intra- and inter-droplet heterogeneity and droplet size on lipid and protein oxidation. Current literature presents conflicting results regarding oxidation in food emulsions; some studies report that smaller droplets oxidize faster due to a higher surface-to-volume ratio[32–39], while others suggest that larger droplets oxidize faster[40–44]. It is important to note that these studies did not consider the spatial distribution of emulsifiers at droplet surfaces due to a lack of adequate methods. The tools developed in this thesis helped to clarify these discrepancies. As discussed in **Chapter 5**, a model system using egg yolk demonstrated that smaller droplets were preferentially covered by phospholipids and larger ones predominantly by proteins. It is recommended to investigate further whether and how the emulsifiers' intra- and inter-droplet heterogeneity in surface coverage is related to the physical and chemical stability of food emulsions.

The introduction of egg yolk in a model emulsion marked a pivotal point, enabling a systematic study of the localization of biomacromolecules at the interface. The use of techniques offering sub-micron resolution combined with molecular specificity offers an attractive tool for the food industry for mechanistic underpinning of natural oxidation control strategies. By suppressing oxidation at its origin, technological routes can be identified for producing sustainable foods with extended shelf life. Thus, the tools and methodologies presented in this thesis can guide rational process and formulation design of sustainable products in industrial settings.

References

1 Mine, Y. Emulsifying Characterization of Hens Egg Yolk Proteins in Oil-in-Water Emulsions. *Food Hydrocolloids* **1998**, *12* (4), 409–415. https://doi.org/10.1016/S0268-005X(98)00054-X.

2 Anton, M. Egg Yolk: Structures, Functionalities and Processes: Egg Yolk: Structures, Functionalities and Processes. *J. Sci. Food Agric.* **2013**, *93* (12), 2871–2880. https://doi.org/10.1002/jsfa.6247.

3 Jabermoradi, A.; Yang, S.; Gobes, M. I.; van Duynhoven, J. P. M.; Hohlbein, J. Enabling Single-Molecule Localization Microscopy in Turbid Food Emulsions. *Phil. Trans. R. Soc. A.* **2022**, *380* (2220), 20200164. https://doi.org/10.1098/rsta.2020.0164.

4 Chantrapornchai, W.; Clydesdale, F.; McClements, D. J. Influence of Droplet Size and Concentration on the Color of Oil-in-Water Emulsions. *J. Agric. Food Chem.* **1998**, *46* (8), 2914–2920. https://doi.org/10.1021/jf980278z.

5 Schermelleh, L.; Heintzmann, R.; Leonhardt, H. A Guide to Super-Resolution Fluorescence Microscopy. *Journal of Cell Biology* **2010**, *190* (2), 165–175. https://doi.org/10.1083/jcb.201002018.

6 Hell, S. W.; Wichmann, J. Breaking the Diffraction Resolution Limit by Stimulated Emission: Stimulated-Emission-Depletion Fluorescence Microscopy. *Opt. Lett., OL* **1994**, *19* (11), 780–782. https://doi.org/10.1364/OL.19.000780.

7 Curd, A. P.; Leng, J.; Hughes, R. E.; Cleasby, A. J.; Rogers, B.; Trinh, C. H.; Baird, M. A.; Takagi, Y.; Tiede, C.; Sieben, C.; Manley, S.; Schlichthaerle, T.; Jungmann, R.; Ries, J.; Shroff, H.; Peckham, M. Nanoscale Pattern Extraction from Relative Positions of Sparse 3D Localizations. *Nano Lett.* **2021**, *21* (3), 1213–1220. https://doi.org/10.1021/acs.nanolett.0c03332.

8 *Evaluation of fluorophores for optimal performance in localization-based super-resolution imaging | Nature Methods*. https://www.nature.com/articles/nmeth.1768 (accessed 2023-09-19).

9 Lehmann, M.; Lichtner, G.; Klenz, H.; Schmoranzer, J. Novel Organic Dyes for Multicolor Localization-Based Super-Resolution Microscopy. *Journal of Biophotonics* **2016**, *9* (1–2), 161–170. https://doi.org/10.1002/jbio.201500119.

10 Hartwich, T. M. P.; Soeller, C.; Baddeley, D. A Simple Chemical Oxygen Scavenging System for Improved DSTORM Tissue Imaging. *Biophysical Journal* **2014**, *106* (2), 401a. https://doi.org/10.1016/j.bpj.2013.11.2258.

11 Jimenez, A.; Friedl, K.; Leterrier, C. About Samples, Giving Examples: Optimized Single Molecule Localization Microscopy. *Methods* **2020**, *174*, 100–114. https://doi.org/10.1016/j.ymeth.2019.05.008.

12 Nahidiazar, L.; Agronskaia, A. V.; Broertjes, J.; Broek, B. van den; Jalink, K. Optimizing Imaging Conditions for Demanding Multi-Color Super Resolution Localization Microscopy. *PLOS ONE* **2016**, *11* (7), e0158884. https://doi.org/10.1371/journal.pone.0158884.

13 Hinderink, E. B. A.; Meinders, M. B. J.; Miller, R.; Sagis, L.; Schroën, K.; Berton-Carabin, C. C. Interfacial Protein-Protein Displacement at Fluid Interfaces. *Advances in Colloid and Interface Science* **2022**, *305*, 102691. https://doi.org/10.1016/j.cis.2022.102691.

14 Ravera, F.; Dziza, K.; Santini, E.; Cristofolini, L.; Liggieri, L. Emulsification and Emulsion Stability: The Role of the Interfacial Properties. *Advances in Colloid and Interface Science* **2021**, *288*, 102344. https://doi.org/10.1016/j.cis.2020.102344.

15 *Correlation between interfacial layer properties and physical stability of food emulsions: current trends, challenges, strategies, and further perspectives - ScienceDirect*. https://www.sciencedirect.com/science/article/pii/S0001868623000301?casa_token=4g9qYnvjBLoAAAAA:rG3mcU8LoIAEP_GYuh_RJI8_2Lb7T1XciEit7Jd7ztNRM6xNxzPK-bLS7YcxaN85D-7-KUC9zQ (accessed 2023-09-28).

16 Niu, H.; Wang, W.; Dou, Z.; Chen, X.; Chen, X.; Chen, H.; Fu, X. Multiscale Combined Techniques for Evaluating Emulsion Stability: A Critical Review. *Advances in Colloid and Interface Science* **2023**, *311*, 102813. https://doi.org/10.1016/j.cis.2022.102813.

17 Willems, J.; MacGillavry, H. D. A Coordinate-Based Co-Localization Index to Quantify and Visualize Spatial Associations in Single-Molecule Localization Microscopy. *Sci Rep* **2022**, *12* (1), 4676. https://doi.org/10.1038/s41598-022-08746-4.

18 Harrison, L. J.; Cunningham, F. E. Factors Influencing the Quality of Mayonnaise: A Review. *Journal of Food Quality* **1985**, *8* (1), 1–20. https://doi.org/10.1111/j.1745-4557.1985.tb00828.x.

19 Ries, D.; Ye, A.; Haisman, D.; Singh, H. Antioxidant Properties of Caseins and Whey Proteins in Model Oil-in-Water Emulsions. *International Dairy Journal* **2010**, *20* (2), 72–78. https://doi.org/10.1016/j.idairyj.2009.09.001.

20 Faraji, H.; McClements, D. J.; Decker, E. A. Role of Continuous Phase Protein on the Oxidative Stability of Fish Oil-in-Water Emulsions. *J. Agric. Food Chem.* **2004**, *52* (14), 4558–4564. https://doi.org/10.1021/jf035346i.

21 Rust, M. J.; Bates, M.; Zhuang, X. Sub-Diffraction-Limit Imaging by Stochastic Optical Reconstruction Microscopy (STORM). *Nat Methods* **2006**, *3* (10), 793–796. https://doi.org/10.1038/nmeth929.

22 Muyldermans, S. Nanobodies: Natural Single-Domain Antibodies. *Annual Review of Biochemistry* **2013**, *82* (1), 775–797. https://doi.org/10.1146/annurev-biochem-063011-092449.

23 Virant, D.; Traenkle, B.; Maier, J.; Kaiser, P. D.; Bodenhöfer, M.; Schmees, C.; Vojnovic, I.; Pisak-Lukáts, B.; Endesfelder, U.; Rothbauer, U. A Peptide Tag-Specific Nanobody Enables High-Quality Labeling for DSTORM Imaging. *Nat Commun* **2018**, *9* (1), 930. https://doi.org/10.1038/s41467-018-03191-2.

24 Carrington, G.; Tomlinson, D.; Peckham, M. Exploiting Nanobodies and Affimers for Superresolution Imaging in Light Microscopy. *MBoC* **2019**, *30* (22), 2737–2740. https://doi.org/10.1091/mbc.E18-11-0694.

25 Cordell, P.; Carrington, G.; Curd, A.; Parker, F.; Tomlinson, D.; Peckham, M. Affimers and Nanobodies as Molecular Probes and Their Applications in Imaging. *Journal of Cell Science* **2022**, *135* (14), jcs259168. https://doi.org/10.1242/jcs.259168.

26 Sharonov, A.; Hochstrasser, R. M. Wide-Field Subdiffraction Imaging by Accumulated Binding of Diffusing Probes. *Proceedings of the National Academy of Sciences* **2006**, *103* (50), 18911–18916. https://doi.org/10.1073/pnas.0609643104.

27 Schnitzbauer, J.; Strauss, M. T.; Schlichthaerle, T.; Schueder, F.; Jungmann, R. Super-Resolution Microscopy with DNA-PAINT. *Nat Protoc* **2017**, *12* (6), 1198–1228. https://doi.org/10.1038/nprot.2017.024.

28 Schueder, F.; Lara-Gutiérrez, J.; Beliveau, B. J.; Saka, S. K.; Sasaki, H. M.; Woehrstein, J. B.; Strauss, M. T.; Grabmayr, H.; Yin, P.; Jungmann, R. Multiplexed 3D Super-Resolution Imaging of Whole Cells Using Spinning Disk Confocal Microscopy and DNA-PAINT. *Nat Commun* **2017**, *8* (1), 2090. https://doi.org/10.1038/s41467-017-02028-8.

29 Filius, M.; Cui, T. J.; Ananth, A. N.; Docter, M. W.; Hegge, J. W.; van der Oost, J.; Joo, C. High-Speed Super-Resolution Imaging Using Protein-Assisted DNA-PAINT. *Nano Lett.* **2020**, *20* (4), 2264–2270. https://doi.org/10.1021/acs.nanolett.9b04277.

30 Diekmann, R.; Deschamps, J.; Li, Y.; Deguchi, T.; Tschanz, A.; Kahnwald, M.; Matti, U.; Ries, J. Photon-Free (s)CMOS Camera Characterization for Artifact Reduction in High- and Super-Resolution Microscopy. *Nat Commun* **2022**, *13* (1), 3362. https://doi.org/10.1038/s41467-022-30907-2.

31 Yang, S.; Verhoeff, A. A.; Merkx, D. W. H.; van Duynhoven, J. P. M.; Hohlbein, J. Quantitative Spatiotemporal Mapping of Lipid and Protein Oxidation in Mayonnaise. *Antioxidants* **2020**, *9* (12), 1278. https://doi.org/10.3390/antiox9121278.

32 Azuma, G.; Kimura, N.; Hosokawa, M.; Miyashita, K. Effect of Droplet Size on the Oxidative Stability of Soybean Oil TAG and Fish Oil TAG in Oil-in-Water Emulsion. *Journal of Oleo Science* **2009**, *58* (6), 329–338. https://doi.org/10.5650/jos.58.329.

33 GOHTANI, S.; SIRENDI, M.; YAMAMOTO, N.; KAJIKAWA, K.; YAMANO, Y. Effect of Droplet Size on Oxidation of Docosahexaenoic Acid in Emulsion System. *Journal of Dispersion Science and Technology* **1999**, *20* (5), 1319–1325. https://doi.org/10.1080/01932699908943855.

34 Jacobsen, C.; Hartvigsen, K.; Lund, P.; Thomsen, M. K.; Skibsted, L. H.; Adler-Nissen, J.; Hølmer, G.; Meyer, A. S. Oxidation in Fish Oil-Enriched Mayonnaise3. Assessment of the Influence of the Emulsion Structure on Oxidation by Discriminant Partial Least Squares Regression Analysis. *Eur Food Res Technol* **2000**, *211* (2), 86–98. https://doi.org/10.1007/s002179900132.

35 Kuhn, K. R.; Cunha, R. L. Flaxseed Oil – Whey Protein Isolate Emulsions: Effect of High Pressure Homogenization. *Journal of Food Engineering* **2012**, *111* (2), 449–457. https://doi.org/10.1016/j.jfoodeng.2012.01.016.

36 Li, Q.; Xie, B.; Wang, Y.; Wang, Y.; Peng, L.; Li, Y.; Li, B.; Liu, S. Cellulose Nanofibrils from Miscanthus Floridulus Straw as Green Particle Emulsifier for O/W Pickering Emulsion. *Food Hydrocolloids* **2019**, *97*, 105214. https://doi.org/10.1016/j.foodhyd.2019.105214.

37 Neves, M. A.; Wang, Z.; Kobayashi, I.; Nakajima, M. Assessment of Oxidative Stability in Fish Oil-in-Water Emulsions: Effect of Emulsification Process, Droplet Size and Storage Temperature. *Journal of Food Process Engineering* **2017**, *40* (1), e12316. https://doi.org/10.1111/jfpe.12316.

38 Yang, H.; Su, Z.; Meng, X.; Zhang, X.; Kennedy, J. F.; Liu, B. Fabrication and Characterization of Pickering Emulsion Stabilized by Soy Protein Isolate-Chitosan Nanoparticles. *Carbohydrate Polymers* **2020**, *247*, 116712. https://doi.org/10.1016/j.carbpol.2020.116712.

39 *Interface Characterization and Aging of Bovine Serum Albumin Stabilized Oil-in-Water Emulsions As Revealed by Front-Surface Fluorescence | Journal of Agricultural and Food Chemistry*. https://pubs.acs.org/doi/full/10.1021/jf001170y?casa_token=FwyPZRnzCgkAAAAA%3Al_izp5-KNw3t-it-tnv9aMCYRrdZYjNwhebVvJZsaEIYzwLGwPrrr7jEJUBFikN3KAGEpV-pKZoAJOg (accessed 2023-10-11).

40 Atarés, L.; Marshall, L. J.; Akhtar, M.; Murray, B. S. Structure and Oxidative Stability of Oil in Water Emulsions as Affected by Rutin and Homogenization Procedure. *Food Chemistry* **2012**, *134* (3), 1418–1424. https://doi.org/10.1016/j.foodchem.2012.02.221.

41 Costa, M.; Losada-Barreiro, S.; Bravo-Díaz, C.; Paiva-Martins, F. Effects of Emulsion Droplet Size on the Distribution and Efficiency of Antioxidants. In *Lipid Oxidation in Food and Biological Systems: A Physical*

Chemistry Perspective; Bravo-Diaz, C., Ed.; Springer International Publishing: Cham, 2022; pp 217–235. https://doi.org/10.1007/978-3-030-87222-9_10.

42 Let, M. B.; Jacobsen, C.; Sørensen, A.-D. M.; Meyer, A. S. Homogenization Conditions Affect the Oxidative Stability of Fish Oil Enriched Milk Emulsions: Lipid Oxidation. *J. Agric. Food Chem.* **2007**, *55* (5), 1773–1780. https://doi.org/10.1021/jf062391s.

43 Ries, D.; Ye, A.; Haisman, D.; Singh, H. Antioxidant Properties of Caseins and Whey Proteins in Model Oil-in-Water Emulsions. *International Dairy Journal* **2010**, *20* (2), 72–78. **https://doi.org/10.1016/j.idairyj.2009.09.001**.

44 Neves, M. A.; Wang, Z.; Kobayashi, I.; Nakajima, M. Assessment of Oxidative Stability in Fish Oil-in-Water Emulsions: Effect of Emulsification Process, Droplet Size and Storage Temperature. *Journal of Food Process Engineering* **2017**, *40* (1), e12316. https://doi.org/10.1111/jfpe.12316.

Summary

Emulsifiers are crucial for the physicochemical stability of food emulsions like mayonnaise, where egg yolk proteins, acting as primary emulsifiers, adsorb at the oil-droplet interfaces. Understanding the composition and distribution of emulsifiers is pivotal for understanding their impact on oxidative stability and, hence, is vital for enhancing the quality of food emulsions. Conventional brightfield microscopy is limited to around 250 nm in spatial resolution and lacks of molecular specificity. As a consequence, researchers were so far primarily using indirect methods to investigate interfaces. These indirect methods can be invasive and may alter protein distribution, thereby compromising the accuracy of the analysis. In contrast, single-molecule localization microscopy (SMLM) offers sub-100 nm resolution and high molecular specificity using targeted antibodies, thereby enabling the direct visualization of proteins at the interface of oil droplets. In this thesis, stochastic optical reconstruction microscopy (STORM) was implemented in combination with quantitative analysis methods to discern protein distribution with sub-100 nm resolution, addressing inter- and intra-droplet heterogeneity.

Chapter 2 described the development of a homebuilt microscope setup, the miCube, enhanced with adaptive optics in the detection path, and a top-hat beam shaper in the excitation path, tailored for imaging high-turbidity emulsions. A deformable mirror (DM) was utilized to correct aberrations and facilitate three-dimensional SMLM image acquisition through PSF engineering. The top-hat beam shaper was implemented to ensure uniform laser excitation across the entire field of view, which is beneficial for STORM data analysis. A first mayonnaise model system was designed, utilizing phosvitin, an iron-binding protein from egg yolk, and sodium dodecyl sulfate (SDS) as emulsifiers to verify the applicability of SMLM to food samples. As for all other model emulsions in this thesis, high-pressure homogenization (HPH) was used for emulsification. Phosvitin was targeted with a primary antibody fluorescently labeled with Alexa Fluor 647, and PSF engineering was used to obtain two- and three-dimensional images of phosvitin-covered oil droplets. This approach allowed to visualize and analyze the spatial distribution of phosvitin across oil droplets at various depths within the sample up to 15 µm. The STORM data yielded a collection of phosvitin localizations at the oil-water interface, which required quantitative analysis. Visual inspection of oil droplets implied a homogeneous distribution of phosvitin in the model system. Therefore, **Chapter 3** introduced a quantitative method to assess the heterogeneity of emulsifiers adsorbed at droplet surfaces. To enhance the robustness of our method, localizations of proteins were simulated with homo- and heterogeneous distributions using Monte Carlo methods. The simulations accounted for an aggregation probability term to reflect varying degrees of heterogeneity. The relative position distribution (RPD) analysis was then employed to extract the histogram of relative distances between all neighboring localizations of a droplet. These histograms consistently revealed an identical distribution pattern for simulations of homogeneous distributions. In contrast, heterogeneous distributions altered the amplitude of the histograms' local maxima. By examining the local maxima and defining the relative peak amplitude, distributions at droplet interfaces were classified as homogeneous, partially heterogeneous, and heterogeneous. Further, this method was applied to a binary model system using both phosvitin and SDS as emulsifiers, which showed a partially heterogeneous distribution of phosvitin around the droplets. Additionally, ternary model emulsions, phosvitin/phospholipid/SDS and apolipoprotein B (apoB)/phospholipid/SDS were designed. Imaging of apoB, labeled with a secondary antibody conjugated to Alexa Fluor 555, revealed a more heterogeneous distribution compared to phosvitin.

The reconstructed images of the binary model emulsion using STORM indicated fewer phosvitin-covered droplets than total droplets observed via confocal microscopy. In **Chapter 4**, the specificity of the phosvitin antibody was first confirmed by comparing the localization of phosvitin covalently labeled with fluorescein isothiocyanate (FITC). Phosvitin-binding, DNA based affimers turned out to exhibit insufficient specificity. Once the specificity of the antibody was validated, the study progressed to investigate the interactions between protein and surfactant at the interface and the effect of protein concentration on their competitive behavior. For this purpose, re-scan confocal microscopy (RCM) on HPH-produced model emulsions revealed a bimodal droplet size distribution, in which small droplets were covered by SDS and large droplets by phosvitin, respectively. This inter-droplet heterogeneity in the coverage of droplets was in line with the time evolution of the emulsifier coverage of droplet interfaces during HPH. Further, STORM showed that the concentration of phosvitin did not affect the intra-droplet distribution at the droplet interface. Moreover, STORM provided a direct visualization of the redistribution of phosvitin in the HPH-prepared emulsions upon prolonged low-shear treatment, resulting in diffusion-assisted exchange of SDS and phosvitin between droplet interfaces and the continuous aqueous phase.

Chapter 5 delved into the most intricate model system examined in this thesis, utilizing egg yolk as an emulsifier to create a mayonnaise model emulsion. Using STORM, we mapped the spatial distribution and co-localization of two egg yolk proteins, phosvitin and apoB, at the oil droplet interfaces. Given the acidic conditions of the emulsion, the weak affinity of phosvitin for pro-oxidant iron ions positions it near sites of lipid radical formation on droplet surfaces. In contrast, the phosphoserine-rich composition of phosvitin makes it less effective at scavenging lipid radicals than apoB. The RPD method revealed heterogeneous distributions for both apoB and phosvitin. Analysis of individual droplets indicated a size-dependent preference for apoB/phosvitin coverage on larger droplets, with smaller ones presumably coated by phospholipids, a pattern influenced by the surface stabilization dynamics during HPH processing. Additionally, oxidation was localized using a three-color detection strategy, including fluorescently labeled antibodies and the fluorescent spin trap CAMPO-AFDye647 as a marker for protein radicals. We validated the coordinate-based co-localization analysis through simulations of protein localization at the interface, ensuring its applicability to our protein localization ring structure. Subsequent co-localization analysis of apoB/CAMPO-AFDye647 and phosvitin/CAMPO-AFDye647 indicated that pro-oxidant, iron-binding phosvitin was less prone to radical formation compared to apoB.

Chapter 6 explored the challenges and possibilities associated with directly visualizing emulsifiers and protein radicals at oil droplet interfaces using super-resolution microscopy. The outlook section presents a strategy for extending this research from model emulsions to full mayonnaise. Smaller, more target-specific probes such as nanobodies may be advantageous over antibodies and DNA-PAINT is to be considered as an alternative to STORM. The chapter concludes by discussing the significance of these methodological advancements in studying food emulsions at the single droplet level, potentially resolving discrepancies in the current literature on protein and lipid co-oxidation rates and enabling and steering the development of antioxidant strategies in the food industry.

Appendix

Acknowledgements
List of publications
Overview of completed training activities
About the author

Acknowledgments

As I look back on my doctoral journey, I find myself immersed in emotions and memories. I would like to express my heartfelt appreciation to the individuals who provided unwavering support and encouragement throughout this enriching experience.

Johannes Hohlbein, thank you for providing me the opportunity to pursue my Ph.D. in your group. Your mentorship has proven invaluable, both within the academic realm and beyond. Under your guidance, I have gained profound insights. I deeply appreciate the emphasis you place on maintaining a critical eye on all details—a lesson I highly value. Your thought-provoking comments and challenging questions consistently prompted me to view my research from different angles, ultimately opening new pathways for exploration.

John van Duynhoven, thank you for your support throughout my Ph.D. Your endless patience and motivation have been invaluable, providing a constant source of encouragement. I am grateful for the guidance and the positive environment you created, which played a significant role in my academic pursuits. Your remarkable expertise in unveiling valuable dimensions, even from my negative or seemingly inconclusive results, has amazed me and ignited my creativity with newfound inspiration.

Suyeon, I feel incredibly fortunate to have you as both a friend and colleague. Your presence at BIP has transformed the Ph.D. journey into an enjoyable research experience. I am grateful for your support, brilliant ideas, and engaging discussions that we have shared. Your delightful Korean cuisine and hospitality, alongside Vincent (Paas), have added a special warmth to this experience. I eagerly anticipate showing you Iran and visiting Korea in the future. Thank you for being my paranymphs. **Mariska**, the four years we spent together on the same project were delightful, filled with inspiring discussions and shared adventures. Your support and positive energy have been invaluable to me. I have seen little people as spirited as you, and I appreciate your kindness. Thank you for being my paranymphs

I'm grateful for the opportunity to collaborate with the *LocalBioFood* project members. **Ilja Voets**, your thoughtful comments and support have been invaluable. I sincerely appreciate your inspiring and fruitful discussions. **Lia**, collaborating with you opened the door to the fascinating world of emulsions during the early stages of my Ph.D., I appreciate our various meetings, discussions and secondments. **Maurien**, your discussions, support, and kindness have been a constant motivation to me. **Lizette**, thank you for your support and kindness. I appreciate the constructive feedback and your sharing of your industry experience as a scientist. **Mariliis**, I greatly appreciate your support and the insightful secondment in Amsterdam. **Sanam**, our wonderful Iranian collaboration in the field of soft matter has been truly enjoyable, and your expertise taught me a lot. I extend my thanks to **Roderick**, **Antonio**, **Nicolas**, **Soledad**, and **Rea** for their valuable discussions and support throughout the consortium meetings.

Next, I want to express my heartfelt appreciation to my colleagues for cultivating an inspiring spirit that greatly contributed to our positive and collaborative working environment. I thoroughly enjoyed our outings and the various fun activities we shared. **Koen**, our collaborative discussions were a delight, and I appreciate your warm assistance when I joined the BIP. **Martijn**, it has been enjoyable to engage in different conversations with you beyond just science. Being part of the same team as both of you has been a pleasure, and I thank you both for the fun activities, dinners, and drinks. **Vincent (**Boerkamp**)**, every time I received a notification with your name on my phone during my Ph.D., I anticipated a great day ahead, as it likely meant we would schedule a lunch together and have exciting discussions. **Benjamin**, you are not only a great colleague but also a great person. Thank you for turning the boring wait during image acquisition into exciting and amazing conversations in the dark room. **Christo**, when you joined us in the Ph.D. room, it completely changed my working days into energetic and fun mornings. Thank you for the laptop holder that you 3D printed for me; it saved me during my writing time at home. **Laavanya**, I always enjoyed talking to you; I had more pleasant coffee breaks when you dropped by the Helix. **Ahmad**, **Tanya**, **Wouter**, **Donny**, and **Raquel**, thank you for the good times during borrels, dinners, and discussions. **Vahid**, thank you for our science and beyond discussions every time you visited Wageningen. I am grateful for our collaboration. **Klaudia**, **Cleo**, **Lennart**, **Keshav**, **David**, **Chenyu**, **Morwarid**, **Dana**, **Jarne**, **Ian**, **Francesco**, and **Sam**, I really enjoyed the moments with you all in the lab, BIP colloquia, lunch, and coffee breaks.

Herbert van Amerongen, I greatly appreciate your support and your always making me feel welcome in your group. **John** (Philippi), thank you for your technical support. Every time I encountered challenges, you swiftly resolved them. We are fortunate to have you at BIP. **Cor**, thank you for all your support with lab supplies. You were always open to help, and I appreciate it. **Arjen**, it was always fun to discuss optics and microscopy with you. Thank you for your support and for sharing optical elements with me. **Emilie**, it was a great pleasure to be a part of the social committee with you (and others). **Sonja**, thank you for our fruitful discussions. Your passion for science not only encourages me but also exceeds my expectations, making academia feel more alive than I could have imagined. **Camilla**, **Rob**, **Henk, Frank**, **Jeremy**, and **Annelies**, thank you for contributing to the pleasant atmosphere at BIP.

I would like to acknowledge my Iranian friends for their invaluable presence in my life. Your friendship has been a source of great support and joy throughout this journey. **Pedram**, and **Leila**, you have always been our sounding board. After you moved to Europe, we have never felt alone anymore. I am so lucky to have such wonderful friends who know what I am thinking without having to say a single word. You are not just friends; you are family. Thanks for all of the laughs, advice, and sweet memories throughout time. **Navid**, **Somayeh**, and **Mahrokh**, you are such a lovely and kind family. We are lucky to have found you in the Netherlands. Thank you for your support and all the fun times we've had together. I hope we can maintain our friendship forever, no matter where we are on this planet.

Most importantly and above all, I would like to express my deepest gratitude to my wife, **Sana**, the love of my life. None of this journey would have been possible without your unconditional support. Your dynamism, and willingness to put your dreams on hold to bolster my aspirations are a testament to your incredible spirit. I strive each day to truly comprehend and cherish your sacrifices. I owe you everything. Furthermore, our family expanded during my last year of pursuing my Ph.D. to include our beloved son. **Mohammad Hasan**, I cannot express my feelings for you. With every smile of yours, a new life breathes into me, and hope blossoms within me. Your presence has propelled me to continue with strength on my path. I am deeply grateful to you for assisting me in writing my thesis. Every day, as I was engrossed in writing my thesis, and you crawled over to my desk, pulling yourself up from my legs to type on the keyboard like me, nothing could make the tedious writing more enjoyable for me than your sweet company.

بابا و **مامان،** از حمایت و عشق بی‌پایان شما ، سپاسگزارم. بدون زحمت‌ها و آموزه‌های شما، امکان دست‌یابی به هیچ یک از این موفقیت‌ها برایم ممکن نبود. فداکاری و دعاهای شما، روشنایی مسیرم برای دست یابی به آرزوهایم بوده است. ممنونم که همواره پشتیبان من بوده اید و به من ایمان داشتید. به دستان شما بوسه می‌زنم.

پدر و **مادر همسرم،** از تمام حمایت‌ها و محبت‌هایی که همیشه به من داشته‌اید، صمیمانه تشکر می‌کنم. بابت زیباترین گل جهان که مراقبت از او را به من سپرده اید، همیشه از شما سپاسگزار هستم.

حسین و **مامان زینب،** بابت تمام حمایت ها و تشویق های شما ممنونم. همیشه از اینکه با خانواده ی گرمتان در کنار هم هستیم احساس خوشبختی می‌کنم. **زینب جانم،** تولد تو زیبایی های زندگی من را پیش از پیش زیباتر کرد. همیشه برای دیدن تو لحظه شماری می‌کنم.

سجاد، با تمام قلبم از تو ممنونم که همیشه کنار من بوده ای. حضورت در زندگی‌ام همیشه برایم ارزشمند بوده و قلبم را سرشار از شادی کرده است. برایت آرزوی خوشبختی و موفقیت دارم.

سینا، از اینکه مثل برادر همراهم بوده ای، متشکرم. برای تو و همسرت بهترین ها را آرزو دارم.

List of publications

This thesis

Jabermoradi, A., Yang, S., Gobes, M. I., Van Duynhoven, J. P., & Hohlbein, J. (2022). Enabling single-molecule localization microscopy in turbid food emulsions. Philosophical Transactions of the Royal Society A, 380(2220), 20200164.

Jabermoradi, A., Van Duynhoven, J. P., & Hohlbein, J. Quantifying the distribution of proteins at the interface of oil-in-water food emulsions. (to be submitted)

Jabermoradi, A., Foroutanparsa, S., Voets, I. K., Janssen, J., Van Duynhoven, J. P., & Hohlbein, J. Super-resolution imaging reveals heterogeneity in the coverage of oil-in-water food emulsions. (to be submitted)

Jabermoradi, A., Yang, S., Van Duynhoven, J. P., & Hohlbein, J. Co-localization analysis of egg yolk proteins and formation of radicals at the interface of oil droplets in a mayonnaise model emulsion (to be submitted)

Other publication:

Martens, K. J., **Jabermoradi, A.**, Yang, S., & Hohlbein, J. (2021). Integrating engineered point spread functions into the phasor-based single-molecule localization microscopy framework. Methods, 193, 107-115.

Khandan, V., Boerkamp, V., **Jabermoradi, A.**, Fontana, M., Hohlbein, J., Verpoorte, E., Chiechi, R. C., & Mathwig, K. (2022). Viscophoretic particle transport. ArXive preprint, 2212.11503.

Overview of completed training activities

Discipline specific activities	**Organizer**	**Year**
SMLMs Delft	TU Delft	2019
Food ingredient functionality	WUR	2019
Dutch biophysics	NWO	2020
Training in re-scan confocal microscopy	Confocal.nl	2020
Dutch biophysics	NWO	2021
Advanced food analysis	VLAG	2022
SMLMs Paris	Institute Langevin	2022

General courses		
VLAG PhD week	VLAG	2019
Scientific Publishing	WGS	2019
Posters and Pitching	WGS	2020
Presenting with Impact	WGS	2020
Efficient Writing Strategies	WGS	2020
Writing Grant Proposals	WGS	2020
Competence Assessment	WGS	2020

Other activities		
Preparation of research proposal	WUR - BIP	2019
LocalBioFood project consortium	WUR, TU/e, Unilever, DSM	2019-2023
Food microscopy group meeting	BIP	2019-2023
Food ingredient functionality	BIP	2019
Colloquium	BIP	2020-2023

About the author

Abbas Jabermoradi was born in Tehran, Iran, on August 3, 1993. His academic journey commenced with a Bachelor of Physics degree from Shahid Beheshti University in 2011, where he graduated *cum laude*. In 2015, Abbas transitioned into the realm of Photonics, embarking on a new educational endeavor at the Laser and Plasma Research Institute of Shahid Beheshti University, where he also graduated *cum laude*. During his study, Abbas engaged in diverse projects, including constructing a Nipkow disk confocal microscope and simulating a 1550 nm fiber amplifier.

In April 2019, Abbas moved to the Netherlands to start his PhD project at the Laboratory of Biophysics (BIP) under the supervision of Prof. Dr. John PM van Duynhoven and Dr. Johannes Hohlbein, and the results of this project are presented in this dissertation.

This work was part of the LocalBioFood project, supported by the Dutch Research Council (NWO), grant number 731.017.204.

Cover design by Sana Shirazi and the author.

Printed by ProefschriftMaken.nl.